Fall 12-22-2010

Integrating Electrophysiological, Mechanical, and Optical Methods to Define the Mechanisms of Painful Facet Joint Injury

Kyle P. Quinn
University of Pennsylvania, kpquinn@seas.upenn.edu

Integrating Electrophysiological, Mechanical, and Optical Methods to Define the Mechanisms of Painful Facet Joint Injury

Abstract
Persistent pain is a common occurrence following whiplash injuries produced during motor vehicle crashes. The cervical facet joint and its capsule have often been identified as the source of chronic pain in patients with whiplash-associated disorders. However, for the majority of patients, no radiographic evidence of cervical spine injury is present. A capsular ligament stretch-based mechanism for initiating facet-mediated pain has been proposed based on human cadaveric studies of the facet joint kinematics during whiplash stimulations. However, without direct evidence of capsule damage during whiplash, the biomechanical and physiological mechanisms by which altered vertebral kinematics produce a facet capsule injury have not been fully elucidated. The goal of this thesis was to identify the facet joint loading conditions that produce microstructural damage to the facet capsular ligament and determine whether such loading can initiate neuronal plasticity in the spinal cord. Using a rat model of cervical facet joint loading, spinal neuron hyperexcitability was quantified from extracellular voltage recordings after imposing joint loading conditions that do and do not produce persistent pain symptoms. To determine whether neuronal hyperexcitability corresponds to a detectable change in the microstructure of the facet capsular ligament, a quantitative polarized light imaging technique was employed to define collagen fiber kinematics during capsule loading. A vector correlation analysis technique was developed to localize anomalies in the fiber kinematics of the human facet capsular ligament during tensile loading and was compared to changes in the mechanical response of the tissue during loading. The collagen fiber kinematics of the rat facet capsular ligament were also defined and compared to the joint loading conditions that produce neuronal plasticity and persistent pain symptoms. Altered fiber alignment and changes in the mechanical function of the human facet capsule were quantified after a subfailure vertebral retraction to determine the potential for microstructural damage in the facet capsule following whiplash-like motion. This work demonstrates that facet capsule stretch can cause microstructural changes to the capsular ligament in the absence of capsule rupture and establishes a framework to identify the mechanisms of facet joint injury and the development of central sensitization and persistent pain.

Degree Type
Dissertation

Degree Name
Doctor of Philosophy (PhD)

Graduate Group
Bioengineering

First Advisor
Beth A. Winkelstein

Keywords
polarized light, facet joint, collagen fibers, whiplash, chronic pain, injury

INTEGRATING ELECTROPHYSIOLOGICAL, MECHANICAL, AND OPTICAL METHODS TO DEFINE THE MECHANISMS OF PAINFUL FACET JOINT INJURY

Kyle P. Quinn

A DISSERTATION

in

Bioengineering

Presented to the Faculties of the University of Pennsylvania in Partial Fulfillment

of the Requirements for the Degree of Doctor of Philosophy

2010

_____

Beth A. Winkelstein, Associate Professor of Bioengineering
Supervisor of Dissertation

_____

Susan S. Margulies, Professor of Bioengineering
Graduate Group Chairperson

Dissertation Committee:

Dawn M. Elliott, Associate Professor of Orthopaedic Surgery
Francis J. Golder, Assistant Professor of Anesthesiology
David F. Meaney, Professor of Bioengineering
Barry S. Myers, Professor of Biomedical Engineering

ACKNOWLEDGMENTS

I am tremendously grateful to my mentor, Dr. Beth Winkelstein, for the time and commitment she has put into my training and development as a professional. I hope to continue to learn from her insight and experience in the years to come. I would also like to thank the members of my thesis committee, Dr. Dawn Elliott, Dr. Frank Golder, Dr. David Meaney, and Dr. Barry Myers for their insightful questions and guidance on this thesis work.

I would like to specifically thank Dr. Frank Golder for the training and assistance he provided in developing the electrophysiological studies in this thesis. I am very appreciative for the use of his laboratory equipment, resources, and software for the completion of those experiments. I would also like to thank Sharon Martinez for her assistance throughout the time that I spent in the Golder Laboratory.

I am very grateful to all of the current, and former, members of the Spine Pain Research Lab for their support and friendship over the years. I would like to specifically acknowledge the lab members who assisted with the development and completion of the research presented in this thesis, including Joel Bauman, Kiersten Craig, Nate Crosby, Martin Davis, Ling Dong, Jeff Kras, and Katie Lee.

I would like to thank my family for their encouragement, constant support, and advice over the years. Finally, I would like to thank my wife Jen, for her love, her patience, and her support.

ABSTRACT

INTEGRATING ELECTROPHYSIOLOGICAL, MECHANICAL, AND OPTICAL METHODS TO DEFINE THE MECHANISMS OF PAINFUL FACET JOINT INJURY

Kyle P. Quinn

Beth A. Winkelstein

Persistent pain is a common occurrence following whiplash injuries produced during motor vehicle crashes. The cervical facet joint and its capsule have often been identified as the source of chronic pain in patients with whiplash-associated disorders. However, for the majority of patients, no radiographic evidence of cervical spine injury is present. A capsular ligament stretch-based mechanism for initiating facet-mediated pain has been proposed based on human cadaveric studies of the facet joint kinematics during whiplash stimulations. However, without direct evidence of capsule damage during whiplash, the biomechanical and physiological mechanisms by which altered vertebral kinematics produce a facet capsule injury have not been fully elucidated. The goal of this thesis was to identify the facet joint loading conditions that produce microstructural damage to the facet capsular ligament and determine whether such

loading can initiate neuronal plasticity in the spinal cord. Using a rat model of cervical facet joint loading, spinal neuron hyperexcitability was quantified from extracellular voltage recordings after imposing joint loading conditions that do and do not produce persistent pain symptoms. To determine whether neuronal hyperexcitability corresponds to a detectable change in the microstructure of the facet capsular ligament, a quantitative polarized light imaging technique was employed to define collagen fiber kinematics during capsule loading. A vector correlation analysis technique was developed to localize anomalies in the fiber kinematics of the human facet capsular ligament during tensile loading and was compared to changes in the mechanical response of the tissue during loading. The collagen fiber kinematics of the rat facet capsular ligament were also defined and compared to the joint loading conditions that produce neuronal plasticity and persistent pain symptoms. Altered fiber alignment and changes in the mechanical function of the human facet capsule were quantified after a subfailure vertebral retraction to determine the potential for microstructural damage in the facet capsule following whiplash-like motion. This work demonstrates that facet capsule stretch can cause microstructural changes to the capsular ligament in the absence of capsule rupture and establishes a framework to identify the mechanisms of facet joint injury and the development of central sensitization and persistent pain.

TABLE OF CONTENTS

LIST OF TABLES

LIST OF FIGURES

CHAPTER 1

Introduction

The annual incidence of neck pain in the general population is estimated at nearly 20% (Croft et al., 2001), and for many individuals, the symptoms can become chronic and debilitating (Hogg-Johnson et al., 2008). Chronic neck pain affects over 15.5 million individuals in the United States annually and represents nearly $30 billion in health-related expenses (Freeman et al. 1999). Whiplash is a common cause of chronic neck pain, with 19-60% of people affected reporting pain lasting two years or more after injury (Gargan and Bannister 1994; Radanov et al. 1995). As such, whiplash-associated disorders are responsible for nearly half of patient-care costs from motor vehicle crashes (Quinlan et al. 2004). The cervical facet joint and its capsule have been identified as the site of chronic pain following whiplash in an estimated 25-62% of cases (Aprill and Bogduk, 1992; Barnsley et al. 1994). Yet, despite the high incidence of facet-mediated pain, the biomechanical and physiological mechanisms by which altered vertebral kinematics produce a mechanically-induced facet joint injury and persistent pain have not been fully elucidated.

Human cadaveric studies of the facet joint kinematics during whiplash implicate excessive stretch of the cervical facet capsular ligament as a cause of joint injury, and possibly pain, following whiplash (Deng et al., 2000; Kaneoka et al., 1999; Panjabi et al., 1998; Pearson et al., 2004; Sundararajan et al., 2004; Yang and King, 2003; Yoganandan et al., 1998). A capsular ligament stretch-based mechanism for initiating facet-mediated pain has been further substantiated by goat and rat models of facet joint loading. Acute electrophysiological studies in the goat demonstrate primary afferent neuron firing to be correlated with the magnitude of imposed facet capsule stretch (Chen et al., 2005; Lu et al., 2005). In a rat model of cervical facet joint loading, behavioral hypersensitivity has been shown to be sustained for up to 42 days (Rothman et al., 2008). In that model, nociceptive and inflammatory responses throughout the peripheral and central nervous systems have been also shown to be modulated by the magnitude of facet capsule stretch and to be associated with pain symptoms (Dong et al., 2008; Dong and Winkelstein, 2010; Lee et al., 2004a, 2008; Lee and Winkelstein, 2009). Collectively, these animal models suggest that facet capsule stretch of a sufficient magnitude can activate nociceptive primary afferent neurons, which in turn may alter pain-related biochemical markers in the spinal cord and produce sustained behavioral hypersensitivity. However, despite this growing evidence, there is no direct measure of sensory neuron modulation in the spinal cord following facet loading to elucidate the central neuronal contributions for chronic pain from such peripheral tissue injuries.

Identifying the mechanisms of facet-mediated pain and preventing whiplash-associated disorders has remained a challenge because capsule ruptures are not a prerequisite for development of chronic pain in clinical studies or animal models (Lee et al., 2008; Lee and Winkelstein, 2009; Lord et al., 1996a; Pettersson et al., 1997; Voyvodic et al., 1997). In addition, facet capsule ruptures are not visible during or after whiplash-like simulations of osteoligamentous cervical spine specimens (Grauer et al., 1997; Panjabi et al., 1998a; Pearson et al., 2004; Siegmund et al., 2000, 2001; Yoganandan and Pintar, 1997). Accordingly, without direct evidence of capsule damage or mechanical failure, strain measurements based on bony displacements or ligament tissue deformation have been used to define if, and by how much, the facet joints exceed their normal range of motion and magnitude of deformation during subfailure whiplash-like loading (Grauer et al., 1997; Panjabi et al., 1998a; Pearson et al., 2004; Siegmund et al., 2000, 2001; Yoganandan and Pintar, 1997). Although facet capsule stretch has been defined as "excessive" during certain cervical spine motions, no study has investigated if microstructural damage in the capsular ligament is produced during subfailure capsule stretch or determined the collagen fiber responses for the loading conditions that may initiate the development of chronic pain.

The overall objective of the studies in this thesis was to determine whether subfailure facet joint loading produces microstructural damage to the capsular ligament and initiates the development of neuronal plasticity in the spinal cord. Using an established rat model of C6/C7 facet joint loading (Lee et al., 2008; Lee

and Winkelstein, 2009), spinal neuron hyperexcitability was quantified from extracellular voltage recordings after imposing different joint loading conditions that do and do not produce persistent pain symptoms. To determine whether spinal neuronal hyperexcitability corresponds to a detectable change in the microstructure of the facet capsular ligament, a polarized light technique was employed to quantify collagen fiber kinematics during tissue loading. This polarimetric-based approach was used to localize anomalies in the fiber kinematics of the capsular ligament during joint loading and was compared to the joint's overall mechanical response. This analysis of the collagen fiber kinematics of the capsular ligament was also compared to the loading conditions that produce neuronal plasticity and persistent pain symptoms. Lastly, microstructural and mechanical changes to the human facet capsular ligament were assessed during and after joint retraction to determine whether microstructural damage can be produced during vertebral motions relevant to whiplash kinematics.

Collectively, the studies detailed in this thesis are organized into chapters that summarize the relevant experiments. Chapter 2 presents background information on cervical spine and facet anatomy, whiplash-associated disorders, facet joint kinematics during whiplash, and techniques to quantify microstructural damage. In Chapter 3, the hypotheses and specific aims of this thesis are presented. Chapter 4 summarizes the studies related to Aim 1 that define neuronal hyperexcitability in the spinal cord following facet joint loading in the rat. Chapter 5 presents studies related to Aims 2a and 2c, which establish a polarized light

analysis technique to identify anomalous collagen fiber responses in the human facet capsular ligament. In Chapter 6, the studies related to Aim 2b are detailed, presenting the application of polarimetric techniques to determine the potential for anomalous collagen fiber responses in the rat facet capsule under a loading paradigm simulating those conditions used in the in vivo studies in Chapter 4. In Chapter 7, studies related to Aim 3 quantify changes to the collagen fiber alignment in human facet capsular ligaments during and after whiplash-like retraction of isolated joints. Additionally, full field strain measurements based on fiber alignment pattern tracking were quantified and compared to fiber-based outcomes in Chapter 7. Finally, all of the studies detailed in this thesis are synthesized and placed in the broader context of clinical and experimental studies of whiplash in Chapter 8. The limitations of this work and the future directions for related research are also presented in Chapter 8.

CHAPTER 2

Background

The cervical facet joint has been identified as the source of pain in over half of whiplash patients (Barnsley et al., 1993, 1995; Lord et al., 1996a). Biomechanical studies demonstrate that the facet capsular ligament is at risk for excessive loading during whiplash, but those studies report no obvious indications of capsule rupture or mechanical failure during or after loading (Deng et al., 2000; Kaneoka et al., 1999; Panjabi et al., 1998; Sundararajan et al., 2004; Yogandandan and Pintar, 1997). A variety of mechanical, microstructural, and cellular changes have been attributed to subfailure loading and may indicate soft tissue damage sufficient to produce physiological dysfunction and pain (Bruns et al., 2000; Gimbel et al., 2004; Panjabi et al., 1996, 1999, 2001; Pollock et al., 2000; Provenzano et al., 2002, 2005; Thomopoulos et al., 2003). However, the relationships between subfailure ligament loading, microstructural damage, and neuronal dysfunction following loading to the facet joint are not well-defined; in order to understand the mechanisms of persistent facet-mediated pain after a whiplash event, the relationship between structural damage in facet capsule and the development of plasticity in central nervous system plasticity must be defined.

This chapter reviews the relevant cervical spine anatomy, clinical and experimental evidence of facet-mediated pain, whiplash kinematics, and general hallmarks of collagenous tissue injury. Additional detailed background information related to the specific studies for each aim are also provided at the beginning of Chapters 4 through 7.

2.1. Cervical spine & facet joint anatomy

The human cervical spine consists of seven articulating bony vertebrae that are stabilized by a variety of surrounding soft tissues, including musculature, ligaments, and cartilage. On the anterior side of the spine, intervertebral discs connect adjacent vertebral bodies to provide support and facilitate limited translation and rotation in all directions. Posterolateral to the vertebral bodies, two articular bony columns span the length of the spine and are connected to the vertebral body at each level through the bony pedicle (Figure 2.1). Laminae at each vertebral level extend in a medial and posterior direction from the articular columns until joining together to form a spinous process that extends in a superior and posterior direction (Figure 2.1). Collectively, the pedicles, articular processes, and spinous process form an arch to protect the spinal cord.

Facet joints (or zygapophysial joints) are located along the articular columns in between each level where the superior and inferior portions of two articulating bony facets contact each other (Figures 2.1 and 2.2). The articulating

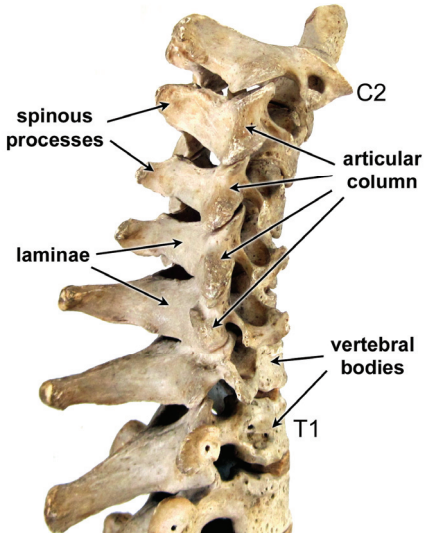

Figure 2.1. Lateral view of the cervical spine bony structures spanning the C2-T1 levels.

bony facet surfaces are covered by articular cartilage which is lubricated by synovial fluid. These articular surfaces are oriented obliquely, but in the lower cervical spine have approximately a 45° orientation from the horizontal in the sagittal plane. The facet capsular ligament envelopes the outer joint surface from pedicle to lamina, while the ligamentum flavum encloses the joint along its inner medial surface. This joint capsule provides a closed environment for the inner synovial membrane and the articular cartilage.

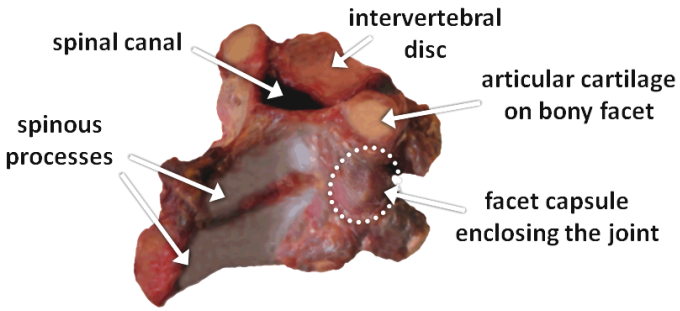

Figure 2.2. A posterior-lateral view of a C6/C7 spinal motion segment with the right facet joint circled and its capsule labeled.

The facet capsular ligament consists primarily of a dense network of collagen fibers approximately 50-100 nm in diameter (Figure 2.3). Ligament tissue is approximately 65-70% water by weight, but the primary load bearing component is type I collagen (70-80% dry weight) (Ralphs and Benjamin, 1994; Woo et al., 2006). Additional collagen types, glycoproteins, proteoglycans, and fibroblasts are also found in ligament tissue (Hakkinen et al., 1993; Woo et al., 2006). Histological studies of human, goat, rabbit, and rat facet joints have identified both proprioceptive and nociceptive nerve fibers throughout the facet capsule which encode the magnitude of joint loading (Cavanaugh et al., 1989, 1996; Chen et al., 2006; Inami et al., 2001; McLain, 1994). Evidence of nerve fibers in the facet capsule that are reactive for neuromodulators, such as substance P and calcitonin gene-related peptide, demonstrate the capability of these afferent fibers to transmit nociceptive signals (Beaman et al., 1993; el-Bohy et al., 1988; Inami et al., 2001; Kallakuri et al., 2004; Yamashita et al., 1993). The proprioceptive and nociceptive fibers in the facet capsule converge in the spinal nerves located just superior and inferior to each joint; the facet joint is innervated by the medial branches of the dorsal rami of the superior and inferior levels (Bogduk and Marsland, 1988; Lang 1993). The afferents terminate in the dorsal horn of the spinal cord and synapse with interneurons that process and relay the sensory information.

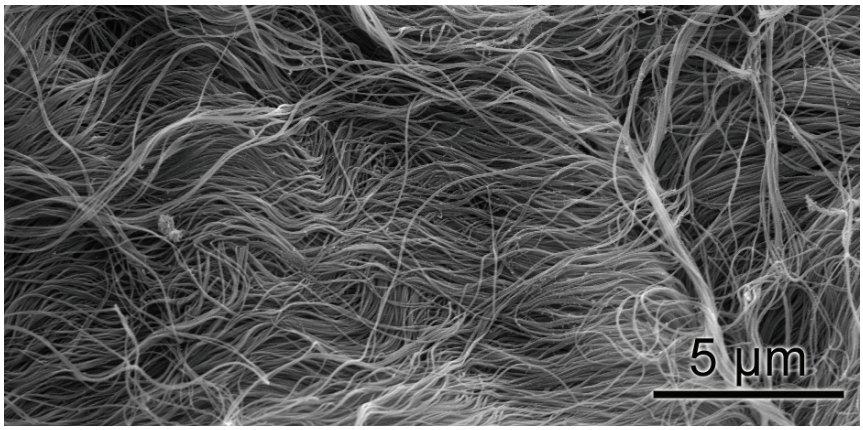

Figure 2.3. A scanning electron microscopy image of human cervical facet capsular ligament tissue reveals a dense layer of collagen fibers.

The dorsal horn of the spinal cord contains a complex arrangement of neurons that integrate different afferent sensory information. Most neurons in the dorsal horn are excitatory or inhibitory interneurons arranged in networks at each spinal segmental level to enable signal processing. After interneuron processing, the afferent signal can be sent to motor neurons or propriospinal neurons to produce a spinal reflex motion, such as a withdrawal response to noxious stimuli (Vierck, 2006). The afferent signal may also be relayed by projection neurons with axons ascending to a variety of supraspinal structures in the central nervous system (CNS), such as the brainstem and thalamus. Prolonged nociceptive afferent input can produce central sensitization and/or synaptic plasticity within the spinal cord, which can result in persistent pain (Woolf and Salter, 2006). Additional background on the spinal cord cytoarchitecture and plasticity is provided in Chapter 4 as it relates to the studies of spinal neuron hyperexcitability in Aim 1.

2.2. Whiplash-associated disorders & facet joint injury

Patients that sustain a whiplash-related injury can present with a variety of symptoms that are collectively referred to as whiplash-associated disorders. The primary complaint reported in clinical studies is neck pain, which can radiate to the head, shoulders, and/or arms (Holm et al., 2008; Spitzer et al., 1995). In addition, neck stiffness, headache, and paresthesias are also frequently reported (Curatolo et al., 2001; Hildingsson and Toolanen, 1990; Norris and Watt, 1983; Radanov et al., 1991). Yet, most clinical studies of whiplash patients report no radiographic evidence of any injury to the structures of the neck (Bogduk and Yoganandan, 2001; Pettersson et al., 1997; Taylor and Twomey, 1993; Voyvodic et al., 1997). Patients with chronic pain after whiplash injury demonstrate increased sensitivity to stimuli that are normally non-noxious (i.e. allodynia) and noxious (i.e. hyperalgesia) (Curatolo et al., 2001; Greening et al., 2005; Sheather-Reid and Cohen, 1998; Sterling et al., 2006). Hypersensitivity to electrical and mechanical stimuli extends across the neck to the lower limbs in whiplash patients (Curatolo et al., 2001; Scott et al., 2005). This widespread hypersensitivity to different stimulus modalities exhibited well-beyond the initial location of neck injury suggests that the central nervous system becomes sensitized. Furthermore, decreased spinal reflex thresholds to electrical stimuli were measured by electromyography in whiplash patients, which strongly suggests neuronal plasticity in the spinal cord (Banic et al., 2004). Central sensitization would explain the presence of persistent pain and hypersensitivity identified in many whiplash cases in the absence of any

evidence of injury from diagnostic imaging. Furthermore, sensitization and long-term plasticity in the spinal cord is attributed as the driving mechanism responsible for chronic pain in many animal models (Ji and Woolf, 2001; Scholz and Woolf, 2002; Woolf and Salter, 2000). Cervical facet capsule stretch in the rat produces the same anatomical patterns of hypersensitivity observed in whiplash patients (Lee et al., 2008; Lee and Winkelstein, 2009), but no study has directly linked behavioral hypersensitivity to a change in neuronal excitability in the spinal cord following whiplash or a facet joint injury.

Synovial joint capsules throughout the body are capable of producing pain following injury (Resnick and Niwayama, 1981), and the cervical facet joint and its capsule have been identified as a source of pain in many clinical studies (Bogduk and Marsland, 1999; Barnsley et al., 1995; Lord et al., 1995, 1996a, b; Manchikanti et al., 2002). In patients with chronic neck pain, the cervical facet joint has been identified as the source of pain in 54-62% of cases originating from whiplash injury and idiopathic causes (Barnsley et al., 1995; Lord et al., 1996a; Manchikanti et al., 2002). In whiplash cases, the lower cervical spine levels (C5-C7) are the most commonly reported sites of pain (Barnsley et al., 1995; Bogduk and Marsland, 1999). Comparative local anesthetic blocks using placebo-control intra-articular injections identify the cervical facet joint as the source of pain in as many as 60-72% of patients with whiplash-associated neck pain (Barnsley et al. 1993; Lord et al. 1996a). A radiofrequency neurotomy of the medial branches of the dorsal rami that innervate painful facet joints can produce long-lasting relief for more than half

of whiplash patients receiving treatment (Lord et al., 1995, 1996b). Additionally, stimulation of the cervical facet joints in normal volunteers through the injection of a contrast medium produced pain patterns that are representative of those observed in patients with chronic neck pain (Dwyer et al., 1990). These clinical studies demonstrate that the facet joint is capable of producing pain in the general population and is often the source of pain in whiplash-related cases even without any capsule tears evident though radiography or magnetic resonance imaging.

2.3. Cervical spine & facet joint kinematics during whiplash

With clinical evidence that points to the facet joint's involvement in painful whiplash injury, a variety of biomechanical studies using volunteers and cadavers have characterized the cervical spine and facet joint kinematics during whiplash. During the first 130 ms after a low-speed rear-end impact, the torso rises upward and forward imposing compressive and shear forces in the cervical spine (McConnell et al., 1993). Based on volunteer studies involving low-speed impacts and high-speed X-ray imaging, the cervical spine is believed to straighten during the first 50 ms and then form an "S" shape as the lower cervical spine extends and the upper cervical spine flexes (Kaneoka et al., 1999; Ono et al., 1997) (Figure 2.4). After approximately 120 ms, the head begins to rotate backwards eventually producing cervical spine extension at all spinal levels (Bogduk and Yoganandan, 2001; McConnell et al., 1993; Ono et al., 1997). Although the spinal kinematics

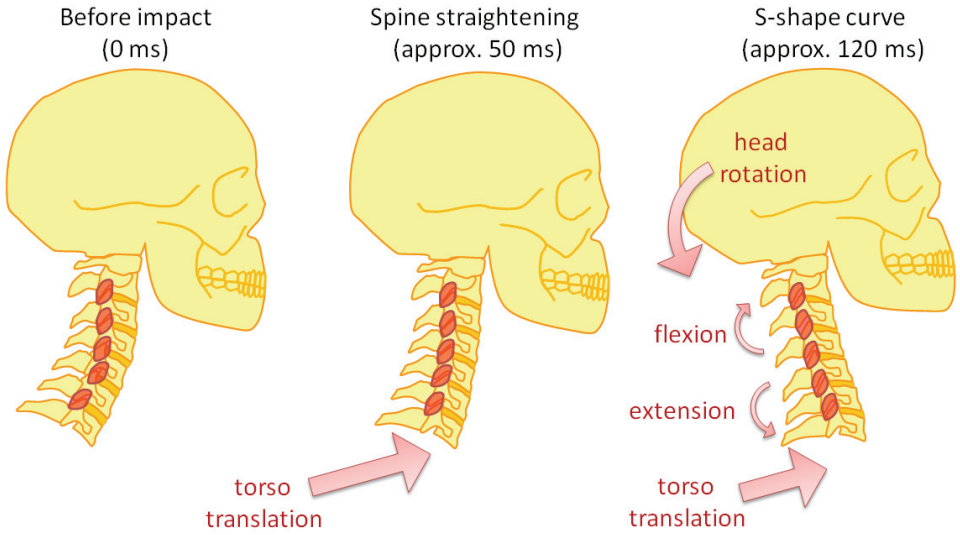

Figure 2.4. Cervical spine kinematics during whiplash. The cervical spine straightens during the first 50 ms after impact, and then forms an "S" as the lower cervical segments undergo extension and the upper segments undergo flexion.

during whiplash deviate from what is experienced during the activities of daily living, these overall neck kinematics do not exceed the normal range of neck rotation in the sagittal plane (Matsushita et al., 1994; McConnel et al., 1993; Szabo et al., 1996).

Within the first 120 ms of rear-end vehicle impact, the cervical facet capsular ligament is believed to undergo excessive stretching due to the abnormal spinal motions experienced during whiplash (Bogduk and Yoganandan, 2001; Kaneoka et al., 1999; Ono et al., 1997; Panjabi et al., 1998; Sundararajan et al., 2004) (Figures 2.4 and 2.5). Human cadaveric studies have defined the local kinematics of the cervical facet joints during whiplash simulations by tracking bony displacements (Cusick et al., 2001; Deng et al., 2000; Ito et al., 2004; Luan et al.,

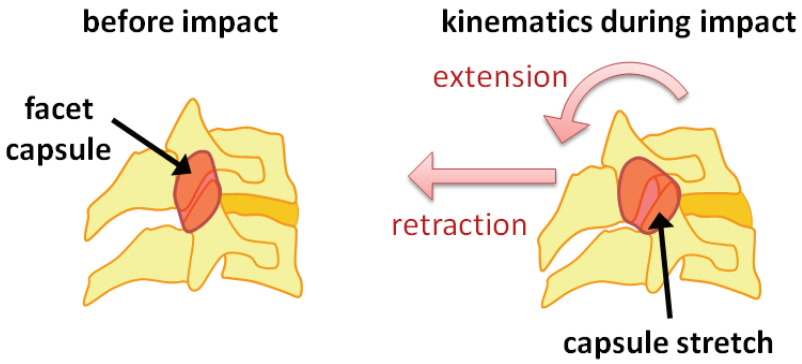

Figure 2.5. Facet joint kinematics during whiplash. Capsule stretch is produced by a combination of vertebral retraction and extension.

2000; Panjabi et al., 1998; Sundararajan et al., 2004; Yoganandan and Pintar, 1997; Yoganandan et al., 1998). In isolated cervical spine specimens, the articular processes in the lower cervical spine translate during whiplash-type loading to produce facet joint loading that may exceed its normal range of motion (Grauer et al., 1997; Ito et al., 2004; Pearson et al., 2004; Stemper et al., 2005; Yoganandan and Pintar, 1997; Yoganandan et al., 1998). In a study of isolated cervical spines that simulated low-speed, rear-end impacts by imposing horizontal T1 accelerations ranging from 3.5-8 g, facet capsular ligament strains were estimated from bony markers across the joints (Pearson et al., 2004). In that study, the C6/C7 facet capsular ligament sustained a peak strain of 39.9±26.3% during an 8 g impact, which significantly exceeded the strains (10.7±9.3%) measured during normal spinal motions (Pearson et al., 2004). Whiplash simulations involving whole cadavers during low-speed (4.5-9.5 mph) impacts estimated that retraction of the

facet joint ranged from 2.2-4.2 mm in the lower cervical spine (Deng et al., 2000; Luan et al., 2000; Sundararajan et al., 2004). In a study of isolated cervical spine motion segments, a combination of compression, extension, and shear loading was applied to simulate whiplash kinetics (Siegmund et al., 2000, 2001). In that study, maximum vertebral retractions between 2.2-2.5 mm were produced at 135 N of shear force, which corresponds to the peak horizontal force at the atlanto-occipital joint during low-speed rear-end impacts in volunteers (Ono et al., 1997; Siegmund et al., 2000, 2001). Together, all of these cadaveric studies suggest that the cervical facet joint may undergo an excessive retraction during whiplash, but rupture of the facet capsular ligament has not been typically reported to occur during loading (Deng et al., 2000; Luan et al., 2000; Panjabi et al., 1998; Pearson et al., 2004; Siegmund et al., 2000, 2001; Sundararajan et al., 2004; Yoganandan et al., 1998). Although there is a lack of clinical and experimental evidence of facet capsule damage following whiplash, no study has determined whether microstructural damage can be detected before gross tissue rupture, which could provide an explicit definition of when vertebral motions actually become "excessive".

Many studies have investigated the mechanical properties of the isolated cervical facet joint to define the structural and material limits of the facet capsular ligament. The mechanical properties of the human cervical facet capsule have been defined at gross failure under tension and shear (Mykelbust et al., 1988; Siegmund et al., 2000, 2001; Winkelstein et al., 1999, 2000; Yoganandan et al., 2000). A number of these cadaveric studies also demonstrated mechanical injury of the facet

capsule to occur prior to gross ligament failure in both isolated and full cervical spine specimens (Panjabi et al., 1998; Siegmund et al., 2001; Winkelstein et al., 1999, 2000; Yoganandan et al., 2001). Partial failures, defined by a decrease in load with increasing displacement, were noted prior to gross failure of isolated cervical facet capsules (Siegmund et al., 2000, 2001; Winkelstein et al., 1999, 2000). The occurrence of these partial ligament failures (previously termed "sub-catastrophic" failures) strongly suggests that the structure of the facet capsular ligament may be altered in the absence of overt ligament rupture. Although these studies collectively provide an estimate of the mechanical tolerance of the human facet joint and its capsule, the strains and bony displacements reported for partial failure of the facet capsular ligament usually are not reached during whiplash simulations. Therefore, ligament damage that may be produced during loading without any detectable failure may be sufficient to activate nociceptors in the capsule and initiate the development of facet-mediated neck pain.

2.4. Evidence of subfailure ligament damage

Ligament sprains are among the most common injuries sustained during sports-related activities and motor vehicle crashes (Beynnon et al., 2005; Braun, 1999; Yawn et al., 2000). According to the American Academy of Orthopaedic Surgeons, Grade I sprains correspond to a mildly damaged ligament with no tearing, Grade II sprains correspond to a partial tear of the ligament, and Grade III sprains correspond to a complete rupture (O'Donoghue, 1976). Significant

advances have been made in biomechanical research to define and prevent gross ligament ruptures, but less severe, Grade I and II, sprains also have the potential to lead to debilitating chronic conditions (Bogduk and Yoganandan, 2001; Jones et al., 2009). In failure studies of rat facet capsular ligament tissue, ligament yield (defined by a decrease in the tangent stiffness of the tissue) was identified before partial or gross failures (Quinn and Winkelstein, 2007). The first visual evidence of ligament rupture coincided with the detection of partial failure in that study, which suggests that ligament loading to its yield point may correspond to a Grade I sprain. However, without supporting data that identify changes to the tissue microstructure or overall ligament function, the detection of ligament yield during isolated ligament loading does not provide conclusive evidence of a subfailure tissue injury.

It has been suggested that loading ligaments beyond their yield point produces permanent deformation (McMahon et al., 1999; Yoganandan et al., 1989). Many studies have shown that subfailure loading of ligaments produces laxity, decreases stiffness, and alters the viscoelastic response (Panjabi et al., 1996, 1999, 2001; Pollock et al., 2000; Provenzano et al., 2002). Pollock et al. (2000) reported 4.6±2.0% in residual laxity after distracting the human glenohumeral ligament to just-below tissue failure. Using a similar study design, Iatridis et al. (2005) detected an increase in laxity following loading to 80% of the ultimate tensile strain in annulus fibrosus samples. After the application of a single, variable subfailure displacement magnitude and ten minutes of viscoelastic recovery, Provenzano et al.

(2002) determined the threshold for laxity in rat medial collateral ligaments to be 5.14% strain. Panjabi et al. (1996) also reported increased laxity and a decrease in stiffness in rabbit anterior cruciate ligaments after a stretch to 80% of its ultimate tensile strength, despite not detecting changes in the failure properties. Although subfailure loading can produce changes in the mechanical properties of ligaments, the confounding effects of tissue preconditioning can make defining a threshold for ligament damage problematic when based solely on altered mechanical properties.

2.5. Polarized light imaging to quantify collagen fiber organization

Polarized light techniques offer an effective method to quantify the organization of the load-bearing collagen microstructure in ligament and tendon (Boorman et al., 2006; Diamant et al., 1972; Dickey et al., 1998; Gathercole and Keller, 1991; Järvinen et al., 2004; Niven et al., 1982; Whittaker and Canham, 1991; Yeh et al., 2003). Through a variety of optical arrangements, collagen fiber directions can be inferred in a tissue by utilizing collagen's natural linear birefringence which causes light to travel through the tissue at a speed that is dependent on the orientation of the collagen (Wang and Wu, 2007). Both the collagen fiber direction and the magnitude that the light speed is retarded can be quantified from a series of polarized light images. In studies where polarized light passes through a tissue sample with multiple layers of fibers, the light retardation can be used to estimate the strength of alignment through the thickness of the tissue (Tower et al., 2002).

Polarized light microscopy has been used to quantify differences in the distribution of collagen fiber directions in rat and sheep ligaments and tendons in order to characterize the changes in the microstructural organization of a tissue after injury (Bruns et al., 2000; Gimbel et al., 2007, 2004; Quinn et al., 2007; Thomopoulos et al., 2003). In a rat model of tendon repair, the strength of collagen fiber alignment in the supraspinatus tendon was significantly lower two weeks after surgical detachment compared to uninjured control tissue (Gimbel et al., 2004). After painful subfailure facet capsular ligament loading in a rat model, a decrease in fiber alignment was also measured in the lateral aspect of the capsular ligament through polarized light microcopy analysis of tissue sections (Quinn et al., 2007). The decrease in fiber alignment detected in the capsular ligament may explain the production of laxity that was also measured in isolated joints in that study. Interestingly, the fiber alignment did not change significantly in the dorsal aspect of the capsule, where the largest strains were measured during loading of isolated joints (Quinn et al., 2007). The discrepancy between the location of maximum strain and the location of altered microstructural organization in that study suggests that alternative experimental approaches are needed in order to detect and localize microstructural damage that has not yet expanded into a visible rupture.

2.6. Summary

During a rear-end automotive impact, the facet capsular ligaments in the lower cervical spine are at risk for excessive loading and have been identified as the

source of pain in the majority of whiplash patients (Barnsley et al., 1993, 1995; Bogduk and Yoganandan, 2001; Deng et al., 2000; Kaneoka et al., 1999; Lord et al., 1996a, b; Panjabi et al., 1998; Sundararajan et al., 2004; Yogandandan and Pintar, 1997). Facet-mediated pain can produce widespread hypersensitivity in anatomical regions that are too distant from the neck to be explained by the modulation of peripheral neurons (Banic et al., 2004; Curatolo et al., 2001). This finding suggests that neuronal plasticity in the spinal cord may be a large contributor to the maintenance of chronic pain in these cases. However, the absence of any measurable capsule ruptures after whiplash loading in both clinical and experimental studies has made it difficult to define thresholds for facet joint injury or to determine the underlying mechanistic causes of facet-mediated pain. The overall objective of this thesis is to identify the different facet joint loading conditions that produce sustained neuronal plasticity in the spinal cord and to define the occurrence of microstructural damage in the facet capsule in an effort to determine the mechanisms behind facet-mediated pain following whiplash.

CHAPTER 3

Rationale, context & hypotheses

3.1. Rationale & context

The cervical facet joint is a frequent source of neck pain in 54-60% of the chronic neck pain cases originating from whiplash injury or idiopathic causes (Barnsley et al., 1995; Lord et al., 1996; Manchikanti et al., 2002). Patients with unresolved neck pain after whiplash often demonstrate secondary hyperalgesia (Banic et al., 2004; Curatolo et al., 2001; Greening et al., 2005; Sheather-Reid and Cohen, 1998), which suggests that central sensitization may contribute to chronic neck pain. However, no study has identified any direct evidence of spinal neuron plasticity following facet joint loading. Diagnosing facet-mediated pain and understanding its mechanisms has been complicated by a lack of any evidence of overt tissue damage or injury in the cervical spine (Pettersson et al., 1997; Voyvodic et al., 1997; Yoganandan et al., 2001). Furthermore, visible rupture of the cervical facet capsule is not produced in cadaveric studies that do report facet capsular ligament stretch during whiplash simulations (Cusick et al., 2001; Deng et al., 2000; Grauer et al., 1997; Ito et al., 2004; Luan et al., 2000; Pearson et al., 2004; Stemper et al., 2005; Yoganandan and Pintar, 1997). Although these clinical

and biomechanical studies suggest a relationship between facet capsule stretch and chronic pain, there is no clear understanding of the loading conditions that initiate the onset of facet capsular ligament damage or whether those loading scenarios can produce central sensitization and/or symptoms associated with persistent pain. The primary goal of this thesis is to identify the facet joint loading conditions that produce microstructural damage to the facet capsular ligament and to determine whether subfailure joint loading can initiate neuronal plasticity in the spinal cord. By optically detecting microstructural damage to the facet capsule through the analysis of the ligament's collagen fiber alignment during joint loading, the work in this thesis both establishes a novel approach to detect capsule injury without the need for traditional mechanical data and also enables the definition of mechanical tolerance for a class of subfailure ligament injury that is associated with the development of persistent facet-mediated pain..

Using an established rat model of C6/C7 facet joint loading, the first aim of this thesis quantified neuronal plasticity in the lower cervical dorsal horn after facet joint loading. Extracellular voltage recordings in the dorsal horn were compared among three different vertebral displacements that produce facet capsule stretch and known behavioral outcomes: 0.7 mm to induce sustained behavioral sensitivity, 0.2 mm to stretch the capsule but not induce behavioral sensitivity, and 0 mm as an unloaded control (Lee and Winkelstein, 2009; Rothman et al., 2008). The frequency of neuronal firing evoked during the application of light brush, pinch, and von Frey stimuli to the forepaw was compared among the vertebral

displacement groups (Aims 1a and 1b). Based on their firing responses, neurons were classified as *low threshold mechanoreceptive* or *wide dynamic range*, and the proportion of neurons with each classification were compared among the groups (Aim 1c). Finally, differences in the frequency of spontaneous discharges prior to stimulation (Aim 1d) and afterdischarges following forepaw stimulation (Aim 1e) were compared among the displacement groups. Collectively, these different electrophysiological outcomes establish whether the magnitude of facet joint loading modulates functional plasticity of the neurons in the dorsal horn in association with behavioral outcomes.

The second aim of this thesis focused on developing an optical technique to determine whether atypical capsular ligament microstructural changes occur within the magnitudes of vertebral displacement that produce pain. A quantitative polarized light imaging (QPLI) system that takes advantage of the birefringence of collagen (Tower et al., 2002) was implemented to measure the collagen fiber kinematics of facet capsular ligament tissue during loading. Facet capsular ligaments were loaded in tension to utilize the simplest loading conditions in order to develop an analysis technique to identify anomalous changes in the microstructural response. The local fiber realignment patterns of the facet capsular ligament during loading were quantified by measuring the vector correlation between sequential fiber alignment maps and defined as "anomalous" if the correlation significantly decreased (Aim 2a). The onset of anomalous collagen fiber realignment was identified in both the rat and human facet capsular ligaments

during loading and compared to the simultaneous, but independent, mechanical measurements of ligament yield and failure during loading (Aims 2b and 2c). The vertebral displacements that produced anomalous fiber realignment in the rat facet capsule were compared to the corresponding vertebral displacements that induced behavioral hypersensitivity in Aim 1 (Aim 2b). In the human facet capsule, the regions of the facet capsular tissue that sustained anomalous realignment were compared to the locations of maximum first principal strain and visible tissue rupture that were sustained during tensile loading (Aim 2c).

With an understanding of how the capsular ligament's collagen fibers respond during tensile failure tests, changes to the collagen fiber responses during and after whiplash-like retraction of isolated human cervical facet joints were investigated in Aim 3. A retraction of the C6 articular process was applied to simulate the lower cervical facet joint kinematics that have been reported in whiplash studies using cadavers and cervical motions segments (Siegmund et al., 2001; Sundararajan et al., 2004). Using the vector correlation technique developed in Aim 2, the potential for anomalous fiber realignment during retraction was assessed in the capsular ligament (Aim 3a). It has been suggested that facet joint laxity is also produced following whiplash exposures (Ivancic et al., 2008); accordingly, laxity and unrecovered strain after retraction were also quantified in the studies in this aim (Aim 3b). By measuring the vector correlation between tissue regions, altered collagen fiber alignment in the ligament after retraction was also assessed (Aim 3c). Finally, the co-localization between the regions with

unrecovered strain and the regions with altered fiber alignment was assessed, and the magnitude of strains produced during retraction were compared between regions with and without measurable changes in strain and fiber alignment after loading (Aim 3d).

3.2. Hypotheses & specific aims

The goal of this thesis is to define if, and under what conditions, facet joint motions simulating whiplash-like joint kinematics produce structural damage to the facet capsular ligament and initiate the development of persistent pain despite a lack of any visible tissue injury. To this end, an in vivo model of facet joint distraction (Aim 1) was integrated with cadaveric studies of facet joint mechanics and collagen fiber kinematics (Aims 2 and 3). The **overall hypothesis** of this work is that certain subfailure facet joint motions can produce altered collagen fiber alignment in the facet capsular ligament, changes in the mechanical response of the capsular ligament, and spinal neuron plasticity. Specifically, it is hypothesized that subfailure cervical facet joint motions that produce sustained behavioral hypersensitivity are sufficient to induce neuronal hyperexcitability in the spinal dorsal horn 7 days after joint loading. The facet joint motions that produce behavioral and electrophysiological outcomes suggestive of pain also induce microstructural changes to the capsular ligament that are detectable through polarized light imaging analysis. Furthermore, a whiplash-like retraction of the human facet joint will also produce changes to the collagen microstructure in the

capsular ligament and the joint's overall mechanical response. The overall hypothesis will be tested through the following specific hypotheses and aims.

Hypothesis 1. Sensory neurons in the dorsal horn of the spinal cord demonstrate functional plasticity after facet joint loading that is sufficient to produce sustained mechanical hyperalgesia. A higher proportion of dorsal horn neurons have wide dynamic range responses and fire spontaneously after joint loading (*painful*) that induces mechanical hyperalgesia compared to joint loading that does not (*non-painful*). After facet joint loading that induces sustained mechanical hyperalgesia, dorsal horn neurons have a higher firing frequency during and immediately following forepaw stimulation compared to neurons after joint loading that does not produce hyperalgesia.

Aim 1. Using an established rat model of controlled C6/C7 facet joint loading, measure extracellular voltage recordings of neurons in the deep laminae of the C6-C8 dorsal horn 7 days after joint loading, and compare firing responses between *painful* and *non-painful* vertebral displacements of the C6/C7 facet joint and *sham* surgeries. Evaluate how the frequency of neuronal firing evoked during the application of light brush, pinch, and von Frey stimuli to the forepaw differs among the displacement groups. Classify neurons as *low threshold mechanoreceptive* or *wide dynamic range*, based on their response to a noxious pinch stimulus, and compare the proportion of neurons with each classification among the *painful*, *non-*

painful, and *sham* groups. Compare neuronal afterdischarge responses following the application of von Frey filaments to the forepaw among the displacement groups.

1a. Measure the number of action potentials produced in extracellular voltage recordings of neurons during light brushing and noxious pinch applied to the plantar surface of the forepaw and compare differences in firing frequency between *painful*, *non-painful*, and *sham* groups.

1b. Measure the number of action potentials evoked by a range of non-noxious (1.4 g, 4 g) and noxious (10 g, 26 g) von Frey filament stimulations applied to the forepaw. Compare the evoked firing among *painful*, *non-painful*, and *sham* groups for each stimulation, and identify any interactions between groups, von Frey stimulus magnitudes, and the order of stimulus application.

1c. Classify single unit recordings as coming from *wide dynamic range* or *low threshold mechanoreceptive* neurons, based on the frequency of firing during noxious pinch, and compare the proportion of neurons classified as *wide dynamic range* among the displacement groups.

1d. Identify the proportion of neurons in each joint displacement group that fire spontaneously prior to von Frey stimulus application, and compare the proportions among the *painful*, *non-painful*, and *sham* groups.

1e. Quantify neuronal afterdischarge following non-noxious and noxious von Frey filament stimulations between displacement groups by measuring the difference between firing frequency prior to stimulus application and after

stimulus removal. Compare the neuronal afterdischarge rates among the groups, and determine the interaction effects between groups, stimulus magnitudes, and order of stimulus application.

Hypothesis 2. During tensile loading of the facet capsular ligament, localized regions of collagen fibers deviate from their normal realignment kinematics, and undergo anomalous fiber realignment, well-before tissue rupture occurs. Anomalous fiber realignment during loading is associated with the onset of ligament yield. During tensile loading of the rat facet capsular ligament, anomalous fiber realignment first occurs between the magnitudes of joint displacement that produce *non-painful* and *painful* behavioral outcomes, respectively. Anomalous fiber realignment during tensile loading of the human facet capsular ligament is associated with the spatial location of visible rupture but not with the location of maximum first principal strain.

Aim 2. Implement a quantitative polarized light imaging (QPLI) system to quantify the collagen fiber kinematics of isolated facet capsular ligament tissue during tensile loading. Use the QPLI system to define the local fiber realignment patterns of the capsule *during* loading by measuring the vector correlation between sequential fiber alignment maps of the capsule tissue. Identify if anomalous fiber realignment occurs during tensile loading of isolated rat facet joints. Evaluate whether the occurrence of anomalous collagen fiber realignment in the rat facet

capsule is associated with ligament yield under tension. Compare the vertebral displacements in the rat that are required to induce anomalous fiber realignment with those that induce mechanical hyperalgesia in vivo. Determine if anomalous fiber realignment can be detected in the human facet capsule, and evaluate whether the regions of the facet capsular tissue that sustain anomalous realignment are associated with the locations of maximum first principal strain and/or visible tissue rupture sustained during tensile loading.

2a. Develop a QPLI system to generate collagen fiber alignment maps of the facet capsular ligament during continuous tissue loading. Establish a method to quantify the changes in the fiber alignment throughout the capsular ligament using a pixel-wise vector correlation calculation between sequential fiber alignment maps. Based on a decrease in vector correlation measured during loading, identify any anomalous fiber realignment in the capsular ligament tissue.

2b. Identify whether anomalous fiber realignment occurs in the capsular ligament during tensile loading of isolated C6/C7 rat facet joints. Calculate the sensitivity and specificity of anomalous fiber realignment to occurrences of ligament yield during loading prior to gross tissue failure. Determine whether the initial detection of anomalous realignment is correlated with and/or significantly different from the initial detection of ligament yield and/or failure. Compare the average vertebral displacement required to induce initial anomalous fiber realignment in the capsule with

corresponding vertebral displacement magnitudes from Aim 1 that do and do not produce mechanical hyperalgesia in the rat.

2c. Identify whether anomalous fiber realignment can be detected during tensile loading of human facet capsular ligament tissue, and compare the onset of anomalous realignment with the occurrence of ligament yield and failure. Evaluate whether the regions of the human facet capsule in which anomalous fiber realignment is detected are associated with the location of initial visible tissue rupture. Compare the regions of tissue in which anomalous fiber realignment is detected *during* loading with the location of maximum first principal strain measured on the tissue surface.

Hypothesis 3. Facet joint retraction simulating the human vertebral and facet joint kinematics sustained during whiplash-like neck motions produces anomalous collagen fiber realignment in the capsular ligament. Facet joint retraction in whiplash-like cervical spine kinematics produces joint laxity and a decrease in capsule stiffness. The regions of the facet capsule that sustain the highest strains *during* those joint retractions are associated with unrecovered tissue deformation and altered fiber alignment that are detected *after* joint retraction.

Aim 3. Quantify the mechanical and collagen fiber kinematic responses in isolated human cervical facet joints during and after facet joint retraction simulating whiplash-like cervical spine kinematics. Using the vector correlation techniques

developed in Aim 2, determine if anomalous fiber realignment occurs in the facet capsule during retraction. Determine if joint retraction induces changes in the mechanical response of the capsular ligament, produces capsule strain that is not immediately recovered after retraction, and/or alters the collagen fiber alignment in the ligament. By measuring the deformation of the collagen fiber network in the capsular ligament though a vector correlation technique, evaluate whether tissue regions with unrecovered strains or altered fiber alignment detected immediately *after* retraction sustained higher strains *during* joint retraction.

3a. Identify whether anomalous fiber realignment, yield, or failure occurs in the isolated human C6/C7 facet capsular ligament during a joint retraction simulating whiplash-like vertebral motions. Track the deformation of the collagen fiber network within the facet capsular ligament during retraction by correlating the local fiber alignment patterns. Quantify the first principal strain and maximum shear strain fields in the facet capsule during retraction and compare the location of maximum strain to capsule locations sustaining anomalous fiber realignment during retraction.

3b. Quantify changes in facet joint laxity and capsule stiffness induced by joint retraction. Identify if there are regions in the facet capsule immediately after joint retraction in which strain is unrecovered relative to its initial configuration before retraction.

3c. Using vector correlation, compare the fiber alignment in the facet capsule after joint retraction with the fiber alignment measured prior to retraction.

Identify if there are regions of the facet capsular ligament in which altered fiber alignment is produced by joint retraction.

3d. Evaluate whether tissue regions with unrecovered strain and regions with altered fiber alignment after retraction are co-localized. Compare the magnitude of strains that are sustained during retraction between the regions *with* unrecovered strain or altered alignment, and the regions *without* any detectable changes following retraction.

CHAPTER 4

Neuronal hyperexcitability in the spinal dorsal horn after facet joint loading

Parts of this chapter were adapted from:

Quinn, K.P., Dong, L., Golder, F.J., Winkelstein, B.A. (2010). Neuronal hyperexcitability in the spinal dorsal horn after painful joint injury. *Pain* 151(2): 414-421.

4.1. Overview

Clinical and biomechanical studies implicate excessive stretch of the cervical facet capsular ligament as a cause of chronic pain following whiplash (Barnsley et al., 1995; Deng et al., 2000; Kaneoka et al., 1999; Lord et al., 1995, 1996a, b; Pearson et al., 2004; Sundararajan et al., 2004; Yang and King, 2003; Yoganandan et al., 1998). This work has been further supported by animal models that link facet capsule stretch to primary afferent signaling and nociceptive and inflammatory markers in the spinal cord (Chen et al., 2005; Dong et al., 2008; Dong and Winkelstein, 2010; Lu et al., 2005a,b; Lee et al., 2008; Lee and Winkelstein, 2009). Furthermore, cervical facet capsule stretch in the rat can produce sustained behavioral hypersensitivity for up to 42 days (Rothman et al., 2008). However, despite these clinical and experimental studies supporting facet

capsule stretch as modulating pain, the underlying mechanisms in the central nervous system (CNS) that drive the onset and maintenance of chronic pain following facet joint loading have not yet been fully elucidated.

This chapter describes the development and implementation of an electrophysiological approach to identify whether spinal neuron excitability is modulated by the magnitude of facet joint loading and/or related to the persistence of facet-mediated pain. This study encompasses the objectives outlined in Aim 1, and tests the hypothesis that sensory neurons in the spinal cord demonstrate functional plasticity after facet joint loading that is sufficient to produce sustained mechanical hyperalgesia. Using a rat model of C6/C7 cervical facet joint loading that produces behavioral hypersensitivity, the presence of neuronal hyperexcitability was characterized 7 days after the joint loading was imposed. Specifically, firing evoked by different mechanical stimuli applied to the forepaw was characterized for facet joint loading conditions that do and do not produce mechanical hyperalgesia (Aims 1a and 1b). From the evoked firing responses, the proportion of neurons with wide dynamic range responses was compared between rats with non-painful and painful outcomes after facet joint loading (Aim 1c). Lastly, differences in spontaneous neuronal discharges (Aim 1d) and afterdischarges immediately following forepaw stimulation (Aim 1e) were also compared between these painful and non-painful loading groups. Collectively, these sub-aims identify whether painful facet joint loading conditions produce neuronal plasticity in the spinal cord. This study provides physiological context for

the investigations in Aims 2 and 3, which investigate the relationship between facet capsular ligament loading, structure and function, and tissue injury.

4.2. Background

The cervical facet capsule is innervated by proprioceptive and nociceptive primary afferents that encode the magnitude of load transmitted through the structure (Inami et al., 2001; McLain, 1993; Yamashita et al., 1990). Nerve fibers in the facet capsule reactive for the neuropeptides, such as substance P and calcitonin gene-related peptide, support the potential for nociceptive signaling from this joint (Beaman et al., 1993; el-Bohy et al., 1988; Inami et al., 2001; Kallakuri et al., 2004; Yamashita et al., 1993). The application of substance P to lumbar facet joints is excitatory when coupled with mechanical stimulation of proprioceptive and nociceptive afferents in that tissue (Yamashita et al., 1993). In the rat, increased substance P expression in the dorsal root ganglia is sustained at 7 days after facet joint stretch that also produces mechanical hyperalgesia and allodynia (Lee and Winkelstein, 2009). In a caprine model, both nociceptor firing during cervical facet joint loading and sustained afferent discharges after loading were produced in the absence of any rupture of the joint's capsule (Cavanaugh et al., 2006; Chen et al., 2005; Lu et al., 2005a, b). These in vivo models demonstrate that certain magnitudes of facet capsule stretch can induce nociceptive firing, alter neurotransmitter expression in the peripheral nervous system, and produce persistent behavioral hypersensitivity. However, the neuronal mechanisms in the

CNS responsible for the maintenance of pain after injury-related facet joint loading remain undefined.

Patients with chronic pain after whiplash injury report mechanical hyperalgesia and allodynia along the neck and upper extremities (Banic et al., 2004; Curatolo et al., 2001; Greening et al., 2005; Sheather-Reid and Cohen, 1998). Because this hypersensitivity extends beyond the receptive fields of afferents in the facet joints, it suggests there to be a development and maintenance of increased neuronal excitability in the central nervous system. Central sensitization has been cited as the underlying mechanism maintaining chronic pain symptoms, and it can be initiated through a variety of different processes in the spinal cord (Ji and Woolf, 2001; Scholz and Woolf, 2002; Woolf and Salter, 2000). Sensitization can initially result when a barrage of nociceptive signals causes an increase in excitatory post-synaptic potentials (Woolf and Salter, 2000). This bombardment of afferent activity causes an influx of calcium into the neuron, which can activate silent receptors, initiate more AMPA and NMDA expression at the neuronal synapse, and produce increases in receptor conductance through phosphorylation (Koltzenburg et al., 1992; Zou et al., 2000). Neighboring neurons and glia can also produce sensitization through the release of substance P, glutamate, neurotrophins, or cytokines that can modulate and enhance synaptic transmission (Kerr et al., 1999; Watkins et al., 2001). Transcriptional changes, disinhibition of excitatory neurons through GABAergic interneuron death, and the rearrangement of synaptic contacts can also occur after extended hyperexcitability and can contribute to the

maintenance of chronic pain (Moore et al., 2002; Ren et al., 1992; Woolf and Salter, 2000).

Multi-receptive or wide dynamic range (WDR) neurons in the dorsal horn modulate central sensitization in many chronic pain states (Christensen and Hulsebosch, 1997; Coghill et al., 1993; Hains et al., 2003a; Hao et al., 1992; Herrero and Headley, 1995; Sandkuhler, 2000; Seal et al., 2009). WDR neurons receive input from both nociceptive and non-nociceptive primary afferents (Figure 4.1), and, therefore, are thought to play a critical role in processing nociceptive stimuli (Sorkin et al., 1986; Willis and Coggeshall, 1991). WDR neurons are primarily found in the deeper laminae of the spinal cord and can be involved in

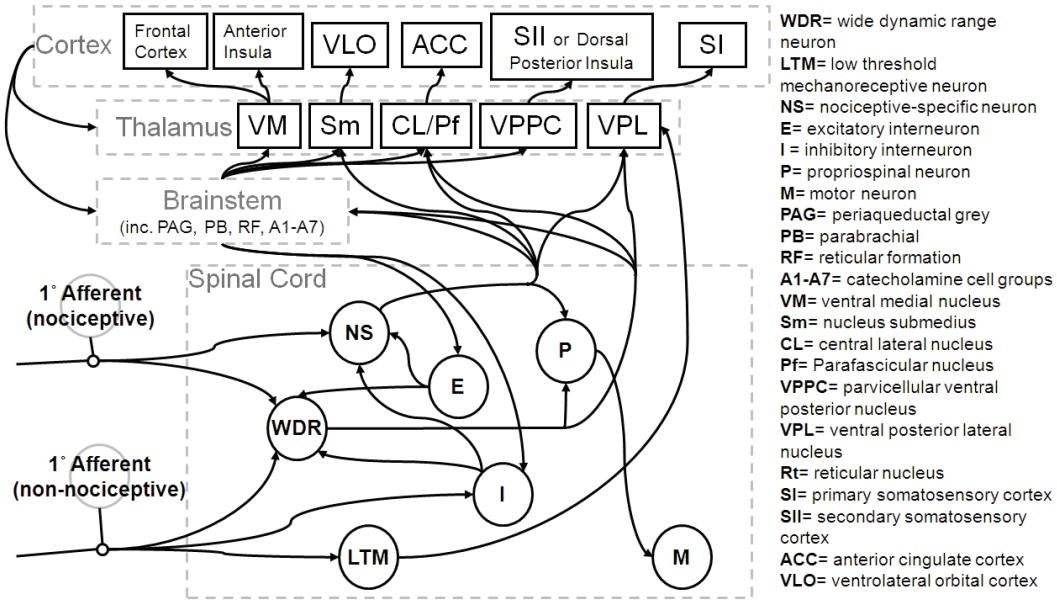

Figure 4.1. Schematic of the ascending and descending nociceptive pathways in the CNS. Wide dynamic range (WDR) neurons receive input from both nociceptive and non-nociceptive afferents and can project to a variety of supraspinal structures, such as the brainstem and ventral posterior lateral nucleus of the thalamus.

motor reflexes or relaying afferent signals to supraspinal structures (Figure 4.1) (Schouenborg et al., 1995; Willis, 1985). Electrophysiological studies of spinal cord activity in different pain models have identified an increase in WDR excitability to mechanical and thermal stimuli following injury to peripheral tissues and the spinal cord (Chang et al., 2009; Christensen and Hulsebosch, 1997; Hains et al., 2003a, b). In addition, an increase in the proportion of neurons in the spinal cord that exhibit WDR responses also has been reported following spinal cord injury (Hains et al., 2003a). However, the role of WDR neurons in facet-mediated pain remains unclear owing to a lack of investigations probing neuronal plasticity in the spinal cord.

The goal of this study was to investigate the development of neuronal hyperexcitability in the spinal cord of the rat after loading to the C6/C7 facet joints. Facet capsule stretch was applied using separate magnitudes that do and do not produce behavioral hypersensitivity in the neck and forepaw at day 7 (Lee et al., 2008; Lee and Winkelstein, 2009) to assess whether painful facet capsule stretch is associated with neuronal hyperexcitability in the spinal cord. It was hypothesized that spinal dorsal horn neurons are more excitable in response to forepaw stimulation 7 days after facet joint loading that induces mechanical hyperalgesia. Extracellular voltage recordings were made in the deep laminae of the dorsal horn at day 7, and the frequencies of baseline, evoked, and afterdischarge firing were assessed to characterize the neuronal response to mechanical stimuli.

4.3. Methods

4.3.1. Facet capsule stretch

All experimental procedures were approved by the Institutional Animal Care and Use Committee of the University of Pennsylvania and followed the guidelines of the Committee for Research and Ethical Issues of the International Association for the Study of Pain (Zimmermann, 1983). Male Holtzman rats (356-460 g; Harlan Sprague-Dawley; Indianapolis, IN) were housed under USDA- and AAALAC- compliant conditions with food and water available ad libitum.

Rats were anesthetized through the inhalation of isoflurane (4% for induction, 2.5% for maintenance). A controlled bilateral displacement was applied across the cervical C6/C7 facet joints using a custom loading device, as previously described (Lee et al., 2008) (Figure 4.2). Rats were placed in a prone position and the paraspinal musculature was carefully separated from the spinous processes between C4 and T2. The laminae and facet joints at the C6 and C7 levels were exposed and musculature was cleared from the dorsal surface of the facet capsule. Microforceps were attached to the spinous processes of both C6 and C7. Vertebral displacements were imposed by separating the microforceps to apply tensile deformation across the facet joint's capsule; the C6 microforceps translated rostrally while C7 was held stationary (Figure 4.2). Each rat underwent a single prescribed vertebral displacement at one of three magnitudes (n=6 per group) to induce known behavioral outcomes: 0.7 mm to induce sustained behavioral

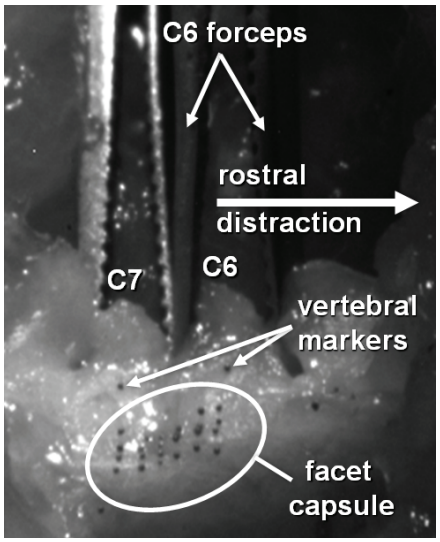

Figure 4.2. Forceps are attached to the C6 and C7 spinous processes and C6 is displaced to apply capsule stretch. Vertebral markers are used to determine the magnitude of the applied vertebral displacement.

sensitivity (painful), 0.2 mm to stretch the capsule but not induce behavioral sensitivity (non-painful), or 0 mm (sham) (Lee and Winkelstein, 2009; Rothman et al., 2008). Previous work with this facet model has demonstrated no detectable difference in the behavioral sensitivity or inflammatory responses at day 7 between naïve rats and those having undergone a sham surgery (Dong et al., 2010; Lee et al., 2008; Lee and Winkelstein, 2009). In order to target the specific capsule stretch magnitudes, the magnitude of vertebral displacement that was applied to the joint was measured by tracking polystyrene markers (0.17±0.01 mm diameter; Spherotech, Inc.; Libertyville, IL) placed on each lamina at C6 and C7. The maximum change in the relative distance measured between the centroids of those markers during applied vertebral displacements was taken as the magnitude of each facet capsule stretch. The magnitudes of vertebral displacement between the

painful and non-painful groups were compared through an unpaired Student's t-test. Following surgery, the incisions were closed using 3-0 polyester suture and surgical staples; rats were permitted to recover from anesthesia.

4.3.2. Mechanical hyperalgesia assessment

Mechanical hyperalgesia was assessed prior to facet capsule stretch and on the day of electrophysiological testing to verify that behavioral hypersensitivity in each group in the current study were consistent with previous reports using the same vertebral displacement magnitudes (Lee and Winkelstein, 2009). Hyperalgesia was measured in the forepaw using a modified Chaplan's up/down method to quantify the threshold for tactile sensitivity to a von Frey stimulus (Chaplan et al., 1994; Hubbard and Winkelstein, 2005; Lee et al., 2008; Lee and Winkelstein, 2009). In each testing session, for both the left and right forepaw, the threshold to elicit a withdrawal response was determined in three rounds of testing. For each round, a series of filaments with logarithmically-increasing strengths (0.4, 0.6, 1.4, 2, 4, 6, 8, 15, 26 g) (Stoelting Co.; Wood Dale, IL) was applied to the forepaw. Each filament was applied five times before using the next filament; if two consecutive filament strengths elicited a response, the lower of the two filament strengths was taken as the threshold. Any rat failing to respond to any of the filaments in any round was assigned a threshold of 26 g. The average threshold from the three rounds was calculated for each forepaw of each rat on both the baseline and electrophysiological testing days. A paired t-test was used to verify

that there were no significant differences between the left and right forepaw withdrawal thresholds. Changes in behavioral sensitivity between baseline responses prior to surgery and responses on the day of electrophysiological testing were assessed for each group using a paired t-test of the average withdrawal threshold of each rat.

4.3.3 Electrophysiology protocol

To determine the effects of facet capsule stretch on neuronal excitability in the dorsal horn of the cervical spinal cord, electrophysiological recordings were acquired in the C6-C8 spinal cord on day 7 after facet joint injury for both the painful and non-painful groups. Electrophysiological recordings were taken on day 6 for the sham group to provide a more liberal estimate of any effects of surgery on neuronal excitability. For surgical procedures, anesthesia was induced with isoflurane (4% in O_2, then 2.5% in O_2 for maintenance), and the left lateral tail vein was cannulated to administer fluids over the course of the experiment (1:1 mixture of lactated Ringer's and 6% hetastarch solutions; 4 ml/kg/h i.v.). The mid-cervical trachea was exposed ventrally and cannulated to allow mechanical ventilation at 60-70 cycles/min with a 2.5-3.0 ml tidal volume (Harvard Small Animal Ventilator Model 683; Harvard Apparatus; Holliston, MA), and the end tidal concentration of CO_2 was monitored continuously (Capnogard; Novametrix Medical Systems; Wallingford, CT). The right femoral artery also was exposed and cannulated to monitor arterial blood pressure (Model P122; Grass Telefactor; West Warrick, RI).

Following surgical instrumentation, the rat was immobilized in a stereotaxic frame using ear bars and a vertebral clamp at T2 (Figure 4.3). Core temperature was maintained between 36-37˚C using a heating plate with a temperature controller and an isolated rectal probe (model TCAT-2DF; Physitemp Instruments, Inc.; Clifton, NJ). A thoracotomy was performed with a lateral intercostal approach to minimize respiratory-related spinal cord movement during extracellular recordings (Figure 4.3). The C6-C8 spinal cord was then exposed via bilateral dorsal laminectomy, and the overlying dura was resected. Rats were then converted to urethane anesthesia (1.2 g/kg i.v.) as isoflurane was slowly discontinued. The fraction of inspired O_2 was set to 0.50 through a 1:1 mixture of O_2 and N_2 and was delivered via mechanical ventilation for the remainder of the

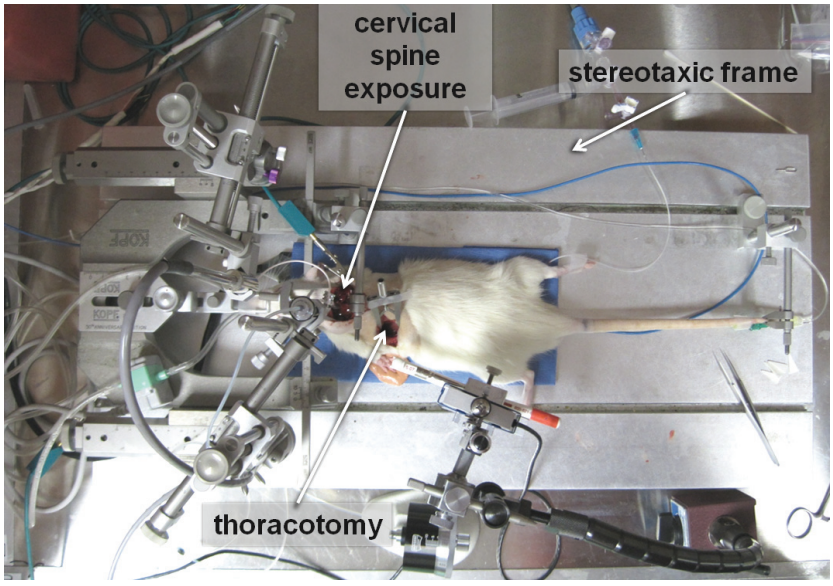

Figure 4.3. Rat immobilized in the stereotaxic frame. An intercostal thoracotomy was performed to reduce respiratory-related spinal cord movement during recording, and the cervical spinal cord was exposed to facilitate electrode placement for extracellular recording.

experiment. After conversion to urethane anesthesia, 1.5 hours elapsed before neuronal recordings were taken in order to provide sufficient time for isoflurane washout. Anesthetic depth was continuously monitored and was maintained by urethane injection (0.12 g/kg i.v.) following any withdrawal response or mean arterial blood pressure increase of more than 15 mmHg in response to a hind paw pinch.

Extracellular voltage potentials were continuously recorded using a 5-8 μm diameter carbon fiber electrode (Carbostar-3; Kation Scientific, Inc.; Minneapolis, MN) and were amplified with a gain of 3000 (ExAmp-20KB; Kation Scientific, Inc.; Minneapolis, MN). The amplified signal was processed with a 60 Hz noise eliminator (Hum Bug; Quest Scientific; North Vancouver, BC), and then digitized and stored at 25 kHz (MK1401/Spike 2; CED; Cambridge, UK). The electrode was placed in locations along the spinal cord just medial to the dorsal root entry zone at the C6, C7, and C8 levels. Sensory neurons within the dorsal horn (400-1000 μm below the pial surface) were identified using a light brush stroke applied to the plantar surface of the forepaw with a cotton swab in order to minimize peripheral sensitization during the search for evoked responses. Search times were limited to 2.5 hours for each side of the spinal cord to reduce the temporal effects of the surgical procedure on the extracellular recordings. Only the forepaw ipsilateral to the electrode was used to identify sensory neuronal activity. Once an evoked potential was identified, the forepaw location that evoked the maximum response

was marked, and a stimulation protocol was performed that included brushing, noxious pinch, and a series of non-noxious and noxious von Frey filaments (Carlton et al., 2009; Chang et al., 2009; Christensen and Hulsebosch, 1997; Hains et al., 2003a, b) (Figure 4.4). The neuron search methods and forepaw stimulation protocol are detailed in Appendix A. Extracellular recordings were stored for the entire duration of the stimulation protocol. Specifically, 10 consecutive brush strokes were applied to the targeted location on the forepaw with a cotton swab, and the location was then pinched for 10 s using a vascular clip calibrated to apply a 60 g force (World Precision Instruments, Inc.; Sarasota, FL). This vascular clip was selected because it did not produce any tissue damage or leave any permanent redness to the application area. Von Frey filaments were mounted to a load cell (5 N capacity; SMT S-Type Model; Interface, Inc.; Scottsdale, AZ) and the load cell

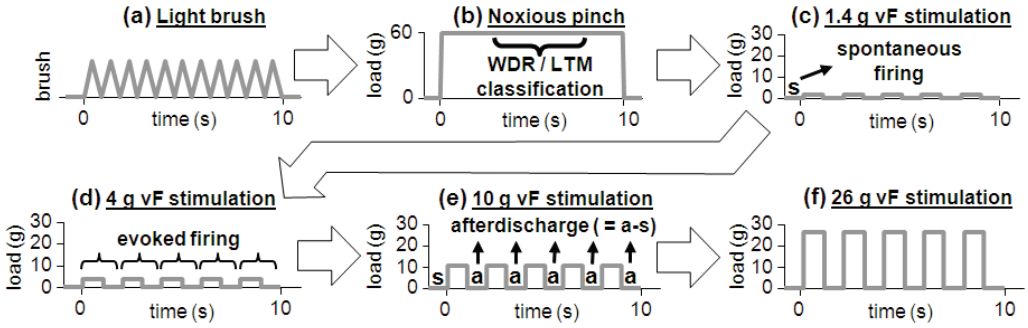

Figure 4.4. Forepaw stimulation protocol. (a) Light brush, **(b)** noxious pinch, and **(c-f)** von Frey (vF) filament stimulation were applied to the forepaw. Neurons were classified as wide dynamic range (WDR) or low threshold mechanoreceptive (LTM) based on firing during noxious pinch. Spontaneous and evoked firing were quantified during the von Frey stimulation protocols. Afterdischarge following von Frey stimulation was defined as the difference between firing immediately after stimulation (a) and spontaneous firing (s).

position was adjusted to apply the filaments to the identified location on the forepaw (Figure 4.5). Load cell voltages were amplified by a signal conditioner (model 9820; Interface, Inc.; Scottsdale, AZ) and then recorded by the Spike 2 acquisition system to synchronize the mechanical stimulus application with the extracellular recordings (Figure 4.5). Four logarithmically-spaced filament strengths that included non-noxious (1.4 and 4 g) and noxious (10 and 26 g) magnitudes used in behavioral assessment were applied to the forepaw location that

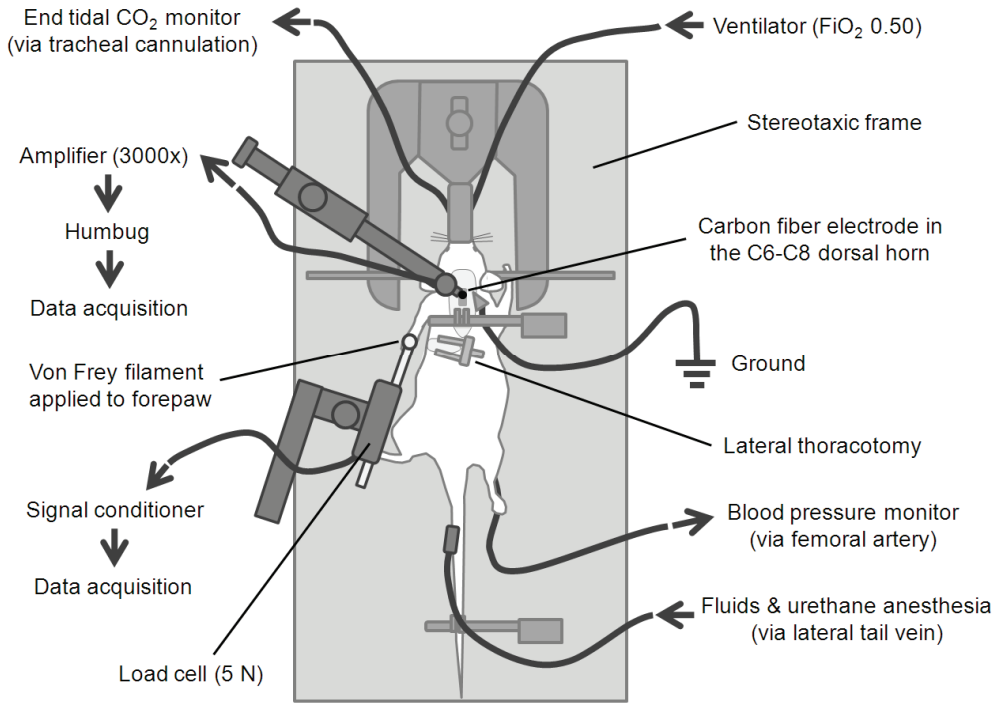

Figure 4.5. Schematic of a rat instrumented with electrophysiological equipment for extracellular recordings in the spinal cord during forepaw stimulation. A carbon fiber electrode measured extracellular signals in the dorsal horn during stimulation of the forepaw using a von Frey filament mounted to a load cell. Both the stimulus load and the extracellular voltages were processed, and then recorded by the data acquisition software.

evoked the most activity during light brushing. Five stimulations spaced approximately 1-2 s apart were applied with each of the four filament strengths (Figures 4.4). Approximately 60 s elapsed between the brush and pinch stimuli, and the use of the different von Frey filament magnitudes.

4.3.4. Analysis of electrophysiological measurements

Recordings during the stimulation protocol of each neuron were spike-sorted using Spike 2 software (CED; Cambridge, UK) to ensure that only the firing of a single unit was measured from each recording. A description of the spike-sorting methods can be found in Appendix A. The total number of spikes during the 10 light brush strokes and number of spikes during the 10 s noxious pinch were counted for each neuron. Neurons were classified as either a low threshold mechanoreceptive (LTM) or a wide dynamic range (WDR) neuron based on their response to the noxious pinch. Neurons were classified as WDR if firing exceeded one action potential during the period between the application and removal of the clip (3-8 s into pinch application). A nociceptive-specific neuron classification was not considered in this study because neurons were identified based on an evoked response to light brushing and this cell type is typically not found in the deep laminae of the dorsal horn (400-1000 μm) in rats (Hains et al., 2003a).

The number of spikes from the initial application of a von Frey filament to 1 s after the removal of the filament was also counted as evoked firing for each neuron (Figure 4.2). Baseline firing prior to stimulation with each von Frey

filament was assessed by counting the number of spikes during the 1 s immediately before the first of the five applications of a given filament (Figure 4.2). Each neuron was either classified as spontaneously firing or not, based on whether baseline firing had occurred at any point during the 1 s prior to the first application of any of the four von Frey filaments. Afterdischarge following each von Frey application was computed as the difference between the firing rate recorded during the 1 s after the stimulus and the baseline firing rate recorded during the 1 s prior to the first von Frey application with that filament (Figure 4.2).

Statistical analyses were performed using JMP 8 (SAS Institute Inc.; Cary, NC). Electrophysiological data were log-transformed due to a positive skew, and a normal distribution was verified after the transformation by plotting the residuals from the statistical models. To test for differences in the firing responses to light brush and noxious pinch between the painful, non-painful, and sham groups, mixed-effect ANOVAs were used with neurons nested within rats, and rats nested within groups. Post-hoc Tukey HSD tests evaluated differences between the three individual groups. A mixed-effect ANOVA with the same levels of nesting was used to analyze differences between groups, von Frey stimulation magnitudes, the order of stimulus application, and their interactions (Figure 4.6). This mixed-effect ANOVA structure (Figure 4.6) was also used to evaluate afterdischarge following von Frey stimuli. An additional mixed-effect ANOVA for evoked firing was created to factor in the spinal level in which each neuron was located and the interaction between spinal level and the other effects. The number of neurons that

were spontaneously firing during any of the baseline recordings was compared between groups through Pearson's chi-square tests to evaluate whether spontaneous firing differed among injury groups. Differences in the proportion of WDR and LTM neurons between groups were also assessed though Pearson's chi-square tests. These statistical tests were performed with α=0.05.

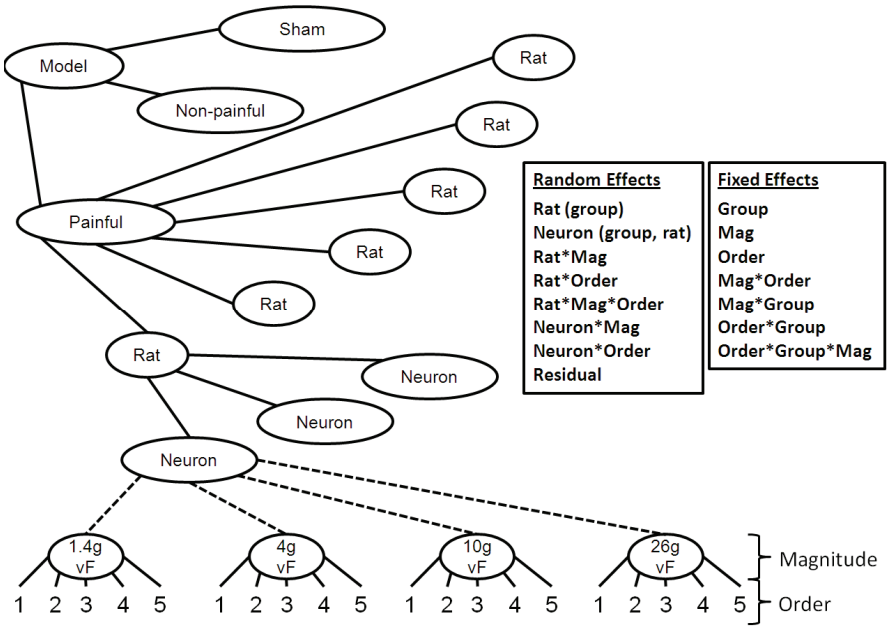

Figure 4.6. Mixed effect ANOVA structure for comparing the firing response to von Frey filament stimulation between groups. Rats were nested within groups, and neurons were nested within rats and groups. The effects of group, filament magnitude, order of filament application, and their interactions were determined. This structure was modified in a separate ANOVA to include the fixed effect of the spinal level at which each neuron was identified. The corresponding interactions between spinal level and the other effects were also included in that additional ANOVA.

4.4. Results

The different capsule stretch magnitudes imposed during vertebral displacement at day 0 produced significantly different behavioral responses. The

mean vertebral displacement imposed in the painful group was 0.68±0.06 mm, and was significantly greater ($p<0.0001$) than the mean displacement applied in the non-painful group (0.23±0.04 mm) (Table 4.1). During the vertebral displacement, no facet capsule ruptures were visible for any rat from video recordings taken. The threshold for paw withdrawal in the mechanical hyperalgesia testing was not.

Table 4.1. Mechanical and behavioral outcomes measured for each group.

Group	Rat	Displacement (mm)	Baseline threshold (g)	Post-operative threshold (g)
sham	31	0	18.7	16.8
sham	34	0	16	16.8
sham	38	0	24.2	26
sham	40	0	24.2	22.3
sham	43	0	18.7	20.5
sham	46	0	16.8	15
sham	**Mean**	**0**	**19.8**	**19.6**
	S.D.	**0**	**3.6**	**4.1**
non-painful	35	0.24	15	15
non-painful	36	0.3	15.7	10.7
non-painful	37	0.19	14.2	18.7
non-painful	41	0.23	20.5	22.3
non-painful	44	0.2	12.2	12.7
non-painful	45	0.21	16.8	18.7
non-painful	**Mean**	**0.23**	**15.7**	**16.3**
	S.D.	**0.04**	**2.8**	**4.3**
painful	28	0.61	16	7
painful	29	0.74	10.2	6.7
painful	30	0.72	15	6.7
painful	33	0.64	18.7	8.7
painful	39	0.65	20.5	18.8
painful	42	0.74	16.8	8
painful	**Mean**	**0.68**	**16.2**	**9.3**
	S.D.	**0.06**	**3.5**	**4.7**

significantly different between the left and right side for any of the groups, so the withdrawal threshold was computed as the average of both sides for each rat. Furthermore, the average baseline threshold was not significantly different between groups. The withdrawal threshold did not change significantly in the sham group between baseline values (19.8±3.6 g) and day 6 (19.6±4.1 g) or in the non-painful group between baseline (15.7±2.8 g) and day 7 (16.3±4.3 g) (Table 4.1 and Figure 4.7). However, there was a significant decrease (p=0.004) in the withdrawal threshold measured at day 7 (9.3±4.7 g) in the painful group compared to its baseline values (16.2±3.5 g) (Table 4.1 and Figure 4.7).

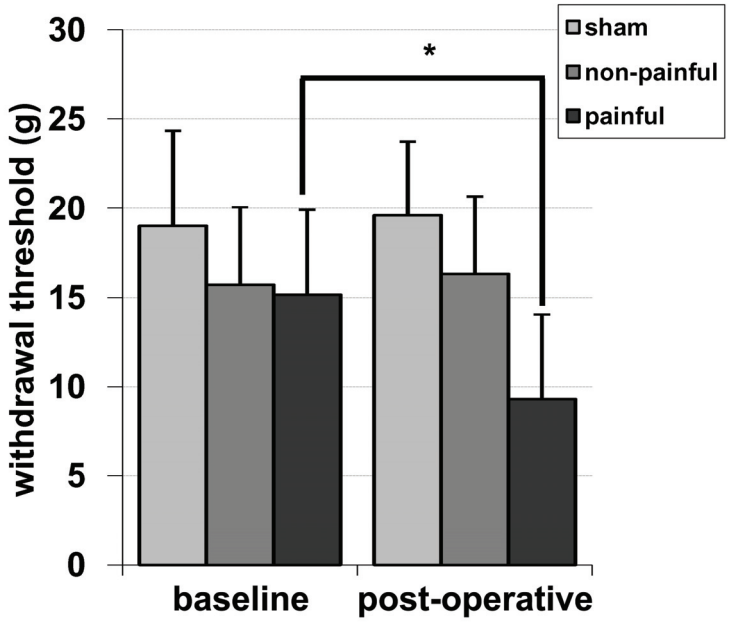

Figure 4.7. Mechanical hyperalgesia was only produced in the painful group 7 days after facet joint loading. The withdrawal threshold was significantly lower (*p=0.004) at post-operative day 7 in the painful group compared to corresponding baseline values. No significant changes from baseline were measured in the non-painful group at day 7 or the sham group at day 6.

A total of 117 neurons were identified in the spinal cord at an average depth of 638±157 µm. The majority of the neurons (n=81) were located at the C7 or C8 spinal level, while 36 neurons were identified at the C6 level. For 34 neurons, light brushing of one of the pads on the forepaw produced the most robust firing response, while firing from the remaining 83 neurons was most robust in response to stimulation of one of the digits of the forepaw (Figure 4.8). The raw action potential counts for light brushing, pinch, and each von Frey application for each neuron recording is detailed in Appendix B. Light brushing produced significantly more firing ($p=0.038$) in the painful group (94±125 spikes/10 strokes) relative to sham (53±32 spikes/10 strokes) (Figure 4.9). Yet, firing in the non-painful group (56±32 spikes/10 strokes) was not significantly different from either the painful or sham group (Figure 4.9). Noxious pinch to the forepaw evoked significantly more firing ($p<0.0182$) after a painful capsule stretch (137±164 spikes/10 s) than compared to either the non-painful (51±57 spikes/10 s) or sham (39±31 spikes/10 s) groups (Figure 4.9). In the painful group, 69% of neurons (22 of 32) were

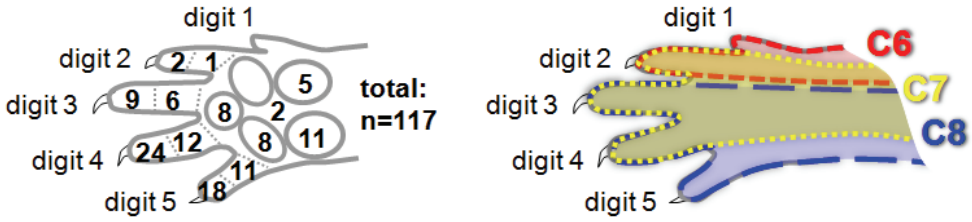

Figure 4.8. Forepaw locations that evoked maximal dorsal horn firing and the corresponding dermatome maps. The distal ends of digits 4 and 5 were the most frequently identified locations from the 117 neurons that were recorded. Dermatomes indicating spinal nerve innervations of the forepaw are indicated and were taken from those defined by Takahashi and Nakajima, 1996.

classified as wide dynamic range neurons, which was significantly higher than the 44% classified as WDR in the non-painful group (20 of 45; p=0.0348) or the 43% classified in the sham group (17 of 40; p=0.0251) (Figure 4.10).

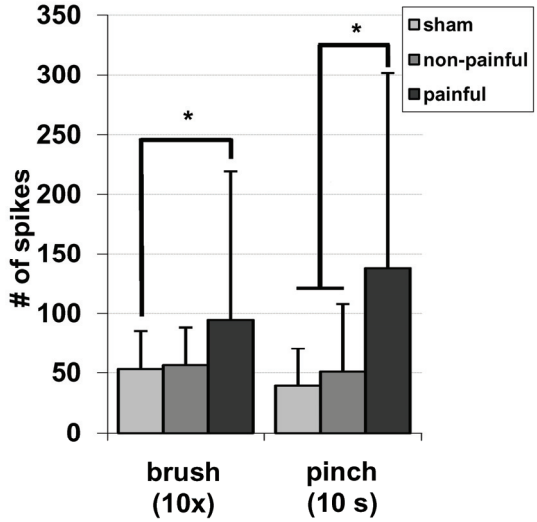

Figure 4.9. Evoked neuronal firing in response to forepaw brush and pinch increased at day 7 after facet joint loading only in the painful group. The number of spikes counted in the painful group was significantly greater ($p<0.038$) compared to sham for brush and pinch. The painful group was also significantly greater ($p<0.0182$) than the non-painful group for the pinch stimulus.

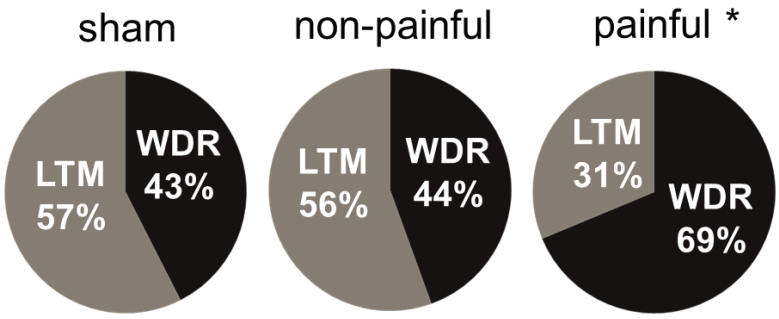

Figure 4.10. Wide dynamic range (WDR) neuron responses were more likely to be identified in the painful group than the other non-painful groups. A significantly greater proportion of neurons responded as a WDR neuron rather than a low threshold mechanoreceptive (LTM) neuron in the painful group compared to the sham and non-painful control groups ($p<0.0348$).

Overall, neuronal firing in response to von Frey stimuli was significantly higher ($p<0.001$) in the painful group than either the non-painful or sham groups (Figure 4.11). The 26 g filament evoked an average of 101±77 spikes over the five applications in the painful group, and this was significantly greater ($p<0.004$) than the number of spikes produced during the five applications of that filament in either the non-painful (46±36 spikes) or sham (45±39 spikes) groups (Figure 4.11 and 4.12). Firing was also significantly higher in the painful group compared to the non-painful and sham groups for the 10 g ($p<0.0156$) and 4 g ($p<0.005$) von Frey filaments (Figure 4.11), but no significant differences in firing were found between groups for stimulation with the 1.4 g filament.

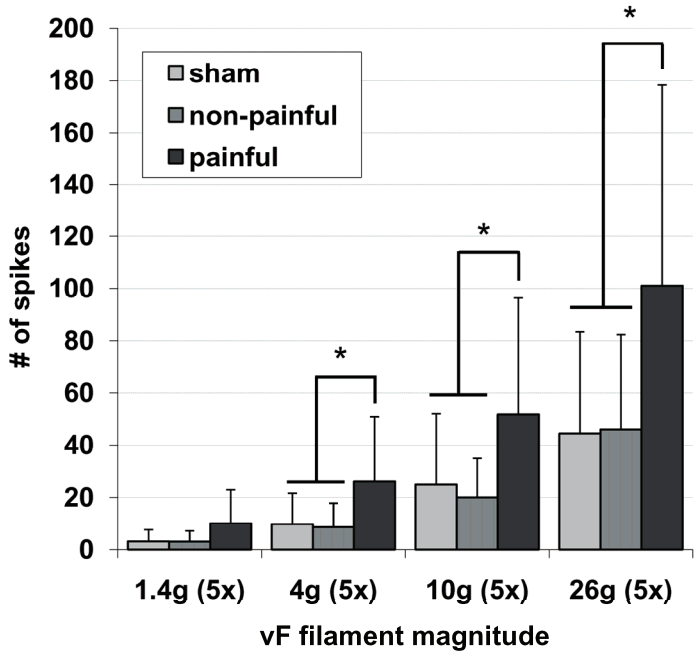

Figure 4.11. Evoked neuronal firing increased with increasing von Frey (vF) stimulus magnitude. The number of evoked spikes during five applications (5x) of the filament in the painful group was significantly greater (*$p<0.0156$) than the non-painful and sham groups for stimulation by the 4, 10, and 26 g von Frey filaments.

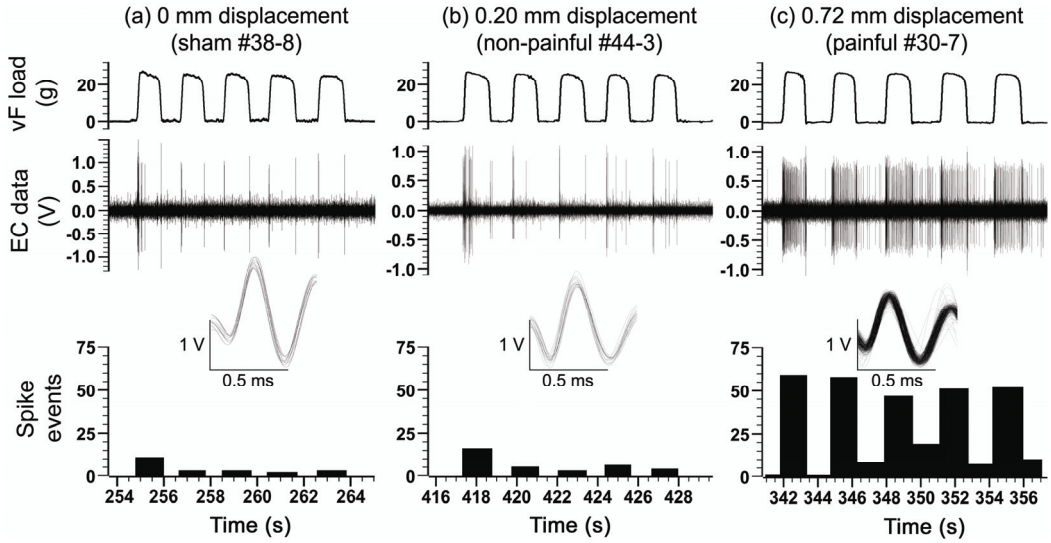

Figure 4.12. Representative extracellular recordings during the application of a 26 g von Frey filament to the forepaw after facet joint loading. Extracellular (EC) data were spike-sorted and the superimposed traces of all single unit activity that was counted in the histograms are provided. Firing was evoked predominantly during the initial application of the filament and upon its removal in **(a)** sham and **(b)** non-painful groups. In the **(c)** painful group, firing was more frequent throughout the entire stimulation protocol.

The average evoked firing was significantly different among the von Frey stimulus magnitudes ($p<0.0001$) and among the five applications within each magnitude ($p<0.0001$). For the average set of five applications with any von Frey filament, the first application produced significantly more firing than the subsequent four later applications ($p<0.0001$), and the second application produced significantly more firing than the fourth and fifth applications (Figure 4.13). A significant interaction was also found between the magnitude of the von Frey stimulus applied to the forepaw and the order of application ($p<0.0001$). Firing during the first application of the 26 g von Frey filament was significantly greater

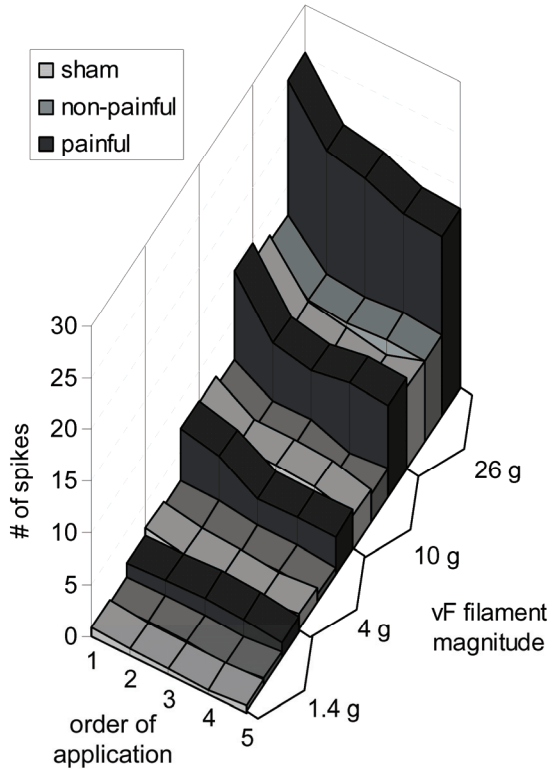

Figure 4.13. The average number of spikes evoked during von Frey filament stimulation of the forepaw increased with respect to the filament strength and depended on the order of application. A significant interaction effect was found between the von Frey (vF) magnitude and the ordinal rank of the stimulus application ($p<0.0001$); at greater filament magnitudes, firing was greater in response to the first application of the filament relative to the subsequent applications at that magnitude.

than all other combinations of stimulus magnitude and order of application ($p<0.0001$) (Figure 4.12). Firing from neurons located in the C6 spinal segment did not differ from neurons at the C7 or C8 levels ($p=0.6146$) that innervate the majority of the forepaw locations probed (Figure 4.8). In addition, there was no significant interaction between injury group and spinal level ($p=0.4927$), and the incorporation of spinal level into the ANOVA did not change the other significant

fixed-effect factors (injury group, filament magnitude, filament application order, magnitude-order interaction). The lack of any significant spinal level effect demonstrates that forepaw stimulation evokes a similar frequency of neuron firing throughout the entire spinal cord in the lower cervical spine (C6-C8), and that increases in spinal neuron firing in the painful group are not specific to a particular spinal level. Accordingly, the spinal level factor was not included in any additional analyses in this study.

The average evoked firing frequencies for each rat during the five applications of each von Frey stimulus were correlated with the magnitude of vertebral displacement applied across the facet capsule (Figure 4.14). Every non-noxious (1.4 and 4g) and noxious (10 and 26 g) von Frey filament evoked a firing response that was significantly correlated ($p>0.0032$) with the imposed vertebral

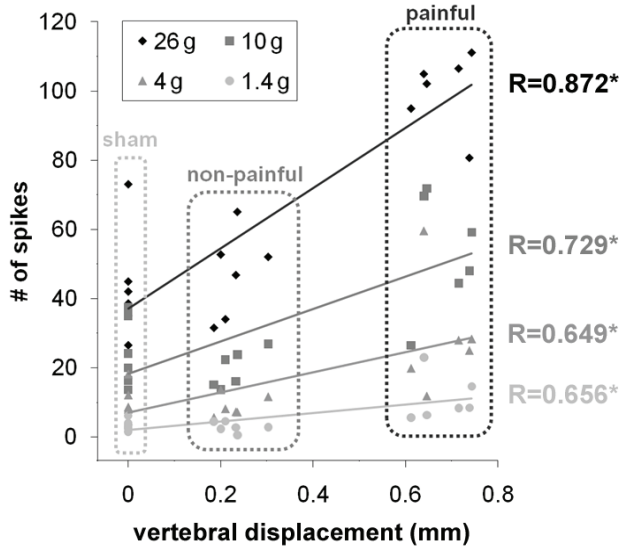

Figure 4.14. The firing frequency in response to forepaw stimulation was significantly correlated with the magnitude of vertebral displacement. All correlations were significant ($p<0.0032$).

displacement (Figure 4.14). This correlation with vertebral displacement was strongest when compared for the 26 g von Frey application (R=0.872; p<0.0001). In addition, the paw withdrawal threshold of each rat during the behavioral assessment on the day of electrophysiological recording was significantly correlated with the firing responses to 1.4 g (p=0.0253), 4g (p=0.0044), and 26 g (p=0.0035) filaments (Figure 4.15).

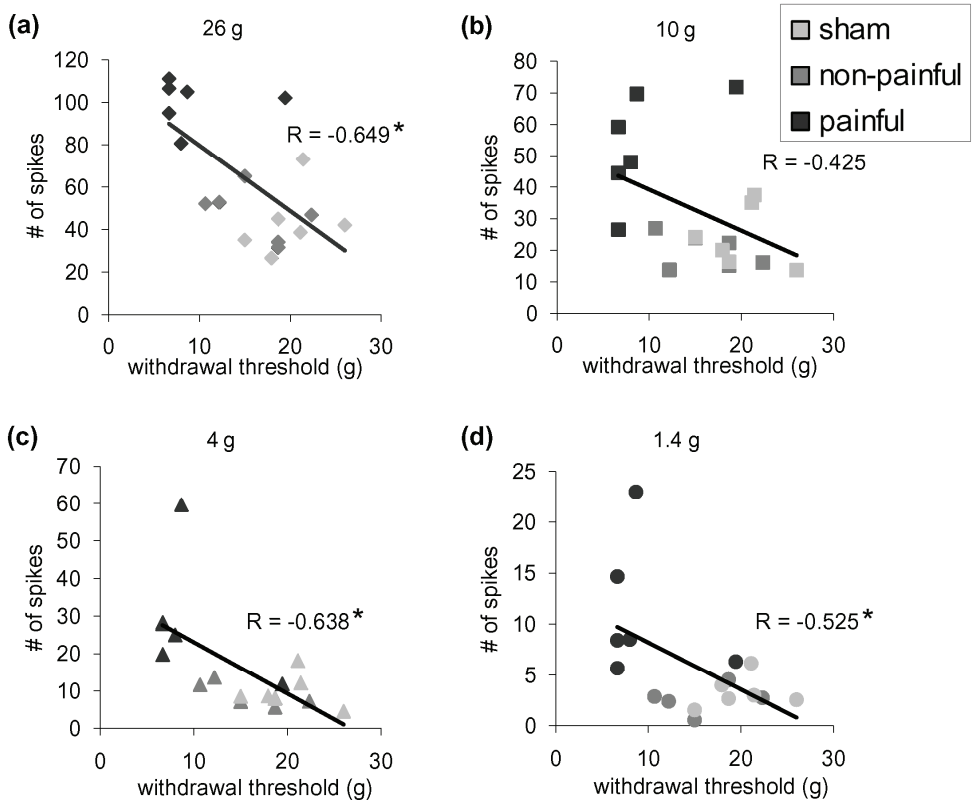

Figure 4.15. The firing frequency in response to forepaw stimulation was significantly correlated with the paw withdrawal threshold. (a) The correlation with the paw withdrawal threshold was strongest (R=-0.649; p=0.0035) with the 26 g filament. **(b)** No significant correlation was found in the 10 g filament. **(c-d)** The non-noxious filaments were significantly correlated with withdrawal threshold (p<0.0253).

The overall average spontaneous firing rate prior to von Frey filament stimulation was 0.068±0.190 spikes/s, and firing only occurred in 21 of the 117 neurons. The number of neurons spontaneously firing in the painful group (11 of 32) was significantly greater ($p=0.0042$) than expected when compared to the sham group (3 of 40), but not the non-painful group (7 of 45). Afterdischarge rates, measured by the difference in firing immediately following forepaw stimulation relative to the spontaneous rate (Figure 4.4), were significantly greater ($p=0.0307$) overall in the painful group compared to sham; yet, this was not significantly greater than that in the non-painful group. The average afterdischarge rate following a noxious 26 g stimulus (1.37±2.47 spikes/s increase over spontaneous discharge rates) was significantly greater ($p<0.0002$) than the non-painful (0.44±1.31 spikes/s increase) or sham (0.31±0.87 spikes/s increase) groups, but no significant differences were identified in the less noxious 1.4, 4, or 10 g filaments (Figure 4.16). Significant group-magnitude ($p=0.0013$) and group-magnitude-application order ($p=0.0290$) interactions were found for afterdischarge firing. These interactions were attributable to the significantly higher afterdischarge rates in the painful group after a 26 g stimulus compared to all other combinations of groups and magnitudes ($p>0.0006$) (Figure 4.16). Furthermore, afterdischarge in the painful group after a 26 g stimulus was significantly lower for the first application compared to the second and third ($p>0.0029$).

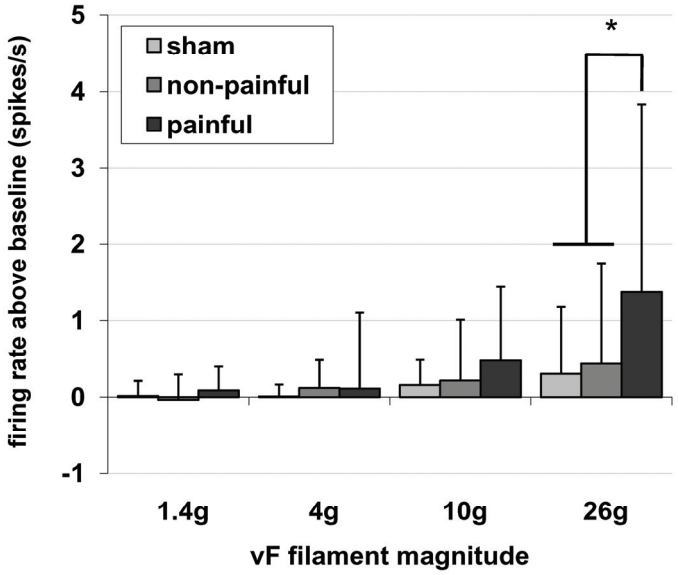

Figure 4.16. Afterdischarge rates increased in the painful group in response to von Frey filament stimulation of the forepaw. Afterdischarge was measured as the increase in firing rate above spontaneous baseline firing rates. The afterdischarge rate was significantly higher after 26 g filament stimulation in the painful group compared to non-painful and sham groups (*$p<0.0006$).

4.5. Discussion

This study demonstrates that the excitability of dorsal horn neurons in the cervical spinal cord can be modulated by the magnitude of prior facet joint loading (Figures 4.9-4.14), and suggests that sufficient capsule stretch induces central sensitization. Seven days after a C6/C7 facet joint capsule stretch, forepaw stimulation using a variety of mechanical stimuli evoked an exaggerated firing response that was correlated with an increase in behavioral hypersensitivity (Figures 4.9, 4.11 and 4.15). Hypersensitivity to forepaw stimulation in this pain model suggests a significant expansion of the zone of secondary hyperalgesia outside of the site of the initial joint injury, which has previously been reported in

other pain models (Chang et al., 2009; Hylden et al., 1989; McMahon and Wall, 1984). Neuronal firing in the dorsal horn in response to non-noxious brushing and 4 g von Frey stimulation in the painful group was elevated relative to the firing frequencies of noxious von Frey stimuli in the non-painful and sham groups (Figures 4.9-4.11), which supports previous behavioral evidence of the mechanical allodynia observed in this model (Dong and Winkelstein, 2010; Lee et al., 2004a, b). Furthermore, the increased neuronal firing during noxious 10 g and 26 g filament applications in the painful group relative to controls (Figure 4.11) supports the lowered withdrawal threshold observed during the behavioral assessment of hyperalgesia in this study (Figure 4.7), and previous studies with this model (Lee et al., 2008; Lee and Winkelstein, 2009). Although the withdrawal responses measured in this study and previous work using this rat model likely reflect spinal reflexes being invoked at mechanical thresholds lower than that required to produce pain sensation (Le Bars et al., 2001), the electrophysiological evidence of hyperexcitability throughout the dorsal horn in the painful group in this study supports the use of paw withdrawal tests in evaluating changes in nociceptive responses. Collectively, this study supports the hypothesis that central sensitization is responsible for the development of mechanical allodynia and hyperalgesia in this rat model as evidenced by spinal neuron hyperexcitability following non-noxious and noxious stimuli, respectively. Furthermore, the hyperexcitability of spinal neurons following facet joint injury may explain reports of mechanical hypersensitivity extending along the neck and upper extremities of patients with

whiplash-associated disorders (Banic et al., 2004; Curatolo et al., 2001; Sterling et al., 2003).

The underlying mechanisms driving chronic whiplash-associated pain are poorly understood due to the frequent absence of evidence of any injury to spinal tissues or other structures (Riley et al., 1995). Given that anesthetic facet joint blocks can provide short-term relief of chronic neck pain for approximately 50% of patients (Barnsley et al., 1993; Barnsley et al., 1995; Lord et al., 1996), it is likely that peripheral neuron firing is a requisite for the maintenance of pain in those cases where joint blocks relieved the pain. The current study suggests that when facet joint loading is sufficient to induce sustained hypersensitivity, the wide dynamic range neurons in the dorsal horn respond to non-noxious 4g von Frey stimulation of the forepaw as though it were a noxious 10 g filament stimulation (Figures 4.11 and 4.13). These changes in the dorsal horn firing frequencies in the painful group may be related to the phenotypic switch to a WDR neuronal response also observed in that group (Figure 4.10). The electrophysiological evidence of spinal neuron hyperexcitability and changes in neuronal phenotype following facet joint injury in the rat suggests that for some whiplash patients, non-noxious proprioceptive information from the facet joints or other spinal structures may also be misinterpreted as nociceptive under certain neck motions. However, neck musculature and other connective tissues were disrupted during the surgical approaches for both the capsule stretch and the electrophysiological assessments performed in this study. Future work in this chronic pain model using

electrophysiological techniques that only require minimally invasive surgery may help to assess the contribution of proprioceptive afferent signaling from neck structures (Lam et al., 2008; Vernon et al., 2009).

Primary afferent firing has been shown to be altered during, and immediately after, certain magnitudes of capsule stretch in a goat model (Cavanaugh et al., 2006; Chen et al., 2005; Lu et al., 2005a, b). The nociceptor firing and mechanoreceptor afterdischarge in response to the initial mechanical injury in that study may be a sufficient input to initiate the modulation of secondary somatosensory neurons measured seven days after facet capsule stretch in the current study (Figure 4.12). Increased levels of substance P mRNA (Lee and Winkelstein, 2009) and increased expression of the metabotropic glutamate receptor-5 (mGluR5) (Dong and Winkelstein, 2010) in the spinal cord at the same time point (day 7) following similar degrees of facet capsule stretch also demonstrate sustained, facet-mediated glial or neuronal transcriptional changes in the spinal cord. When placed in the context of the neuronal hyperexcitability demonstrated in the current study (Figures 4.9 and 4.11), these transcriptional changes in the spinal cord may involve dorsal horn neurons. Because mGluR5 is a G protein-coupled receptor, it may initiate intracellular signaling that is capable of potentiating NMDA receptors, which would increase the responsiveness of neurons (Aniksztejn et al., 1992; Mills et al., 2002). Collectively, these studies suggest that the intracellular protein kinase cascades of glutamatergic dorsal horn neurons are modulated following painful facet capsule stretch, which causes an increase in

synaptic efficacy and produces the increased neuron excitability detected in this study.

The significant increase in the number of wide dynamic range neurons classified in the painful group (69% of neurons; $p>0.0348$) in this study suggests that a phenotypic shift in the response of the neuronal population in the deep laminae of the dorsal horn may play a key role in modulating chronic pain after this facet joint injury (Figure 4.10). The classification of neurons following sham procedures in this study (43% WDR and 57% LTM) is similar to the proportion of WDR neurons reported in other electrophysiological studies of neuron properties in the dorsal horn of the rat and sheep (Dado et al., 1994; Hains et al., 2003a; Herrero and Headley, 1995) and supports the classification methodology used in the current study. Also, the increase in the number of WDR neurons identified in the deep laminae following facet capsule stretch in the painful group is similar to the phenotypic shift identified in the dorsal horn following spinal cord hemisection (Hains et al., 2003a). An increased responsiveness of dorsal horn neurons to noxious stimuli has also been reported in models of joint inflammation (Kitagawa et al., 2005), peripheral neuropathy (Palecek et al., 1992), peripheral burn injury (Chang et al., 2010), and spinal cord injury (Hains et al., 2002, 2003a, b). The increase in the number of WDR responses from dorsal horn neurons detected in the painful group could be the result of either LTM or nociceptive-specific (NS) neurons shifting towards a WDR phenotype. However, this study identified neurons based only on an evoked response to light brush and, therefore, NS

neurons were not similarly evaluated. Due to an inability to identify NS neurons in this study, no definitive conclusions can be made regarding the phenotype of WDR neurons prior to facet joint distraction in the painful group. Therefore, it remains unknown whether the phenotypic shift is produced by WDR or LTM neurons becoming more responsive to nociceptive input or NS neurons that become more responsive to non-nociceptive stimuli following painful injury. However, previous studies have characterized the conversion of nociceptive-specific neurons to WDR neurons in response to inflammatory pain (Latremoliere and Woolf, 2009). Therefore, the hyperexcitability of dorsal horn neurons across a range of mechanical stimuli (Figures 4.9 and 4.11) in this study may be the result of the increased responsiveness of nociceptive-specific neurons in the spinal cord.

Although the design of the current study presented here provides a direct comparison to mechanical hyperalgesia assessments (Figure 4.15) using similar forepaw stimulation protocols, its scope did not encompass all regions along the C6-C8 dermatomes that may be sensitized following facet joint injuries. Furthermore, hypersensitivity is frequently observed along the back of the shoulder and neck in whiplash patients (Banic et al., 2004; Curatolo et al., 2001; Sterling et al., 2006). However, behavioral evidence of shoulder sensitivity in this rat model of facet capsule stretch has been noted (Lee et al., 2008; Lee and Winkelstein, 2009), suggesting that neuronal hyperexcitability may extend to these regions as well. Although no significant differences were found between firing in the C6-C8 spinal levels in this study, additional studies defining the range of neuronal

hyperexcitability beyond those levels in the spinal cord that encode the forepaw may help to elucidate the mechanisms of central sensitization, and possible contribution of peripheral sensitization. Specifically, the identification of widespread hyperexcitability in the spinal cord both above and below the spinal levels that innervate the facet joints and forepaws would be a possible indication of a systemic sensitization brought on by inflammatory modulators such as prostaglandins. The order of the brush, pinch, and filament stimuli used in this protocol was based on previous electrophysiological studies of dorsal horn hypersensitivity (Chang et al., 2009; Hains et al., 2002, 2003a, b) and does not account for an effect that noxious pinch may have on the firing evoked by von Frey filament stimulation. However, immediately after a noxious pinch, the five applications of the 1.4 g von Frey filament did not exhibit any dependence on the order of application (Figure 4.13), suggesting that the 60 g pinch magnitude did not produce a significant effect on spinal neuron firing. Although spontaneous discharges were also identified in 18% of neurons, the average spontaneous discharge rate (0.068±0.190 spikes/s) was substantially lower than the firing frequencies observed during evoked responses (Figures 4.9, 4.11, and 4.12). This study characterized the spontaneous and evoked activity of dorsal horn neurons at a single time point (7 days) after a capsule stretch that produced hypersensitivity, so the development of neuronal plasticity and the long-term effects still remain unknown. However, behavioral hypersensitivity in our model of facet capsule stretch has been shown to persist for up to 42 days after initial injury (Rothman et

al., 2008), suggesting that neuronal hyperexcitability may be associated with long-term changes to the central nervous system, such as functional plasticity or possibly the anatomical rearrangement of neuronal synapses.

These electrophysiological findings support the hypothesis that chronic pain following whiplash may be driven, in part, by central sensitization. Certainly, additional studies are needed to elucidate the biochemical and/or anatomical changes that produce neuronal hyperexcitability and a change in the phenotypic response of neurons to noxious stimuli. Nonetheless, this study provides the direct evidence of spinal neuron plasticity in the lower cervical spinal cord at a non-acute time point after facet capsule stretch. This work provides a foundation to continue to understand the neuronal mechanisms driving the maintenance of chronic pain and the relationship between mechanical tissue loading and pain for whiplash and other neck injuries.

4.6. Integration

This study supports the hypothesis in Aim 1 that sustained functional plasticity of dorsal horn neuronal activity can be modulated by the magnitude of applied facet capsule stretch (Figure 4.14). Furthermore, the classification of the evoked neuronal responses in this study supports the hypothesis of a phenotypic switch of neurons in the deep laminae of the dorsal horn to wide dynamic range responses after painful facet joint injury. Although these findings demonstrate an increase in spontaneous and evoked firing after joint loading sufficient to produce

sustained mechanical hyperalgesia, this study was not able to determine *how* a vertebral displacement to 0.68±0.06 mm can initiate sustained hyperexcitability without any visible evidence of capsule tearing. A histological investigation of the facet capsular ligament in the rat demonstrated a decrease in collagen fiber organization at day 1 after a vertebral displacement to 0.7 mm (Quinn et al., 2007), suggesting mechanically-induced damage to the capsule's collagen microstructure to be related to the development of spinal neuron dysfunction.

The subsequent chapters of this thesis describe the development of optical and mechanical analyses to detect facet capsule injury in the absence of its overt ligament rupture. The average evoked firing responses of each rat (Figure 4.14) to von Frey stimuli suggest that vertebral displacements between 0.3-0.6 mm may be capable of producing facet capsular ligament damage that initiates persistent pain. Chapter 5 describes the development of a polarized light technique to detect abnormal collagen fiber kinematics *during* facet capsular ligament loading. In studies presented in Chapter 6, that optical technique was applied to an investigation of isolated rat facet joint loading that replicates the joint motions that produced neuronal plasticity and persistent pain symptoms in the current study. Collectively, the studies in this thesis provide evidence that facet-mediated chronic pain may be initiated by subtle changes in capsule microstructure and driven, in part, by central sensitization.

CHAPTER 5

Development of a vector correlation technique for the pixel-wise detection of collagen fiber realignment during injurious loading

Parts of this chapter were adapted from:

Quinn, K.P., Winkelstein, B.A. (2009). Vector correlation technique for pixel-wise detection of collagen fiber realignment during injurious tensile loading. *Journal of Biomedical Optics* 14: 054010.

Quinn, K.P., Winkelstein, B.A. (2008). Collagen fiber kinematics can localize the onset of mechanical injury in ligament. *Journal of Applied Physiology* 52: 33-58.

5.1. Overview

Mechanical trauma to the cervical facet capsule has previously been defined by force-based measurements of mechanical failure and/or evidence of a visible rupture of the ligament tissue (Myklebust et al., 1988; Siegmund et al., 2001; Winkelstein et al., 2000; Yoganandan et al., 2000, 2001). However, as demonstrated in Chapter 4, loading to the cervical facet joint that does not any visible capsule rupture is capable of producing spinal neuronal plasticity and sustained mechanical hyperalgesia in the rat. Owing to the inability to visualize mechanically-induced damage that occurs without overt rupture, macro-scale strain measurements have been used to define injury tolerances and to identify the

location of potential tissue damage (Bain and Meaney, 2000; Gefen et al., 2009; Lee et al., 2004a, b; Lu et al., 2005a, b; Siegmund et al., 2001; Winkelstein et al., 2000). However, several biomechanical studies have demonstrated that full field strain measurements may depend on the length scale at which the strain is measured (DeFrate et al., 2006; Phatak et al., 2007; Screen et al., 2004). Therefore, the strain measured from an array of fiduciary markers on a ligament surface may not directly correspond to the strains experienced by the collagen fibers of the tissue. As a result, macro-scale strain fields may not have the spatial resolution to accurately localize microstructural damage that occurs without producing overt rupture in soft tissue during loading. Thus, the detection of microstructural damage during mechanical loading is needed to develop an integrative understanding of the relationship between facet joint loading and the conditions that produce facet-mediated pain.

This chapter describes the development of an optical technique to localize anomalies in the collagen fiber kinematics during tissue loading as a proxy to define the onset and location of tissue injury. These studies are directed at work outlined in Aim 2. Specifically, this chapter describes the development of a quantitative polarized light imaging system capable of measuring the collagen fiber kinematics of the facet capsule during loading (Aim 2a). Work in this chapter also tests the hypothesis that some regions of collagen fibers will deviate from the normal realignment kinematics of fibers during loading before the occurrence of visible rupture. To address this hypothesis, an analysis technique using a vector

correlation calculation was developed to identify fiber realignment during loading that was "anomalous" compared to the normal patterns of fiber reorientation that exist elsewhere in the tissue. The onset of this anomalous fiber realignment was compared to the independent mechanical measures of yield and failure during tensile loading of the isolated human facet capsular ligament (Aim 2c). In addition, the location where anomalous realignment was detected was also compared to macro-scale strain fields and the location of visible rupture (Aim 2c). In order to simplify the loading scenario for the development of this optical analysis technique, ligament tissue from the lateral aspect of the human facet capsule was isolated and tension was applied until complete rupture. The methods in this chapter form the basis for the analysis techniques used in Aims 2 and 3, and studies presented in Chapters 6 and 7.

5.2. Background

Tensile loading of ligament and tendon tissue can induce collagen fiber disorganization, fibroblast necrosis, and nociceptor activation in the absence of visible tissue rupture and before any gross tissue failure (Gimbel et al., 2004; Lu et al., 2005a, b; Provenzano et al., 2002; Quinn et al., 2007). However, conventional imaging techniques, such as computed tomography or magnetic resonance imaging, often cannot identify less severe tissue damage that can be sustained during ligament sprains and other painful injuries (Kliewer et al., 1993; McMahon et al., 2009; Yoganandan et al., 2001). Biomechanical studies of tissue injury have been

primarily focused on defining ligament tolerances at mechanical failure, where tissue rupture is unmistakably detectable by visual inspection and an associated decrease in tensile force (Kliewer et al., 1993; Noyes and Grood, 1976; Siegmund et al., 2001). In the absence of overt tissue rupture, strain measurements of neural and collagenous tissue have been used previously to localize the site of injury and to define thresholds for damage (Bain and Meaney, 2000; Cater et al., 2006; Deng et al., 2000; Gefen et al., 2008; Lee et al., 2004a, b; Lu et al., 2005a, b). Although defining strain-based thresholds for tissue tolerance has provided valuable advances in preventing subfailure injuries to many anatomical structures, those macro-scale strain measurements may not be suitable to localize damage to the collagen microstructure of the facet capsular ligament. Fiber level strains may differ from those measured at a macroscopic scale when a tissue has spatial variability in its microstructural organization; scale-dependent strain measurements may also be produced when collagen fiber sliding and reorientation occur within a tissue during deformation (Screen et al., 2004). Therefore, the direct detection of mechanically-induced microstructural damage during loading is needed to determine if and when trauma to the facet capsule occurs without any evidence of visible tissue tears or mechanical failure. This type of measurement of peripheral tissue damage could provide an explanation for (and possibly a means to detect) the pathophysiological sequelae that follow certain facet joint loading conditions.

Non-invasive imaging techniques capable of characterizing the collagen microstructure in a tissue have the potential to enable a direct assessment of the

onset and location of damage during mechanical loading. Polarized light imaging, optical coherence tomography, confocal microscopy, and small angle light scattering techniques have all been used to quantify collagen fiber alignment in soft tissue under different loading conditions (Billiar and Sacks, 1997; Hansen et al., 2002; Robinson and Tranquillo, 2009; Snedeker et al., 2008, 2006; Tower et al., 2002). Of these techniques, quantitative polarized light imaging (QPLI) has the unique ability to acquire data with high temporal resolution and adjustable spatial resolution (Geday et al., 2000; Robinson et al., 2008; Sander et al., 2009a, b;Tower et al., 2002), which facilitates a non-destructive measure of the collagen fiber kinematics by transmitting light through a tissue sample during *continuous* loading. Previous work using QPLI has described a change in the collagen fiber realignment patterns during the tensile loading of engineered tissue constructs upon tissue rupture (Tower et al., 2002). However, no study has used this imaging technique to quantitatively detect and localize the microstructural damage that is thought to occur in the facet capsular ligament during neck injuries without overt tissue rupture, such as whiplash.

The cervical facet capsule is particularly well-suited for QPLI due to the strong linear birefringence of its collagen fibers and its relatively planar geometry, which enables quasi-ballistic photon transmission without the need to section the ligament tissue or to employ optical clearing methods. Using QPLI, both the mean fiber direction and the strength of alignment in that mean direction (based on the retardation of light) can be defined at each pixel from the acquired polarized light

images (Geday et al., 2000; Tower et al., 2002; Tower and Tranquillo, 2001a, b). A digital image correlation technique that utilizes both fiber direction and alignment strength at the full pixel-wise resolution of the QPLI data is required to localize the occurrence of microstructural changes in the facet capsule tissue during loading (Hanson et al., 1992; Sviridov et al., 2006; Zhang and Arola, 2004). For studies assessing fiber realignment in this chapter, pixel-wise vector correlation calculations were performed between sequential fiber alignment maps that were obtained during loading. A vector correlation measurement that was previously used to compare maps of wind velocity was adapted to compute a correlation value at each pixel of the fiber alignment maps (Hanson et al., 1992; Kaufmann and Weber, 1998). In this study, it was assumed that when a collagen fiber or crosslink breaks under tension, the surrounding fiber network that remains intact will substantially realign in an effort to redistribute the tensile forces that are distributed across the tissue. Based on this assumption, a decrease in the vector correlation of collagen alignment was used to identify any "anomalous" fiber realignment during the continuous loading of facet capsular ligament tissue to visible rupture.

Given the increased afferent neuron firing, fibroblast remodeling, and altered collagen fiber organization within ligaments and tendons after loading without overt rupture (Lu et al., 2005a, b; Provenzano et al., 2002, 2005; Quinn et al., 2007), it was hypothesized that anomalous fiber realignment in the human facet capsular ligament can be detected prior to any indication of gross mechanical failure or visible tissue tearing. To test this hypothesis, a QPLI system was

designed that could be integrated with a commercially-available materials testing machine. Fiber direction measurements from the QPLI system were validated through a comparison to collagenous tissue with a known measurable fiber direction. Isolated facet capsular ligament tissue was then loaded to its complete rupture in the QPLI system, and the onset of a decrease in the correlation between fiber alignment maps was compared to mechanical metrics (e.g. yield, partial failure, gross failure) of damage. To demonstrate that this methodology to detect anomalous fiber realignment is capable of identifying the location of a known damaged region within the tissue, the regions that sustained anomalous realignment were compared with the location of visible rupture. In addition, the location of initial anomalous fiber realignment was compared to first principal strain fields measured in the ligament midsubstance. By developing a technique capable of identifying abnormal collagen fiber responses prior to visible rupture, this study enables the definition of a lower bound for mechanical tolerance in facet capsular ligament tissue with a greater relevance to potential physiologic dysfunction than the more liberal estimates of tolerances defined by mechanical failure or visible tissue rupture.

5.3. Methods

5.3.1. Development of a quantitative polarized light system integrated with a material testing machine

A quantitative polarized light imaging system for measuring collagen fiber alignment was assembled based on the optical train reported by Glazer et al. (1996) and Tower et al. (2002). The system was modified to operate and interface with an Instron 5385 testing machine (Instron Corporation; Norwood, MA) (Figure 5.1) and can generate pixel-wise fiber alignment maps during continuous mechanical testing. The optical train of this system consists of a rotating linear polarizer, a tissue sample, and a circular analyzer (Figures 5.1 and 5.2). The light source is provided by a fiber optic illuminator with focusing lens (Edmund Optics Inc.; Barrington, NJ), and is transmitted through a 20-cm rotating linear polarized disc

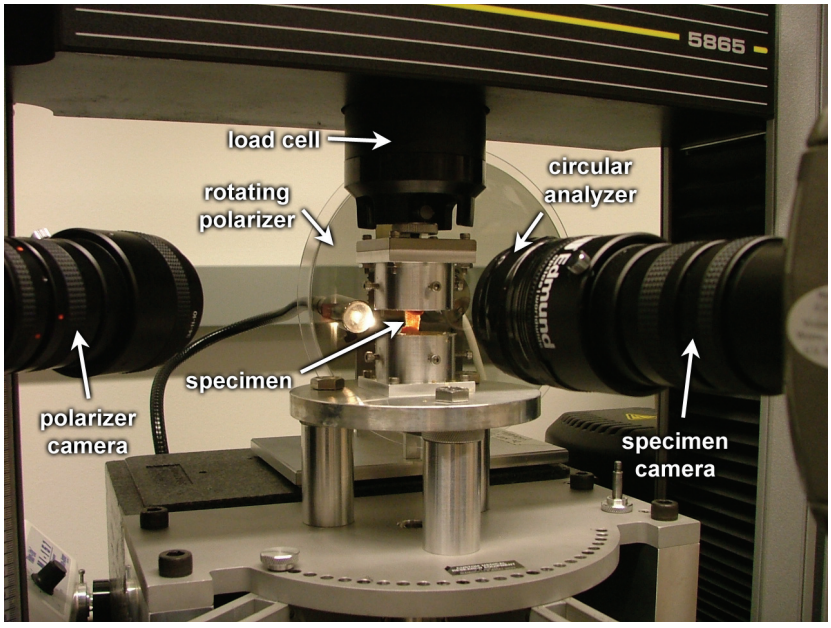

Figure 5.1. QPLI system integrated with an Instron 5865.

(Edmund Optics Inc.; Barrington, NJ) that is driven by a NEMA 17 stepper motor system (Lin Engineering; Santa Clara, CA). A circular analyzer consisting of a Mica quarter-wave plate (Optosigma Corp.; Santa Ana, CA) and linear polarizing film (Edmund Optics Inc.; Barrington, NJ) was constructed by positioning the optical axis of the quarter-wave plate 45˚ from axis of the linear polarizing film. This effective circular analyzer is tilted 10˚ about the optical axis of the wave plate to ensure that the average photon emanating from the light source is retarded exactly 90˚. Once the circular analyzer position was calibrated, it was fixed to a 6X macro zoom lens and a high-speed Phantom v5.1 CCD camera (Vision Research Inc., Wayne, NJ). A second Phantom (v4.3) camera records the orientation of the rotating polarizer (Figure 5.1); this measurement is used to calculate the fiber direction of the ligament sample as described below. Both cameras are triggered to begin collecting data prior to specimen loading and are synchronized with the collection of the mechanical data acquired by the Instron.

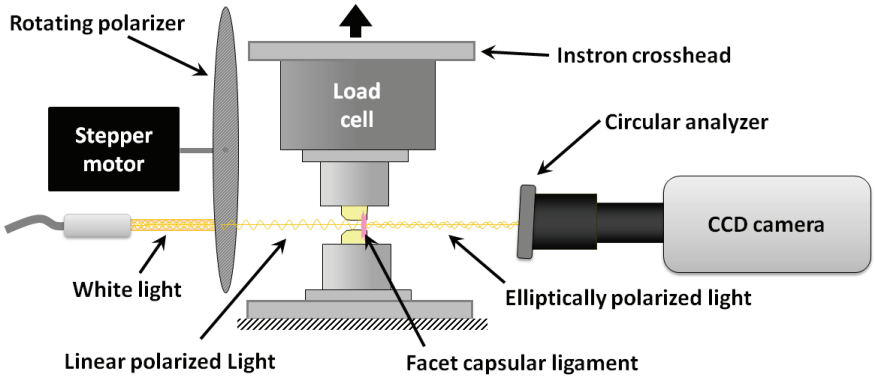

Figure 5.2. Schematic of the QPLI system. White light passes through a rotating polarizer, ligament tissue, and circular analyzer prior to image capture.

Under the premise that ligament tissue can be modeled as a linear birefringent material (Glazer et al., 1996), the intensity of light (I) measured by the CCD camera at any given pixel can be described as:

$$I(\theta) = \frac{1}{2} I_o \left(\sin(\delta)\sin(2\theta - 2\alpha) + 1\right), \tag{5.1}$$

where I_o is the initial intensity of the light source, δ is the retardation, θ is the angle of the rotating linear polarizer, and α is the sample's mean fiber alignment direction. A detailed description of the derivation of Equation 5.1 through Mueller calculus is provided in Appendix K along with a discussion of the potential sources of error that can arise due to the assumptions made for that derivation. The retardation (δ) is taken as a measure of the strength of fiber alignment, or anisotropy, through the tissue thickness (Tower et al., 2002). As the axis of the linear polarizer (θ) undergoes a complete 180˚ rotation, the intensity of light described in Equation 5.1 can be fit to the simple harmonic equation:

$$I(\theta) = A + B\cos(2\theta) + C\sin(2\theta). \tag{5.2}$$

The Fourier coefficients, A, B, and C, can be determined on a pixel-wise basis using a summation approximation of the intensity data at discrete time points over the 180˚ rotation (Tower et al., 2002; Tower and Tranquillo, 2001b). The signed harmonic coefficients, B and C, are scaled by pixel bit depth and used to calculate the retardation (δ) and the fiber alignment direction (α) at each pixel using the following equations (Tower et al., 2002):

$$\delta = \cos^{-1}\left(\sqrt{1 - B^2 - C^2}\right), \tag{5.3}$$

$$\alpha = \frac{1}{2}\tan^{-1}\left(B/-C\right). \tag{5.4}$$

To assess the accuracy of the QPLI system in measuring fiber alignment direction (α), ligament tissue with a known visible collagen fiber direction was compared to the QPLI measurements. Specifically, a 60 μm thick section of caprine anterior cruciate ligament tissue was placed on a glass slide and imaged by the QPLI system. Using the normal bright-field images, any visible fiber direction of the tissue was digitized (Figure 5.3a). Pixels within the bright-field image that were assigned a digitized fiber direction were then compared to the fiber direction measured by the QPLI system. The mean error in fiber direction measurements for ligament tissue was -0.59±6.12˚ using the QPLI system, which suggests the average error in the fiber direction measurements is less than the 9˚ polarizer step between each QPLI image collected during data acquisition (Figure 5.3).

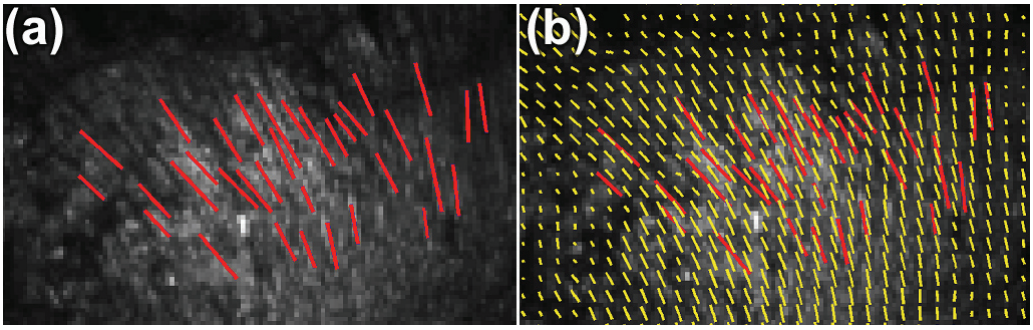

Figure 5.3. Comparison of visible fiber direction with QPLI-based fiber direction measurements. (a) Image showing where the visible fiber direction of a caprine anterior cruciate ligament tissue section was digitized (red lines). **(b)** Overlay of those digitized fiber directions and the direction of the collagen fibers derived from the QPLI system (yellow lines) at those pixels.

5.3.2. Facet capsular ligament preparation & testing

Right and left cervical facet joints (n=16) were removed from the C4/C5 spinal motion segments of fresh, unembalmed human cadavers (57±13 years of age). The ages and donor information of individual specimens for this study are summarized in Appendix C. Through fine dissection, all musculature and tendon insertions on the surface of the facet capsules were removed. The lateral aspect of the facet capsular ligament was isolated, and the articular processes of the joint were removed to allow for transmission of polarized light through the ligament tissue (Figure 5.4). The bone-ligament-bone specimens were cast with FlowStone (Whip Mix Corporation; Louisville, KY) in aluminum cups that were then fixed to the Instron. Using a felt-tipped pen, an array of 15 to 24 (mean of 18.9±2.9) fiduciary markers was placed covering the ligament midsubstance surface in order to track tissue displacement for macro-scale strain field measurements during

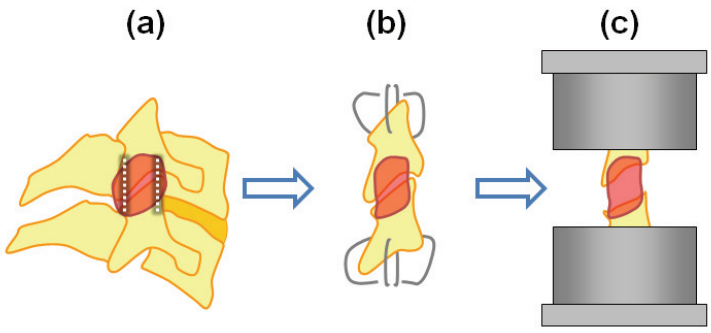

Figure 5.4. Specimen preparation process. (a) Facet joints were removed from C4/C5 motion segments and a strip of the lateral aspect of the capsular ligament was isolated as shown by the dotted lines. **(b)** K-wire was inserted into the C4 and C5 lateral masses. **(c)** Articular bone and cartilage were removed to facilitate light transmission and the specimens were potted using the K-wires and FlowStone.

loading. The cross-sectional area of each unloaded specimen was estimated by measuring the sample's width and thickness with digital calipers to approximate the average tissue stress during loading (see Appendix C for the cross-sectional area of individual specimens). To reduce variability between specimen tests, the reference position for the start of loading was set at a 5 kPa pre-stress, based on the lowest measurable stress within the accuracy of the load cell (100 N load cell capacity). Prior to loading to rupture, all specimens were mechanically preconditioned for 30 cycles of tensile loading between 0 and 0.5 mm, which corresponds to less than 5% of the average load to failure (Winkelstein et al., 1999).

For each test, the inferior articular facet of C4 was displaced at 0.5 mm/s to impose tension across the C4/C5 capsular ligament until complete rupture of the ligament was produced. During each test, load and displacement data were collected by the Instron Bluehill software at 1 kHz, and the CCD cameras collected images from a 196x400 pixel window, at 500 fps with 12.5 pixel/mm resolution and 8-bit pixel depth. The linear polarizer rotated at 750 rpm, which corresponds to a 9˚ rotation between each image that was acquired. Pixel-wise fiber alignment maps (Figure 5.5) were then created using Matlab 7 (The Mathworks, Inc.; Natick, MA) for every 0.04 seconds during loading using a corresponding set of 20 consecutive images and the harmonic analysis methods described above (see Appendices K and L for a complete description of the calculations and Matlab code). The loading and image acquisition rates were both chosen so that the local tissue movement during the displacement of the joint corresponded to less than 0.3

pixels per alignment map. This minimization of tissue movement between alignment maps enabled the comparison of the fiber alignment at a single pixel between consecutive maps.

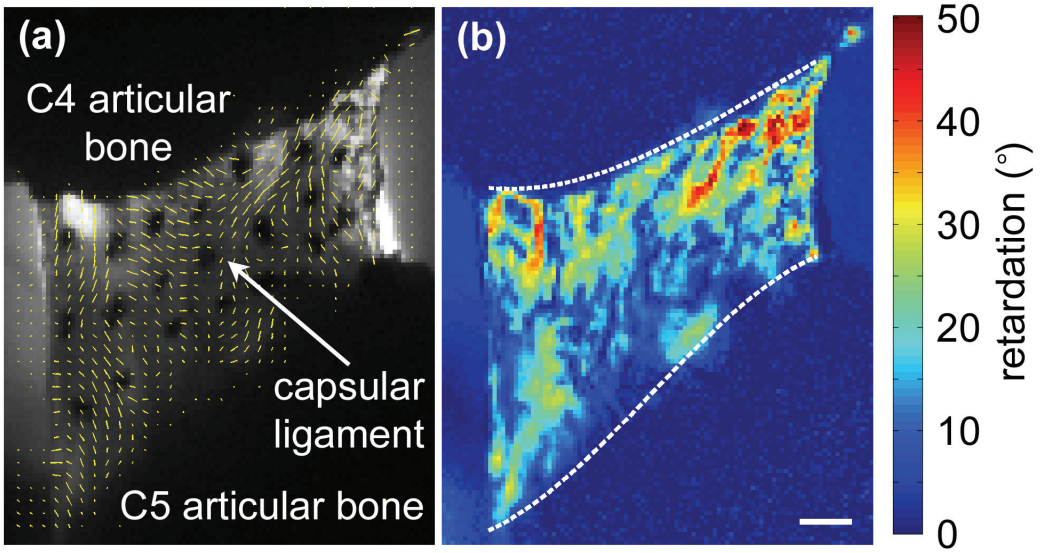

Figure 5.5. Fiber alignment (a) and retardation (b) maps of Specimen #4. **(a)** Alignment vectors are plotted over the bright field image with each vector representing a mean fiber direction with a length scaled to the degree of retardation. **(b)** Retardation values correspond to the strength of fiber alignment at each pixel. The dotted lines represent the digitized ligament insertion boundaries, and the scale bar (1 mm) in (b) applies to both images.

5.3.3. Identifying anomalous realignment via vector correlation

An analysis technique to detect microstructural damage via inferred fiber realignment was established using the correlation of consecutive alignment maps. Vector correlation is utilized to create a robust measure of anomalous fiber realignment that includs both the mean fiber direction and the strength of alignment in that mean direction (i.e. retardation) (Hanson et al., 1992; Kaufmann and Weber, 1998). For every alignment map that is generated, vector correlation measurements

are made using the maps immediately preceding and following it. A distinct correlation value is computed for each pixel in the alignment maps using just the fiber alignment data at, and surrounding, that pixel. Specifically, for each pixel in an image, a correlation value is determined by comparing the data between alignment maps in a 5x5 pixel window centered at that pixel (Figure 5.6). Within that window of pixels, the pixel with the greatest vector difference between maps is removed from the correlation measurement in order to minimize the spatial propagation of error produced by any single aberrant pixel, which results in a set of 24 alignment vectors per window. For implementation into a vector correlation measure, the retardation (δ) and fiber direction (α) at each pixel are first converted

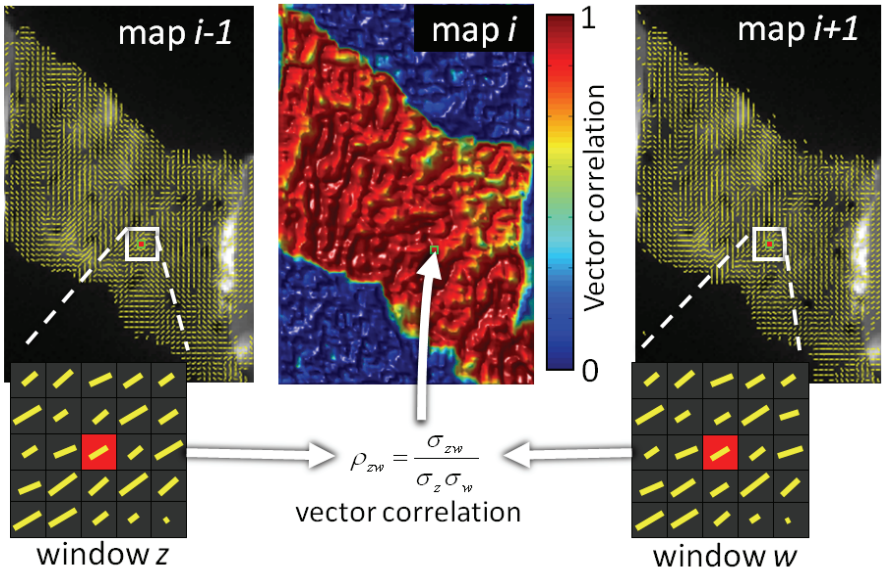

Figure 5.6. Schematic of the pixel-wise vector correlation calculation. The vector correlation for each pixel in a given map (*i*) is calculated from the alignment surrounding the pixel in the maps immediately preceding (*i-1*) and following (*i+1*) it according to Equations 5.5-5.8. Normal realignment patterns throughout the ligament tissue are demonstrated by correlation values near 1.

to x- and y-components of an alignment vector. To create the alignment vector of a pixel, the axial fiber direction (α) is converted to circular data with an orientation of 2α. The magnitude of the vector is defined as $\sin^2(\delta)$ to provide a linear measure of alignment strength that is proportional to the strength of the harmonic signal. To compute the correlation coefficient at a pixel, two groups (z and w) of alignment vectors are created from the 5x5 pixel window of the preceding and following alignment maps (Figure 5.6). The variances (σ^2_z, σ^2_w) and covariance (σ_{zw}) of the two sets of 24 alignment vectors (z and w) are computed as:

$$\sigma_z^2 = \frac{1}{24}\sum_{j=1}^{24}\left(z_j - \bar{z}\right)*\left(z_j - \bar{z}\right), \tag{5.5}$$

$$\sigma_w^2 = \frac{1}{24}\sum_{j=1}^{24}\left(w_j - \overline{w}\right)*\left(w_j - \overline{w}\right), \tag{5.6}$$

$$\sigma_{zw} = \frac{1}{24}\sum_{j=1}^{24}\left(z_j - \bar{z}\right)*\left(w_j - \overline{w}\right), \tag{5.7}$$

where the x- and y-coordinates of the vectors in windows z and w are represented in complex form, and $\bar{z}$ and $\overline{w}$ represent the mean vectors of the window in each map (Hanson et al., 1992). The vector correlation (ρ_{zw}) between alignment maps in a given pixel window is then defined as (Figure 5.6):

$$\rho_{zw} = \frac{\sigma_{zw}}{\sigma_z \sigma_w}. \tag{5.8}$$

The magnitude of this complex correlation measurement is computed to produce an analog to traditional scalar correlation values (Hanson et al., 1992). This vector correlation measurement is computed for the fiber alignment surrounding each

pixel in the alignment maps, and ranges from 0 to 1, with 1 representing synchronized fiber realignment between maps.

Using the pixel-wise vector correlation calculation, correlation maps were produced for each fiber alignment map throughout the duration of applied loading for these studies (Figure 5.6). Of note, correlation was low in any region of the image where the sample alignment was not well-defined because of poor light transmission through the tissue. To identify those regions of the image with an undefined fiber alignment, pixel-wise maps were generated to quantify the signal-to-noise ratio (SNR) of the harmonic light intensity response. As in standard SNR descriptions, the root mean square amplitude of the harmonic response of the light intensity during polarizer rotation represented the "signal". The "noise" was associated with the residual of the harmonic fit to the intensity response of a given pixel during the rotation of the polarizer. Pixels with an SNR of less than 5 were prone to large fluctuations in their correlation values during the continuous acquisition of fiber data in static ligaments that were not loaded; accordingly, any pixels with an SNR less than 5 were not included in any further analysis of anomalous realignment.

Changes in the vector correlation between maps were quantified in order detect any anomalous fiber realignment that may have occurred when a collagen fiber network sustained localized microstructural damage during tissue loading. Anomalous fiber realignment was defined at any pixel with acceptable SNR where the vector correlation decreased by 0.2 or more relative to its correlation value in

the previous correlation map (Figure 5.7). Matlab code for the detection of anomalous fiber realignment can be found in Appendix M. A threshold of 0.2 was defined to ensure that fiber realignment would not be detected during correlation measurements made of static specimens that did not undergo any loading (Figure 5.7). Regions of tissue were defined as sustaining anomalous fiber realignment if realignment simultaneously occurred in 9 or more pixels that were connected to each other (based on 8-neighbor pixel connectivity). The 9-pixel requirement was chosen to eliminate the potential for detection of anomalous realignment because of random noise and was confirmed through a parametric analysis comparing the effect of the pixel threshold on the displacement at initial anomalous realignment

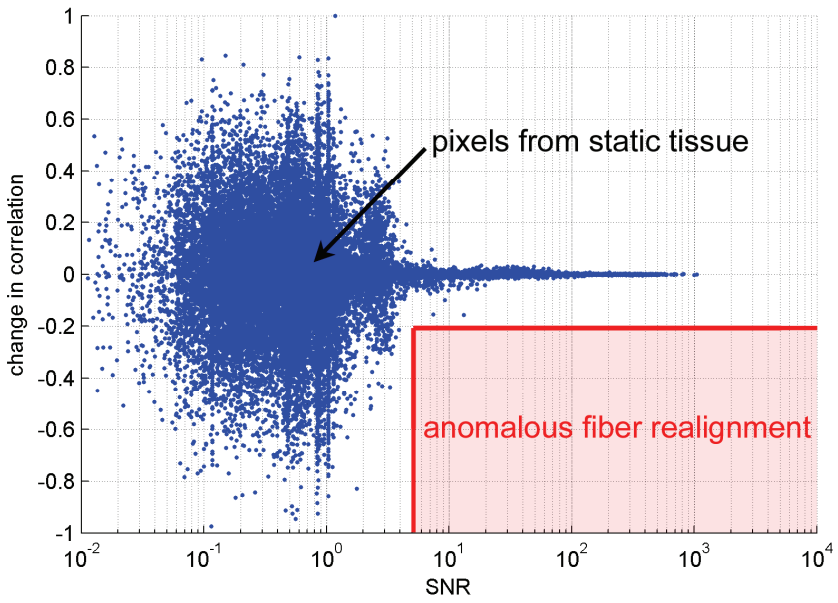

Figure 5.7. Anomalous fiber realignment was defined in regions where the change in vector correlation was less than -0.2 and signal-to-noise ratio (SNR) was greater than 5. These thresholds were determined to ensure that anomalous realignment would not be detected at any pixel in static specimens.

detection. For a comparison of anomalous realignment with mechanical data, the onset (force and displacement) and location of anomalous fiber realignment were also noted.

5.3.4. Mechanical data analyses

The average stress and strain in each specimen were calculated during loading to provide mechanical context for the onset of any anomalous fiber realignment that was detected, and to facilitate comparisons between realignment and traditional measures of tissue damage. Average ligament strain was calculated from the bright field images in order to quantify the average material response of the tissue and to provide a comparison with previous mechanical studies of this ligament. Average strain was determined by digitizing and tracking the ligament insertion into the superior and inferior bones (Figure 5.5b). The average length between the superior and inferior insertions of the ligament was calculated from each alignment map, and the average one-dimensional (1-D) Lagrangian strain was computed during tissue loading using the length measurements. The average stress, strain, force, and displacement at the first detection of anomalous fiber realignment were measured for each specimen.

To identify whether anomalous fiber realignment occurs in the same location in the facet capsule tissue that undergoes the largest strains, the first principal strain (ε_1) field on the surface of the ligament midsubstance was also calculated using the corresponding positions of the fiduciary markers throughout

loading (Figure 5.8). The fiduciary marker locations on the ligament midsubstance were digitized for each alignment map, and four-node elements were created from that digitized array. Through isoparametric mapping and plane strain theory, Lagrangian strain was computed in each of these elements to provide full field ε_1 measurements of the ligament midsubstance for every fiber alignment map (Figure 5.8). Matlab code for the Lagrangian strain calculations can be found in Appendix N. The element with the maximum ε_1 was also noted for every alignment map during loading. Because strain could not be computed at the pixel level in this study, the number of pixels with anomalous fiber realignment in each strain element on the ligament midsubstance was computed throughout loading in order to identify whether the realignment that was detected also corresponded to regions of the tissue that sustained higher strains.

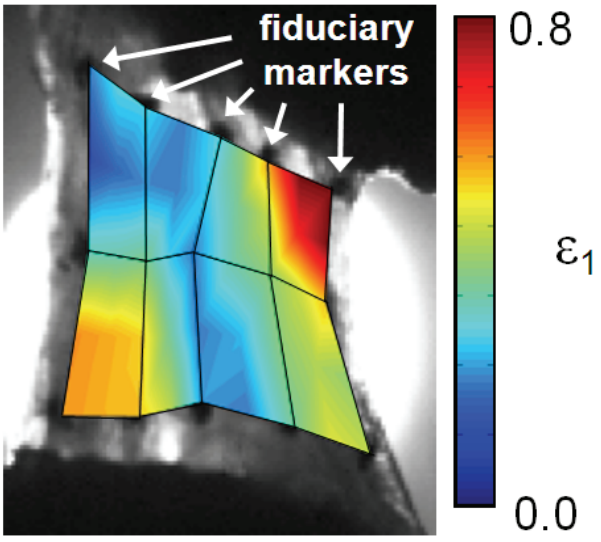

Figure 5.8. Full field strain (ε_1) at 2.26 mm (Specimen #12). Lagrangian plane strain was calculated based on the deformation of fiduciary markers on the ligament surface.

Gross failure, partial failure, and yield of the ligament tissue were assessed from the mechanical data collected by the Instron during loading in order to quantify structural damage and to provide mechanical context for the occurrence of anomalous collagen fiber realignment. Prior to the analysis of failure or yield, force data were digitally filtered using a 10-point moving average with zero-phase distortion. Gross failure was defined by a drop in force after the maximum force during loading, and partial failure was defined by a decrease in force with increasing displacement between any two data points prior to gross failure. To provide the most conservative detection of a loss of structural integrity using the force-displacement data, ligament yield was defined based on a decrease in stiffness (Yoganandan et al., 1989). Tangent stiffness was calculated for each data point during loading using a centered finite difference approximation:

$$k_i = \frac{F_{i+1} - F_{i-1}}{\delta_{i+1} - \delta_{i-1}}, \tag{5.9}$$

where the stiffness (k_i) at a given data point i, was calculated from the difference in force (F) and displacement (δ) between the previous ($i–1$) and following ($i+1$) data points. Yield was defined for any continuous drop in tangent stiffness of at least 10% of the specimen's peak stiffness value in order to provide a detection algorithm that was independent of scale. There was no limit to the displacement over which yield could occur, but stiffness was required to decrease in each sequential data point over the entire 10% drop. Matlab code for the detection of yield and failure is provided in Appendix O. Through parametric analysis, it was

determined that the detection of yield did not vary significantly when the threshold for detecting a decrease in stiffness was between 3 and 18% (Figure 5.9). For each specimen, all occurrences of yield or partial failure were identified during loading up to the gross failure of the specimen, and any occurrences of yield or failure during the initial detection of anomalous fiber realignment were also noted. The onset and location of visible tissue rupture in each specimen were also defined through an evaluation of the bright field images. The criteria to identify visible rupture included rapid tissue movement during loading or the development of a visible hole or tear in the tissue; the evaluator was blinded to the mechanical and polarized light data.

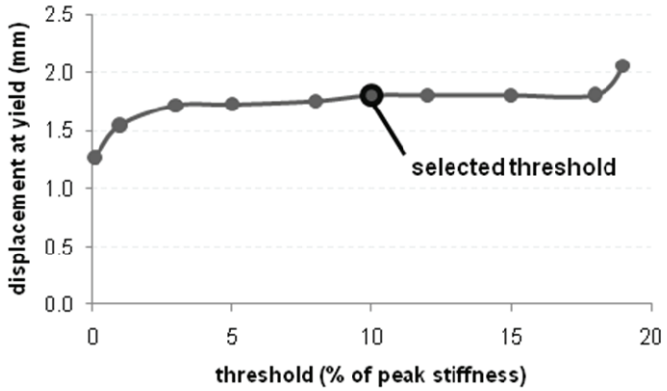

Figure 5.9. The displacement at which yield is detected does not depend on the threshold for a decrease in stiffness between values of 3-18%. For this study, yield was defined by a decrease in tangent stiffness of 10% from the specimen's peak stiffness value.

5.3.5. Statistical analyses

To validate the utility of anomalous fiber realignment in identifying microstructural damage in the facet capsule, the location of realignment was

compared to the location of visible rupture, and the onset of realignment was compared with the occurrence of mechanical injury events (e.g. yield, partial failure, gross failure). At the onset of visible tissue rupture, the number of pixels that had sustained fiber realignment during loading was counted in each of the elements in the ligament's midsubstance. A two-by-two contingency table of the midsubstance elements from all specimens was created to compare those elements sustaining any fiber realignment with those sustaining visible rupture, using Fischer's exact test. To assess the relationship between strain and anomalous realignment, the frequency of initial anomalous realignment occurring within the element with the maximum ε_1 was compared to the overall probability of initial realignment occurring within an element of the strain field using a binomial test. A binomial test was also employed to test for a significantly higher frequency of visible rupture occurrences within the location of maximum ε_1 at failure. The displacements and average 1-D strains at each of the first detection of fiber realignment, visible rupture, and gross failure were compared using one-way ANOVAs and post-hoc Bonferroni tests. Significance for each ANOVA was defined by $p<0.05$; all tests were performed using JMP 7 (SAS Institute Inc., Cary, NC).

5.4. Results

Anomalous fiber realignment was detected in 15 of the 16 specimens during tissue loading up to visible rupture (Figure 5.10; Table 5.1). Realignment could not

be detected in one specimen (#10) due to poor light transmission which resulted in an insufficient SNR (Table 5.1). The average percentage of pixels in the midsubstance of the ligament specimens with an acceptable SNR (≥ 5) was 90.7±8.4% at the beginning of loading, and the average percentage throughout the entire loading test was 84.5±12.4%. The average percentage of pixels that had sustained anomalous fiber realignment in the midsubstance elements up to the point

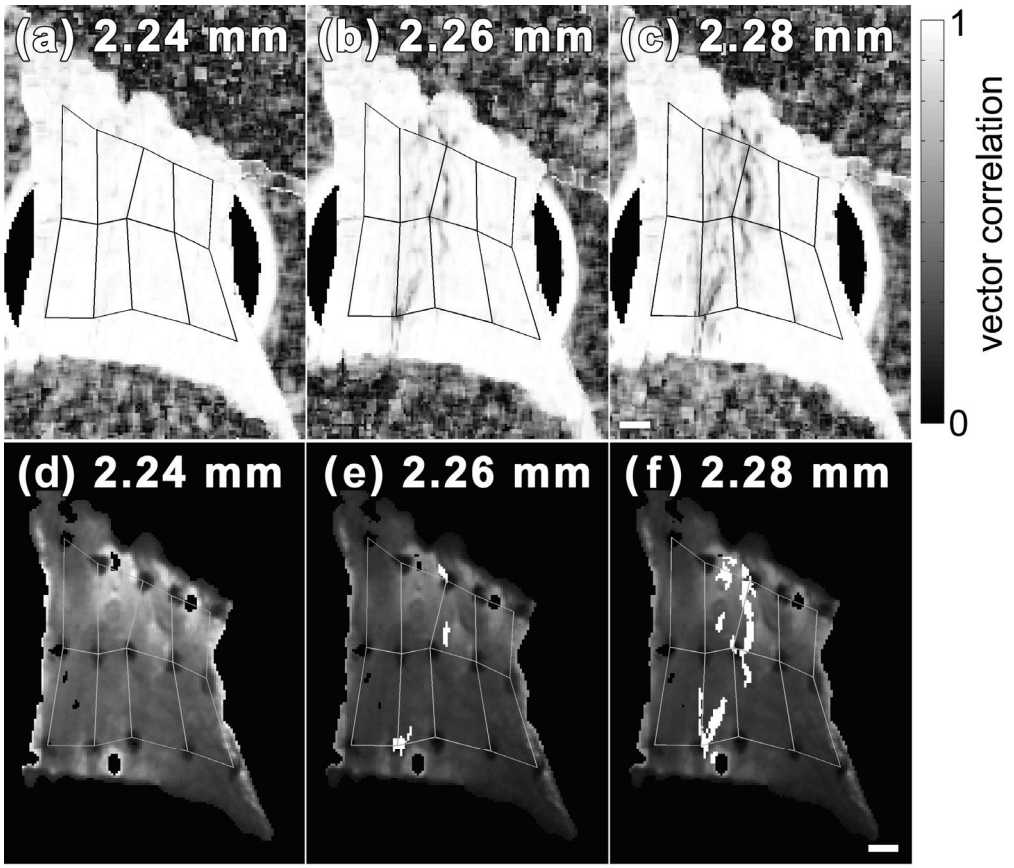

Figure 5.10. Maps of vector correlation and anomalous realignment for a representative specimen (#12) during loading. (a-c) Sequential vector correlation maps demonstrate a decrease in correlation through the midsubstance of the ligament over consecutive frames. **(d-f)** Anomalous fiber realignment (white pixels) is initially detected at 2.26 mm in three regions in this specimen where the vector correlation in **(b)** decreases by more than 0.2. The scale bars (1 mm) in **(c)** and **(f)** apply to all images.

of visible rupture was 6.2±9.0% from an average total midsubstance area of 3757±1157 pixels. Individual maps of the initial detection of anomalous realignment in each specimen are detailed in Appendix E. The mean thickness of these specimens was 0.451±0.092 mm, and ranged from 0.300 to 0.632 mm.

Table 5.1. Mechanical data at first detection of anomalous fiber realignment.

Specimen	Force (N)	Displacement (mm)	Stress (MPa)	Average 1-D Strain	Mechanical event associated with realignment*
1	24.19	3.79	7.77	1.22	1st failure (5th yield)
2	17.54	1.97	4.78	0.91	1st failure (3rd yield)
3	25.94	3.00	8.42	0.59	4th yield
4	3.74	1.49	1.90	0.43	1st failure (1st yield)
5	2.94	1.62	1.44	0.49	2nd failure (2nd yield)
6	13.45	3.43	2.61	0.65	7th yield
7	0.51	1.16	0.15	0.20	1st failure (1st yield)
8	28.39	2.56	8.08	0.83	2nd failure (3rd yield)
9	8.80	3.20	3.07	0.99	2nd failure (8th yield)
10	Low SNR/ no realignment detected				
11	19.10	3.29	5.13	0.91	3rd failure (7th yield)
12	3.82	2.26	1.41	0.54	1st yield
13	15.82	3.29	4.68	0.68	1st failure (8th yield)
14	23.48	2.99	6.36	0.93	2nd failure (9th yield)
15	26.90	3.65	11.06	0.82	1st failure (4th yield)
16	12.79	2.24	4.55	0.70	1st failure (2nd yield)
Mean	**15.16**	**2.66**	**4.76**	**0.73**	
S.D.	**9.54**	**0.83**	**3.11**	**0.26**	

* Ordinal rank of failure or yield defines its occurrence relative to other such events during loading of that specimen.

In all 15 specimens with sufficient SNR, visible rupture occurred in a region of the tissue that had previously sustained anomalous fiber realignment. Visible rupture was first detected as rapid tissue movement away from the direction of loading in 11 of the 16 specimens, and as a hole in the tissue in the five other

specimens. Visible rupture first occurred at 3.47±0.96 mm of sample displacement, which corresponded to an average 1-D strain of 1.02±0.35 (Table 5.2). In six specimens, visible rupture was initially identified in the ligament midsubstance in a total of nine elements. All nine of those elements with visible rupture had sustained prior fiber realignment during loading (Tables 5.2 and 5.3). An additional 45 other elements (out of a total of 173 elements) sustained fiber realignment in the absence of any visible rupture. The relationship between visible rupture and the localization of anomalous fiber realignment was significant ($p<0.001$). The location of visible rupture matched the element with maximum ε_1

Table 5.2. Mechanical data at the first detection of visible rupture.

Specimen	Displacement (mm)	Average 1-D strain	Associated mechanical event	Visualization criteria
1	4.53	1.54	gross failure	visible hole *
2	3.27	1.76	5th failure	rapid tissue movement *
3	3.64	0.74	gross failure	visible hole *
4	1.69	0.50	2nd failure	rapid tissue movement
5	3.64	1.33	gross failure	rapid tissue movement
6	3.95	0.78	gross failure	rapid tissue movement *
7	4.56	1.00	gross failure	visible hole
8	2.58	0.84	2nd failure	rapid tissue movement
9	3.22	1.00	2nd failure	rapid tissue movement
10	2.85	0.96	gross failure	rapid tissue movement
11	4.08	1.20	gross failure	visible hole
12	2.28	0.55	1st yield	rapid tissue movement
13	5.31	1.24	gross failure	rapid tissue movement
14	3.81	1.27	gross failure	visible hole *
15	3.85	0.88	gross failure	rapid tissue movement *
16	2.26	0.71	1st failure	rapid tissue movement
Mean	**3.47**	**1.02**		
S.D.	**0.96**	**0.35**		

* Rupture occurred within elements in the midsubstance.

Table 5.3. Summary of initial fiber realignment and associated strains.

Specimen	Number of pixels	Area of realignment (mm^2)	Number of elements with realignment	ε_1 in element with most realignment	Maximum ε_1 in the entire specimen
1	47	0.278	3	0.82	0.82
2	16	0.095	below elements		
3	48	0.284	2	0.10	0.76
4	17	0.101	1	0.07	0.63
5	93	0.550	right of elements		
6	13	0.077	above elements		
7	54	0.320	above elements		
8	105	0.621	2	0.18	0.24
9	137	0.811	5	0.59	1.32
10	N/A*				
11	12	0.071	above elements		
12	74	0.438	3	0.36	0.68
13	11	0.065	below elements		
14	9	0.053	1	0.35	0.43
15	12	0.071	above elements		
16	39	0.231	2	0.13	0.46
Mean	**45.80**	**0.271006**	**19 of 173**	**0.32**	**0.67**
S.D.	**40.19**	**0.237785**		**0.27**	**0.33**

* Low SNR- no realignment was detected.

in three of the six specimens in which visible rupture occurred within the elements. The co-localization of visible rupture and maximum ε_1 in three specimens significantly exceeded the average probability of visible rupture anywhere within the strain field ($p=0.0474$).

In every specimen, the first detection of anomalous fiber realignment coincided with the occurrence of a mechanical event that suggested a loss of structural integrity (Table 5.1). In 11 specimens, this anomalous fiber realignment first occurred during the first or second occurrence of tissue failure (Table 5.1). In three other specimens, anomalous realignment was detected during yield, but prior

to any measurable tissue failure (Table 5.1). On average, fiber realignment was first detected at 2.66±0.83 mm of joint displacement and 15.16±9.54 N of load (Table 5.1). This corresponded to an average 1-D strain of 0.73±0.26 and stress of 4.76±3.11 MPa (Table 5.1). The average area over which the initial fiber realignment was detected corresponded to 45.8±40.2 pixels or 0.271±0.238 mm^2 (Table 5.3). In half of the specimens, this initial realignment occurred within the elements defined on the ligament midsubstance (Table 5.3).

Gross mechanical failure of the specimens occurred at an average load of 21.53±7.21 N and displacement of 3.62±0.49 mm. These structural data corresponded to a mean ultimate tensile stress of 6.17±2.18 MPa and strain of 1.12±0.43. Partial failure first occurred earlier at 15.78±9.17 N and 2.64±0.93 mm, which correspond to an average stress and strain of 4.91±3.04 MPa and 0.72±0.27, respectively. Ligament yield occurred at 9.48±6.11 N and 2.01±0.57 mm, and corresponded to 2.93±2.01 MPa of stress and 0.53±0.18 strain. The mean displacement and strain at the first detection of anomalous fiber realignment were significantly lower than both the occurrence of gross failure ($p<0.004$) detected from the mechanical response and the first evidence of any tissue rupture ($p<0.004$) identified from the bright field images. The force-displacement responses for each specimen in this study are summarized in Appendix D.

In the eight specimens in which initial anomalous fiber realignment occurred in the elements in the midsubstance of the ligament, the average ε_1 of the element with the greatest number of pixels detected to have anomalous realignment

was 0.32±0.27 (Table 5.3). However, the maximum ε_1 in those eight specimens at initial realignment (0.67±0.33) was significantly greater ($p=0.006$) in the element with the most fiber realignment. In fact, the location of maximum ε_1 only matched the element with the most fiber realignment in one specimen (#1; Table 5.3). Initial detection of anomalous realignment occurred within the element with maximum ε_1 in three specimens; this frequency of detection in the element with maximum ε_1 was not significantly higher than the overall probability of anomalous realignment occurring within an element ($p=0.253$). The full field ε_1 measurements at both the initial detection of anomalous fiber realignment and at gross failure are provided for all specimens in Appendix F.

5.5. Discussion

This chapter describes the implementation of a vector correlation technique to identify changes in collagen fiber realignment in the human cervical facet capsular ligament under tensile loading. Through QPLI analysis, both the mean fiber direction and the strength of fiber alignment at each pixel were calculated during continuous loading. Both of these measurements were incorporated into a pixel-wise vector correlation (Hanson et al., 1992) in order to fully utilize the QPLI data to identify anomalous fiber realignment. Anomalous fiber realignment in facet capsular ligament tissue is associated with an apparent loss of tissue integrity, as defined by the traditional metrics of mechanical failure and visible rupture (Tables 5.1 & 5.2). In addition, the first detection of anomalous fiber realignment in this

study occurred well-before any visible rupture of the tissue during loading (Tables 5.1 & 5.2), coinciding with either ligament yield or partial failure in every specimen (Table 5.1). Additional analysis of the potential relationship between fiber realignment and putative damage revealed that the spatial location where anomalous realignment was produced during loading was significantly associated with the regions in the tissue where visible rupture ultimately developed ($p<0.001$). These findings demonstrate a method capable not only of measuring fiber realignment sensitive to mechanical trauma, but also of localizing the development of those changes with pixel resolution.

Because collagen fiber alignment data were collected with a temporal resolution sufficient to facilitate continuous loading of ligament tissue, the onset of anomalous realignment can be directly compared to previous traditional biomechanical studies of the facet capsule. The stresses and strains measured at both partial failure and gross failure in this study are consistent with other reports for the rat and human cervical facet capsule (Quinn and Winkelstein, 2007; Siegmund et al., 2001; Winkelstein et al., 2000; Yoganandan et al., 2000). However, the detection of anomalous fiber realignment during loading suggests that there may be material limits for capsular ligament tissue that are substantially lower than that defined by failure (Table 5.1). Anomalous fiber realignment may be an indication of microstructural damage and suggests a potential threshold for mild (grade I) ligament sprains and/or the development of increased ligament laxity that has been previously reported (Jones et al., 2009; Panjabi et al., 1996;

Provenzano et al., 2002). By utilizing a detection technique with pixel-level resolution, the current approach identified initial anomalous fiber realignment to occur in a region that is much smaller (0.271 ± 0.238 mm^2) than the size of the elements used to measure strain (Figures 5.8 and 5.10). As such, tissue strain fields may lack the sensitivity needed to detect subfailure tissue damage, which may explain the spatial disconnect between the location of maximum ε_1 and the location where realignment was first detected in this study (Table 5.3). The size of the elements used in this study were chosen to match the spatial resolutions used in other studies of the facet capsule (Lu et al., 2005a, b; Winkelstein et al., 2000; Siegmund et al., 2001), but a finer resolution in tissue strain field measurements may have facilitated better agreement between maximum ε_1 and the location of anomalous realignment in this work. In Chapter 7, a strain measurement technique is presented that utilizes collagen fiber alignment patterns to track tissue deformation with enhanced spatial resolution (Quinn et al., 2010a). With that alternative tracking technique, strain measurements may be able to better capture the inhomogeneity of the capsular ligament deformation, which could actually facilitate better agreement between strain maxima and the locations where anomalous fiber realignment are detected. However, any image-based strain measurement is limited by pixel resolution and cannot account for variability in regional tissue tolerances. This study localizes anomalous fiber realignment to individual pixels through vector correlation, which allows for a direct detection and

localization of altered microstructure without needing to rely on scale-dependent strain measurements for the determination of mechanically-induced injury.

This analysis technique to detect anomalous fiber realignment requires only three fiber alignment maps acquired over 0.2 seconds in order to measure a change in vector correlation. With such a small number of fiber maps required to identify anomalous realignment, tissue regions that may lack sufficient light transmission during the initial portion of loading are still able to be assessed for realignment if light transmission improves for a period of time during the loading of the tissue. Also, using this analysis approach, a vector correlation map can be created between any two alignment maps in which the tissue is in the same location, regardless of the time-history or map sequence. Because of the relatively few requirements for quantifying changes in alignment through vector correlation, this technique could be adapted to other imaging modalities, such as second harmonic generation microscopy or optical coherence tomography, that are capable of measuring fiber alignment in an in vivo setting (Hansen et al., 2002; Psilodimitrakopoulos et al., 2009; Snedeker et al., 2006). Ultimately, an assessment of anomalous fiber realignment during tissue loading in vivo could provide unique insight into the relationship between microstructural injury and the physiologic consequences of excessive facet joint loading, such as nociceptor firing, spinal neuron plasticity, and secondary hyperalgesia (Lee et al., 2004 a, b; Lee and Winkelstein, 2009; Lu et al., 2005a, b; Quinn et al., 2010b).

Using quantitative polarized light imaging, fiber alignment can be measured continuously anywhere in a planar, collagenous soft tissue. Accordingly, changes to the collagen fiber network, and possibly damage, can be evaluated by transmitting light through the total area of any given tissue sample. However, accurate fiber measurements may be limited to ligament samples with thicknesses less than 0.6 mm, given the occasional poor light transmission in the thickest samples measured in this study. Although the application of this technique may be limited by sample thickness, the surface area of entire capsular ligament specimens was able to be accommodated by adjusting the lens magnification and field of view. As a result, the image resolution was insufficient to actually visualize the putative collagen fiber failures that may occur when fiber realignment is detected during loading. As such, an analysis of tissue integrity though an additional, high resolution, imaging modality is needed in the ligament regions where anomalous realignment was detected in order to provide ultrastructural validation of the assumption that collagen fiber failure mediates an atypical pattern of fiber realignment. Studies of tendon fascicle loading have suggested that shear forces generated by the sliding of adjacent collagen fibers can produce failure of the proteoglyan crosslinks (Puxkandl et al., 2002; Screen et al., 2004). Although collagen fibers are more highly aligned in tendons than compared to the facet capsular ligament (Figure 5.5a), fiber shearing may also play a role in the development of anomalous fiber realignment in the facet capsular ligament. However, a better understanding of the extracellular matrix ultrastructure of

capsular ligament tissue is needed to better determine the failure mechanisms of the extracellular matrix associated with anomalous realignment, yield, and failure in this ligament. Because anomalous fiber realignment is presumed to occur in the local fiber network surrounding fiber failure, the specific location(s) of collagen fiber failure within the detected anomalous realignment is unknown. Therefore, the true extent and severity of damage cannot be fully distinguished through this imaging technique, and it remains unclear whether the fiber realignment described in this chapter is permanent or unrecoverable.

Additional investigations are needed to assess if there are any sustained structural and mechanical effects of loading up to the onset of anomalous fiber realignment. Although mechanical detection of tissue yield and/or failure coincided with the initial detection of fiber realignment in every test (Table 5.1), realignment was not detected during or before the first occurrence of partial failure in five of the 16 specimens (Table 5.1). To conclusively determine the accuracy of the vector correlation technique to detect the onset of microstructural damage, collagen fiber alignment information must be acquired for all regions of the tissue. In that way, it would be possible to test if anomalous fiber realignment is actually produced in the soft tissue at every incidence of a failure or yield. Those investigations would also need to account for the potential for failure at the ligament's insertion into the bone or failure within the bone tissue itself. In this study, anomalous fiber realignment could not be assessed near the bony insertion regions, because of the need for light transmission through the ligament tissue.

Despite this technique's utility in localizing anomalous fiber kinematics, its sensitivity in determining each occurrence of damage within an entire structure is limited by the need to measure fiber alignment in every region of that structure. Imaging techniques that utilize light backscattering analysis, such as optical coherence tomography, would not be affected by bony structures behind the capsular ligament and may enable measurements in a larger region of the ligament to provide better sensitivity in anomalous realignment detection.

Nonetheless, with pixel-wise damage detection, the vector correlation-based analysis technique developed here substantially advances the ability to identify and localize microstructural kinematics associated with potential tissue damage during its loading. This polarized light analysis technique cannot be directly adapted to broader applications such as clinical diagnostics or full cadaver testing, because the power of this method lies in the ability to make repeated pair-wise comparisons of the fiber alignment through tissue over a short period of time. However, this analysis technique to detect anomalous fiber realignment during injurious loading provides an experimental framework to understand how the microstructural composition of biological tissue can give rise to region-specific mechanical thresholds of tissue injury. Ultimately, by determining the loading conditions at which mechanically-induced facet capsular ligament damage first begins to occur, it is possible to develop a more complete understanding of how and when excessive joint motions produce changes to the microstructural environment that are capable of producing physiological dysfunction. The occurrence of anomalous fiber

realignment may be an indication of a change in the load-bearing collagen microstructure that is sufficient to deform the sensory fibers that are interwoven within the extracellular matrix. Axonal damage, as evidenced by beaded axons and retraction balls, has been reported in the facet capsule following joint distractions that induce strain magnitudes similar to those measured in the current study (Kallakuri et al., 2008). Such axonal injury may be sufficient to produce the sustained neuronal discharges observed in afferents innervating the joint in a goat model (Lu et al., 2005a, b), which in turn could produce spinal plasticity (Chapter 4) and persistent pain observed in the rat (Lee et al., 2004a, b; Lee and Winkelstein, 2009).

5.6. Integration

The study presented in this chapter supports the hypothesis in Aim 2 that during tensile loading in the facet capsular ligament localized regions of collagen fibers will deviate from their normal realignment patterns prior to the occurrence of visible rupture or gross failure. Furthermore, the results of this polarized light-based analysis support the hypothesis that anomalous fiber realignment is significantly ($p<0.001$) associated with the eventual location of visible rupture (Quinn and Winkelstein, 2009). The fiduciary markers used to produce strain fields in this chapter matched the spatial resolution imposed in previous studies that identified human cervical facet capsule injury tolerances for subfailure loading (Siegmund et al., 2000, 2001, 2008; Winkelstein et al., 1999, 2000). However, the

lack of association between the locations of anomalous realignment and maximum ε_1 in this study is consistent with other studies of collagenous tissue that suggest that microstructural strains may not correspond to macro-scale measurements (DeFrate et al., 2006; Phatak et al., 2007; Quinn and Winkelstein, 2009; Screen et al., 2004). In Chapter 7, this pixel-wise vector correlation technique is adapted to a digital image correlation tracking algorithm in order to improve the resolution of capsule strain field measurements and to further investigate the utility of strain measurements for localizing subfailure damage.

Tensile facet joint loading was imposed in the study in this chapter to determine the utility of using quantitative polarized light measurements to localize anomalous microstructural responses during a simple tissue loading scenario (Quinn and Winkelstein, 2009). The initial detection of anomalous fiber realignment occurred during ligament yield or failure in every specimen (Table 5.1), suggesting a sudden change in the load-bearing collagen network. In this study, specimens were loaded beyond the points of yield, failure, and visible rupture in order to provide an independent assessment of damage that was compared the onset and location of anomalous realignment (Table 5.1 and 5.2). Having placed anomalous realignment in the context of mechanical failure in this study, the vector correlation technique is applied to a subfailure facet retraction loading scenario in Chapter 7 to identify if anomalous collagen fiber changes occur during a facet joint retraction that simulates the cervical vertebral motions during low-velocity rear-end impacts. The changes in the organization of a collagen

network during facet joint loading observed here may be sufficient to load and activate nociceptors (Lu et al., 2005a, b) and to inititate a cascade of physiological changes resulting in the development of spinal neuron plasticity and persisitent pain symptoms as described in Chapter 4. In Chapter 6, this vector correlation technique (Quinn and Winkelstein, 2009) is applied to isolated cervical facet joints from the rat that undergo the same vertebral motions that were used to produce painful injury in the in vivo rat model described in Chapter 4. Specifically, anomalous fiber realignment is assessed in the rat facet joint to determine whether the joint displacements that produced pain symptoms in the studies in Chapter 4 correspond to the displacements that produce changes in the microstructure of the facet joint. With an improvement in the spatial resolution of QPLI-derived fiber alignment maps in the study in Chapter 6, the association between the detection of anomalous fiber realignment and ligament yield is also tested in more detail to continue to define the relationship between fiber kinematics and a loss of structural integrity.

CHAPTER 6

Anomalous fiber realignment during tensile loading of the rat facet capsular ligament

Parts of this chapter were adapted from:

Quinn, K.P., Bauman, J.A., Crosby, N.D., Winkelstein, B.A. (2010). Anomalous fiber realignment during tensile loading of the rat facet capsular ligament identifies mechanically induced damage and physiological dysfunction. *Journal of Biomechanics* 43(10): 1870-1875.

6.1. Overview

Biomechanical studies have identified collagen fiber disorganization, fibroblast necrosis, nociceptor activation, and persistent pain to result from the subfailure loading of ligaments (Lee et al., 2004a; Lu et al., 2005b; Provenzano et al., 2002b; Quinn et al., 2007). In Chapter 5, an optical technique was developed to detect and localize mechanically-induced microstructural changes in collagenous tissue during loading. In that work, anomalous collagen fiber realignment was detected to occur during loading at displacements significantly below those needed to produce visible rupture. That work suggested that the mechanical threshold for structural damage to the cervical facet capsule may be lower than that previously defined by gross failure. Yet, those studies did not provide context for the development of neuronal plasticity and/or mechanical hyperalgesia that was

associated with the subfailure facet joint loading in the study using the rat model presented in Chapter 4. An assessment of anomalous fiber realignment in the rat facet capsular ligament is needed to determine whether the development of microstructural changes in the facet capsule is associated with the subfailure loading conditions that produce facet-mediated pain.

In this chapter, the vector correlation technique described in Chapter 5 is implemented to assess putative microstructural damage to the facet capsular ligament during tensile loading of isolated rat facet joints. Experiments relate to Aim 2b and test the hypothesis that anomalous fiber realignment first occurs during tensile loading between the magnitudes of joint displacement that produce non-painful and painful behavioral outcomes. In addition, the hypothesis that there is a relationship between ligament yield and anomalous fiber realignment is tested in this chapter by comparing when anomalous realignment and yield were each detected during loading. Because the quantitative polarized light system used in this thesis requires the transmission of polarized light through ligament tissue, this study could not be performed in vivo. Accordingly, isolated rat facet joints were tested using a custom-built interface to simulate the in vivo facet joint loading conditions that were used in the rat in the studies described in Chapter 4. This study determines whether abnormal changes to the collagen fiber networks of the rat facet capsule may be associated with the development of local pathology and pain in the absence of any mechanical or visual evidence of failure.

6.2. Background

Several imaging techniques have been used in conjunction with mechanical testing to relate the structure and function of various collagenous tissues (Billiar and Sacks, 1997; Hansen et al., 2002; Lake et al., 2009; Tower et al., 2002). Quantitative polarized light imaging is unique in its ability to rapidly generate fiber alignment data, which makes it particularly amenable to evaluations of mechanically-induced damage (Tower et al., 2002). In fact, the ability of QPLI to provide unique insight into the collagen fiber responses to tissue damage was demonstrated through a description of abnormal fiber kinematics during rupture of engineered constructs under tension (Tower et al., 2002). Although that study provided a qualitative description of how collagen fibers reorient during construct failure, the context of such fiber kinematics during painful injuries sustained by native tissues, like the facet capsular ligament is lacking.

In Chapter 5, correlations between collagen fiber alignment vectors in sequential QPLI-derived alignment maps were measured to identify anomalous fiber realignment during loading in human cadaveric facet capsular ligament tissue (Quinn and Winkelstein, 2009). In that study, the vector correlation between alignment maps was calculated on a pixel-by-pixel basis using both the fiber orientation and retardation (i.e. strength of alignment) from each of the surrounding pixels. Anomalous fiber realignment was identified by a decrease in the vector correlation throughout a tissue region; that approach was sensitive to rapid changes in the patterns of fiber realignment, which may occur when fibers or their

crosslinks fail and loads are redistributed to other intact fibers in the local network. The initial detection of anomalous realignment coincided with a measured decrease in tangent stiffness during loading and was detected at significantly lower displacements than for visible tissue rupture (Quinn and Winkelstein, 2009). In that study, the anomalous collagen fiber kinematics detected before visible rupture were hypothesized to be related to microstructural damage, but the tissue tolerances that were defined by anomalous realignment for human tissue do not provide direct physiological context because they are derived from studies using cadaveric tissues.

The structural and physiological consequences of excessive capsular ligament stretch have been previously investigated using the in vivo rat model described in Chapter 4. Subfailure distractions of the rat cervical facet capsule to 0.7 mm produce persistent behavioral hypersensitivity mimicking clinical pain symptoms (Lee et al., 2004b; Lee and Winkelstein, 2009). After the same subfailure in vivo loading paradigm, histological sections of the lateral aspect of the facet capsule demonstrated significantly more fiber disorganization compared to uninjured rats (Quinn et al., 2007). The presence of fiber disorganization after subfailure joint loading in that study suggests that the lateral aspect of the rat facet capsule may sustain microstructural damage during loading to magnitudes that produce pain symptoms. The goal of the studies in this chapter was to identify the onset of anomalous fiber realignment in the lateral aspect of the facet capsule of the rat to determine the potential for localized microstructural damage during tensile joint loading to failure. Because behavioral hypersensitivity is produced following

vertebral displacements of 0.7 mm but not for displacements between 0-0.2 mm (Lee et al., 2004b; Lee and Winkelstein, 2009), the initial detection of anomalous fiber realignment was hypothesized to also occur between 0.2-0.7 mm of vertebral displacement.

The effect of the spatial resolution of QPLI images on the sensitivity of anomalous realignment detection also has not been defined. The magnification of the camera lens used during QPLI image acquisition was increased to accommodate the smaller-scale specimens (i.e. rat facet joint) in this study. It was proposed that by increasing the resolution of the images, the optically-based vector correlation technique employed in this study may have more sensitivity to detect initial microstructural damage than compared to force-based metrics of yield and failure, in which the accuracy depends on the signal-to-noise ratio (SNR) of load cell measurements. As such, the occurrences of anomalous realignment with and without the simultaneous detection of yield were compared in these studies in order to determine whether the sensitivity of anomalous realignment or yield detections may depend on the loading conditions at which putative damage occurs.

6.3. Methods

6.3.1. Specimen preparation & data acquisition

The C6/C7 motion segment was isolated from male Holtzman rats (n=7; 377±12 g), and the left facet joint was carefully removed en bloc at the pedicles and spinous processes, as previously described (Quinn et al., 2007). These methods

were approved by the University of Pennsylvania Institutional Animal Care and Use Committee. The ligamentum flavum, interspinous ligament, supraspinous ligament, and dura mater were transected, and the surface of the facet capsule was carefully cleared of all musculature. A custom-built interface with an Instron 5865 (Instron; Norwood, MA) applied tension across the C6/C7 facet joint by gripping each of the laminae and transverse processes of the C6 and C7 vertebrae with micro-forceps (Figure 6.1). The superior (C6) grips attached to a 10 N load cell (Instron; accuracy of 0.25% measured value).

The Instron was integrated with a quantitative polarized light imaging system capable of acquiring pixel-wise collagen fiber alignment maps during continuous loading from the transmission of polarized light through the tissue, as

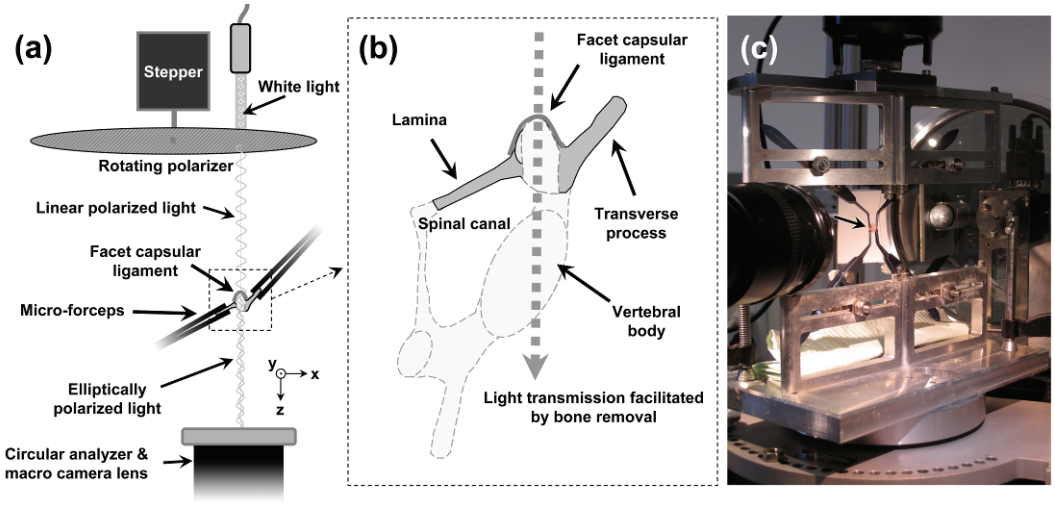

Figure 6.1. QPLI setup for isolated rat facet joint testing. (a) Schematic of an overhead view of the specimen (in square) and the QPLI components. **(b)** Articular bone was removed to enable light transmission through the ligament only. **(c)** Four micro-forceps attached to the laminae and transverse processes of C6 and C7 to apply tension across the joint (specimen indicated by arrow).

described in Chapter 5. To facilitate polarized light transmission through only the rat facet capsule tissue, the articular bone was removed near the C6/C7 joint line. Specimens were positioned with the lateral aspect of the facet capsule facing the rotating polarizer (Figure 6.1), and the articular bone was removed from the secured specimens with a high-speed micro drill equipped with a 0.7 mm diameter steel burr (Fine Science Tools; Foster City, CA).

After the articular bone was removed, the unloaded reference position of the specimen was set to have a distance of 2.53 mm between the midpoints of the C6 and C7 laminae, as was customarily done in the previous in vivo studies of this joint (Dong et al., 2008; Dong and Winkelstein, 2010; Lee et al., 2008; Lee and Winkelstein, 2009; Quinn et al., 2007). This intervertebral distance was set also to match the unloaded vertebral positions measured prior to facet joint loading in the in vivo studies of neuronal hyperexcitability in Chapter 4. Specimens were loaded in tension at a rate of 0.08 mm/s until complete rupture, with force and displacement data collected at 1 kHz. Fiber alignment maps were generated using the QPLI system as described in Chapter 5. In this study, imaging was performed using a Phantom-v9.1 camera (Vision Research; Wayne, NJ), at 200 Hz and a resolution of 40 pixels/mm. Light from the fiber-optic illuminator was transmitted through both the linear polarizer, which was rotating at 300 rpm, and the birefringent ligament tissue before entering a 6X zoom lens outfitted with a circular analyzer (Figure 6.1). Collagen fiber alignment maps were generated from every 20 QPLI images, corresponding to a full 180˚ rotation of the polarizer. As a result,

alignment maps were produced at a rate of 10 Hz, which ensured that the tissue movement during loading would not exceed 0.32 pixels per alignment map. As in Chapter 5, the intensity of light measured by the camera at each pixel was fit to a harmonic equation over every 20 frames (see Equation 5.2). Based on the linear birefringence of the collagen fibers in the ligament tissue, the average fiber direction and retardation at each pixel were determined (see Equations 5.3 and 5.4) for implementation into the detection of anomalous fiber realignment (Tower et al., 2002).

6.3.2. Detection of anomalous fiber realignment

The vector correlation of consecutive fiber alignment maps was used to detect anomalous fiber realignment. This approach is described in detail in Chapter 5, and the Matlab code used for vector correlation analysis is provided in Appendix M. For every alignment map that was acquired, correlation measurements were made to identify changes in fiber realignment using the maps immediately preceding and following it. For each pixel, a vector correlation value was determined by comparing the data between alignment maps in a 5x5 pixel window centered at that pixel. This vector correlation measurement included both the mean fiber direction and the strength of alignment in that mean direction (i.e. retardation), and ranged from 0 to 1, with 1 being consistent alignment between maps (Quinn and Winkelstein, 2009). Vector correlation maps were produced for each fiber alignment map throughout the applied loading regime based on these

pixel-by-pixel correlation calculations. The vector correlation was low in regions of the sample where light transmission was poor due to obstruction by bone or synovial tissue (Figure 6.2). Pixels with an insufficient harmonic intensity response due to poor light transmission were identified through pixel-wise maps of the SNR. Pixels with an SNR<2 produced inconsistent vector correlation values in static unloaded specimens; accordingly, any pixels below that value were removed from further analysis.

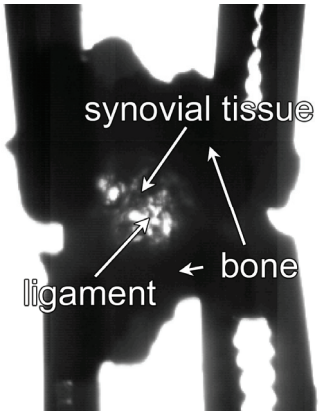

Figure 6.2. Bright field image of an isolated rat facet joint. Light transmission through the ligament was obstructed in some places by synovial tissue and bone.

Anomalous collagen fiber realignment was defined by a decrease in the vector correlation between alignment maps (Quinn and Winkelstein, 2009). Specifically, anomalous realignment was defined at any pixel with an SNR≥ 2 where the vector correlation decreased by at least 0.35 relative to its correlation value in the previous correlation map. As in Chapter 5, this decrease in the vector correlation was selected based on a parametric analysis comparing the effect of the

threshold value for a decrease in correlation on the displacement at initial anomalous realignment detection (Figure 6.3). The displacement for initial detection showed little covariance with the threshold near a value of 0.35, and this threshold was also confirmed by the absence of detection of any anomalous realignment during data acquisition at 0 mm of displacement (Figure 6.3). Regions of the capsular ligament were defined as sustaining anomalous fiber realignment when at least 9 connected pixels were simultaneously detected as sustaining anomalous realignment. Given that the vector correlation measurement was derived from a 5x5 window surrounding each pixel, the 9-pixel requirement ensured that any anomalous realignment that was detected would span pixel windows that could not share a majority of the same alignment vectors. The force and displacement at each alignment map in which a region of anomalous fiber realignment was detected in the specimens were recorded. Those data were used for statistical comparisons to the mechanical outcomes described in Section 6.3.3.

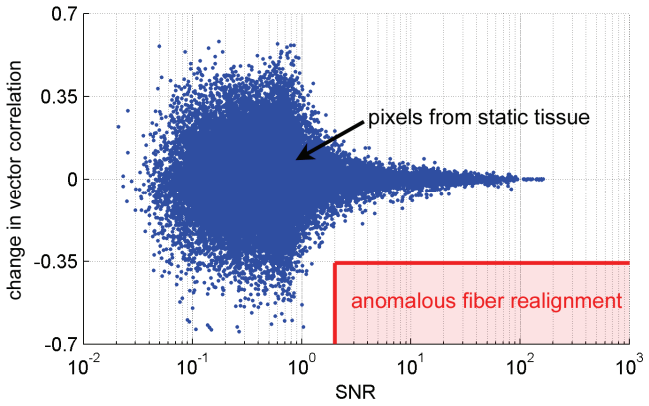

Figure 6.3. Threshold for anomalous fiber realignment was evaluated by measuring the change in vector correlation and SNR at each pixel in static tissue.

6.3.3. Mechanical data analyses

Gross failure, partial failure, and yield in each specimen were defined from the mechanical data in order to measure structural damage and to provide context for the occurrence of anomalous fiber realignment. Prior to the analysis of failure or yield, force data were digitally filtered to eliminate random noise with a 10-point moving average with zero-phase distortion using the *filtfilt* function in Matlab. Gross failure was defined by the data point after the maximum force during loading. Partial failure was defined by any decrease in force with increasing displacement prior to gross failure, and ligament yield was defined by a decrease in the maximum tangent stiffness of at least 10% (see Chapter 5 for more details; Appendix O for Matlab code). By definition, for any data point where failure was detected, yield was also detected because the tangent stiffness during failure would have decreased enough to become negative. For each specimen, all occurrences of yield or partial failure were identified during loading up to its gross failure.

6.3.4. Statistical analyses

The force and displacement at each of the initial detection of anomalous fiber realignment, yield, partial failure, and gross failure were compared through one-way ANOVAs with post-hoc Bonferroni tests. To determine whether anomalous fiber realignment was significantly associated with the occurrence of yield and/or failure throughout loading, analysis was performed using a 2x2 contingency table. Data for the contingency table were calculated by partitioning the displacement

data into sections based on whether or not yield or anomalous fiber realignment was detected from 0 mm to gross failure in each specimen (Figure 6.4). If neither was detected over a continuous section of displacement data, a single true-negative was counted in the contingency table (D in Figure 6.4). Likewise, if yield was detected over a period of displacement, and it coincided with the detection of realignment within that period, a single true-positive count was made (A in Figure 6.4). If either yield or realignment was solely detected over a section of the displacement response, a count was made in one of the off-diagonal cells of the contingency table (B or C in Figure 6.4). Once the contingency table was assembled, each cell was checked to verify that its sample size was at least 10, and Pearson's chi-square test was used to analyze the association between yield and anomalous fiber realignment. Although the *sensitivity* of anomalous fiber

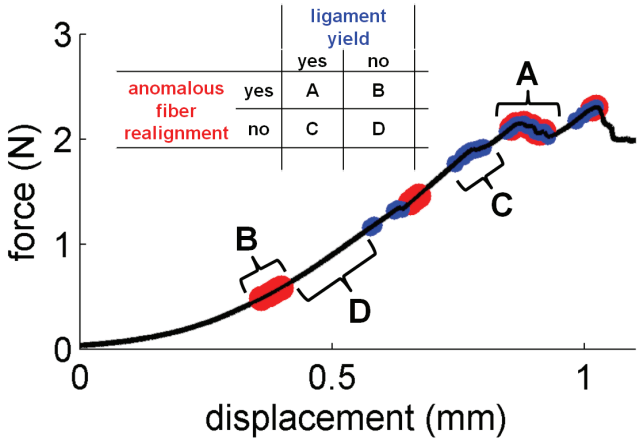

Figure 6.4. Contingency table assembly through displacement data partitioning. The association between ligament yield and anomalous fiber realignment was measured by classifying displacement data based on the occurrence of each metric. Continuous sections of data with the same classification were assigned a single count in the contingency table.

realignment to yield depends on the proportion of the entire facet capsular ligament being analyzed during loading, the *specificity* to yield is unaffected by this factor because yield is derived from the total of the structural response of the specimen and does not depend on any spatial information. To provide context for the specificity of anomalous fiber realignment to yield, the size of the realignment region (number of pixels) and occurrence of realignment (force and displacement) were compared between false-positive and true-positive detections for yield. The occurrences of these false-positives and true-positives were compared using an unpaired t-test; the size of the realignment region was compared between groups using a Wilcoxon rank-sum test because the data significantly deviated from normality. Significance was defined by α=0.05 in all tests.

6.4. Results

Anomalous fiber realignment was detected in only 4.3% of all of the alignment maps generated during loading to gross failure for all specimens in this study. Realignment occurred across an average area of 0.033±0.049 mm^2 (53±78 pixels) out of a total analyzed ligament area of 2.67±0.69 mm^2 (4273±1105 pixels) (Figure 6.5). Anomalous fiber realignment was first detected at 0.62±0.32 mm and 1.08±0.79 N of loading (Tables 6.1 & 6.2). Appendix G provides maps of the change in vector correlation at the first detection of anomalous realignment for each specimen as well as the individual force-displacement plots indicating the occurrences of yield and anomalous realignment. The initial detection of

realignment was significantly correlated (R=0.903, p=0.005) with the initial detection of ligament yield (0.64±0.24 mm, 1.12±0.46 N). The first occurrence of failure occurred prior to the specimen reaching its peak load in 6 of the 7 specimens, and this initial detection of failure was measured at 0.88±0.18 mm and 2.03±0.83 N (Tables 6.1 and 6.2). Gross failure of the ligament occurred at a significantly greater displacement (1.14±0.19 mm, p=0.004) and force (2.69±0.47 N, p=0.014) compared to initial anomalous fiber realignment (Tables 6.1 and 6.2). Although the displacement at gross failure was significantly greater than at anomalous realignment, the displacements at these two events were significantly correlated (R=0.769, p=0.043) (Table 6.1).

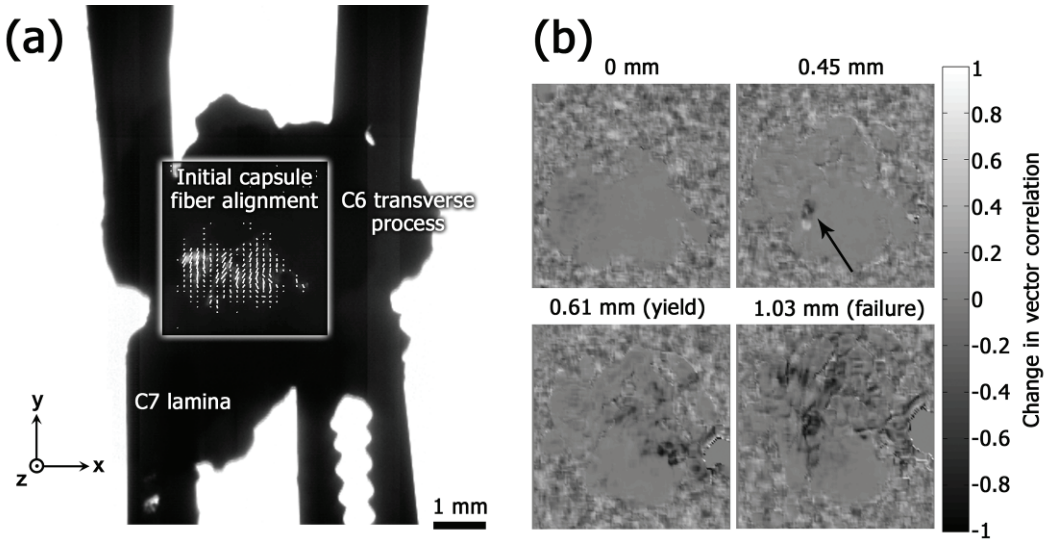

Figure 6.5. Detection of anomalous fiber realignment in Specimen AZ. (a) Fiber alignment vectors plotted every 5 pixels show the tissue region with sufficient SNR before loading. **(b)** Anomalous fiber realignment was first observed at 0.45 mm of displacement (indicated by arrow), but was also detected at yield and gross failure.

Table 6.1. Displacements (mm) at the initial detection of gross failure, partial failure, yield, and anomalous realignment with standard deviations (S.D.).

Specimen	Gross failure	Partial failure	Yield	Anomalous realignment
AZ	1.03	0.62	0.61	0.45‡
N3	1.07	0.96	0.63	0.84
N4	0.93	0.93†	0.26	0.20‡
N5	1.16	0.99	0.55	0.49‡
N6	1.50	0.93	0.91	0.91
N7	1.02	0.63	0.57	0.36‡
N8	1.28	1.07	0.97	1.07
Mean	**1.14**	**0.88**	**0.64**	**0.62**
S.D.	**0.19**	**0.18**	**0.24**	**0.32**
Correlation	0.769*	0.556	0.903*	

‡ Anomalous realignment was detected without yield.
† The first failure event that was detected was at gross failure.
* Correlation with initial anomalous realignment was significant.

Table 6.2. Forces (N) at the initial detection of gross failure, partial failure, yield, and anomalous realignment with standard deviations (S.D.).

Specimen	Gross failure	Partial failure	Yield	Anomalous realignment
AZ	2.41	0.92	0.90	0.37‡
N3	2.39	2.08	1.01	1.69
N4	3.54	3.54†	0.75	0.60‡
N5	2.36	2.27	0.55	0.45‡
N6	3.14	1.84	1.77	1.75
N7	2.30	1.34	1.15	0.48‡
N8	2.70	2.25	1.68	2.25
Mean	**2.69**	**2.03**	**1.12**	**1.08**
S.D.	**0.47**	**0.83**	**0.46**	**0.79**
Correlation	0.165	0.126	0.790*	

‡ Anomalous realignment was detected without yield.
† The first failure event that was detected was at gross failure.
* Correlation with initial anomalous realignment was significant.

The detection of anomalous realignment and ligament yield were significantly associated (p=0.013) through the contingency table analysis (Table 6.3). The sensitivity of anomalous realignment to yield was 30.4%, and the

specificity was 87.2%, leading to an overall accuracy of 63.4% for detecting yield through anomalous realignment. Although the detection of realignment was highly specific to yield during loading, the *initial* detection of realignment occurred in the absence of yield in 4 of the 7 specimens (Figure 6.6; Table 6.1). Anomalous realignment without any detected yield or failure event (false-positive for yield) occurred at mean displacements (0.51±0.17 mm) and forces (0.85±0.48 N) that

Table 6.3. Contingency table comparing the detection of yield with the detection of anomalous fiber realignment.

		Ligament yield		* p = 0.013
		yes	no	total
Anomalous fiber realignment	yes	17	10	27
	no	39	68	107
	total	56	78	134

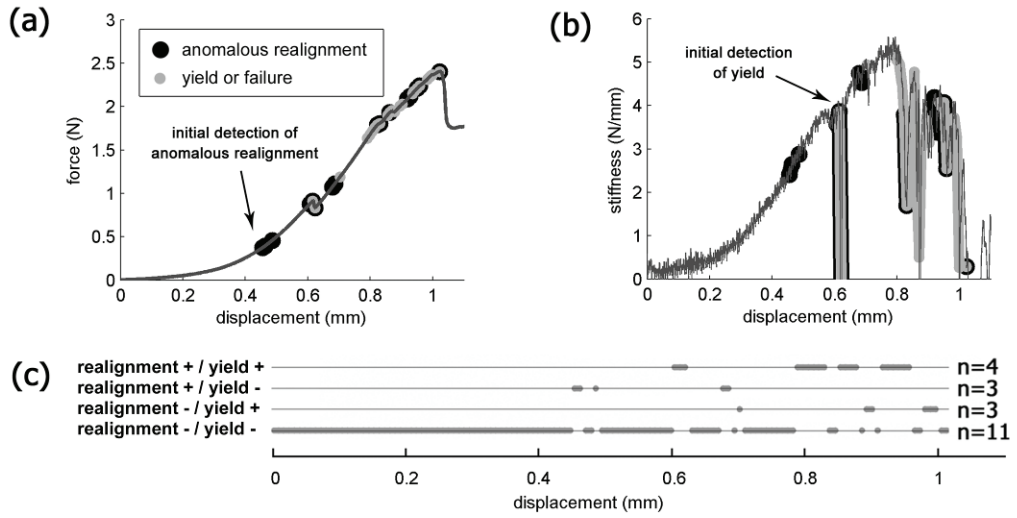

Figure 6.6. Mechanical data from a representative specimen (AZ). (a) Anomalous fiber realignment was first detected at 0.45 mm of displacement with no measurable decrease in force or stiffness. **(b)** The first occurrence of yield was detected at 0.61 mm. **(c)** Displacement data were partitioned for contingency table analysis based on whether realignment and/or yield were detected.

were significantly ($p<0.001$) lower than realignment that coincided with a yield event (true-positive), which occurred at 0.91±0.20 mm and 1.99±0.47 N. Although anomalous fiber realignment without yield occurred earlier in the loading than realignment *with* yield (Figure 6.6), the average area of realignment was highly variable and not significantly different between events with (68±92 pixels; 0.0426±0.0575 mm^2) and without (25±26 pixels; 0.0156±0.0164 mm^2) yield.

6.5. Discussion

Vector correlation analysis was employed in this study to localize inferred microstructural damage during loading of the rat facet joint independent of any mechanical data. Ligament yield was also identified by a decrease in tangent stiffness in the force-displacement curve. Although these two indications of a loss of structural integrity were calculated independently, anomalous fiber realignment *was* significantly associated ($p=0.013$) with ligament yield. Overall, anomalous fiber realignment was highly specific (87.2%) for the occurrence of yield (Table 6.3), but when anomalous realignment did occur without the detection of yield, it took place at significantly lower ($p<0.001$) magnitudes of loading than realignment *with* yield. This finding that false-positive detections of yield occur at significantly lower displacements, suggests that the optical detection of anomalous realignment could, in fact, be more sensitive to microstructural damage than yield or failure at lower magnitudes of loading. Yield may be particularly insensitive to damage

during the initial portion of the tissue's response to loading because decreases in stiffness due to the breaking of fibers could be offset by the increasing stiffness of the rest of the tissue as additional collagen fibers become engaged. Although the use of this vector correlation technique with human tissue (see Chapter 5) did not identify any anomalous realignment without yield of the ligament (Quinn and Winkelstein, 2009), the sensitivity of anomalous realignment detection was likely enhanced by the 10-fold increase in spatial resolution afforded by using a higher lens magnification in the current study for use of these smaller specimens coming from the rat. In fact, the rat facet capsule is approximately 6-fold smaller in its rostral-caudal length compared to the human capsule. With increased spatial resolution and fewer fiber responses averaged within a single pixel, the detection of anomalous realignment in Chapter 5 could possibly be enhanced with improved image acquisition, and may similarly lead to the detection of anomalous realignment prior to initial failure or yield in the human facet capsular ligament.

This study of the rat facet capsular ligament builds upon the findings in Chapter 5, and suggests that a vector correlation technique is capable of localizing microstructural damage at the pixel-level in this tissue. Yet, there is an inherent difficulty in validating a methodology to identify a previously undetectable class of injuries. In lieu of actually visualizing when a collagen fiber breaks during loading, this study measured the local fiber kinematic response and examined the relationship between mechanics and anomalous realignment to evaluate the potential for microstructural damage. Although a significant relationship was

found between mechanical evidence of damage (i.e. yield) and anomalous realignment (Tables 6.1 & 6.2), additional histological or ultrastructural studies are needed to confirm the presence of any structural damage at the initial detection of anomalous realignment. Such evaluations are not possible because of the variability in the initial onset of anomalous realignment (Table 6.1), and would require a real-time assessment of vector correlation. As a result, it remains unknown whether anomalous realignment results from the breaking of a collagen fiber or crosslink under tension, or whether detection can also be the byproduct of other phenomena, such as the rapid untangling of two or more fibers. Although the underlying mechanism of anomalous realignment has yet to be validated, these findings clearly demonstrate an atypical change in both the microstructural and mechanical responses that may explain the development of physiological dysfunction following subfailure facet joint loading. In fact, the occurrence of anomalous realignment (Table 6.1) within the displacements thought to initiate the production of neuronal plasticity and persistent pain (Lee et al., 2008; Lee and Winkelstein, 2009; Quinn et al., 2010b) support the hypothesis that these fiber responses have physiological relevance.

The measurements of yield and failure from the mechanical data are derived from an integration of all load-bearing components spanning the entire ligament. Accordingly, these force-based measurements provide a means to evaluate the limited field of view that is inherent in any two-dimensional imaging technique. The low sensitivity of anomalous realignment to yield (30.4%) highlights this

limitation in scope using a QPLI approach. Because the capsular ligament in the rat covers the facet joint from the lamina to the transverse process (Figure 6.1), only a portion of the capsule was imaged in this study. Thus, any microstructural damage that may have occurred in the other dorsal-medial and ventral-lateral regions of the capsular ligament that were not imaged would have been missed by the vector correlation technique. This limitation would suggest that the average structural threshold for anomalous realignment in the *entire* capsular ligament may be lower than 0.63±0.32 mm (Table 6.1). If the first detection of either yield or anomalous realignment is taken from each specimen, the average initial detection of an anomalous response is actually 0.57±0.28 mm. This estimate of tolerance to microstructural damage may also prove to be too liberal if anomalous realignment detection is more sensitive to microstructural damage than yield during loading within the toe-region of the curve. In fact, given the strong specificity of anomalous realignment to yield (87.2%), the average displacement at those detections of anomalous fiber realignment without the occurrence of yield (0.51±0.17 mm) may represent a more appropriate estimate of when the rat facet capsule is likely to first sustain microstructural damage during tensile loading. Regardless of the limitations in specimen preparation and field of view, within the portion of the lateral capsule that was imaged, anomalous realignment may provide the most sensitive detection of microstructural damage given that it can be assessed on a pixel-by-pixel basis rather than from the overall mechanical response of the tissue.

Structural damage has been inferred in previous biomechanical studies of ligaments through the identification of unrecoverable laxity and reduced stiffness after subfailure loading (Panjabi and Courtney, 2001; Panjabi et al., 1996, 1999; Provenzano et al., 2002; Quinn et al., 2007). The production of unrecoverable laxity following a low-grade medial collateral ligament sprain in the rat was also associated with an increase in the number of necrotic cells in the ligament (Provenzano et al., 2002). When placed in the context of the current study, the development of ligament laxity may be initiated by the same process that causes anomalous fiber kinematics in the facet capsular ligament. Furthermore, the occurrence of anomalous fiber realignment and yield may define collagenous damage that, in an in vivo setting, could be associated with fibroblast necrosis. After facet joint loading in the rat model described in Chapter 4, cellular debris associated with necrosis could be present in the ligament and may be sufficient to initiate inflammatory responses in the joint. Joint inflammation could help explain the collection of painful peripheral sensory system responses that have been attributed to subfailure ligament loading (Cavanaugh et al., 2006; Lee and Winkelstein, 2009; Lu et al., 2005a, b).

This study demonstrates that the fiber kinematics within a capsular ligament significantly deviate from their normal realignment patterns before gross tissue failure occurs. Anomalous collagen fiber realignment can occur without visible changes that are obvious on the tissue's surface. Yet, the initial detection of realignment is strongly correlated with the independent measure of ligament yield,

suggesting that anomalous realignment *is* associated with a loss of structural integrity (Tables 6.1 & 6.2). The anomalous realignment of the load-bearing collagen fibers may be sufficient to deform the sensory receptors that are interspersed throughout the facet capsule (McLain, 1993; Ohtori et al., 2001), and shown to be injured during certain loading conditions (Kallakuri et al., 2008). Accordingly, these changes in collagen fiber kinematics may initiate ectopic afferent firing; electrophysiological studies in the goat have demonstrated that primary afferent discharges may be sustained for over 4 minutes *after* a subfailure cervical facet capsule stretch (Lu et al., 2005b). Such afferent firing would provide an explanation for the development of spinal neuron plasticity, increased expression of pain-related neuromodulators in the peripheral and central nervous systems, and persistent pain after facet joint loading just beyond the displacement (0.7 mm) required for anomalous realignment in the current study (Dong and Winkelstein, 2010; Lee et al., 2008; Lee and Winkelstein, 2009; Quinn et al., 2010b). By identifying the abnormal fiber kinematics that would result from fiber ruptures within a collagen network, this optical technique describes a direct method to define the loading magnitudes that produce moderate ligament sprains, and may provide a means to compare mechanical tolerances for neuronal dysfunction and persistent pain across different tissues and species without needing complex scaling algorithms.

6.6. Integration

This study identified anomalous fiber realignment in the rat facet capsule within the range of vertebral displacements that coincide with the development of mechanical hyperalgesia in other in vivo studies. Anomalous fiber realignment was produced in the lateral aspect of the rat facet joint during a C6 vertebral displacement at an average of 0.62±0.32 mm of displacement (Table 6.1). In Chapter 4, in vivo displacements of 0.68±0.06 mm of the C6 vertebra produced both mechanical hyperalgesia and neuronal hyperexcitability, but vertebral displacements of 0.23±0.04 mm did not produce either of those behavioral or neuronal changes. Furthermore, a 0.7 mm vertebral displacement in that rat model has been shown to also produce facet capsular ligament laxity and fiber disorganization in the lateral aspect of the joint (Quinn et al., 2007). The current study suggests that the behavioral, electrophysiological, and structural changes that are observed after facet joint loading in vivo may be attributable to collagen fiber ruptures that produce anomalous fiber realignment during loading. However, the long-term effects of anomalous fiber realignment on the collagen fiber organization and mechanical function of the capsular ligament were not investigated. Chapter 7 presents a study of facet retraction to determine whether anomalous fiber realignment is associated with a change in the mechanical response and microstructural organization of the facet capsular ligament after loading.

The findings in this chapter support hypotheses from Aim 2 that were also tested in Chapter 5 using human facet capsular ligament tissue. As in human

tissue, anomalous realignment in the rat facet capsular ligament was detected significantly before gross failure of the ligament. In Chapter 5, the occurrence of either ligament yield or failure coincided with the initial occurrence of anomalous realignment; in this study of the rat capsule, the relationship between yield and anomalous fiber realignment is further substantiated by establishing an association between the two independent measurements throughout loading up to gross failure (Table 6.3). Additionally, the initial detection of realignment is strongly correlated with the initial detection of yield (Tables 6.1 and 6.2). Although the study of human tissue in Chapter 5 compared the locations of maximum first principal strain (ε_1) and anomalous fiber realignment, an accurate measurement of ligament strain fields was not possible in the current chapter due to the experimental constraints related to articular bone removal in the rat joint, which required that the capsule be imaged with its inner surface facing the camera (Figure 6.1) However, in previous biomechanical studies of rat facet joint loading, maximum ε_1 was more likely to occur in the dorsal aspect of the rat facet capsule, rather than the lateral aspect. Collagen fiber disorganization has previously been identified in the lateral aspect of the joint, but not the dorsal aspect (Quinn et al., 2007). This discrepancy between fiber disorganization and maximum ε_1 indicates that the strain outcomes in the current study would not have differed from those in Chapter 5, which demonstrated that maximum ε_1 does not co-localize with the location of anomalous fiber realignment. In Chapter 7, a new technique for tracking collagen fiber network deformations is implemented to determine whether the disconnect between

anomalous fiber realignment and surface strain fields may be explained by a lack of sufficient spatial resolution. Nonetheless, this study demonstrates that anomalies in the collagen fiber kinematics are associated with a loss of structural integrity in the rat facet capsular ligament and suggests that facet-mediated pain, without visible capsule injury, may be driven by changes in the capsule's collagen fiber organization.

CHAPTER 7

Altered collagen fiber alignment & unrecovered laxity in the human cervical facet capsular ligament following joint retraction

Parts of this chapter were adapted from:

Quinn, K.P., Winkelstein, B.A. (2010). Full field strain measurements of collagenous tissue by tracking fiber alignment through vector correlation. *Journal of Biomechanics* 43(13): 2637-2640.

7.1. Overview

Experimental and computational studies of the cervical spine kinematics during whiplash simulations demonstrate that vertebral retraction produces higher facet joint strains than experienced during normal range of motions (Grauer et al., 1997; Ito et al., 2004; Luan et al., 2000; Pearson et al., 2004; Stemper et al., 2005). Although the strains measured during whiplash simulations may exceed those of normal cervical spine motions, failure or rupture of the facet capsule has not been reported under such whiplash conditions (Pearson et al., 2004; Siegmund et al., 2000; Winkelstein et al., 1999; Stemper et al., 2005). Chapters 5 and 6 described mechanical and optical analysis techniques that were implemented to detect and localize capsular ligament damage during subfailure loading (Quinn and

Winkelstein, 2009; Quinn et al., 2010a). The detection of ligament yield and anomalous fiber realignment coincide with the magnitudes of joint loading necessary to produce central sensitization and behavioral hypersensitivity (Chapters 4 and 6) (Lee and Winkelstein, 2009; Quinn and Winkelstein, 2007; Quinn et al., 2010b). Although relevant to painful loading, anomalous fiber realignment has not been measured during cervical facet joint retraction similar to that experienced during whiplash. Without evidence of microstructural damage, it remains unclear whether the excessive joint loading conditions previously reported during whiplash are capable of producing a capsule injury.

The study described in this chapter measured anomalous fiber realignment during a whiplash-like facet joint retraction to determine whether fiber realignment *during* loading is associated with a change in the mechanical response and microstructural organization *after* loading. These objectives encompass the studies associated with Aim 3 and use the integrated QPLI system developed in Chapter 5. Specifically, anomalous fiber realignment and mechanical measurements of failure and yield were assessed during retraction of isolated human cervical facet joints up to 2.5 mm, which simulates the vertebral motion during whiplash (Aim 3a) (Figure 7.1). By tracking the fiber realignment patterns in the capsular ligament during retraction, full field strain measurements were made during and after retraction (Figure 7.1). First principal strain (ε_1) and maximum shear strain (γ_{max}) in the capsular ligament were measured after retraction to determine if any unrecovered

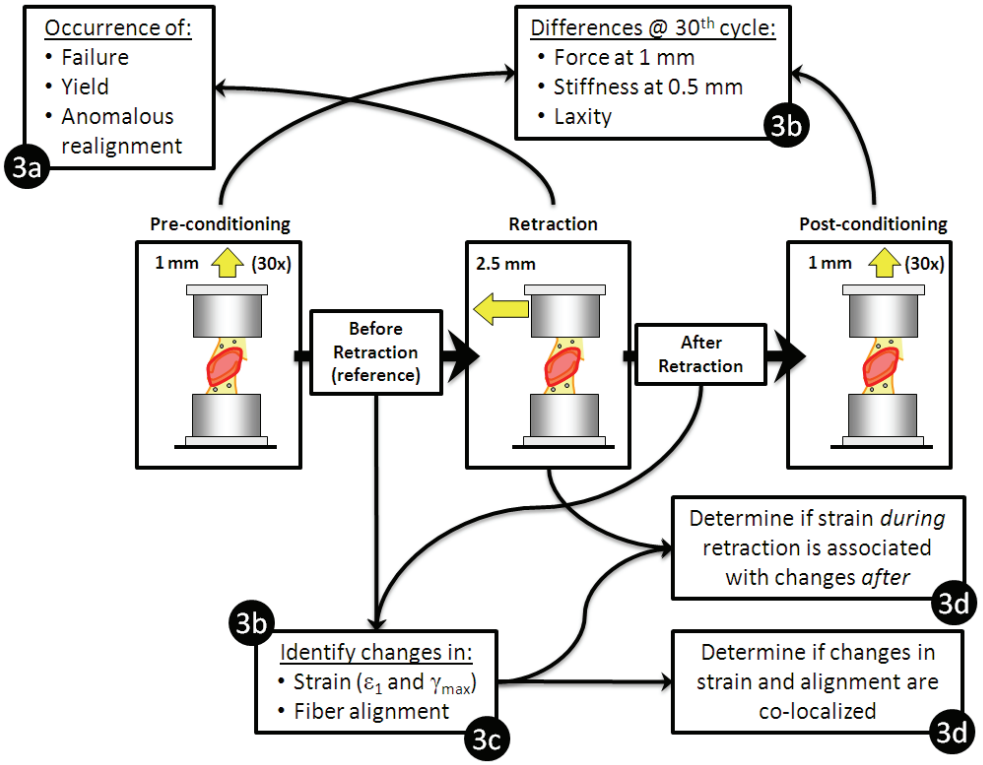

Figure 7.1. Schematic of the loading protocol and the outcomes associated with the sub-aims in Aim 3.

deformation remained once the joint was unloaded (Aim 3b) (Figure 7.1). In addition, cyclic tensile loading between 0 and 1 mm was applied to the joint before (i.e. pre-conditioning) and after (i.e. post-conditioning) retraction to measure changes in ligament force, stiffness, and laxity produced by whiplash-like motions (Aim 3b) (Figure 7.1). To provide context for any change in mechanical function, the potential for altered fiber alignment to remain after retraction was evaluated by a modified vector correlation technique (Aim 3c) (Figure 7.1). In addition, the regions of the capsular ligament sustaining unrecovered strain and altered fiber alignment after retraction were compared and placed in the context of the strain

field during retraction (Aim 3d) (Figure 7.1). Collectively, these sub-aims address the hypothesis that facet joint retraction in whiplash produces anomalous fiber realignment in the capsular ligament during loading and altered microstructural organization and mechanical function of the ligament after loading.

In order to determine whether the fiber alignment of the facet capsular ligament changed after the imposed facet retraction, it was necessary to modify the vector correlation technique presented in Chapter 5 to account for the potential for unrecovered deformation to be present after loading. In Chapter 5, the fiber alignment at a specific pixel location was compared between two alignment maps (Quinn and Winkelstein, 2009). Because the rate of image acquisition in that study was high (500 frames/s), the maximum possible tissue displacement between alignment maps was small (less than 0.3 pixels between consecutive maps). Based on these conditions, an "Eulerian description" of a change in fiber alignment at specific pixel locations was sufficient to localize changes within the tissue (Quinn and Winkelstein, 2009). However, when comparing the fiber alignment in maps acquired before and after facet joint retraction, it cannot be assumed a priori that the tissue before retraction returns to the same pixel location after retraction. Thus, a "Lagragian description" of the changes in fiber alignment was required in order to determine whether the fiber alignment of a specific *tissue region*, and not a specific *pixel location*, was changed between maps acquired before and after retraction. Accordingly, this chapter is divided into two sections detailing two separate studies. In the first section (Section 7.2), the development of a vector correlation

technique to track fiber alignment during tissue loading is presented. Not only does this technique allow for the Lagrangian description of fiber alignment that is needed to address Aims 3c and 3d, but it also facilitates a unique measure of tissue deformation that tracks the displacement of the collagen microstructure rather than relying on surface markers. With this approach in place, the study presented in the second part of the chapter (Section 7.3) tests the hypotheses associated with Aim 3. Collectively, the studies in this chapter quantify the changes in facet capsular ligament structure and function following joint retraction to determine whether whiplash-like loading is capable of producing microstructural damage in the absence of any capsule rupture or mechanical failure.

7.2. Full field strains calculated through vector correlation tracking

7.2.1. Background

Quantifying strain fields during loading is often necessary to localize tissue damage or to define region-specific mechanical properties, but capturing the local deformation can be technically challenging because of inhomogeneities in the tissue morphology or local material properties. Recent automated image analysis techniques take advantage of the spatial variability in a tissue's optical or acoustic properties and utilize cross-correlation techniques to track displacements based on the unique features of the surrounding tissue (Korstanje et al., 2010; Michalek et al., 2009; Snedeker et al., 2006). In cases where tissue lacks a measurable spatial pattern, fiduciary markers or textures have been applied to the tissue surface to

enable feature tracking (Derwin et al., 1994; Gilchrist, et al., 2007; Jacquemoud et al., 2007). However, those techniques are limited to measuring only surface strains, which may differ from the strains experienced by the load-bearing collagen microstructure throughout the thickness of a tissue.

Measuring the local deformation of a collagen fiber network within a tissue has previously been accomplished by capitalizing on the linear birefringence of collagen fibers to create unique patterns in different regions of the tissue, which can be tracked using digital correlation algorithms. For example, in aortic valve tissue, the interference colors were created by collagen birefringence, fiber alignment, and tissue thickness through the transmission of polarized light (Doehring et al., 2009). The different interference color patterns that were produced in that study were tracked to enable the measurement of local collagen network strains during tensile loading. It was hypothesized in the current study that enhanced accuracy and improved resolution of the strain field could be achieved by quantifying the fiber direction and alignment strength at each pixel prior to tracking. By using the integrated QPLI system developed in Chapter 5 to obtain fiber alignment maps, a method using a vector correlation tracking technique was developed to directly measure fiber network strains. This markerless tracking algorithm enables the simultaneous measurement of collagen fiber alignment and full field tissue strains to more directly compare tissue structure and function. The tracking algorithm developed here was employed in the study in Section 7.3 to identify the changes in

fiber alignment and strain in the facet capsular ligament during and after joint retraction.

7.2.2. Methods

Vector correlation tracking algorithm

The vector correlation technique used to quantify anomalous fiber realignment in Chapters 5 and 6 was employed to track the deformation of capsular ligament tissue based on the fiber alignment of the tissue. The tracking algorithm utilized the pixel-wise collagen fiber alignment maps acquired from the QPLI system during continuous tissue loading (Chapter 5). At each pixel in the fiber alignment maps, the axial fiber direction (α) and retardation (δ) values were transformed into an alignment vector with an orientation of 2α and a length of $\sin(\delta)$. A grid of virtual markers spaced four pixels apart was superimposed over the first alignment map generated by the QPLI system. For each virtual marker, the fiber alignment from a 9x9 window of pixels centered around the virtual marker was used as the set of reference vectors for tracking the virtual marker (Figure 7.2). To track the marker displacement between any two alignment maps, the reference alignment vectors for each virtual marker from the first of the two alignment maps were correlated with corresponding alignment vector sets generated from 9x9 windows in the second alignment map. The vector correlation values in the second alignment map were determined within a 13x13 search window centered about the location of the virtual marker in the initial map (Figure 7.2). The size of the search

window was selected to encapsulate any marker displacements that might occur based on the rate of tissue loading and image acquisition. A two-dimensional spline interpolation of the 13x13 array of vector correlation values was performed within the search window to identify the location of the maximum correlation with 0.05 pixel resolution. The Cartesian coordinates of the location of maximum correlation were then taken as the temporary position of the virtual marker in the next map (labeled *B'* in Figure 7.2).

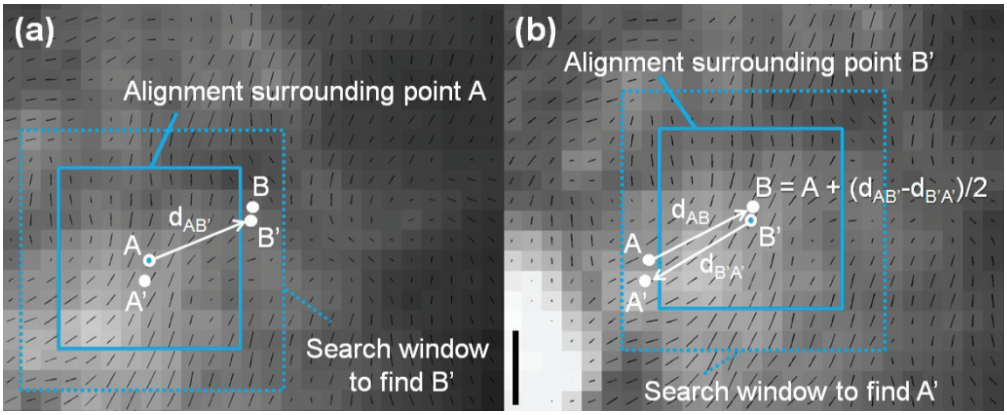

Figure 7.2. Vector correlation tracking between two fiber alignment maps. **(a)** The location of the fiber alignment (black lines) surrounding point *A* was initially determined by identifying the location of the maximum vector correlation (point *B'*) with the alignment in the next frame. **(b)** Using the fiber alignment surrounding point *B'*, the location of point *B'* was tracked back to a location (*A'*) in the initial alignment map. A combination of the forward ($d_{AB'}$) and backward ($d_{B'A'}$) displacements was then used to define the displacement (d_{AB}) from point *A* to point *B*. The scale bar represents 0.2 mm.

To enhance the accuracy of the virtual marker displacements between maps, tracking was also performed in the reverse sequence at each step. Once the location of a virtual marker (*B'*) was identified by tracking forward to the next frame, the alignment surrounding that location was used to track backwards to the

previous frame and identify the former location of the marker (*A'* in Figure 7.2b). An average of the marker's displacements during forward and backward tracking ($d_{AB'}$ and $d_{B'A'}$ in Figure 7.2) was then used to define the displacement between frames and identify the final marker location in the next frame (*B*). This approach also allowed an assessment of error in the tracking method at each step. If the distance between a virtual marker's actual previous location (*A* in Figure 7.2) and the location predicted by tracking forward and back (*A'* in Figure 7.2) was greater than 2 pixels, the marker was removed from subsequent tracking and analysis. A two-pixel threshold for marker removal was a conservative metric that only eliminated markers in regions without measurable fiber alignment. To minimize the propagation of error in determining the marker position, the reference set of alignment vectors used to track forward was retained throughout multiple steps. A new reference vector set for a marker was taken from the alignment surrounding the marker only when the maximum vector correlation between maps decreased below 0.9. The customized Matlab code (Mathworks; Natick, MA) that was written to implement this tracking algorithm is provided in Appendix P.

Strain field determination

Using the grid of virtual markers constructed in the first alignment map, a mesh of elements was generated through Delaunay triangulation (Delaunay, 1934). Matlab code previously used to calculate Lagrangian strain in four-node shell elements (Chapter 5) was modified to compute strain in each of the triangular

elements in every alignment map using the virtual marker displacements. First principal strain (ε_1) was determined from the maximum eigenvalue of the derived strain tensor of each element. The strain tensor values at each node were average to produce continuous full field strain maps for every alignment map generated (Polgar et al., 2003).

Error measurements & validation of the vector correlation tracking technique

To assess error in the tracking algorithm, excised human facet capsular ligaments (n=3; 71±6 years of age) were fixed to glass slides so that they could not deform during testing. The glass slide was rigidly fixed to the crosshead of an Instron 5865 (Instron; Norwood, MA). A 2.5 mm vertical crosshead displacement was applied at a rate of 0.40 mm/s, with displacement data acquired at 1 kHz. A Phantom v9.1 camera (Vision Research; Wayne, NJ) acquired images at 500 Hz with a resolution of 18.52 pixels/mm as the linear polarizer in the QPLI system rotated at 750 rpm. Alignment maps were generated from every 20 frames, and the acquisition parameters were selected to ensure that tissue displacement between maps was less than 0.3 pixels to enable continuous crosshead displacement. A grid of virtual markers spaced four pixels apart was superimposed over the ligament tissue and tracked during the translation of the slide. The absolute differences in the displacements between the Instron crosshead and the virtual markers assigned to the ligament tissue during vector correlation tracking were computed. Because the glass slide translated the undeformed ligament tissue, ε_1 was calculated from

the tissue on the slide to assess the error in strain measurements using this tracking technique.

To evaluate the ability of the vector correlation technique to measure large tissue deformations, intact facet capsular ligaments (n=4; 50±17 years of age) were loaded in tension as described in Chapter 5. Before tensile loading, fiduciary markers were placed on the surface of the ligaments to enable a comparison between virtual marker locations and surface fiduciary marker locations. Vector correlation tracking was performed up to the detection of anomalous fiber realignment in each specimen. The locations of fiduciary markers were digitized manually and also tracked using a standard intensity-based feature tracking program (ProAnalyst; Xcitex; Cambridge, MA). In the center of the samples, where fiber alignment surrounding the fiduciary markers could be measured, the locations of fiduciary markers (n=15 total markers) defined by both digitization and the feature tracking program were compared to vector correlation tracking measurements. The vector correlation tracking technique could not directly be compared to tracking techniques that require the application of a random speckle pattern because these patterns would attenuate a substantial amount of the light transmission required to measure fiber alignment. Because of this limitation the only appropriate comparison between vector correlation tracking, traditional feature tracking, and marker digitization was by computing the difference in the measured fiduciary marker position during loading. The ε_1 strain fields were produced using vector correlation and also the relatively coarser fiduciary marker tracking

techniques (with spatial resolutions of 21.8±5.6 pixels) in order to determine whether fiduciary markers capture the local inhomogeneity in facet capsular ligament strains.

7.2.3. Results

A total of 854 virtual markers were created from the ligament tissue (n=3) on the glass slides (285±101 markers for each test). After a 2.5 mm (46.38 pixels) displacement of the glass slide by the Instron crosshead, the average virtual marker from vector correlation tracking had displaced 46.38±0.10 pixels (Figure 7.3). The

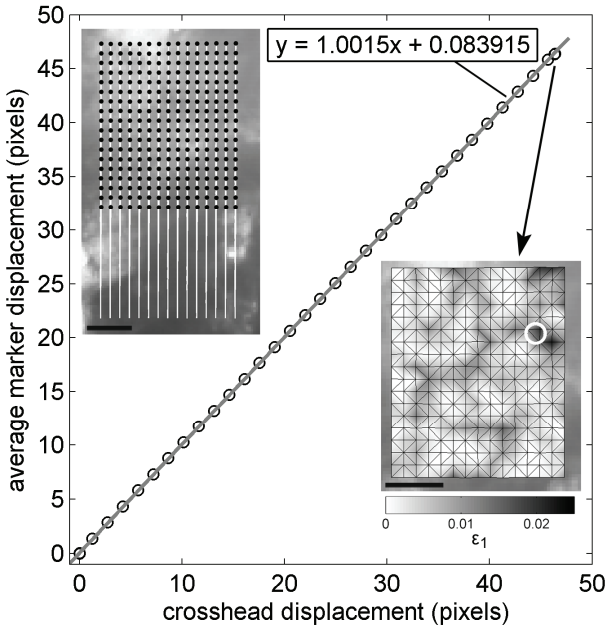

Figure 7.3. Error analysis of the vector correlation tracking technique for a representative sample. The average virtual marker displacement follows the displacement of the Instron crosshead during a 2.5 mm translation of ligament tissue. The paths of the virtual markers (left inset) produced small ε_1 values and a maximum ε_1 of 0.045 (circle in right inset). The scale bars in the insets each represent 1 mm.

average absolute difference between marker displacements and the crosshead displacement was 0.07±0.06 pixels. Error in the virtual marker locations at 2.5 mm produced an average ε_1 of 0.012±0.016 from all 1508 elements (Figure 7.3).

During tensile loading of facet capsular ligament tissue, the average difference in the displacements of the virtual markers and the digitized fiduciary markers was 0.17±1.18 pixels in the direction of loading (y-axis). Perpendicular to the direction of loading (x-axis), the average difference between virtual marker and fiduciary marker displacement was -0.24±0.98 pixels. This variability in marker positions suggested that the systematic error between digitization and vector correlation tracking was less than 0.30 pixels; random error produced an average distance of 1.39±0.61 pixels between marker locations measured by the two techniques. The differences in marker position could be attributable to either error in the vector correlation tracking and digitization processes or actual differences between the deformation of the collagen microstructure and the surface of the ligament. By comparison, the average distance between the digitized marker location and that location determined by feature tracking using ProAnalyst was 1.67±0.57 pixels, and the average distance between the vector correlation and feature tracking was 1.75±0.61 pixels. In the strain fields produced by tracking virtual markers, the average ε_1 was 0.503±0.238 upon the detection of anomalous fiber realignment, which was substantially greater than the error that was estimated from the average ε_1 values (0.012±0.016) that were calculated during glass slide translation. The strain fields determined using vector correlation tracking indicated

inhomogeneity in the tissue deformation that was not previously detectable using fiduciary marker tracking (Figure 7.4).

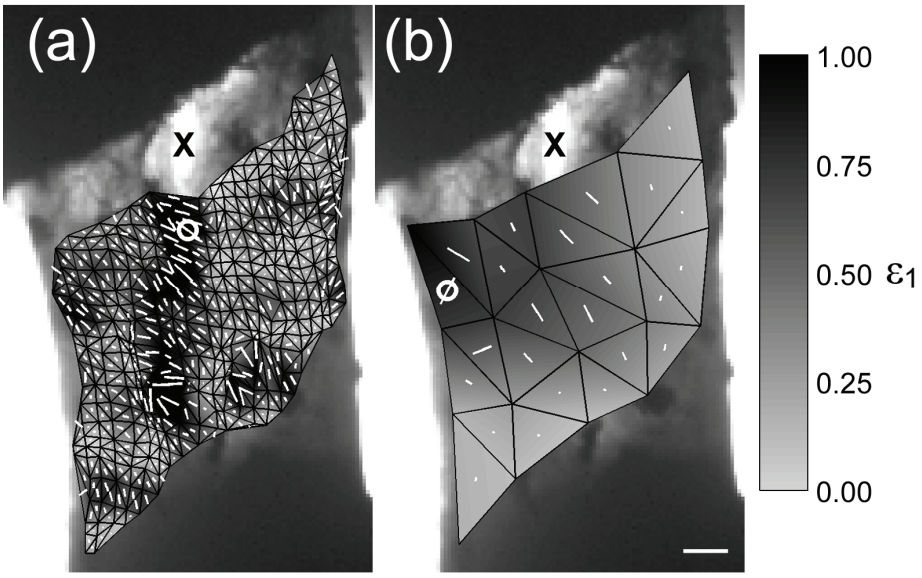

Figure 7.4. Full field ε_1 measurements produced by (a) vector correlation tracking and (b) fiduciary marker tracking at the point of anomalous fiber realignment for Specimen #15. The location of maximum ε_1 (circled) differs between tracking techniques. The site of a tear that was beginning to develop in the tissue is indicated by an 'X'. The scale bar in **(b)** represents 1 mm and also applies to **(a)**.

7.2.4. Summary

The vector correlation tracking technique described in this section demonstrates that a measurement of the deformation of the load-bearing collagen fiber network in the facet capsular ligament is possible using quantitative polarized light imaging. Full field ε_1 measurements were made with a mean error of 1.2% in strain using virtual markers spaced 4 pixels apart. Local tissue displacement was measured by tracking quantitative fiber alignment data within a 9x9 pixel window, which improved the strain field resolution compared to similar polarized light-

based tracking techniques that are based on interference colors (Doehring et al., 2009). By using the same vector correlation calculation previously employed in Chapter 5 to detect changes in collagen fiber realignment, this tracking technique has the unique ability to compare local deformation to local changes in microstructural organization. In the next section, this tracking algorithm is applied to measurements of facet capsule deformation during and after whiplash-like retraction to assess the relationship between strain and altered fiber alignment.

7.3. Evidence of subfailure damage following whiplash-like cervical facet joint retraction

7.3.1. Background

Volunteer and cadaveric studies have identified atypical cervical spine and facet joint motions during whiplash simulations (Bogduk and Yoganandan, 2001; Cusick et al., 2001; Deng et al., 2000; Kaneoka et al., 1999; Ono et al., 1997; Panjabi et al., 1998; Yoganandan and Pintar, 1997). Within 120 ms of bumper contact during a low-speed rear-end impact, the torso moves upward and forward and the head begins to extend backward (Kaneoka et al., 1999; McConnell et al., 1993, 1995; Ono et al., 1997). This torso displacement causes the lower cervical spine to undergo a combination of compression, shear and extension (Deng et al., 2000; Kaneoka et al., 1999; Ono et al., 1997). The combination of forces and moments in the lower cervical spine primarily results in retraction of each vertebra

relative to the adjacent inferior vertebra (Deng et al., 2000; Siegmund et al., 2001; Sundararajan et al., 2004). By tracking bony displacements during whiplash simulations, studies have estimated that facet capsular ligament strains do, in some cases, exceed the strains measured during the cervical spine's normal range of motion (Grauer et al., 1997; Ito et al., 2004; Luan et al., 2000; Pearson et al., 2004; Stemper et al., 2005). Although existing cadaveric studies of facet kinematics demonstrate that the facet joint may be at risk for excessive motion during vertebral retraction, evidence of some sort of tissue damage is needed to determine if and when facet capsule injury occurs during whiplash-like spine motions.

The failure properties of isolated cervical facet joints undergoing both tension and retraction have been defined in order to provide biomechanical context for the facet joint motions during whiplash simulations (Myklebust et al., 1988; Siegmund et al., 2000, 2001; Winkelstein et al., 1999; 2000; Yoganandan et al., 2000). A subset of those studies identified partial failures in some specimens prior to their gross rupture at capsule strain magnitudes that may be sustained during whiplash (Siegmund et al., 2000, 2001; Winkelstein et al., 1999; 2000). Isolated cervical spine studies have also established the potential for subfailure injuries to the facet capsule following exposure to whiplash-like inertial spine loading (Ivancic et al., 2008; Yoganandan et al., 2001). Facet joint laxity, defined by an increase in capsular ligament displacements to forces ranging from 0 to 5 N, was identified in cervical spines that were exposed to 8 g impacts (Ivancic et al., 2008). Cryomicrotomy sections of a cervical spine following a 3.3 g impact also revealed

facet joint diastasis (Yoganandan et al., 2001). The identification of a disproportionate gap between the articulating facets in that study provides additional evidence of unrecovered capsular ligament laxity following whiplash. Collectively, these biomechanical and imaging studies suggest that under certain spinal loading conditions, the facet capsular ligaments can sustain partial failures and/or plastic deformation during whiplash, which may lead to joint laxity or radiographic evidence of diastasis. However, in vivo models indicate capsule failure may not be required to initiate facet-mediated pain (Lee and Winkelstein, 2009; Lu et al., 2004a, b; Quinn et al., 2007). Although capsule rupture may not be required for the production of pain, altered collagen fiber organization and facet capsular ligament laxity has been identified following painful facet joint loading magnitudes (Quinn et al., 2007). Accordingly, an assessment of mechanical and microstructural changes to the capsular ligament during and after a subfailure facet retraction could provide a more conservative estimation of facet injury with physiological relevance.

The goal of this study was to use the quantitative polarized light imaging (QPLI) system previously described in Chapter 5 to evaluate the collagen fiber kinematics *during* a whiplash-like retraction of the C6/C7 human facet joint and to quantify changes in fiber alignment and mechanical function *after* that loading. Anomalous fiber realignment has previously been identified to occur during subfailure facet capsular ligament loading as presented in Chapters 5 and 6 (Quinn et al., 2010; Quinn and Winkelstein, 2009). Additionally, the occurrence of

anomalous fiber realignment in those studies coincided with the magnitudes of joint loading necessary to produce central sensitization and behavioral hypersensitivity in Chapter 4 (Quinn et al., 2010b). Therefore, the potential for anomalous fiber realignment to develop in the human facet capsular ligament was assessed during retraction in the current study. It was hypothesized that whiplash-like facet joint retraction produces anomalous realignment, which results in unrecovered strain and altered fiber alignment after loading. Because unrecovered strain was hypothesized to be present after retraction, the location of specific tissue regions was assumed to have changed between the alignment maps acquired before and after retraction. Therefore, the vector correlation tracking algorithm developed in Section 7.2 (Quinn and Winkelstein, 2010) was utilized to quantify both unrecovered tissue deformation and altered fiber alignment after retraction. To place the strain and fiber alignment outcomes in the context of previous subfailure ligament biomechanical studies, changes to the mechanical response following facet retraction were also evaluated through low-load cyclic tensile loading.

7.3.2. Methods

General loading protocol

The loading protocol for Aim 3 consisted of a whiplash-like facet retraction and a series of tensile loading cycles imposed both before and after the retraction. A 2.5 mm retraction of C6 was imposed because it approximates the magnitude of vertebral motion experienced by that joint during the cervical spine whiplash

kinematic (Siegmund et al., 2001; Sundararajan et al., 2004). Cyclic tensile loading was used to evaluate any change in mechanical function because the capsular ligament is loaded primarily under tension during normal sagittal bending (Teo and Ng, 2001; Zdeblick et al., 1993). For mechanical testing, each isolated facet capsular ligament specimen was fixed to the Instron 5865 testing machine (Instron; Norwood, MA) while preserving its original orientation within a motion segment (Figure 7.5). Each specimen was mechanically pre-conditioned with 30 cycles of tensile loading between 0 and 1 mm at 0.4 mm/s (Figure 7.5). The 1 mm displacement for pre-conditioning was selected because no anomalous fiber realignment is produced (see Chapter 5), and the load sustained at this magnitude corresponds to approximately 5% of the ultimate tensile failure load of the human facet capsular ligament (Winkelstein et al., 2000). After pre-conditioning, specimens were rotated 90° within the Instron in order to apply joint retraction rather than tension (Figure 7.5). A 2.5 mm retraction of C6 was imposed at 0.4

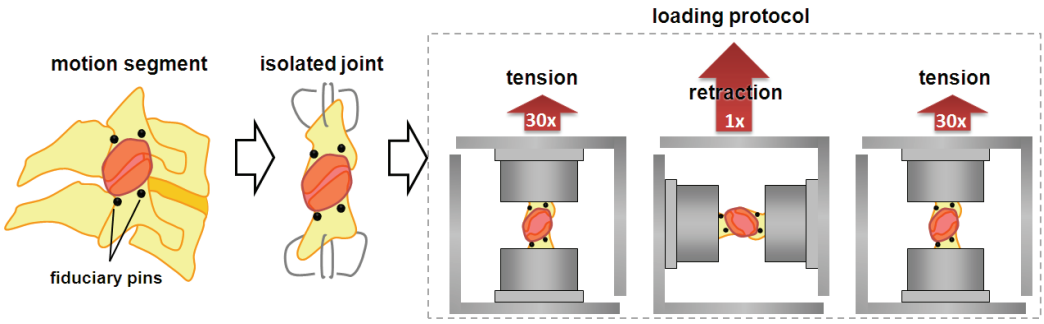

Figure. 7.5. Facet joints were isolated from motion segments and loaded in different configurations. Cyclic tension was applied in order to pre-condition the joint. Then, the joint was rotated and retracted to 2.5 mm. After retraction, the specimen was rotated back and the Cyclic tension was again applied. Fiduciary pins were used to confirm that the joint's original configuration in the motion segment was maintained.

mm/s, while QPLI images of the specimen were collected at 500 Hz and a resolution of 18.52 pixels/mm using a Phantom v9.1 camera (Vision Research; Wayne, NJ). Finally, specimens were then rotated back to the tensile configuration and the same pre-conditioning protocol was repeated in order to assess changes in the mechanical response of the joint following retraction (Figure 7.5). Force and displacement data were acquired during loading at all three of these test configurations at 1 kHz. Between each of the test configurations, the specimen was allowed to rest for 20 minutes to allow re-hydration and viscoelastic recovery (Iatridis et al., 2005; Pollock et al., 2000).

Specimen preparation

Five C6/C7 motion segments were removed from the cervical spine of fresh unembalmed human cadavers (58±12 years of age), and the right and left facet joints were isolated. The ages and donor information of the isolated facet joints (n=8) used in this study are summarized in Appendix C. Through fine dissection, all musculature and tendon insertions on the surface of the facet capsules were removed. Prior to joint isolation, two fiduciary pins (3.175 mm diameter head; 0.5 mm diameter shaft) were inserted into each of the C6 and C7 articular processes of the left and right facet joints (Figures 7.5 and 7.6a). In order to determine the reference configuration to establish for mechanical testing, a digital image (18.52 pixels/mm resolution) of the left and right side of the motion segment was acquired

(Figure 7.6a). After imaging, the facet joints were removed en bloc at the pedicles and laminae. Two Kirschner wires were drilled in a crossed configuration into both the superior articular process of C6 and the inferior process of C7 (Figure 7.5). The ligamentum flavum was transected and articular bone and cartilage were removed along the medial-lateral axis to allow for light transmission through the lateral aspect of the facet capsular ligament (Figure 7.6b). The posterior surface of the C6 articular bone was left intact to ensure that capsule deformation during retraction was not affected by the tissue preparation to optimize for QPLI imaging of the ligament.

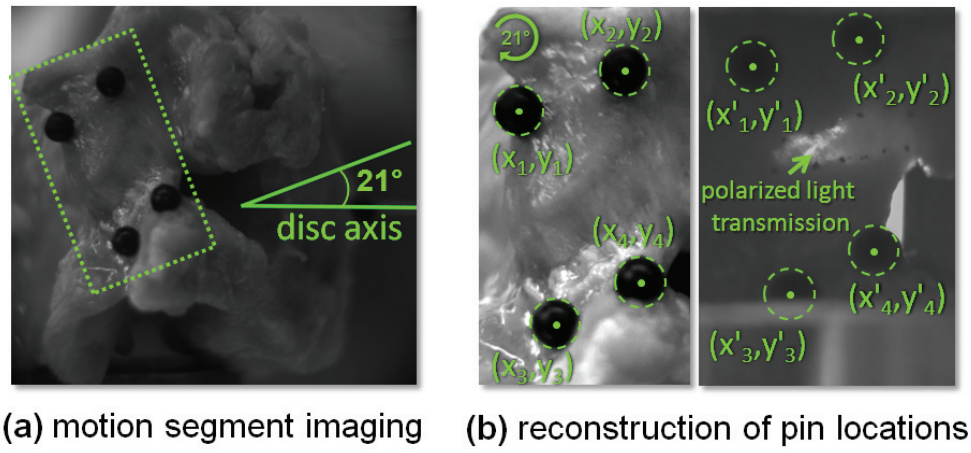

Figure 7.6. Fiduciary pin locations were used to recreate the facet orientation of a seated occupant during joint loading. (a) Motion segments were imaged and the intervetebral disc orientation was digitized. **(b)** The motion segment image was rotated and the fiduciary pin locations (x_i,y_i) were digitized. After bone removal to enable light transmission, the pin locations (x'_i,y'_i) of the isolated specimens were set to match those in the motion segment configuration.

The locations of the fiduciary pins in the images of each motion segment were used to determine the position of the isolated joint for mechanical testing. For

each motion segment image, the approximate sagittal orientation of the C6/C7 intervertebral disc was digitized, and a 21° angle from the axis of the disc was established (Figure 7.6a). Each motion segment image was rotated so that the C6/C7 disc orientation was 21˚ below the horizontal in order to simulate the position of the facet joint in the seated occupant (Matsushita et al., 1994; Winkelstein et al., 1999). The coordinates of the fiduciary pins were then digitized from the rotated motion segment images, and these coordinates were reproduced when positioning the isolated joint specimens in the Instron (Figure 7.6b). Once the position of the C6 pins relative to the C7 pins were within 1 pixel of the original motion segment configuration, the bony ends of the isolated facet specimens were cast in aluminum testing cups with FlowStone (Whip Mix Corporation; Louisville, KY).

In order to apply either tension or retraction to the isolated facet joints, a customized Instron testing interface was designed to allow for interchangeable testing cup configurations (Figures 7.5 and 7.7). Using a clamp system that was designed to grip both of the testing cups, specimens could be rotated 90˚ into a retraction configuration after tensile pre-conditioning was applied. Positioning micrometers were used to adjust the C6 cup position relative to the C7 cup in the retraction configuration in order to replicate the distance between fiduciary pin locations that was used in the tensile configuration (Figure 7.7). The C6 cup was displaced by the Instron crosshead in both configurations, and a 100 N load cell

attached to the C6 cup frame recorded the load during displacement (Instron; accuracy of 0.25% measured value).

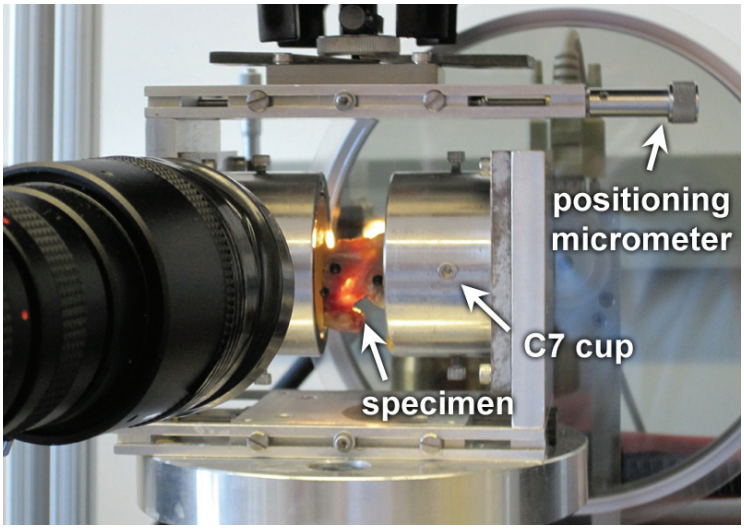

Figure 7.7. An adjustable interface facilitated mechanical testing in both tension and retraction. An isolated left C6/C7 facet joint (Specimen #23) illuminated by polarized light is shown in the retraction configuration.

Data analyses of joint retraction

The joint mechanics, collagen fiber kinematic, and full-field capsule strain data were acquired during facet joint retraction. The force-displacement data acquired during retraction were analyzed to assess if there were any occurrences of ligament yield or failure. Ligament yield was defined by any decrease in the maximum tangent stiffness of at least 10%, and failure was defined by any decrease in force with increasing displacement (Chapter 5 provides a detailed description of these analyses). For each specimen, any occurrences of yield or failure were documented during the joint retraction to 2.5 mm, and the force at 2.5 mm was recorded for each specimen.

The vector correlation of consecutive fiber alignment maps during retraction was used to assess anomalous fiber realignment as described in Chapters 5 and 6 (Quinn and Winkelstein, 2009; Quinn et al., 2010). In regions of the facet joint where articular bone could not be removed (e.g. the posterior surface of the C6 articular process), light transmission was not sufficient to permit polarized light analysis. These regions were defined by pixels where the harmonic polarized light intensity exhibited a signal-to-noise ratio (SNR) of less than 10. As in Chapters 5 and 6, the vector correlation values of static capsular ligaments were used to determine the threshold for anomalous fiber realignment. Anomalous realignment was defined at any pixel with an SNR greater than or equal to 10 and a decrease in the vector correlation between maps of at least 0.35. The identification of anomalous realignment required the detection of a decrease in vector correlation in at least 9 connected pixels simultaneously in order to eliminate potential random noise. For each specimen, any occurrence of anomalous fiber realignment during retraction was noted.

Based on the vector correlation tracking method developed in Section 7.2, tissue deformation was defined throughout retraction. A grid of virtual markers with 4-pixel spacing was assigned to the first alignment map created from the QPLI images and marker displacements were calculated by maximizing the correlation of the local fiber alignment pattern between maps during the retraction. To determine strain values at each marker location, a mesh of three-node elements was generated through Delaunay triangulation using the virtual marker positions in the first

alignment map, as described earlier (Section 7.2). Using plane strain theory, the Lagrangian strain tensor was derived for each element in each alignment map. The strain tensor values at each node were determined by averaging the strains from all of the elements connected to the node. First principal strain (ε_1) was determined from the maximum eigenvalue of the strain tensor, and maximum shear strain (γ_{max}) was defined as one-half of the difference between the two eigenvalues. Values for ε_1 and γ_{max} were determined for each node in the alignment map at 2.5 mm of retraction, and the average and maximum values for ε_1 and γ_{max} were tabulated for each specimen.

Data analyses of altered joint function & microstructure after retraction

Changes in laxity, ligament stiffness, and peak force during tensile cyclic loading were measured before and after joint retraction to characterize any altered ligament function that was produced by joint retraction (Figure 7.5). Laxity in the facet capsular ligament was defined as an increase in the displacement needed to produce a defined force (Eagar et al., 2001; Ivancic et al., 2008). For each specimen, the force measured at 0.5 mm during the first cycle of tensile loading prior to retraction was used as the reference load to determine laxity; the increase in displacement that was required to reach that reference load in subsequent cycles was defined as laxity. Tangent stiffness was calculated from the force-displacement responses during all cycles of tensile loading before and after

retraction. The force at 1 mm, stiffness at 0.5 mm, and laxity were determined for each cycle both before and after retraction for each specimen.

These mechanical outcomes were compared between the cyclic loading before and after retraction to identify if any change in the ligament's functional response was produced. For each of the three measurements (force, stiffness, laxity), a three-way ANOVA with specimens, cycles, order of loading, and their interactions was used to assess which factors contributed to changes in the mechanical response. To determine whether specimens were producing a consistent mechanical response by the 30^{th} cycle of tension, post-hoc Tukey HSD tests were used to define which cycles were not significantly different from each other. To eliminate any confounding effects due to the viscoelasticity of the tissue, data from the 30^{th} cycle of each set of applied tension were used to evaluate changes in the mechanical response due to retraction. Differences between the force, stiffness, and laxity before and after retraction were compared at the 30^{th} cycle using paired t-tests.

Unrecovered strain and altered fiber alignment produced by retraction were assessed through vector correlation tracking between the alignment maps that were acquired before and after retraction. Although this technique enables measurements of tissue strain that was not recovered *immediately* after retraction, it is unknown whether such changes would be *permanently* unrecoverable over time or after additional loading scenarios. Virtual markers were tracked through a sequence of five alignment maps: two maps acquired before the retraction, two

maps acquired after retraction, and another map acquired before retraction. This last alignment map corresponded to a static unloaded configuration before retraction and was acquired immediately after the alignment map that was used as the reference for strain calculations. Virtual marker tracking through a sequence that ended with a map acquired before retraction ensured that the changes after retraction could be separated from any potential propagation of error during tracking. Both the first and last map were acquired from different images of the specimen taken before retraction, so if the position of a virtual marker differed by more than 0.5 pixels between those maps, the virtual marker position was deemed unstable and removed from the analysis. This tracking requirement ensured that only virtual markers placed over capsule tissue with measureable birefringence were used for the subsequent analyses of strain and fiber alignment. Using the same mesh of triangular elements generated for capsule strain measurements during joint retraction, ε_1 and γ_{max} were calculated at each node for the sequence of alignment maps. In addition, the vector correlation values between the positions of each virtual maker in each alignment map were recorded. Analogous to the assessment of anomalous realignment presented in Chapter 5, a change in the vector correlation of a virtual marker between maps was used to determine whether the alignment surrounding that marker had changed after retraction. Full field maps of ε_1, γ_{max}, and the change in vector correlation after retraction were generated for each specimen.

In the full field maps, a node was classified as sustaining unrecovered strain or altered fiber alignment after retraction if the strain or correlation value at that node exceeded the entire distribution of error values obtained from all nodes in all specimens. Error values for strain and a change in vector correlation were determined from the last of the five alignment maps used for vector correlation tracking. Therefore, any strain or changes in vector correlation measured in that map would be produced by error related to tracking back and forth between alignment maps before and after retraction. The maximum ε_1 or γ_{max} value recorded at any node in any specimen did not exceed 0.09 at this last alignment map, and the change in vector correlation at any node did not decrease below -0.10 in this alignment map. Therefore any node with a ε_1 or γ_{max} value above 0.09 after retraction was identified as having unrecovered ε_1 or unrecovered γ_{max}. Likewise, any node with a change in vector correlation that decreased below -0.10 after retraction was defined as having sustained altered fiber alignment. These thresholds were also verified as appropriate through parametric analysis of the threshold value and the percentage of nodes that were detected. For each specimen, the percentage of nodes with unrecovered ε_1, unrecovered γ_{max}, and altered fiber alignment were determined.

To determine whether altered fiber alignment was co-localized with either unrecovered ε_1 or γ_{max}, two-by-two contingency tables were constructed and Pearson's chi-square tests were used to determine whether altered fiber alignment was associated with either unrecovered ε_1 or γ_{max}. Also, to determine whether

altered fiber alignment was associated with higher strains during retraction, the strains that were sustained at 2.5 mm of retraction were compared between the nodes classified with altered alignment and the nodes without any detectable changes in alignment using a two-way ANOVA of alignment classification, specimens, and their interaction. For both ε_1 and γ_{max} measurments, the same ANOVA structure was used to compare the strains at 2.5 mm of retraction among nodes with unrecovered and recovered strain after retraction. Significance was defined by α=0.05 for all tests.

7.3.3 Results

During retraction, neither yield nor failure was detected from the force-displacement response, and the force at 2.5 mm reached an average of 16.08±9.83 N (Table 7.1). In addition, anomalous fiber realignment was not detected in any alignment map acquired during retraction for any specimen. A total of 2497 virtual

Table 7.1. Force and strains (ε_1 and γ_{max}) at 2.5 mm of retraction.

Specimen	Force (N)	Average		Maximum	
		ε_1	γ_{max}	ε_1	γ_{max}
17	10.99	0.41	0.26	3.24	1.58
18	31.84	0.30	0.18	1.70	0.95
19	23.12	0.84	0.44	1.76	0.86
20	5.38	0.41	0.28	1.55	0.86
21	4.74	0.72	0.42	2.66	1.36
22	13.93	0.19	0.18	1.28	0.71
23	12.82	0.26	0.21	3.33	1.69
24	25.80	0.26	0.25	1.88	1.11
Mean	**16.08**	**0.42**	**0.28**	**2.18**	**1.14**
S.D.	**9.83**	**0.23**	**0.10**	**0.79**	**0.36**

markers were tracked during retraction with an average of 312±158 markers assigned to each specimen. At 2.5 mm of retraction, the average ε_1 was 0.42±0.23 and the average γ_{max} was 0.28±0.10 for all specimens (Table 7.1). The full field ε_1 and γ_{max} measurements demonstrated spatial variability across the specimen (Figure 7.8), and the mean maximum ε_1 and γ_{max} values were 2.18±0.79 and 1.14±0.36, respectively (Table 7.1). The force-displacement responses for each specimen during retraction are detailed in Appendix H, and the strain fields at 2.5 mm of retraction are provided in Appendix I.

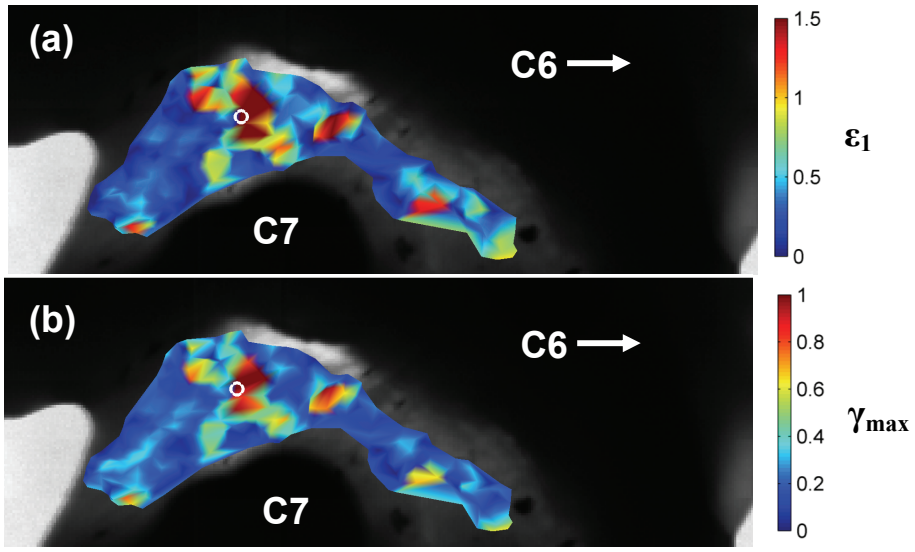

Figure 7.8. Full field strains of (a) ε_1 and (b) γ_{max} at 2.5 mm of retraction for Specimen #17. The location of the maximum value for each metric is circled within the full fields. The arrow indicates the direction of C6 retraction.

Joint retraction produced significant changes in the mechanical response of the facet capsular ligament to cyclic tensile loading. The force at 1 mm during the

30th cycle before retraction was 4.75±3.74 N, which was significantly reduced (p=0.0246) to 3.99±3.15 N during the 30th cycle after retraction (Table 7.2). The tangent stiffness at 0.5 mm in the 30th cycle before retraction was 2.85±2.68 N/mm, but it was significantly decreased (p=0.0186) to 2.08±2.28 N/mm in the 30th cycle after retraction (Table 7.2). In addition, ligament laxity significantly increased (p=0.0065) from 0.10±0.03 mm at the 30th cycle before retraction to 0.15±0.07 mm at the 30th cycle after retraction (Table 7.2; Figure 7.9). Post hoc Tukey HSD tests demonstrated no significant differences in force, stiffness, or laxity between the 20th through 30th cycles for loading before and after retraction. This result verified that a consistent, reproducible force-displacement response had been reached by the 30th cycle for testing both before and after retraction (Figure 7.10).

After joint retraction, an average ε_1 of 0.06±0.04 and an average γ_{max} of 0.05±0.02 were detected in the capsular ligament (Tables 7.3 and 7.4). Strain

Table 7.2. Mechanical parameters for the 30th cycle of tensile loading before and after retraction.

Specimen	Force (N)		Stiffness (N/mm)		Laxity (mm)	
	before	after	before	after	before	after
17	2.15	1.52	1.69	1.00	0.11	0.26
18	4.72	4.05	2.93	2.26	0.09	0.15
19	7.57	6.34	3.73	2.39	0.15	0.21
20	0.25	0.35	0.09	0.13	0.05	0.03
21	2.51	2.21	1.18	0.84	0.08	0.14
22	9.13	6.84	4.06	1.96	0.10	0.21
23	1.56	1.42	0.70	0.68	0.08	0.09
24	10.08	9.17	8.47	7.34	0.10	0.14
Mean	**4.75**	**3.99***	**2.85**	**2.08***	**0.10**	**0.15***
S.D.	**3.74**	**3.15**	**2.68**	**2.28**	**0.03**	**0.07**

* significant difference compared to mean value before retraction

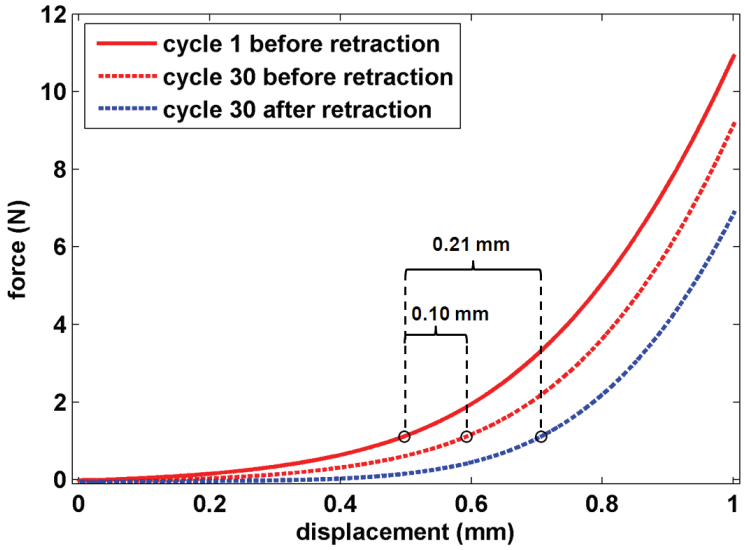

Figure 7.9. Laxity produced by retraction in a representative sample (Specimen #22). Laxity increased from 0.10 mm during the 30th cycle before retraction to 0.21 mm during the 30th cycle after retraction.

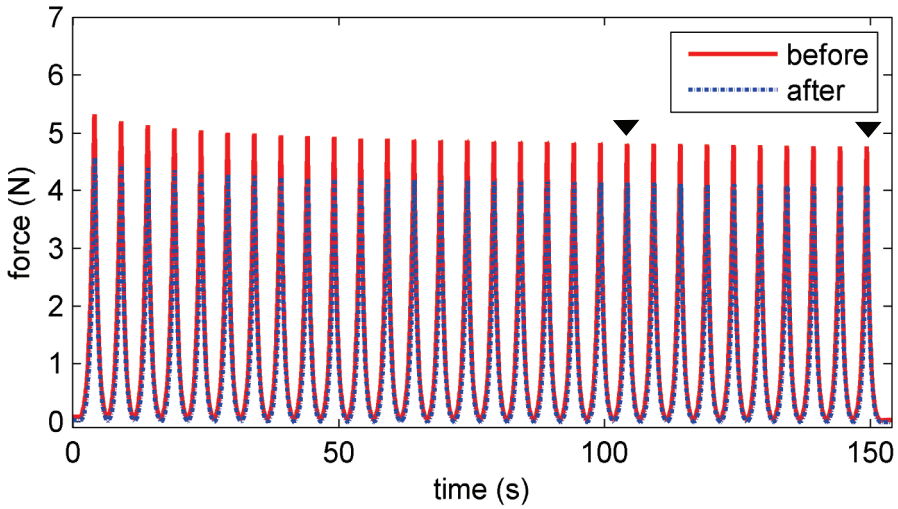

Figure 7.10. The peak force during cyclic tensile loading (Specimen #18) decreases during the first 10 cycles but does not change significantly between the 20th and 30th cycle (indicated by arrowheads).

values varied substantially throughout the tissue for both the ε_1 and γ_{max} measurements (Figure 7.11), and the maximum ε_1 after retraction was 0.93±0.82, while the corresponding maximum γ_{max} was 0.47±0.39 (Tables 7.3 and 7.4). No

trends in the location of the maximum ε_1 and γ_{max} after retraction were observed; full field strains for each specimen can be found in Appendix J. Every specimen contained nodes with unrecovered strain (Tables 7.3 and 7.4) after retraction. In fact, 21.05±17.09% of the nodes sustained unrecovered ε_1 (Table 7.3), and unrecovered γ_{max} was detected in 14.07±11.49% of the nodes (Table 7.4).

Table 7.3. Unrecovered ε_1 after retraction.

Specimen	Average ε_1	Maximum ε_1	% of nodes with unrecovered ε_1
17	0.06	1.17	22.61
18	0.04	0.31	11.98
19	0.12	0.37	56.60
20	0.02	0.19	5.73
21	0.09	1.27	31.70
22	0.02	0.43	4.89
23	0.08	2.67	11.96
24	0.08	1.07	22.92
Mean	**0.06**	**0.93**	**21.05**
S.D.	**0.04**	**0.82**	**17.09**

Table 7.4. Unrecovered γ_{max} after retraction.

Specimen	Average γ_{max}	Maximum γ_{max}	% of nodes with unrecovered γ_{max}
17	0.05	0.58	11.59
18	0.04	0.18	3.65
19	0.08	0.20	35.85
20	0.04	0.15	5.10
21	0.07	0.59	21.13
22	0.03	0.24	2.55
23	0.06	1.31	10.84
24	0.07	0.54	21.88
Mean	**0.05**	**0.47**	**14.07**
S.D.	**0.02**	**0.39**	**11.49**

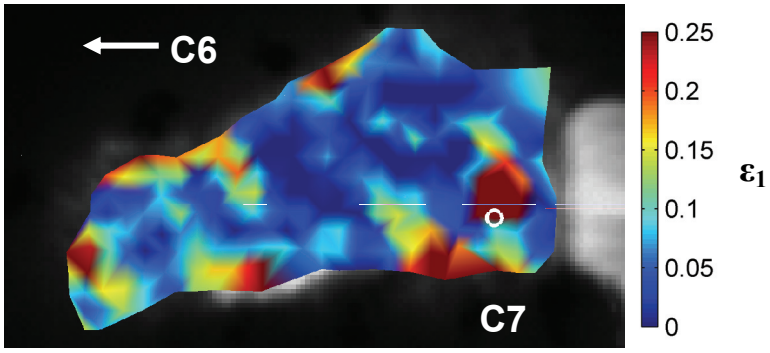

Figure 7.11. Full field ε_1 measurements for Specimen #21 after retraction. The maximum ε_1 for this specimen (circled) is 0.59. The arrow indicates the direction in which C6 facet retraction had been applied.

The average change in vector correlation between alignment before and after retraction was -0.09±0.04, and the maximum decrease in vector correlation was -0.33±0.04 (Table 7.5). As with unrecovered strain, the change in vector correlation after retraction varied spatially for each specimen (Figure 7.12; Appendix J). After joint retraction, 32.67±22.95% of the nodes exceeded the threshold for altered fiber alignment (Table 7.5).

Table 7.5. Change in vector correlation of fiber alignment after retraction.

Specimen	Average change in correlation	Maximum decrease in correlation	% of nodes with altered alignment
17	-0.09	-0.35	32.17
18	-0.08	-0.36	24.74
19	-0.17	-0.36	86.79
20	-0.09	-0.27	28.03
21	-0.09	-0.31	30.94
22	-0.05	-0.34	11.91
23	-0.06	-0.34	17.57
24	-0.07	-0.27	29.17
Mean	**-0.09**	**-0.33**	**32.67**
S.D.	**0.04**	**0.04**	**22.95**

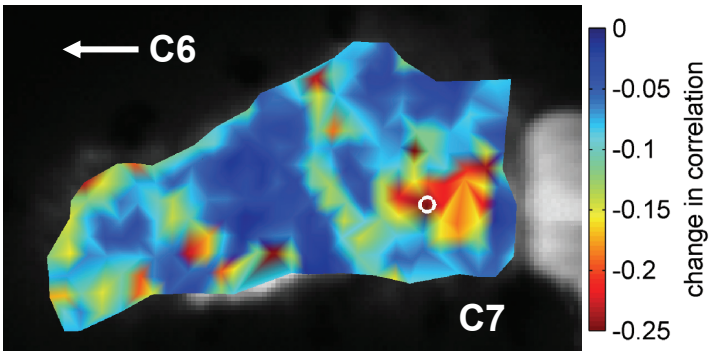

Figure 7.12. Map of the change in vector correlation for Specimen #21 after retraction. The location of the greatest decrease in correlation (circled) indicates the greatest change in fiber alignment. The arrow indicates the direction in which C6 facet retraction had been applied.

The majority of nodes with unrecovered ε_1 or γ_{max} also sustained altered fiber alignment (Figure 7.13). In fact, the location of altered fiber realignment was significantly associated ($p<0.0001$) with the locations of both unrecovered ε_1 and γ_{max}, based on contingency table analysis (Tables 7.6 and 7.7). Maps of the co-localization of unrecovered strain and altered fiber alignment in each specimen are detailed in Appendix J. Nodes with unrecovered ε_1 after retraction (indicated by green or yellow in Figure 7.13) sustained ε_1 values (0.49±0.47) at 2.5 mm of

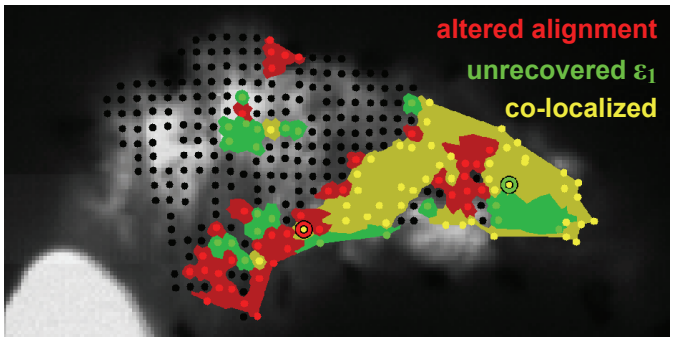

Figure 7.13. Map of the nodes with altered fiber alignment (red) and unrecovered ε_1 (green) after retraction in Specimen #24. Yellow regions show the co-localization of altered fiber alignment and unrecovered strain. The locations with the maximum decrease in correlation (red circle) and maximum ε_1 (green circle) are also indicated.

Table 7.6. Co-localization of unrecovered ε_1 and altered fiber alignment after retraction. Nodes with unrecovered ε_1 (green) and altered alignment (red) were significantly ($p<0.001$) co-localized (yellow).

		Unrecovered ε_1		
		yes	no	total
Altered fiber alignment	yes	228	384	612
	no	172	1713	1885
	total	400	2097	2497

Table 7.7. Co-localization of unrecovered γ_{max} and altered fiber alignment after retraction. Nodes with unrecovered γ_{max} (green) and altered alignment (red) were significantly ($p<0.001$) co-localized (yellow).

		Unrecovered γ_{max}		
		yes	no	total
Altered fiber alignment	yes	192	420	612
	no	78	1807	1885
	total	270	2227	2497

retraction that were significantly higher ($p=0.0399$) than ε_1 values (0.32 ± 0.39) at nodes in which strain was recovered upon unloading (Figure 7.14). In addition, nodes with unrecovered γ_{max} after retraction sustained significantly higher ($p=0.0110$) γ_{max} (0.32 ± 0.21) at 2.5 mm of retraction than compared to nodes without unrecovered γ_{max} (0.23 ± 0.19). However, no significant differences in the strains at 2.5 mm of retraction were identified between nodes with altered and unaltered fiber alignment after retraction ($p=0.0860$ for ε_1; $p=0.0983$ for γ_{max}) (Figure 7.14).

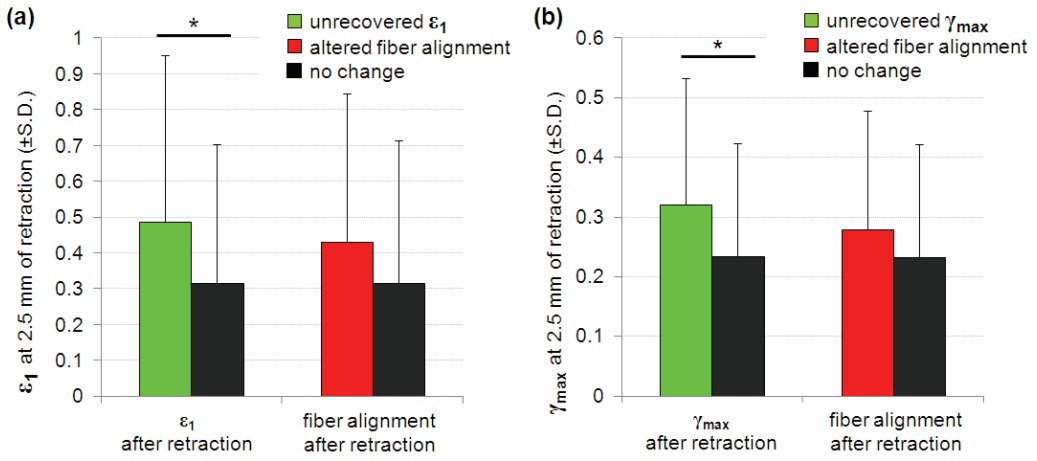

Figure 7.14. Unrecovered ε_1 and γ_{max} after retraction was associated with higher strains during retraction, but altered fiber alignment was not associated with significantly higher strains. **(a)** Nodes with unrecovered ε_1 after retraction sustained significantly higher ε_1 values at 2.5 mm of retraction (* p=0.0399) compared to nodes in which strain was recovered. **(b)** Unrecovered γ_{max} after retraction also corresponded to significantly higher (* p=0.0110) γ_{max} during retraction compared to nodes without changes in strain.

7.3.4. Discussion

This study demonstrates that whiplash-like vertebral retraction can produce significant laxity and reduced stiffness in the ligament (Table 7.2 and Figure 7.9) and alter the collagen fiber alignment in the facet capsular ligament (Table 7.5). The percentage of the capsule region that sustained altered fiber alignment after retraction ranged from 11.91-86.79%, which represents substantial rearrangement of the collagen organization in the facet capsule for some specimens (Table 7.5). Tissue regions with altered fiber alignment after retraction were also significantly co-localized ($p<0.0001$) with regions in which unrecovered strain after retraction was also detected (Figure 7.13). This finding suggests that changes in the

microstructural organization after retraction may contribute to the altered mechanical function. Although these changes in structure and function of this ligament may indicate the presence of damage, no capsule failure, yield, nor anomalous fiber realignment were detected to occur *during* retraction. Additional work is needed to determine whether the unrecovered strain and altered fiber alignment measured immediately after retraction and the altered mechanical response measured during the final cycle of tensile loading are true indicators of microstructural damage; for example, it is necessary to determine whether such changes still persist following long-term hydrostatic recovery periods of at least 24 hours. If the threshold for altering the microstructural organization of the facet capsule is indeed lower than that for rapid, anomalous changes to the collagen realignment patterns during loading, the altered fiber organization detected in this study may be an indication that plastic deformation of proteoglycans or other ground substance materials surrounding the collagen fibers was produced rather than any failures of collagen fibers or crosslinks. This hypothesis of unrecovered proteoglycan deformation is supported by studies using tissue grown from chondrocyte cultures which demonstrate increased laxity during tensile cyclic loading after proteoglycan digestion (Koop et al., 2002).

Capsule regions with unrecovered strain after retraction sustained greater strain magnitudes at the peak 2.5 mm of retraction in this study ($p=0.0399$) (Figure 7.14). However, significantly higher strains *during* retraction were not sustained by the regions with altered fiber alignment (Figure 7.14). This lack of an

association between changes in the fiber organization *after* retraction and capsule strains *during* retraction in this study parallels the difference in locations of anomalous fiber realignment and maximum ε_1 during tensile loading of the capsular ligament described in Chapter 5 (Quinn and Winkelstein, 2009). Collectively, both of these studies suggest that the location of maximum principal strain (ε_1) may differ from the location of maximum principal stress due to regional differences in fiber orientation and organization. Non-affine fiber network models have been developed that relate the macro-scale stress and strain in tissue through the experimentally-derived collagen fiber orientations and a constitutive equation for the fiber mechanical properties (Chandran and Barocas, 2006; Sander et al., 2009a, b). These models have predicted the collagen fiber kinematics and deformation in engineered constructs under complex loading conditions and illustrate differences in the locations of stress and strain maxima (Sander et al., 2009a, b), which suggests that the location of microstructural damage may depend on the regional variability of fiber alignment and organization. Additional studies implementing regional fiber orientation data into a non-affine model of capsule mechanics may be able to better explain the differences between the locations of altered microstructural organization and strain maxima during loading.

In a previous whiplash simulation study, a combination of shear, extension and compression loading was applied to cervical motion segments resulting in 2.2±1.1 mm of vertebral retraction (Siegmund et al., 2000), matching the retraction magnitude selected for this study. In fact, the 2.5 mm of retraction imposed in the

current study was chosen to approximate that study and other whiplash simulations (Siegmund et al., 2000; Sundararajan et al., 2004). However, the maximum ε_1 values at peak retraction (0.178±0.058) in the study by Siegmund et al. were substantially smaller than the maximum ε_1 values measured at 2.5 mm of retraction (2.18±0.79) in isolated specimens in the current study (Table 7.1). In addition, the current study used a substantially smaller capsule area compared to the full capsular ligament in the previous study (Siegmund et al., 2000); a finer spatial resolution (312±158 markers) was also used in the current study. Together, these differences in experimental protocols may help explain the difference in strain magnitudes relative to those measured previously using fiduciary markers for the human facet capsule (Siegmund et al., 2000; Winkelstein et al., 1999). In fact, studies of rat facet joint loading demonstrate that the facet capsule strain field values can double when the number of fiduciary markers used is increased from 4 to 20 (Lee et al., 2004 a,b; Quinn et al., 2007). In addition, strain measurements in the current study were limited by the need to transmit light through the capsule for vector correlation tracking. As a result, all tissue measurements were made primarily from the anterior side of the capsule. In previous studies using fiduciary markers to calculate full field strains over a much larger area of the capsule, the location of maximum ε_1 was significantly more likely to occur in the superior and anterior half of the capsule (Siegmund et al., 2001; 2008). Those previous studies of entire intact joints suggest that the portion of the capsule where strain was measured in the current study corresponds to a region of the capsule that normally sustains

greater deformation, which could also explain, in part, the greater ε_1 values in the current study.

The maximum ε_1 values from the full field measurements of the capsule after retraction (0.93±0.82) far exceeded the average ε_1 values of the full field after retraction (0.06±0.04) (Table 7.3). Aside from their co-localization with altered fiber alignment, no trends in the anatomical location of unrecovered ε_1 or γ_{max} were identified (Figure 7.13; Appendix J). However, for a small percentage of the capsule, large plastic deformations may have been produced by whiplash-like retraction given the maximum unrecovered strain values measured after retraction. The magnitude of the maximum unrecovered ε_1 in over half of the specimens (Table 7.3) exceeded the strain threshold reported to activate nociceptor firing defined in a goat model of facet capsule stretch (Lu et al., 2005a, b). Placed in that context, these regions of the ligament in which there are large unrecovered strain magnitudes in the current study would suggest that acute facet-mediated pain may be produced in the absence of any collagen fiber network disruption. Furthermore, the presence of unrecovered strain in the current study may suggest that strain thresholds (45±15.1%) for sustained afferent afterdischarge following joint loading in that goat study (Lu et al., 2005a, b) may be related to deformation-activated mechanoreceptors firing in response to unrecovered strain. However, it remains to be determined whether the unrecovered strain detected here would persist for later more long-term time points in that work or if those changes contribute to chronic facet-mediated pain. When placed in the context of in vivo studies, the production

of altered fiber alignment and unrecovered strain after facet retraction simulating whiplash kinematics observed for the current study demonstrates how the facet capsule, without any visible tears, may generate sustained nociceptive input, leading to the development and maintenance of pain.

The production of facet capsular ligament laxity in this study following a whiplash-like retraction magnitude is consistent with findings of laxity and radiographic abnormalities (e.g. diastasis) in other whiplash simulations (Ivancic et al., 2008; Yoganandan et al., 2001). An 8 g acceleration of isolated cervical spines produced an average laxity of 0.4±0.3 mm in the C6/C7 capsular ligament at 0 N of load (Ivancic et al., 2008). In the current study, laxity significantly increased to 0.15±0.07 mm after retraction (Table 7.2 and Figure 7.9). The considerably less laxity produced in the current study of joint retraction suggests that substantially more microstructural organization may be produced through dynamic inertial loading of the cervical spine, as observed by Ivancic et al. (2008). However, the larger magnitude of laxity measured in that study may be explained by the greater impact (8 g) that those specimens sustained relative to the 5-6 g impacts imposed in many whiplash simulation studies (Cusick et al., 2001; Luan et al., 2000; Sudararajan et al., 2004; Yoganandan et al., 2002). The co-localization of unrecovered strain and altered fiber alignment in the current study suggests that the development of laxity in this (Figure 7.13) and other whiplash simulation studies may, in fact, be the result of measurable microstructural damage provided that the period of hydrostatic recovery for the facet capsule following the whiplash

simulation was sufficient to reduce the viscoelastic effects of the previous time-history on the mechanical response.

The whiplash kinematic was simplified to a quasi-static facet retraction motion in this study, but previous cadaveric studies demonstrate a more complex vertebral motion over the course of 200 ms that also includes compression and joint sliding (Deng et al., 2000; Pearson et al., 2004; Stemper et al., 2005; Sundararajan et al., 2004). These neck motions associated with whiplash during a rear-end impact occur over a time period that is approximately 50,000-fold shorter than the period of retraction in this study. As a result, this study may be underestimating the facet capsular ligament forces generated during retraction (Table 7.1). However, the displacements required for capsule failure have been shown to not vary significantly between dynamic and quasi-static loading (Winkelstein et al., 2000; Yoganandan et al., 1989). Yet, future studies are needed to confirm whether the mechanisms that produce altered fiber alignment after retraction are also insensitive to the rate of loading. Although this study did not define the viscoelastic behavior of the facet capsule, the change in peak force at each cycle of tensile loading did not depend on whether the loading was before or after retraction ($p=0.114$). Unlike previous studies that indicate subfailure loading can change the viscoelastic characteristics of ligaments (Panjabi and Courtney, 2001), the lack of a significant interaction between cycles and the two tensile loading tests before and after retraction indicates that the time-dependent mechanical response of the capsule measured over 30 cycles may not be modulated by whiplash-like retraction (Figure

7.10). Although the mechanical responses before and 20 minutes after retraction do not appear to converge with an increasing number of tensile loading cycles (Figure 7.10), it is unclear whether the laxity and changes in force and stiffness quantified in this cadaveric study would persist for multiple days or months in vivo when fibroblast-mediated extracellular matrix remodeling occurs in response to injury. Ultimately, the study of mechanical and microstructural changes in an in vivo model of facet joint loading will be needed to determine the long-term effects of whiplash-like loading magnitudes on facet capsule microstructure and aberrant afferent firing.

By identifying altered fiber alignment *after* joint retraction (Table 7.5), in addition to assessing potential anomalous realignment *during* retraction, this study demonstrates that microstructural changes to the facet capsule can be produced by whiplash-like loading. However, anomalous fiber realignment *during* loading did not occur in any test, and may not be a requisite for the altered fiber alignment and unrecovered mechanical changes that were detected *after* retraction. The assessment of altered fiber alignment is derived from the ability to make pair-wise comparisons between the same tissue region before and after loading through vector correlation tracking. Accordingly, the vector correlation analyses presented here cannot be implemented in a clinical setting to diagnose whiplash-associated disorders. Nonetheless, this study demonstrates that whiplash-like motion will produce a change in the collagen fiber alignment of the facet capsule, and this technique can be implemented into future work to help develop and validate

diagnostic tools capable of detecting these subtle, mechanically-induced structural changes.

7.4. Integration

The studies presented in this chapter support some of the hypotheses in Aim 3. Anomalous fiber realignment was not identified during a 2.5 mm retraction of the human facet joint, as hypothesized in Aim 3a. Anomalous fiber realignment was produced between 0-2.5 mm of displacement in 6 of the 16 specimens during the tensile failure tests described in Chapter 5, which makes the lack of *any* anomalous realignment during retraction a somewhat unexpected result. However, previous studies of isolated cervical facet joints have demonstrated that the displacements required for ligament failure in joint retraction are approximately 30% greater than those needed to induce failure in tension (Siegmund et al., 2000, 2001; Winkelstein et al., 1999, 2000). Despite a lack of anomalous fiber realignment during retraction, ligament laxity was produced (Table 7.2), as well as unrecovered strain and altered fiber alignment in some regions of the ligament immediately after retraction (Tables 7.3-7.5). However, this study did not evaluate whether these changes in mechanical and structural properties that were detected persist beyond the short period of time measured in this study. Although the regions of altered fiber alignment were not associated with higher strains during retraction (Figure 7.14), these regions of altered alignment were co-localized with unrecovered strain measured immediately after retraction (Tables 7.6 and 7.7).

This co-localization of strain and altered collagen organization implies the vector correlation tracking technique developed in this chapter may have some utility in relating microstructural changes to more traditional biomechanical metrics such as strain.

For tensile loading of this ligament (Chapter 6), the occurrence of anomalous fiber realignment coincided with the displacements required to produce behavioral hypersensitivity (Lee et al., 2008; Lee and Winkelstein, 2009; Quinn et al., 2010b). Although anomalous fiber realignment was not produced within the specific portion of the facet capsule that was imaged in this chapter, previous work with an in vivo rat model (see Chapter 4) has demonstrated that painful facet joint displacements also induce laxity in the capsular ligament and collagen fiber disorganization in its lateral aspect (Quinn et al., 2007). Collectively, the QPLI-based studies in Chapters 5-7 demonstrate that facet capsule injury can occur at loading magnitudes well-below those required for tissue failure or visible rupture in both tension and retraction. By demonstrating evidence of microstructural changes to the facet capsule during and after joint loading, these studies provide an explanation of how facet-mediated pain can be observed clinically despite a lack of radiographic evidence in many patients with whiplash-associated disorders.

CHAPTER 8

Synthesis & future work

8.1. Introduction

Excessive facet capsular ligament stretch has been implicated as a mechanism of painful injury during whiplash based on biomechanical studies of the kinematics of human cadaveric spines during simulations of rear-end impacts (Cusick et al., 2001; Deng et al., 2000; Grauer et al., 1997; Ito et al., 2004; Luan et al., 2000; Pearson et al., 2004; Stemper et al., 2005; Yoganandan and Pintar, 1997). The facet joint and its capsule are also identified as the primary source of pain in patients with whiplash-associated disorders even though no radiographic evidence of capsule damage is present in those patients (Barnsley et al., 1995; Lord et al., 1996a; Manchikanti et al., 2002; Pettersson et al., 1997; Voyvodic et al., 1997). Absent a means to detect facet capsular ligament damage, there is no clear definition of the loading conditions that initiate capsule injury or the mechanisms that can lead to chronic pain after whiplash. Therefore, the purpose of this thesis was to integrate electrophysiological, optical, and biomechanical data to identify the loading conditions to the facet joint that produce microstructural damage to the

facet capsular ligament and to determine whether subfailure joint loading can initiate neuronal plasticity in the spinal cord and the development of persistent pain.

8.2. Synthesis of aims

Facet capsule stretch sufficient to produce behavioral hypersensitivity produces neuronal hyperexcitability in the dorsal horn of the spinal cord (Chapter 4). The magnitude of capsule stretch is correlated with the frequency of neuronal firing evoked by forepaw stimulation, and less-severe magnitudes of capsule stretch do not produce any evidence of behavioral hypersensitivity or neuronal hyperexcitability (Chapter 4). Clinical evidence has also demonstrated increased tactile sensitivity for whiplash patients with facet-implicated pain, and central sensitization in the spinal cord has been thought to drive the maintenance of pain in patients with whiplash-associated disorders (Banic et al., 2004; Curatolo et al., 2001). Patients who demonstrate chronic pain symptoms after whiplash often present with evidence of post-traumatic stress and/or other psychological disorders (Banic et al., 2004; Offenbaecher et al., 1999; Sterling et al., 2003, 2005). These affective disorders likely alter the neuronal responses of serotonergic supraspinal structures, such as the periaqueductal gray, and through descending modulation, may also alter spinal neuron responses. However, the evidence of dorsal horn hyperexcitability following painful facet joint injury in the rat model presented in this thesis demonstrates that spinal neuron hyperexcitability and mechanical hypersensitivity can be modulated by the severity of mechanical injury to the facet

joint alone. These findings suggest that capsular ligament damage can produce changes in secondary somatosensory neuron activity and persistent pain symptoms regardless of higher-order supraspinal contributions to nociceptive pathways. Certainly, determining the contributory role that altered descending modulation may play in the processing of afferent information from the facet joints is needed to more completely understand how facet-mediated chronic pain is maintained over the long-term in whiplash patients.

The facet joint loading conditions that produce functional plasticity of dorsal horn neurons in the rat do not produce any visible capsule rupture (Chapter 4). The absence of capsule rupture is consistent with the lack of radiographic evidence of any peripheral tissue damage in both clinical studies of whiplash patients and simulation studies of whiplash using cadaveric preparations (Pettersson et al., 1997; Voyvodic et al., 1997; Yoganandan et al., 2001). However, neither the imaging studies in the literature nor the in vivo work described presented in Chapter 4 provide a method to detect local injuries to the facet capsule or to identify the specific loading conditions that produce *injury*. A vector correlation technique to analyze polarized light images was developed (Chapter 5) to detect anomalies in the collagen fiber kinematics of the facet capsular ligament during tensile loading. Anomalous fiber realignment was identified during tensile loading prior to any visible capsule tearing or mechanical failure (Chapters 5 and 6). Additionally, anomalous fiber realignment was statistically associated with the occurrence of ligament yield (Chapter 6), which strongly suggests that the failure of

some of the load-bearing microstructural components in the facet capsular ligament was likely occurring during that anomalous realignment, and well-before the ligament's gross rupture. Collectively, the studies in Chapters 5 and 6 established an imaging technique capable of localizing atypical patterns of fiber kinematics that accurately predicted a loss of structural integrity (i.e. yield or failure) in the facet capsular ligament prior to its visible tearing and independent of traditional mechanical measurements.

Previous studies of isolated facet joint mechanics identified that partial failures of the capsule were induced prior to its reaching its ultimate load in tension, which provided an important advance in defining mechanical thresholds for the occurrence of capsule injury (Siegmund et al., 2000; Winkelstein et al., 1999). However, facet joint loading at displacements below those required to induce partial failure was found to produce spinal neuron plasticity and behavioral hypersensitivity (Chapters 4 and 6). In addition, anomalous fiber realignment was found to occur within magnitudes of loading to the joint that produce behavioral hypersensitivity and electrophysiological evidence of spinal neuron plasticity, which suggests that the detection of ligament damage at the *microstructural* level may be a more appropriate indicator of capsule loading sufficient to produce pain. Previous studies involving acute measurements of neuronal activation during facet joint loading in a goat model provided strain thresholds during capsule stretch that initiated nociceptive firing in the primary afferents of that joint (Lu et al., 2005a, b). By detecting anomalous fiber realignment in the rat capsular ligament at facet

joint displacements that also produce spinal plasticity and persistent pain symptoms 7 days *after* injury (Chapters 4 and 6), work in this thesis independently identifies capsule injury and the development of persistent facet mediated pain rather than relying on assumptions of macroscale strain thresholds for painful injury. As a result, more-conservative mechanical thresholds for initiating *persistent* facet-mediated pain via capsule loading can be developed without the need for complex scaling algorithms between animal models or strain measurement techniques.

Anomalous fiber realignment may be an indicator of a ligament injury that is sufficient to produce persistent pain in the rat, but anomalous fiber realignment was not found to occur during a retraction of the human facet joint to 2.5 mm that replicates a whiplash-like vertebral retraction (Chapter 7). Although anomalous fiber realignment was not detected during loading in that study, significant alterations in fiber alignment and changes in the mechanical function of the capsular ligament *were* identified after retraction. In fact, altered fiber alignment and unrecovered strain detected immediately after retraction were significantly co-localized in some regions of the capsule. This co-localization provides unique evidence of altered structure and function in localized regions of the tissue, and may explain the unrecovered laxity and decreased ligament stiffness that were evident during cyclic tensile loading performed 20 minutes after the joint retraction. When placed in the context of whiplash simulations of whole cadavers (Deng et al., 2000; Sundararajan et al., 2004), these findings suggest that excessive

facet capsule stretch during whiplash may be sufficient to produce functional and microstructural changes that are not evident through traditional diagnostic imaging.

The collection of polarized light imaging analysis techniques used to identify anomalous fiber realignment during facet joint loading and altered fiber alignment after loading are sensitive to small changes in collagen orientation based on the pairwise comparisons made prior to or during loading. Because collagen fiber alignment was quantified based on the transmission of polarized light through the capsular ligament, this approach cannot be directly applied to a clinical setting. However, these image analysis techniques can be used to test and evaluate future imaging approaches targeted for diagnosing and localizing soft tissue injury after a whiplash event.

8.3. Limitations and future work

The work presented in this thesis demonstrates that microstructural and functional changes in the facet capsule are produced during subfailure loading of the joint, and such loading also produces neuronal plasticity in the spinal cord and behavioral symptoms of persistent pain. Yet, there are general limitations to the experimental approaches taken in this thesis, and there are a number of additional investigations, beyond the scope of this thesis, that should be performed in order to identify the specific mechanisms of anomalous fiber realignment, its relationship to the development of persistent pain, and its potential occurrence during the joint kinematics produced during motor vehicle crashes.

The cervical facet joint was loaded at a quasi-static rate in all studies of this thesis. Yet, facet capsule loading during whiplash has been reported to occur within 200 ms of a vehicle impacting the rear bumper of the target vehicle (Bogduk and Yoganandan et al., 2001; Deng et al., 2000; Sundararajan et al., 2004). Although the joint displacement for gross failure of the human facet capsular ligament does not vary with loading rate (Winkelstein et al., 2000), the response of afferent nerve fibers in the facet capsule may be sensitive to loading rate. In fact, an in vitro model of traumatic neuronal injury has previously demonstrated that a high rate of loading produces higher cytosolic calcium levels and more neuron death than quasistatic loading (LaPlaca et al., 1997). If the rate dependence of neuronal injury reported in that in vitro model is extended for inference to the primary afferents in the facet capsule, a high rate of capsule loading may produce afferent nerve fiber injury at a lower strain threshold than would be required for quasistatic rates, even though the threshold for mechanical failure of the capsule tissue does not differ across loading rates (Winkelstein et al., 2000). In addition, the frequency of firing of mechanoreceptors in the knee joint capsule has been shown to be more strongly correlated with stress than with strain (Khalsa et al., 1996). Given the correlation between mechanoreceptor firing and tissue stress in the knee joint capsule, the extrapolation of such a relationship to the cervical facet capsule would suggest that the activation of, and possible injury to, mechanoreceptors in the facet joint may be directly related to the local stress environment of that tissue. Since the stress in the facet capsule depends on the rate

of tissue deformation because of its viscoelastic properties (Quinn and Winkelstein, 2005), the speculative notion that there are stress-activated mechanoreceptors in the facet capsule would imply that the capsule strain threshold for activating afferent firing will decrease also with increasing loading rates. If the strain or displacement thresholds for neuronal firing in the facet capsule are indeed rate-dependent, even though mechanical failure of the capsule is not (Winkelstein et al., 2000), it remains unclear whether ligament damage measured from the kinematics of the load-bearing collagen fibers is associated with the development of pain at higher rates of loading. Therefore, the outcomes related to both capsular ligament damage (e.g. anomalous realignment and yield), and persistent pain (e.g. neuronal hyperexcitability and behavioral hypersensitivity) should be placed in the context of different joint loading rates.

A new experimental approach using dynamic facet joint loading in vivo has recently been developed and applied to the same rat model that was used in this thesis (Dong et al., 2008; Dong and Winkelstein, 2010). In that recent work, the magnitude of vertebral displacement applied across the facet joint is positively correlated with the expression of a metabotropic glutamate receptor in the spinal cord at day 7 (Dong and Winkelstein, 2010), suggesting that the spinal neuron hyperexcitability observed at day 7 following the quasistatic loading conditions in the studies of this thesis may be present after dynamic loading as well. However, additional in vivo work is needed to specifically determine whether the mechanical threshold for either ligament damage or persistent pain depends on loading rate.

Additional ex vivo studies defining the viscoelastic response of the facet capsule could also aid in understanding how rate affects the mechanical response of the ligament and would provide a theoretical model for scaling injury parameters among different rates of loading.

Muscle strain has been proposed as an injury mechanism during whiplash and it has been suggested that muscle spasticity may contribute to whiplash-associated disorders (Freund et al., 2002). In this thesis, musculature was cleared from the capsule and the vertebral laminae in the in vivo model of joint loading, suggesting that muscle strain alone is not a requisite for pain following excessive cervical spinal motions because the interspinal muscles were resected and not stretched. Although muscle strain or injury was not a contributing factor to the physiological outcomes of the in vivo model of facet joint loading, muscle resection during surgery may have initiated some aberrant firing from damaged muscle spindle afferents. However, the lack of spinal neuron hyperexcitability in the sham and non-painful control groups undergoing the same surgery and muscle removal as the painful group suggests that muscle damage for any of the procedures involved in the surgery did not produce the persistent pain symptoms and spinal plasticity that were observed in the in vivo study in Chapter 4. Although muscle removal and a dorsal laminectomy were required in order to measure neuronal activity in the spinal dorsal horn in that study, the use of less invasive electrophysiological measurement techniques (Vernon et al., 2009) in future work could enable measurements of spinal neuron excitability while leaving the

surrounding musculature intact. Furthermore, by stimulating the interspinal muscles and measuring evoked dorsal horn responses, the potential contribution of muscle spindle damage to facet-mediated pain could also be elucidated.

Differences in facet-mediated pain and microstructural injury to the capsule were not evaluated across different levels in the cervical spine. A single cervical level was evaluated in each study of this thesis (either C4/C5 or C6/C7). Clinically, the most symptomatic level in the lower cervical spine is C5/C6 (Lord et al., 1996a), and the magnitude of C5/C6 facet capsular stretch produced during whole cadaver whiplash simulations is approximately twice that of the stretch experienced by upper cervical spinal levels (Luan et al., 2000). Despite a higher incidence of C5/C6 joint injuries (Lord et al., 1996a), the mechanical properties of the facet capsular ligament at gross failure do not differ among levels in the lower cervical spine (Siegmund et al., 2000; Winkelstein et al., 1999; Yoganandan et al., 2000). As a result, the loading conditions that produce anomalous realignment and ligament yield in the studies described in this thesis may be used to make inferences about the mechanical tolerance for microstructural injury in facet joints at other vertebral levels in the lower cervical spine. Furthermore, the similar mechanical responses of facet joints reported for testing from adjacent cervical levels (Siegmund et al., 2000; Winkelstein et al., 1999; Yoganandan et al., 2000) would suggest that the thresholds for capsule injury and physiologic dysfunction may be similar. Also, the higher frequency of symptoms occurring at C5/C6 may be related to the different kinematics that the facet joints at each vertebral level

undergo during whiplash (Deng et al., 2000; Sundararajan et al., 2004; Yang and King, 2003).

The *long-term* effects of subfailure facet capsule damage and spinal plasticity were not evaluated in this thesis. Neuronal plasticity was characterized seven days after facet joint loading that produced behavioral hypersensitivity (Chapter 4). Although the behavioral hypersensitivity observed at that time point does extend to 42 days after injury (Rothman et al., 2008), the mechanisms in the CNS that drive chronic pain symptoms may differ between days 7 and 42. Additional studies should be performed to identify any differences in either functional plasticity or the structural organization within the dorsal horn (e.g. dendritic sprouting or the rearrangement of synaptic contacts) at chronic time points in this model. In addition to investigations of the dorsal horn plasticity at later time points, the extent of extracellular remodeling in the cervical facet capsular ligament following painful injury should be determined in order to identify whether ligament damage remains over the course of persistent facet-mediated pain symptoms. Significant collagen turnover occurs during the healing process following ligament sprains (Provenzano et al., 2005), and this remodeling may eliminate any hallmarks of the initial capsule injury even as chronic pain is maintained due to plasticity in the spinal cord. The presence of altered fiber alignment and unrecovered strain in human cadaveric ligaments was identified immediately after joint retraction in Aim 3, but the application of microstructural imaging approaches to an in vivo model of joint loading is needed to determine

whether collagen fiber disorganization and ligament laxity persist in the presence of potential fibroblast-mediated healing processes after an initial ligament injury. Temporal measurements of the capsule fiber alignment after painful joint injury would help to determine whether it is possible to use any microstructural hallmarks of peripheral tissue injury to diagnose chronic facet-mediated pain.

In addition to the potential mechanical and structural changes to the facet capsule produced by the in vivo healing processes, the long-term viscoelastic effects of tissue loading were not assessed when evaluating unrecovered strain and altered mechanical function in the ex vivo studies presented in Chapter 7. In those studies, changes in the mechanical response of the capsular ligament produced by facet retraction were measured by comparing the force-displacement curves during the application of cyclic tension across the joint before and 20 minutes after retraction. By selecting a 20 minute recovery period that was based on previous studies of laxity in annulus fibrosus and ligament tissue after subfailure loading (Iatridis et al., 2005; Pollock et al., 2000), potential changes in the mechanical properties of the capsule that were produced by variable hydration levels were minimized. Furthermore, comparisons between the mechanical response before and after retraction were assessed only at the 30^{th} cycle of the tensile loading protocol in order to account for any short-term viscoelastic artifacts in the tensile loading response caused by potential stress relaxation in the capsule during its retraction. However, viscoelastic recovery of feline lumbar spines has been demonstrated to continue to occur beyond 20 minutes and up to 24 hours after

loading in in vivo preparations (Solomonow et al., 2000). Because ligament damage was not detected through anomalous fiber realignment in the study in Chapter 7, additional investigations are needed to evaluate whether or not the laxity and reduced stiffness in the facet capsular ligament that were measured immediately following retraction remain permanently and continue to persist as being unrecoverable.

To evaluate whether the 20 minute recovery period used in the studies presented in Chapter 7 was sufficient to rehydrate the facet capsule following retraction, an isolated C6/C7 human facet joint also underwent the same tension-retraction-tension loading protocol described in Chapter 7 (see Figure 7.5 for an overview of the testing protocol) but was allowed to recover for 24 hours before an additional cycle of tensile loading was again applied at 24 hours after the joint retraction. To prevent specimen dehydration over that 24 hour period, the specimen was submerged in a 0.9% saline bath for the duration of the experiment (Quinn and Winkelstein, 2005). Between the tensile loading test performed 20 minutes after the imposed retraction and the tensile testing imposed 24 hours later, there were negligible differences between the mechanical response measured at the 30^{th} cycle of each test. Specifically, only 6% of the force at 1 mm, 5% of the stiffness, and 14% of the laxity were recovered between 20 minutes and 24 hours after retraction (Figure 8.1). The lack of a significant change in the mechanical response over a 24 hour period observed in this pilot study suggests that the majority of the laxity and changes in stiffness and force that were detected 20

minutes after retraction during the 30th cycle of tensile loading would persist regardless of additional recovery time permitted for fluid flow in the specimen to achieve equilibrium.

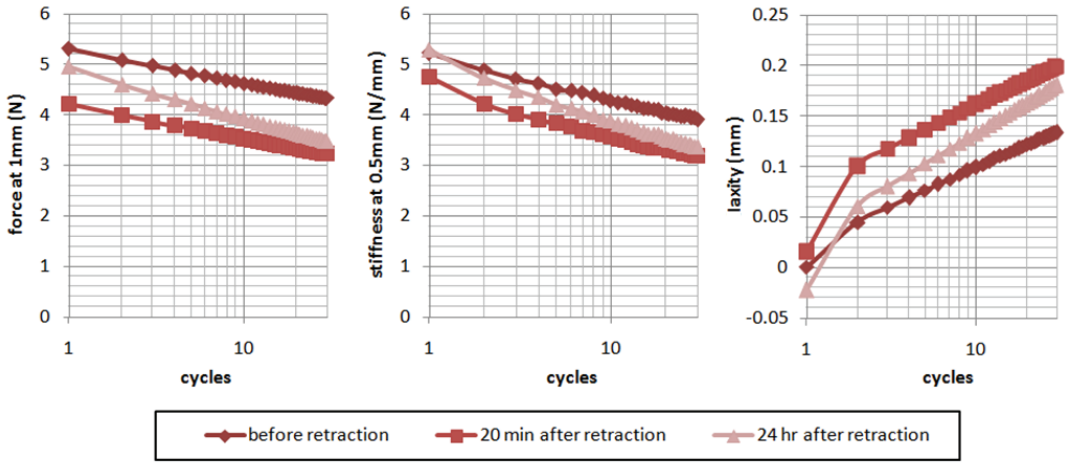

Figure 8.1. Changes in the force, stiffness, and laxity of the capsular ligament during tensile cyclic loading before retraction, 20 minutes after retraction, and 24 hours after retraction. The differences between the force, stiffness, and laxity measurements obtained during the loading before and immediately after retraction at the 30th cycle remain unrecovered following a rest period of 24 hours.

Interestingly, the force, stiffness, and laxity measured at the 1st cycle of tensile loading after a 24 hour recovery period was similar to those measured during the 1st cycle of tensile loading before retraction (Figure 8.1). However, as the number of loading cycles increased for each test session, the force, stiffness, and laxity measured after 24 hours deviated from the measurements obtained during cyclic loading before retraction (Figure 8.1). By the 30th cycle of each test session, the force, stiffness, and laxity after 24 hours were more similar to the

measurements taken at 20 minutes after retraction rather than immediately before retraction (Figure 8.1). Further, the differences between the 1st and 30th cycles during the loading 24 hours after retraction were larger than the differences between cycles both immediately before and after retraction. This finding suggests that the ligament sample may not have been fully hydrated during the initial tension-retraction-tension protocol. Yet, the similar cycle-dependent responses that were observed during the tensile loading before and 20 minutes after retraction in this pilot study (and the study described in Chapter 7) suggests that the altered mechanical responses measured 20 minutes after retraction were not caused by a change in hydration, but rather microstructural changes in the extracellular matrix. Certainly, these pilot findings suggest that the force-displacement response during the 1st cycle is more dependent on differences in sample hydration, and supports the rationale for evaluating differences only at the 30th cycle. The different cycle-dependent mechanical response at 24 hours relative to that immediately before and after retraction highlights the challenges associated with identifying subfailure damage through techniques that are based solely on altered mechanical properties.

Although altered fiber alignment and unrecovered strain were also identified after retraction in the studies in Chapter 7, it is unknown whether those changes correspond to ligament damage and whether they are sufficient to produce facet-mediated pain. Changes in the capsule's fiber organization previously were identified following facet joint loading that produces pain (Quinn et al., 2007). However, the analysis of the directional variance of collagen fibers in histological

sections of the rat facet capsule in that study is not directly applicable to the more sensitive vector correlation-based outcomes used to quantify altered fiber alignment in Chapter 7. No comparisons to that previous histological study can be made because the vector correlation calculation described in Chapter 7 was based on differences in fiber alignment before and after loading of the same tissue. Accordingly, additional studies that quantify altered fiber alignment in isolated rat facet joints through changes in the vector correlation between fiber alignment before and after different subfailure vertebral distractions may help to determine whether the altered alignment identified in the study in Chapter 7 corresponds exclusively to the loading conditions which produce facet-mediated pain.

The sensitivity of any optical technique to quantify ligament damage is limited by its ability to assess all spatial locations where damage could occur. During facet joint loading to failure, anomalous fiber realignment was detected in all but one of the human and rat facet joint specimens tested. However, regions near the capsule's insertion into the bone of the articular facet could not be measured due to an inability to transmit light in those regions. In future work, particularly as these polarized light techniques are evaluated during dynamic loading conditions, the sensitivity of anomalous realignment could decrease given that capsular ligament avulsions are more likely at high loading rates (Winkelstein et al., 1999). In addition to the effect of field of view on anomalous realignment detection, spatial resolution may change the sensitivity of the vector correlation techniques employed in this thesis. Based on the fraction of total tissue volume

that can be represented by the minimum of 9 pixels required for anomalous realignment detection in each QPLI study described in this thesis, it is estimated that anomalous realignment detection in the rat facet capsule study (Chapter 6) was 44% more sensitive than the tensile human facet capsule study (Chapter 5). This difference in estimated sensitivity may explain why anomalous fiber realignment was more likely to be detected without ligament yield or failure in the rat facet capsule compared to the human capsule. Furthermore, the percentage of tissue required for the detection of anomalous realignment (9 pixels) relative to the total ligament volume can be directly compared to the sensitivity of the load cells used in Chapters 5, 6, and 7 (0.25% of the measured value; Instron; Norwood, MA) in order to estimate the relative sensitivities of anomalous realignment and yield. Based on the imaging parameters and specimens used for this thesis, the detection of anomalous fiber realignment was estimated to be more sensitive than the detection of yield by 2.73-fold in the study in Chapter 5, 3.94-fold in Chapter 6, and 20.34-fold in Chapter 7. These estimates suggest that anomalous realignment is more sensitive to damage within the field of view of the camera than are load-based measurements. However, additional experiments using excised tissues in which the entire sample is contained within the field of view are needed to determine how the sensitivity of anomalous realignment detection may change with different tissue thicknesses, image resolutions, loading directions, or other experimental factors.

Collagen fiber orientation was inferred in this study by quantifying the retardation of light transmitted through capsular ligament tissue. As a result, the kinematics of the collagen fibers in response to tissue loading were defined over a scale that is likely to include a large number of collagen fibers (as shown in Figure 2.3; Provenzano and Vanderby, 2006). Because actual fiber or crosslink failure could not be visualized in these studies, additional work is needed to evaluate the presence of failures at the microstructural level and to understand how, and when, such damage propagates into a visible rupture in the tissue. Furthermore, it is unclear which specific microstructural components may fail when anomalous realignment or yield are detected. Although ligament tissue is 80% type I collagen by dry weight (Woo et al., 2006), other tissue components, including elastin, glycoproteins, and fibroblasts may be susceptible to structural failure as well. Anomalous realignment is based solely on fiber direction measurements derived from tissue birefringence, and because elastin and the ligament's ground substance do not exhibit birefringent properties (Korol et al., 2007), the realignment patterns measured in this thesis were assumed to only correspond to collagen fiber responses. However, it remains unclear whether the anomalous collagen fiber kinematics measured in those studies could be produced by the failure of elastin, proteoglycans, or even cells within the extracellular matrix. Through the enzymatic degradation of specific matrix components, the detection of the onset of anomalous realignment in the capsular ligament could be compared to ligaments without

enzymatic treatments in future work to identify whether non-collagenous structures contribute to the initial detection of microstructural damage.

To begin a preliminary investigation into the changes in the capsule ultrastructure produced by subfailure loading, facet capsular ligaments were excised from the human facet joints after the loading protocol described in Section 7.3. For each excised specimen, two capsule regions were demarcated: a region assumed to be damaged based on the detection of altered fiber alignment and unrecovered strain after retraction and an assumed undamaged region in which no changes in fiber alignment or strain were found. Specimens were desiccated, sputter-coated, and then imaged through scanning electron microscopy (SEM) (Hurschler et al., 2003). No consistent indications of fiber failure or disorganization could be identified during blinded evaluations of the SEM images from either the damaged and undamaged regions. Although ruptured collagen fibers were identified in some damaged regions of the capsule and an absence of ruptures was observed in some of the undamaged regions (Figure 8.2), the opposite trends were also observed in a portion of the images. This pilot study highlights the challenges in validating the presence of microstructural damage in the regions in which altered fiber alignment are detected during and after loading. Although SEM offers unparalleled image resolution to evaluate fiber damage, it is limited to an evaluation of the tissue surface. Alternative optical techniques, such as optical coherence tomography or two-photon microscopy may provide a better approach to

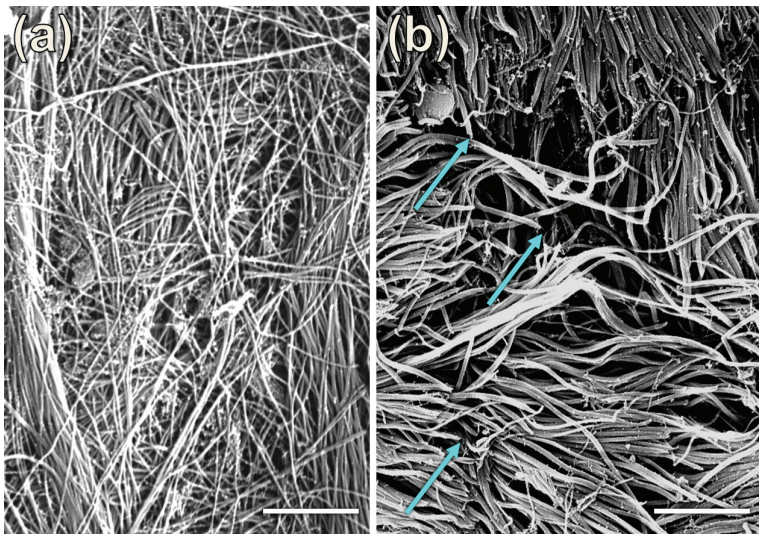

Figure 8.2. SEM images of human cervical facet capsular ligament tissue after subfailure joint retraction. **(a)** No fiber failures were identified in most tissue regions including those where no altered alignment was detected through vector correlation (image taken from Specimen #22). **(b)** Fiber failures were identified in some locations (indicated by arrows) in images taken from regions where altered fiber alignment was detected by vector correlation (taken from Specimen #17). Scale bars represent 2 μm.

validate the polarized light analysis employed in this thesis, as those alternative techniques are able to resolve microstructural information through the thickness of tissue. Future work using two-photon excited fluorescence and second harmonic generation (SHG) imaging could help identify the extracellular matrix components that fail during tensile loading, and could be performed in both in vivo or ex vivo settings. The strong SHG signal produced by collagen could be used to simulate the data recorded by a QPLI system at a given location, which would help define to the relationship between anomalous fiber realignment and microstructural failure.

The tissue locations that sustained anomalous fiber realignment during tensile loading (Chapters 5 and 6) and altered fiber organization after retraction

(Chapter 7) did not match the locations of maximum ε_1 or γ_{max} derived from the Lagrangian strain fields of the tissue during loading. An evaluation of the predictive abilities of additional strain metrics to localize microstructural damage should be performed to determine whether macroscale strain metrics without the incorporation of fiber-based anisotropy have utility in localizing putative microstructural damage. Understanding the local mechanical conditions that produce microstructural damage in the facet capsule will be critical in applying relevant capsule injury thresholds to modeling techniques such as finite element analysis.

Although the underlying microstructural failure mechanisms that produce anomalous fiber realignment and ligament yield during tensile loading remain unknown, the ability to detect and locate a pattern of collagen fiber realignment that is significantly associated with a loss in tissue stiffness makes it possible to localize a previously undetectable class of ligament injury as it occurs. Previous studies have hypothesized that excessive stretching of the facet capsule during whiplash can produce mechanical damage and pain despite a lack of any visible ligament tearing (Deng et al., 2000; Panjabi et al., 1998; Pearson et al., 2004; Lee et al., 2004a, b; Lu et al., 2005a, b; Sundararajan et al., 2004; Yang and King, 2003; Yoganandan et al., 1998). However, until this work, there was no evidence of tissue damage during subfailure facet joint loading. The complementary in vivo work identifying behavioral hypersensitivity and neuronal hyperexcitability after facet joint loading conditions that also produce anomalous fiber realignment in the

capsule suggests that the detection of anomalous realignment may be a suitable indicator of microstructural damage that is sufficient to initiate persistent facet-mediated pain. Certainly, future work is needed to identify how a rapid change in the collagen fiber alignment in the facet capsule may contribute to the activation of primary afferents and the development of persistent pain. In particular, the interactions between afferent fibers and the collagenous extracellular matrix of the capsule should be defined during and after subfailure joint loading to more fully characterize the effectiveness of using collagen fiber responses to detect painful joint injury.

The work in this thesis establishes a novel optical approach to localize subfailure capsular ligament damage during facet joint loading. Through an assessment of the collagen fiber realignment during joint loading, a previously undetectable class of low-grade ligament sprains was identified. Although the optical approach presented in this thesis using polarized light analysis to detect capsule injury is independent of any force-based measurements, anomalous realignment *is* associated with a rapid decrease in ligament stiffness (i.e. ligament yield) (Quinn et al., 2010a), which suggests this technique to be sensitive to the failure of the load-bearing microstructure in the capsule. Interestingly, the loading conditions that produce anomalous fiber realignment in the facet capsule under tension are substantially lower than those at which mechanical failure and capsule rupture occur (Quinn and Winkelstein, 2009; Quinn et al., 2010a). Therefore, this thesis has established anomalous fiber realignment as a potential surrogate endpoint

for *subfailure* ligament damage. Furthermore, anomalous realignment was detected at magnitudes of loading that also produce functional plasticity in the spinal cord and persistent behavioral responses suggestive of pain symptoms, which supports the use of anomalous realignment to establish a more appropriate estimate of the mechanical tolerance for painful capsule injury than compared to traditional load-based metrics such as frank tissue rupture or gross failure.

With an experimental framework created to establish more conservative mechanical thresholds for painful capsule injury, it is possible that the specific vertebral motions that initiate the development of whiplash-associated disorders may be identified and implemented into the development of refined passenger restraint systems. By demonstrating a new approach to identify mechanically-induced soft tissue injuries without the reliance on any of the traditional mechanical engineering approaches to quantifying damage, this thesis provides an important step in defining the complex relationships between cervical spine loading, subfailure facet joint trauma, and facet-mediated chronic pain.

APPENDIX A

Electrophysiology testing protocol

This appendix details the neuron search protocol (A.1) and spike sorting methods (A.2) used in the study described in Chapter 4. After the cervical spine exposure was performed and isoflurane washout was complete, the evoked responses of dorsal horn neurons in the deep laminae (400-100 μm electrode depth) were searched for during light brushing of the forepaw. When a responsive neuron was identified, a stimulation protocol that included brushing, noxious pinch, and von Frey filament stimulations was performed (Carlton et al., 2009; Chang et al., 2009; Christensen and Hulsebosch, 1997; Hains et al., 2003a, b). After data acquisition, single unit firing was isolated from the extracellular recordings through spike sorting (according to methods described in the Spike 2 Training Course Manual and Section A.2). Additional details regarding the electrophysiological methods used in the study are provided in Sections 4.3.3 and 4.3.4.

A.1. Neuron search protocol

1. Identify a target location that is medial to the rootlet insertions and between C6-C8 ipsilateral to the forepaw that is being stimulated.
2. Puncture pia at that location with Dumont forceps.
3. Insert electrode into the hole in the pia; the electrode tip should not bend and the spinal cord should only deform slightly.
4. Adjust micropositioner to achieve a depth of 400 μm.
5. Search for evoked responses on forepaw by brushing with cotton swab.
    a. If no response found, increase electrode depth by 20 μm and repeat.
    b. If response found, repeat brushing and adjust electrode depth to achieve maximum signal-to-noise ratio.
6. Apply a light pressure with the cotton swab and determine the location of the paw that elicits the maximum response.
7. Mark paw location with a fine felt-tipped pen.
8. Wait 5 minutes and ensure Spike 2 acquisition is running.
9. Assign the neuron recording a number and enter the number into the keyboard channel of the recordings in Spike 2.
10. Apply 10 light brush strokes with the cotton swab at approximately 1 stroke per second.
    a. Synchronize brush strokes with a tap on the von Frey load cell to record the timing of the brush strokes in Spike 2.
11. Wait 5 minutes.
12. Apply 60 g vascular clip to the forepaw location for 10 seconds.
    a. Pinch as much tissue as possible to reduce the potential for high stress concentrations and tissue damage.
    b. Synchronize the duration of the pinch with a tap and hold on the von Frey load cell.
13. Wait 5 minutes; set up von Frey stimulator to lower filament onto the forepaw location.
14. Apply a series of von Frey filaments with increasing strengths.
    a. The filament strengths should span the range for behavior testing:
        i. 1.4 g
        ii. 4 g
        iii. 10 g
        iv. 26 g
    b. Apply each filament 5 times at a rate of one application for every 2 seconds. Allow for a one second hold duration.
    c. Wait 60 seconds in between the application of different filament strengths.
15. Once 26 g stimulation is complete, increase the electrode depth until the evoked response from the previous recording site is no longer measureable.
16. If above a depth of 1000 μm, return to step 5.
17. If below a depth of 1000 μm return to step 1.

18. After 2.5 hours of searching for neurons, switch to the other side of the spinal cord and initiate the protocol again.
19. After 5 hours of searching, terminate the surgery and collect cervical spinal cord sample.

A.2. Spike sorting summary

Once data collection is complete, spike sorting to identify single unit recordings can be achieved through offline analysis using Spike 2 (Figure A.1). The Spike 2 Training Course Manual provides a detailed tutorial for spike sorting, but a few additional instructions are required:

- The voltage threshold for identifying a spike should be set to a level above the noise in the system; this threshold must be adjusted for every electrode location from which a recording was taken.
- The waveform period should be adjusted to a window that spans -0.3ms to +0.4 ms in order to characterize the complete shape of the action potential.
- Occasionally Spike 2 will generate very similar templates that represent the same neuron. When this occurs, click and drag the waveform diagram of one template over to the other template. While still holding down the mouse button, superimpose the two waveforms and then release the button to merge the templates.
- The same WaveMark templates should be applied to all of the voltage recordings to be analyzed at a given electrode location.
- Once spike sorting is complete, create a new channel containing the sorted WaveMark codes. Each WaveMark code corresponds to a single template; when counting the number of spikes, only use the frequency of firing from a single WaveMark code (Figure A.1).

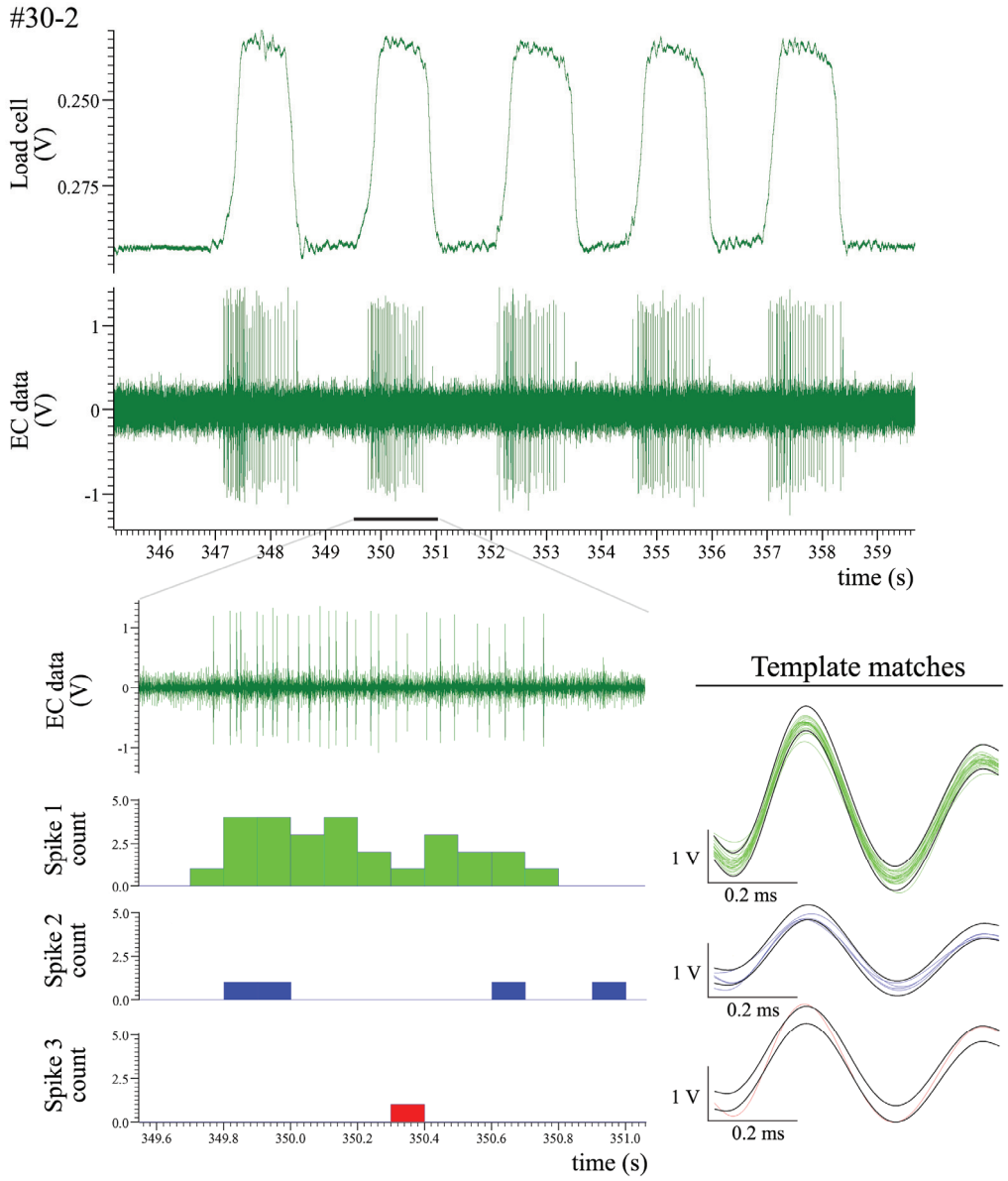

Figure A.1. Spike sorting example from neuron #30-2 in the painful group. The raw voltage recording from a single stimulation is expanded and the histograms and spike templates created during spike sorting at this electrode location are displayed. Only data from the Spike 1 count (green template) were used to characterize evoked activity. The different amplitude and shape of other spikes (blue and red traces) represent the action potentials of different nearby neurons and these spikes were removed from subsequent data analysis.

APPENDIX B

Neuron firing count data

This appendix details the number of action potentials evoked during various forepaw stimulations for individual neuronal recordings as described in Chapter 4. In the table below, neurons are labeled based on the animal in which they were found and the order in which the neuron was found relative to other neurons in that animal (*rat* and *neuron* columns). The *group* column corresponds to whether a painful vertebral displacement (labeled *P*), a non-painful vertebral displacement (*NP*), or a sham surgery (labeled *sham*) was performed. The electrode depth relative to the pial surface and side of the spinal cord (right or left) is also provided. Each neuron is classified as wide dynamic range (*WDR*) or low threshold mechanoreceptive (*LTM*) based on its response to noxious pinch, as described in Chapter 4. The table summarizes the number of action potentials that were evoked during 10 strokes of light brushing (labeled *brush*), 10 seconds of noxious pinch (labeled *pinch*), and the application of four different von Frey (*vF*) filament strengths. Five consecutive applications at each von Frey filament strength were applied, and the firing count for each application is detailed in the table.

rat	neuron	group	depth (μm)	side	class	brush	pinch	1.4g vF					4g vF					10g vF					26g vF				
								1	2	3	4	5	1	2	3	4	5	1	2	3	4	5	1	2	3	4	5
35	1	NP	703	R	WDR	47	247	0	1	1	0	0	2	3	1	1	1	4	6	12	4	3	23	24	24	13	14
35	2	NP	481	R	WDR	76	143	0	0	0	0	2	6	7	5	7	3	13	3	8	3	7	22	19	21	22	26
35	3	NP	693	R	LTM	34	52	0	0	0	0	0	3	1	1	1	1	9	7	9	5	8	23	14	20	18	21
35	4	NP	718	L	LTM	88	23	0	0	0	0	0	0	0	1	0	0	2	3	23	5	1	18	6	6	11	7
35	5	NP	757	L	LTM	60	42	0	0	0	0	0	3	1	0	1	0	6	4	7	3	2	12	8	15	16	12
35	6	NP	970	L	LTM	38	22	0	0	0	0	0	0	0	0	0	0	0	0	0	1	0	5	2	0	1	1
35	7	NP	678	L	WDR	66	44	0	0	0	0	0	1	0	0	0	0	2	1	2	2	2	6	2	4	11	9
36	1	NP	444	R	LTM	37	22	0	0	0	0	0	0	0	0	0	0	1	1	3	2	3	2	1	4	1	3
36	2	NP	650	R	LTM	63	42	0	0	1	0	0	0	1	1	0	0	10	14	0	3	6	9	7	12	6	6
36	3	NP	425	R	LTM	27	33	0	0	0	0	0	3	4	2	0	0	9	5	5	1	3	9	11	3	9	5
36	4	NP	728	R	LTM	24	12	0	0	0	0	0	0	0	0	0	0	5	2	0	1	0	7	2	1	2	2
36	5	NP	410	L	LTM	50	8	0	0	0	0	0	0	1	0	0	0	3	4	2	2	1	7	3	3	3	3
36	7	NP	408	L	WDR	106	66	1	1	2	0	0	10	2	2	9	5	25	11	9	9	7	31	9	15	9	10
36	8	NP	652	L	LTM	35	39	2	2	2	1	4	2	16	10	11	1	11	11	10	5	13	20	10	15	9	6
36	9	NP	876	L	LTM	37	45	4	2	1	0	0	1	3	1	7	1	8	3	3	2	2	28	38	30	30	36
37	1	NP	425	R	WDR	81	75	5	3	2	2	3	5	0	4	2	1	1	6	2	0	5	10	7	5	2	4
37	2	NP	650	R	LTM	48	14	0	0	0	0	0	0	0	0	0	0	1	0	0	0	0	2	3	1	2	0
37	4	NP	430	R	LTM	106	35	0	2	0	0	0	0	1	0	0	0	2	1	1	3	0	10	2	6	0	3
37	5	NP	743	R	LTM	31	6	0	0	0	0	0	0	0	0	0	0	3	0	0	0	0	3	2	1	0	0
37	6	NP	542	L	WDR	27	41	0	1	1	0	4	0	0	0	0	0	7	3	2	1	0	14	1	2	2	2
37	7	NP	623	L	WDR	83	46	0	2	2	3	1	6	4	2	3	0	9	0	4	7	4	25	14	10	10	16
37	8	NP	494	L	LTM	76	36	0	2	2	0	1	3	2	1	3	3	10	9	13	7	7	27	13	9	9	14
37	9	NP	521	L	LTM	32	17	0	0	0	0	0	2	0	1	1	1	2	5	4	0	2	10	6	2	4	0
41	1	NP	920	R	WDR	18	45	0	0	0	0	1	0	0	0	0	1	1	1	0	1	0	9	14	17	14	18
41	2	NP	425	R	LTM	121	6	1	2	1	2	2	3	4	3	2	3	7	5	3	2	3	4	7	5	4	5
41	3	NP	700	L	LTM	40	64	0	0	0	0	1	0	0	1	0	1	5	4	4	6	6	4	6	4	5	4
41	4	NP	837	L	LTM	29	5	0	0	0	0	0	0	0	0	0	0	1	0	0	0	1	11	8	15	34	20
41	5	NP	777	L	WDR	47	77	1	0	2	1	1	3	2	4	0	2	6	4	6	2	5	10	9	9	8	9
41	6	NP	518	L	WDR	118	121	2	0	0	1	1	4	5	4	5	3	8	8	7	6	8	24	20	18	15	8
41	7	NP	595	L	LTM	91	18	0	0	0	0	0	0	0	0	0	0	2	1	2	0	1	17	5	1	0	1
41	8	NP	624	L	WDR	31	27	1	2	0	0	0	1	0	3	2	2	5	3	2	1	2	3	2	3	3	2
44	1	NP	407	R	WDR	168	140	0	0	0	0	0	12	6	4	0	1	1	0	0	1	1	3	0	0	0	2
44	2	NP	594	R	WDR	45	35	0	0	0	0	0	3	3	2	1	4	12	9	2	4	2	26	20	22	14	30
44	3	NP	500	L	WDR	36	131	1	2	2	0	0	4	7	3	1	3	4	1	1	1	1	16	5	3	6	4
44	4	NP	407	L	WDR	38	266	1	1	1	1	2	4	3	1	2	2	8	5	2	2	1	26	13	9	15	9
44	5	NP	590	L	LTM	38	29	0	0	1	0	0	0	0	0	1	1	7	2	1	0	1	11	8	6	8	8
45	1	NP	425	R	WDR	27	8	0	0	0	0	0	0	1	0	0	0	16	1	0	0	0	4	4	1	0	0
45	2	NP	504	L	WDR	63	43	4	4	4	2	4	3	2	4	5	3	8	8	8	4	7	6	4	7	3	3
45	3	NP	612	L	WDR	75	60	2	1	0	0	0	2	3	2	3	3	10	8	6	6	6	18	28	19	26	18
45	4	NP	456	L	WDR	39	4	1	0	0	1	0	1	1	1	0	0	2	0	0	1	0	1	1	2	2	2
45	5	NP	842	L	LTM	61	24	0	1	1	1	1	5	4	5	2	3	11	10	11	9	8	11	7	8	10	8
45	6	NP	588	L	LTM	77	26	0	2	1	1	2	2	3	0	1	0	9	2	6	5	5	13	6	2	10	4

rat	neuron	group	depth (μm)	side	class	brush	pinch	1.4g vF					4g vF					10g vF					26g vF				
								1	2	3	4	5	1	2	3	4	5	1	2	3	4	5	1	2	3	4	5
45	7	NP	785	L	LTM	37	15	1	1	0	0	0	1	2	0	1	0	6	3	2	2	2	8	6	7	9	10
45	8	NP	612	L	WDR	43	33	1	1	0	0	4	3	1	1	0	3	3	3	2	2	5	7	10	3	7	7
45	9	NP	761	L	LTM	12	3	0	0	0	0	0	1	0	0	0	1	0	1	1	2	0	1	1	1	1	1
31	1	sham	419	R	WDR	16	35	0	1	2	0	0	0	0	0	0	0	3	1	1	0	1	24	15	23	14	22
31	2	sham	440	R	LTM	81	53	2	0	1	0	0	5	4	5	6	2	10	5	8	8	6	10	4	5	2	3
31	3	sham	690	R	LTM	52	14	0	0	1	0	1	2	0	0	0	0	2	2	1	1	0	3	0	2	3	5
34	1	sham	410	R	WDR	76	83	4	4	2	1	0	4	7	6	2	1	8	7	1	8	5	21	15	16	17	5
34	2	sham	450	R	LTM	35	43	1	1	1	0	4	1	4	6	7	1	10	10	8	14	3	5	6	4	4	3
34	4	sham	421	R	LTM	28	4	0	0	0	0	2	0	0	2	0	0	1	3	1	0	0	3	0	1	0	0
34	5	sham	598	R	LTM	70	17	0	0	0	0	0	1	0	0	0	1	4	4	3	4	2	8	3	1	4	3
34	6	sham	400	L	LTM	19	9	0	0	0	0	0	0	0	0	0	0	3	0	0	1	0	3	4	2	3	2
38	1	sham	505	R	LTM	45	74	1	0	0	0	1	2	0	0	0	0	10	4	9	12	5	19	14	16	12	5
38	3	sham	669	R	WDR	43	97	0	0	0	0	0	1	0	0	0	0	1	0	0	0	1	6	1	3	5	3
38	4	sham	435	R	WDR	100	79	0	0	0	0	0	0	1	0	0	0	7	0	4	7	1	28	12	10	6	7
38	5	sham	450	L	WDR	93	90	0	0	0	0	1	4	2	2	1	2	4	1	2	1	4	30	15	9	12	21
38	6	sham	682	L	WDR	35	20	0	0	0	0	0	7	1	1	0	0	1	3	2	1	2	10	6	11	4	5
38	7	sham	762	L	LTM	71	21	0	0	0	0	0	0	0	0	0	0	3	1	1	2	1	5	1	2	1	2
38	8	sham	732	L	LTM	12	22	0	0	0	0	0	1	1	0	0	0	6	2	1	1	1	11	3	3	2	3
38	9	sham	578	L	WDR	78	34	9	4	1	2	3	4	1	3	3	4	9	4	3	3	3	11	18	16	8	14
38	10	sham	783	L	LTM	17	8	0	0	0	1	0	0	0	0	0	0	0	0	0	0	0	5	1	1	1	1
40	1	sham	573	R	WDR	34	70	1	0	0	0	0	0	0	0	0	0	2	1	2	2	2	4	8	5	4	3
40	2	sham	606	R	LTM	39	23	0	0	0	0	0	1	0	0	0	4	18	5	5	4	3	11	14	10	16	7
40	3	sham	995	R	WDR	50	98	0	0	0	0	0	6	3	5	2	7	9	5	5	6	0	24	18	12	10	15
40	4	sham	462	L	WDR	38	11	0	0	0	0	1	1	1	0	1	1	5	2	1	3	2	6	9	3	8	6
40	5	sham	596	L	WDR	31	42	1	2	2	1	2	6	6	5	1	6	13	19	25	13	18	63	33	33	35	38
40	6	sham	754	L	WDR	20	16	0	0	0	0	1	0	0	0	0	0	0	1	1	1	2	5	3	0	3	1
40	7	sham	579	L	LTM	65	31	1	2	2	3	5	11	10	8	4	8	19	17	11	12	5	27	19	16	8	12
40	8	sham	993	L	LTM	27	12	0	0	0	0	0	0	0	0	0	0	12	13	12	10	14	27	15	14	19	21
43	1	sham	689	R	LTM	41	30	0	0	0	0	0	1	0	0	0	0	3	1	2	1	0	5	3	0	3	5
43	2	sham	819	R	WDR	106	52	0	1	1	1	0	1	1	1	2	0	7	3	3	1	1	12	9	6	2	14
43	3	sham	589	L	LTM	70	41	3	4	1	2	1	4	3	6	6	6	9	5	6	9	4	11	14	8	7	13
43	4	sham	770	L	WDR	56	115	1	0	0	3	0	14	9	7	5	8	23	23	25	17	12	20	8	9	17	9
43	5	sham	689	L	LTM	20	13	5	0	2	0	1	0	1	4	2	2	7	2	1	3	3	11	5	4	1	5
43	6	sham	748	L	LTM	43	12	2	4	2	1	2	4	10	5	3	4	11	6	9	5	8	9	8	3	8	3
46	1	sham	676	R	LTM	31	6	0	0	0	0	0	0	0	0	0	0	1	0	0	0	0	3	5	0	2	2
46	2	sham	670	R	LTM	22	8	0	0	0	0	0	0	0	0	0	0	1	0	0	1	2	1	2	4	3	6
46	3	sham	574	R	LTM	156	23	0	1	0	1	0	2	0	0	1	5	3	0	1	1	2	9	6	5	3	0
46	4	sham	700	R	LTM	39	4	0	0	0	0	0	0	0	0	0	1	1	0	0	1	0	0	0	0	1	1
46	5	sham	740	L	WDR	128	90	1	1	2	0	2	12	7	2	5	4	35	24	21	14	18	36	10	24	8	37
46	6	sham	805	L	LTM	73	63	1	0	0	0	0	3	1	1	1	0	7	3	1	1	2	10	9	12	11	13
46	7	sham	690	L	LTM	76	36	3	0	1	0	0	8	5	2	1	3	9	8	8	8	7	9	8	5	5	5
46	8	sham	1050	L	WDR	53	41	1	0	0	0	0	2	3	1	3	3	5	6	5	7	6	10	8	6	5	5

rat	neuron	group	depth (μm)	side	class	brush	pinch	1.4g vF					4g vF					10g vF					26g vF				
								1	2	3	4	5	1	2	3	4	5	1	2	3	4	5	1	2	3	4	5
46	9	sham	600	L	WDR	30	28	0	0	0	0	0	0	1	0	0	0	3	2	3	0	0	6	6	6	3	6
28	1	P	670	L	WDR	85	82	2	2	2	2	1	8	11	5	4	4	13	9	6	4	3	12	8	7	5	3
28	2	P	798	L	WDR	39	62	2	1	0	3	4	5	4	4	4	5	3	6	4	9	8	4	6	6	10	7
28	3	P	953	L	LTM	39	28	0	0	0	0	0	0	0	0	0	0	1	0	0	1	1	4	4	3	3	2
28	4	P	849	L	WDR	54	267	1	2	2	1	1	5	2	3	3	3	14	11	8	4	9	48	53	62	40	41
28	5	P	681	L	WDR	203	397	4	0	3	0	0	8	14	9	5	9	12	7	3	8	4	42	42	44	45	45
28	6	P	799	L	LTM	53	10	0	0	1	0	0	3	0	0	1	0	4	0	1	0	6	8	4	3	3	6
29	1	P	572	L	WDR	26	18	1	2	0	2	0	10	9	6	4	5	21	19	22	18	15	35	36	36	10	27
29	2	P	400	L	WDR	68	147	14	15	12	6	9	18	17	16	9	14	45	31	28	39	16	63	55	44	36	45
29	3	P	792	L	WDR	44	10	2	2	1	1	0	5	1	3	4	2	12	7	6	2	2	23	16	9	15	12
29	4	P	955	L	LTM	56	51	4	3	1	2	1	4	3	3	3	5	6	5	7	5	1	11	4	9	5	5
29	5	P	400	L	LTM	75	27	1	1	0	0	1	1	2	1	1	1	3	2	0	1	2	10	1	1	6	3
29	6	P	522	R	WDR	103	116	2	1	3	1	0	5	2	5	6	5	14	8	7	3	8	33	28	26	37	26
30	1	P	590	R	WDR	39	126	1	3	1	1	1	10	7	3	6	4	10	4	2	9	7	22	19	10	13	15
30	2	P	550	R	LTM	65	58	0	0	0	0	0	12	4	4	1	1	22	10	10	6	7	39	27	30	32	27
30	3	P	552	R	WDR	148	154	5	4	4	6	7	11	18	9	8	9	25	12	8	9	8	44	28	18	23	21
30	4	P	840	L	WDR	23	95	0	0	0	0	0	1	0	0	0	1	3	2	1	1	1	6	0	2	1	1
30	5	P	681	L	WDR	32	15	3	4	1	2	1	3	2	5	2	4	3	1	6	3	5	7	7	3	1	4
30	6	P	571	L	LTM	22	27	0	2	1	1	1	1	5	1	1	0	9	3	3	0	1	15	4	3	5	7
30	*7*	P	697	L	WDR	90	521	1	1	5	3	0	24	15	11	8	5	36	25	19	20	20	60	66	66	58	62
33	1	P	614	R	LTM	89	74	1	2	1	1	1	7	1	4	3	4	5	1	3	2	4	9	11	5	10	3
33	2	P	455	L	WDR	51	464	6	1	1	1	3	17	13	4	9	5	28	24	20	25	21	44	23	25	32	28
33	3	P	420	L	WDR	699	601	0	0	22	21	8	26	31	18	23	14	19	10	15	19	13	28	27	30	22	18
39	1	P	777	R	WDR	21	25	1	0	2	0	1	2	4	0	0	0	11	4	3	5	6	45	25	36	32	25
39	2	P	694	R	WDR	201	451	0	0	0	0	0	3	3	3	2	3	9	5	4	7	11	29	20	19	7	11
39	3	P	627	R	WDR	79	61	3	5	2	1	2	5	5	4	4	4	5	4	7	6	5	19	11	10	10	6
39	4	P	533	R	LTM	280	133	2	6	2	4	4	10	2	2	4	7	30	27	25	33	52	15	20	29	39	40
39	5	P	583	L	WDR	33	37	0	0	0	0	0	0	0	0	0	0	19	30	21	31	27	16	26	22	17	14
39	6	P	692	L	LTM	56	53	0	1	2	0	0	1	1	1	0	1	16	10	6	8	4	18	21	11	10	10
42	1	P	943	R	WDR	56	87	1	1	0	2	0	3	2	0	0	1	17	4	1	0	0	16	9	5	7	7
42	2	P	633	R	LTM	36	25	0	0	0	0	0	1	1	1	0	2	4	6	3	3	1	15	4	6	4	8
42	3	P	631	L	WDR	71	73	0	6	1	2	2	14	10	5	8	9	25	16	19	10	16	37	25	25	24	25
42	4	P	830	L	WDR	83	108	6	3	2	3	5	9	14	4	10	6	28	4	14	11	10	35	22	21	15	13

APPENDIX C

Summary of information for human facet capsular ligament samples

This appendix details the specimen donor information for the human cadaver tissue samples used in this thesis. For all studies, facet joints were removed from fresh, unembalmed human cervical spines. In the study described in Chapter 5, 16 right and left C4/C5 facet joints were removed from 11 separate cervical spine specimens. In those studies, the posterior half of the lateral aspect of the capsular ligament was isolated for testing as described in Section 5.3.2 of Chapter 5; the cross sectional area of each tissue specimen was determined from digital caliper measurements of the width and thickness of the tissue. The donor information, as well as the cross-sectional area (CSA), are summarized in Table C.1 for all specimens tested in the study described in Chapter 5.

In Chapter 7, eight isolated C6/C7 facet joints underwent subfailure tensile loading and a facet joint retraction. Facet joints used in Section 7.3 of Chapter 7 contain specimens from a subset of the 11 donor spines dissected for studies in Chapter 5. In these retraction studies (Section 7.3), the entire facet capsular ligament was left intact, so no meaningful geometric measurements were made.

Table C.2 details the donor information for the specimens used in the study described in Section 7.3.

Table C.1. Isolated facet capsular ligaments used in Chapter 5.

Specimen	Donor ID	Level	Side	Sex	Age (years)	CSA (mm^2)
1	C390	C4/C5	L	F	74	3.15
2	C457	C4/C5	R	F	39	5.08
3	C846	C4/C5	L	M	64	3.75
4	C846	C4/C5	R	M	64	2.54
5	C947	C4/C5	R	M	66	2.52
6	C500	C4/C5	L	M	63	5.32
7	C500	C4/C5	R	M	63	4.62
8	C457	C4/C5	L	F	39	5.66
9	C611	C4/C5	L	M	79	2.99
10	C277	C4/C5	R	M	49	3.77
11	C536	C4/C5	L	M	54	3.78
12	C446	C4/C5	L	M	47	2.71
13	C588	C4/C5	R	M	44	3.43
14	C012	C4/C5	R	M	75	3.72
15	C536	C4/C5	R	M	54	2.60
16	C588	C4/C5	L	M	44	2.81
Mean					**57**	**3.65**
SD					**13**	**1.03**

Table C.2. Isolated facet capsular ligaments used in Section 7.3.

Specimen	Donor ID	Level	Side	Sex	Age (years)
17	C012	C6/C7	L	M	75
18	C536	C6/C7	L	M	54
19	C536	C6/C7	R	M	54
20	C446	C6/C7	R	M	47
21	C277	C6/C7	R	M	49
22	C277	C6/C7	L	M	49
23	C446	C6/C7	L	M	47
24	C846	C6/C7	L	M	64
Mean					**55**
SD					**10**

APPENDIX D

Force-displacement responses of human facet capsular ligament under tensile loading

This appendix details the force-displacement curves of the facet capsular ligament specimens during tensile loading from the studies in Chapter 5. Ligament tissue from the posterior half of the lateral aspect of the capsular ligament was isolated and loaded in tension until complete rupture. The first detection of yield, partial failure, and gross failure are indicated in each plot. Partial failure was not detected prior to gross failure in Specimens #6, 10, 12, and 15. The initial detection of anomalous fiber realignment is also indicated in each plot, and the force and displacement at this point are specified on each plot. Anomalous fiber realignment was not detected in Specimen #10. The corresponding maps of anomalous fiber realignment for each specimen are summarized in Appendix E. Additionally, principal strain fields at the detection of anomalous realignment and gross failure are detailed in Appendix F. The methods for the detection of these mechanical phenomena are described in detail in Chapter 5 and the Matlab code for the detection of yield and failure from these data are provided in Appendix O.

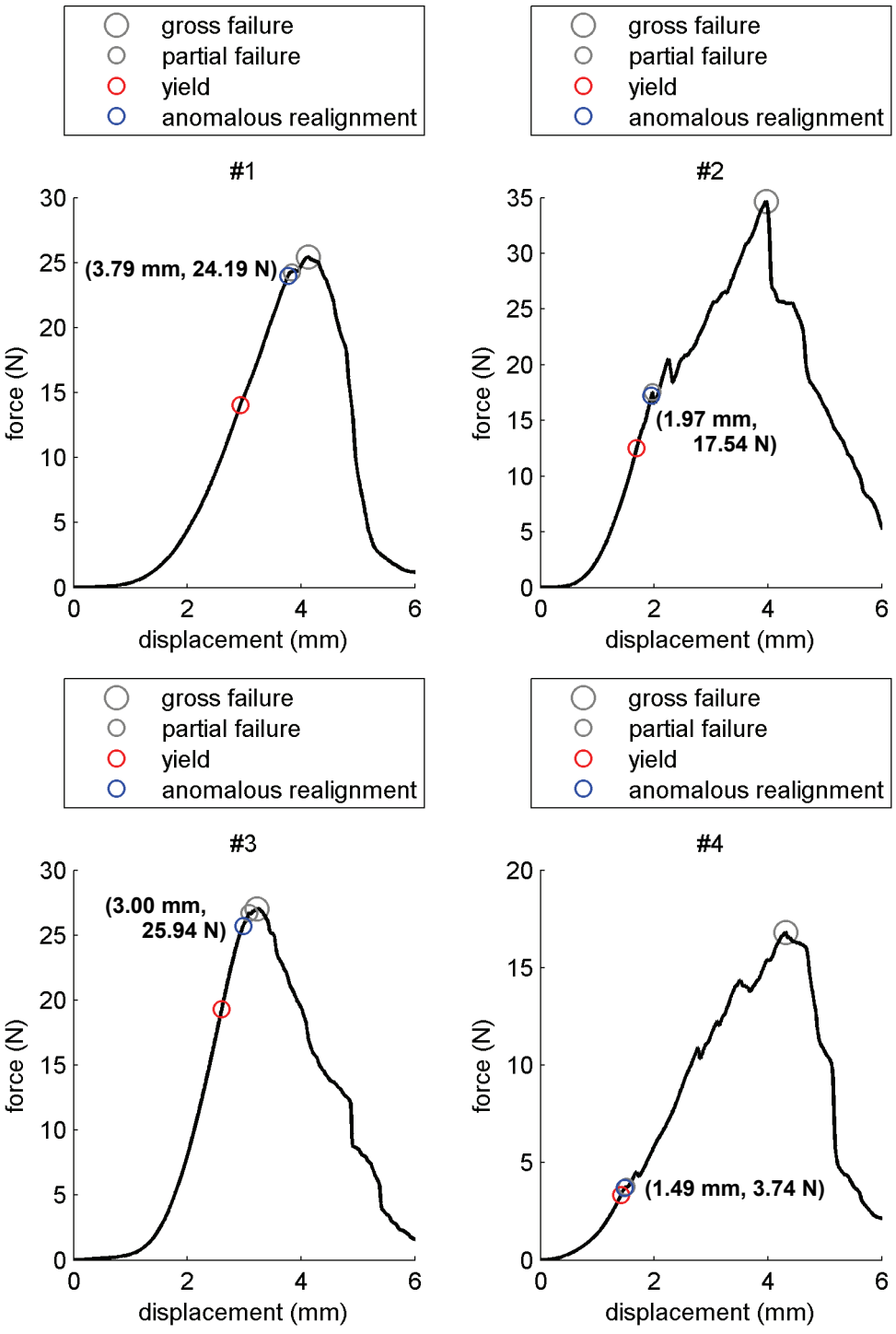
gross failure
partial failure
yield
anomalous realignment
#1
(3.79 mm, 24.19 N)
force (N)
displacement (mm)
#2
(1.97 mm,
17.54 N)
#3
(3.00 mm,
25.94 N)
#4
(1.49 mm, 3.74 N)

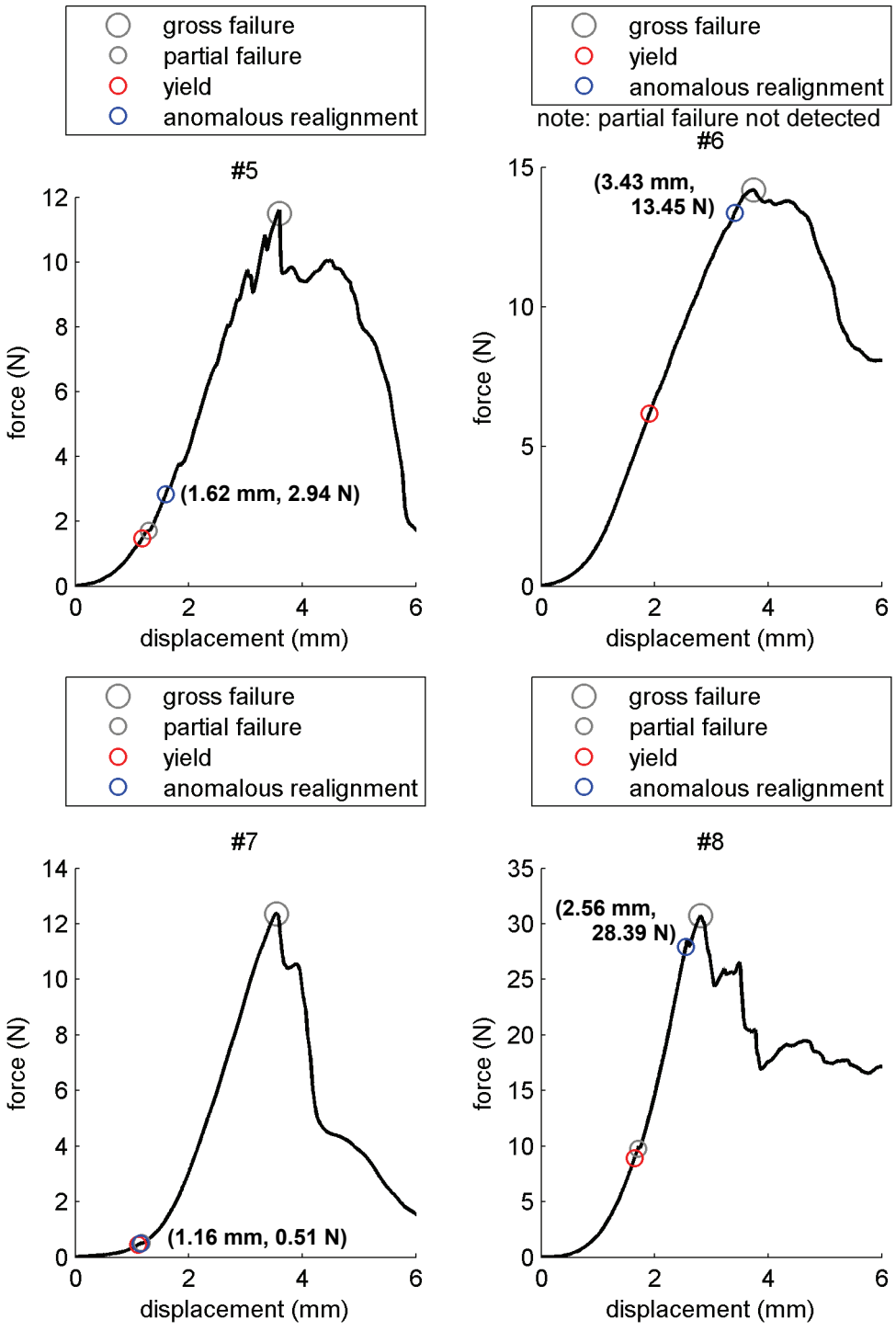
gross failure
partial failure
yield
anomalous realignment
#5
force (N)
displacement (mm)
(1.62 mm, 2.94 N)
gross failure
yield
anomalous realignment
note: partial failure not detected
#6
(3.43 mm, 13.45 N)
force (N)
displacement (mm)
gross failure
partial failure
yield
anomalous realignment
#7
force (N)
displacement (mm)
(1.16 mm, 0.51 N)
gross failure
partial failure
yield
anomalous realignment
#8
(2.56 mm, 28.39 N)
force (N)
displacement (mm)

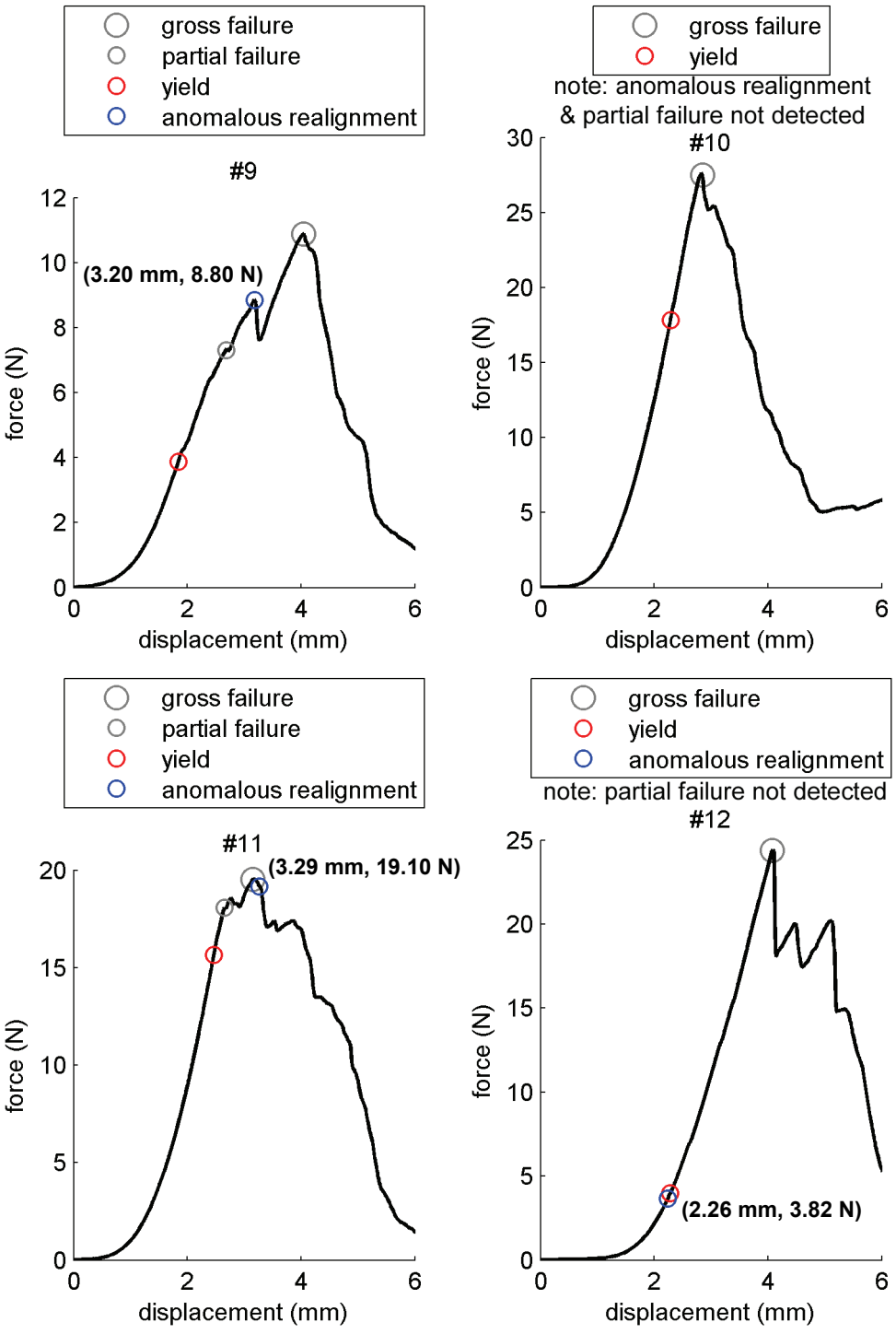
gross failure
partial failure
yield
anomalous realignment
#9
(3.20 mm, 8.80 N)
force (N)
displacement (mm)
gross failure
yield
note: anomalous realignment
& partial failure not detected
#10
force (N)
displacement (mm)
gross failure
partial failure
yield
anomalous realignment
#11
(3.29 mm, 19.10 N)
force (N)
displacement (mm)
gross failure
yield
anomalous realignment
note: partial failure not detected
#12
(2.26 mm, 3.82 N)
force (N)
displacement (mm)

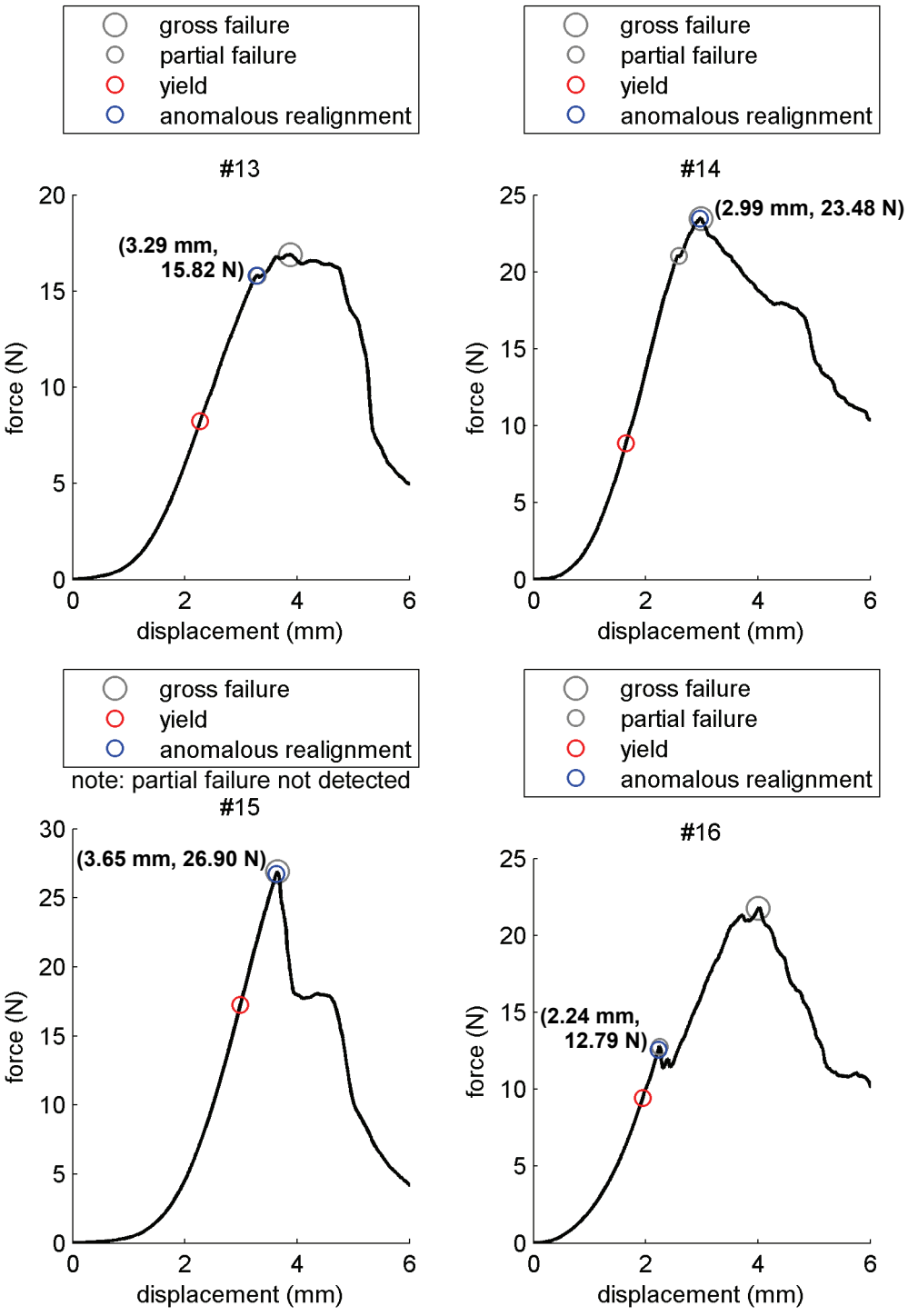
gross failure
partial failure
yield
anomalous realignment
#13
(3.29 mm, 15.82 N)
force (N)
displacement (mm)
gross failure
partial failure
yield
anomalous realignment
#14
(2.99 mm, 23.48 N)
force (N)
displacement (mm)
gross failure
yield
anomalous realignment
note: partial failure not detected
#15
(3.65 mm, 26.90 N)
force (N)
displacement (mm)
gross failure
partial failure
yield
anomalous realignment
#16
(2.24 mm, 12.79 N)
force (N)
displacement (mm)

APPENDIX E

Anomalous realignment maps of human facet capsular ligament

This appendix presents the individual maps of the initial detection of anomalous fiber realignment during tensile loading of human facet capsular ligament tissue described in Chapter 5. This detection point is labeled on the corresponding force-displacement curves in Appendix D. Specific details regarding the mechanical conditions at the initial detection of anomalous realignment and the number of pixels detected with anomalous realignment are summarized in Tables 5.1 and 5.3, respectively. In each map here, the pixels having a sufficient signal-to-noise ratio for an assessment of fiber realignment have been indicated by color and those pixels with an insufficient signal remain in grayscale. The location(s) of anomalous fiber realignment are highlighted in red and the pixels with normal fiber realignment are highlighted in green. The element mesh used in strain analysis is also plotted over the surface using white gridlines. Strain fields for each of these specimens at the corresponding initial detection of anomalous realignment are provided in Appendix F. The Matlab code that was

developed for the detection of anomalous fiber realignment is provided in Appendix M.

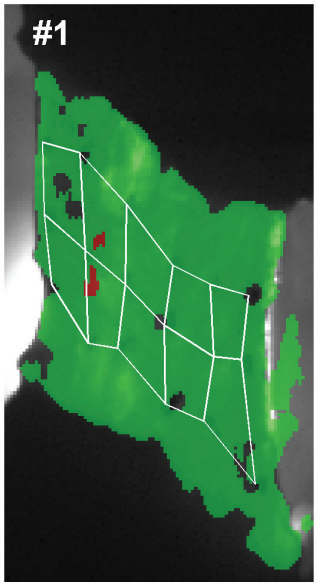

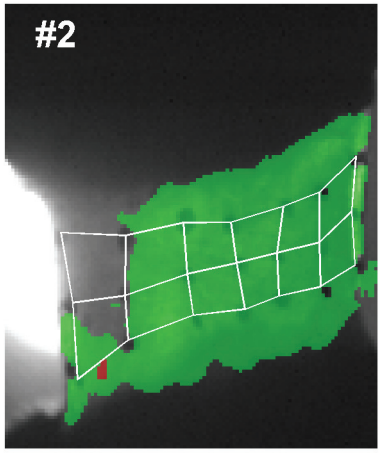

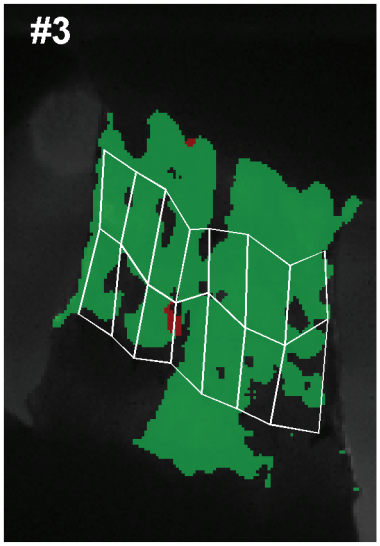

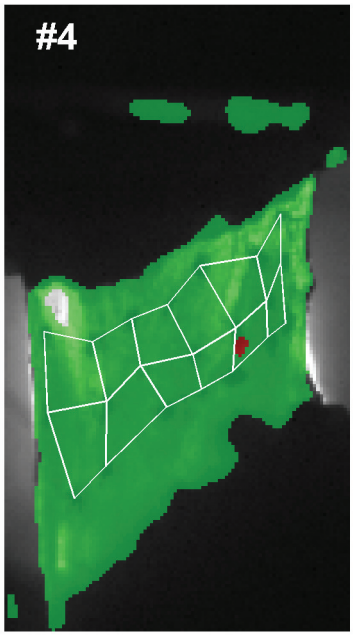

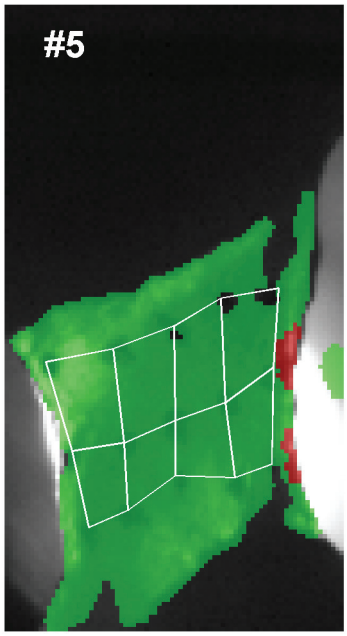
#5

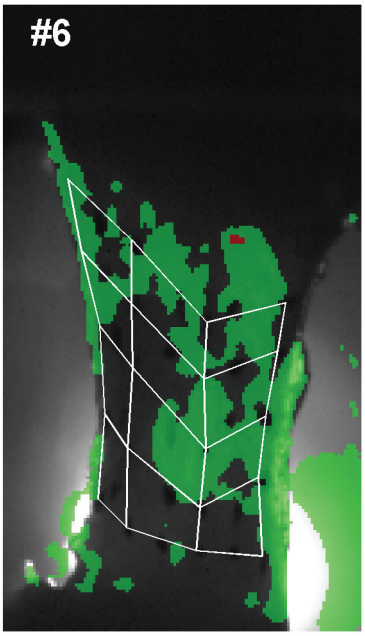
#6

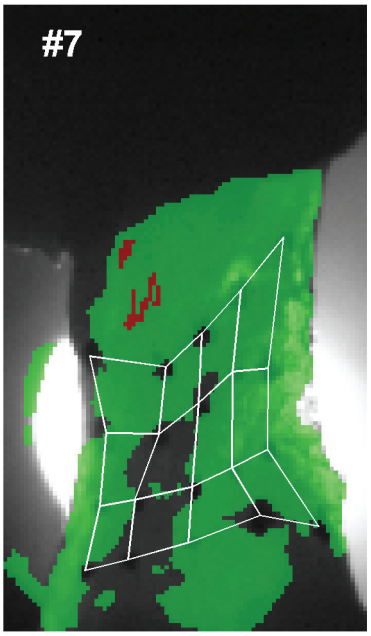
#7

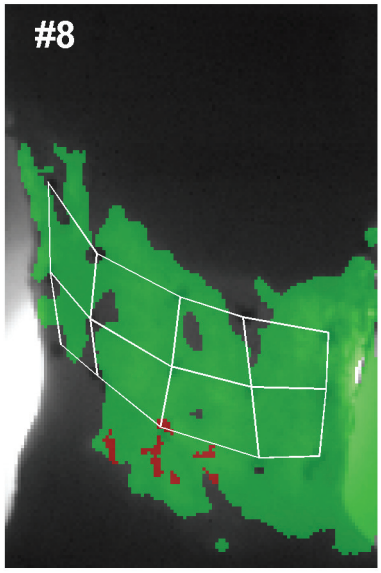
#8

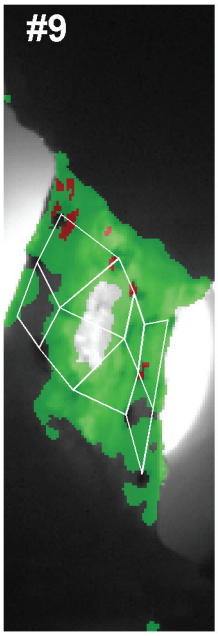
#9

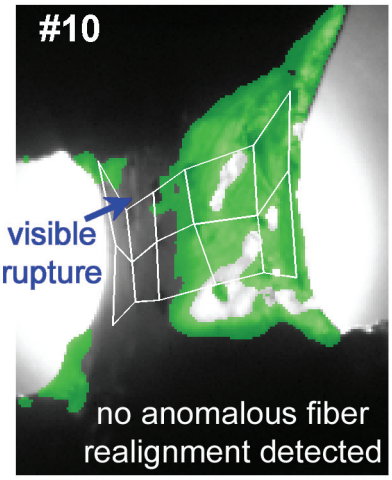
#10
visible
rupture
no anomalous fiber
realignment detected

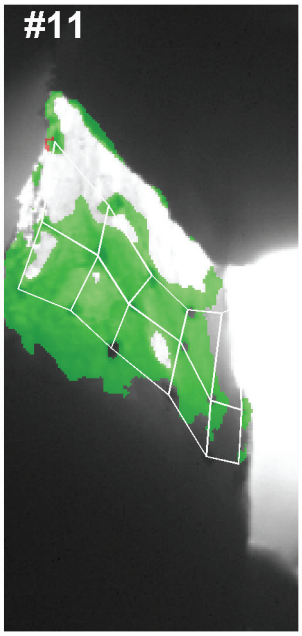
#11

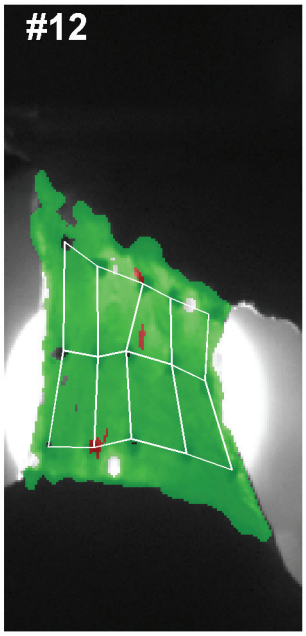
#12

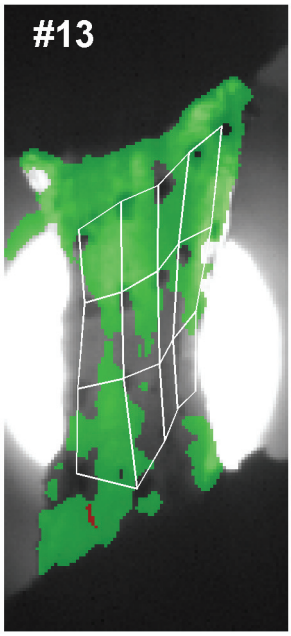
#13

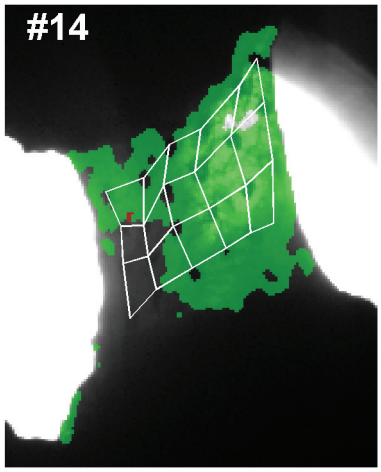
#14

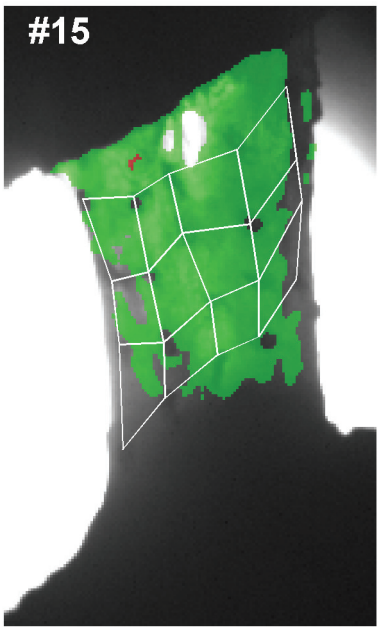
#15

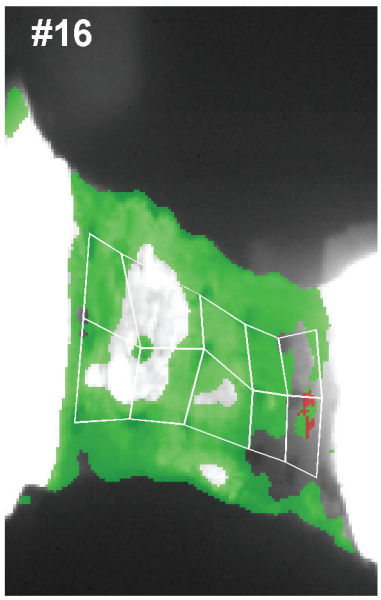
#16

APPENDIX F

Strain fields at initial anomalous realignment & gross failure for human facet capsular ligament

This appendix summarizes the individual principal strain fields produced by tracking fiduciary markers on the surface of human facet capsular ligament tissue, as described in Chapter 5. For more details regarding the mechanical conditions at the initial detection of anomalous realignment or gross failure, please find Table 5.1 in Chapter 5. Matlab code that was used to calculate Lagrangian strain in the elements based on plane strain theory can be found in Appendix N.

In this appendix, there are two subsections. Strain field maps are provided for each specimen at both the initial detection of anomalous fiber realignment (F.1) and at gross failure of the ligament (F.2). For each strain field, the element in which the maximum ε_1 was measured is indicated by a white circle.

F.1. Full field ε_1 at initial detection of anomalous fiber realignment

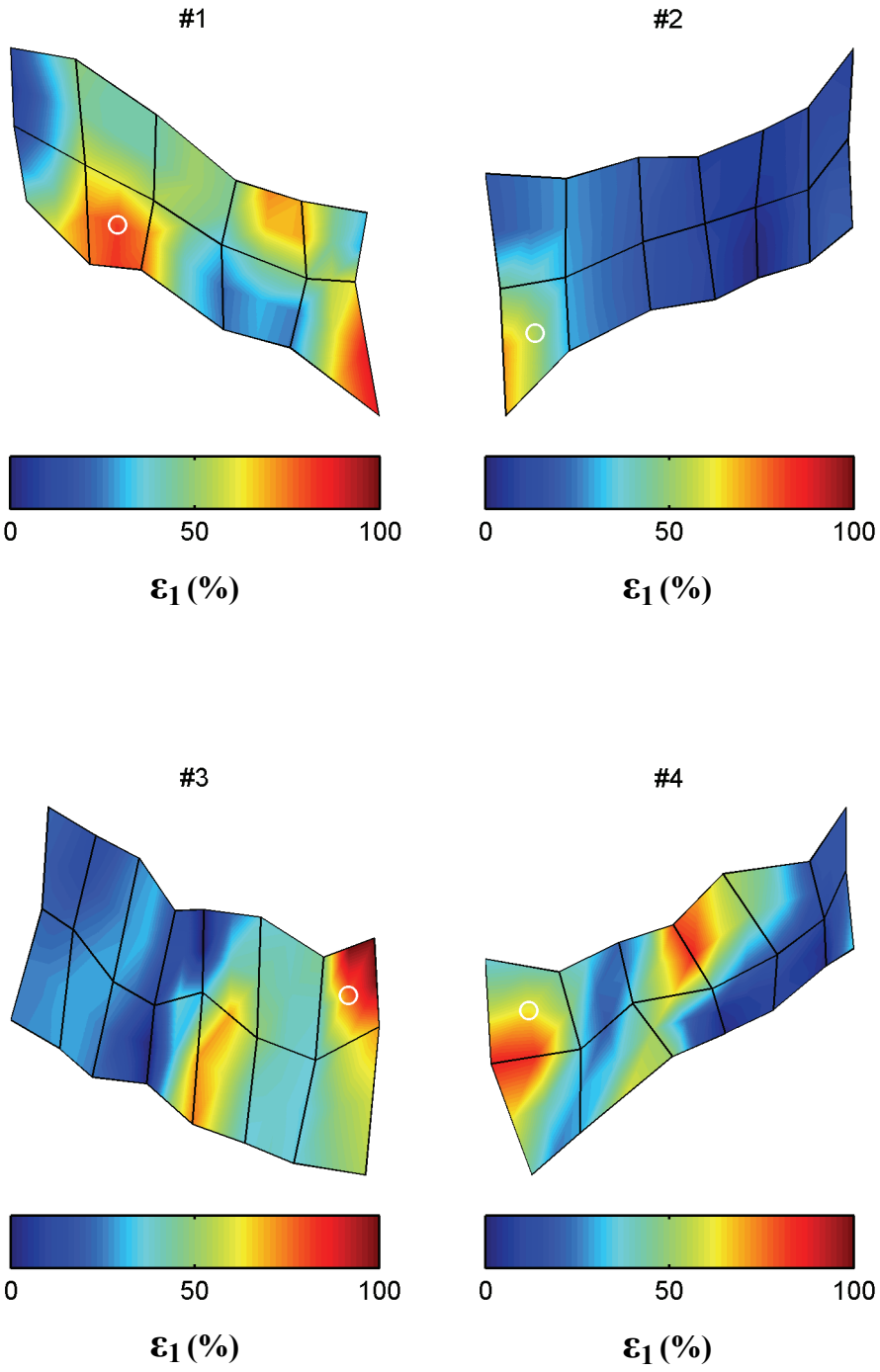

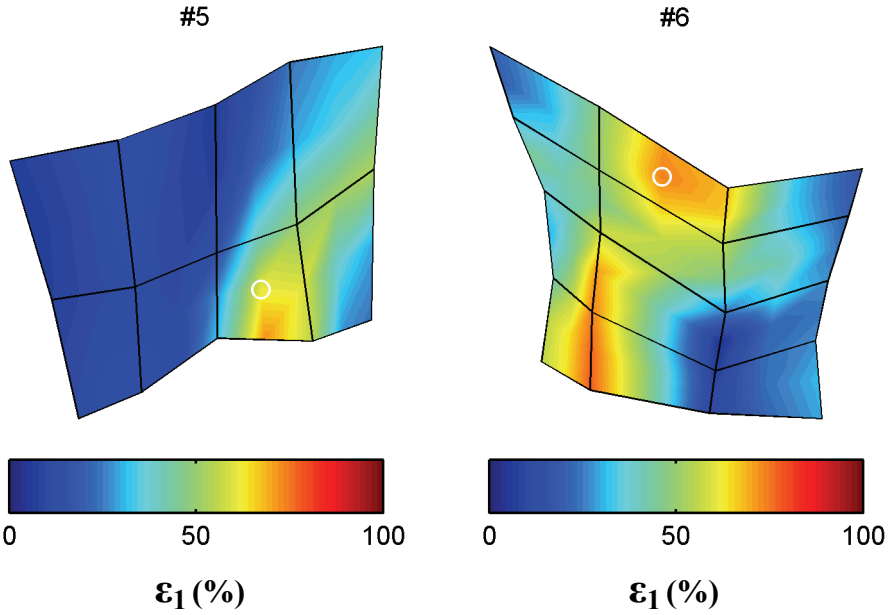
#5
#6
0
50
100
ε_1 (%)
0
50
100
ε_1 (%)

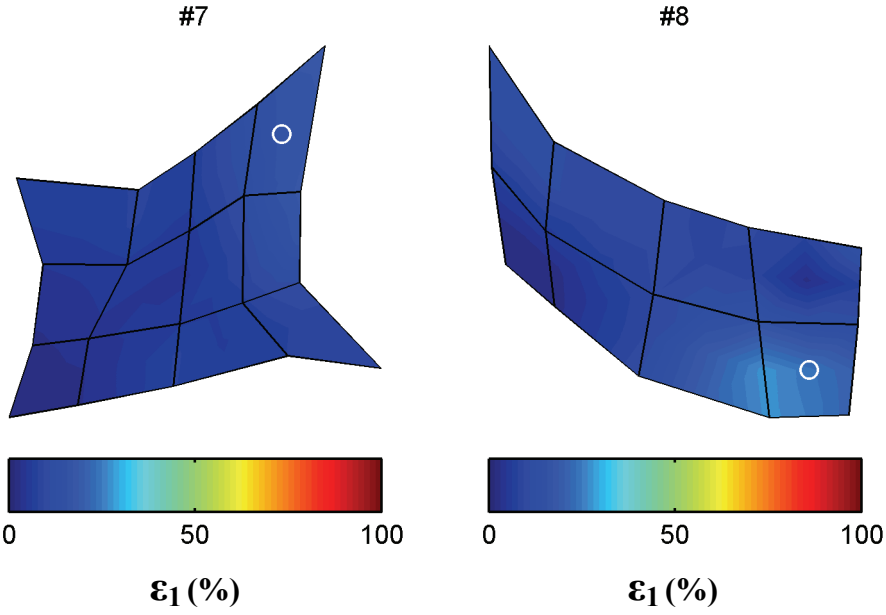
#7
#8
0
50
100
ε_1 (%)
0
50
100
ε_1 (%)

#9

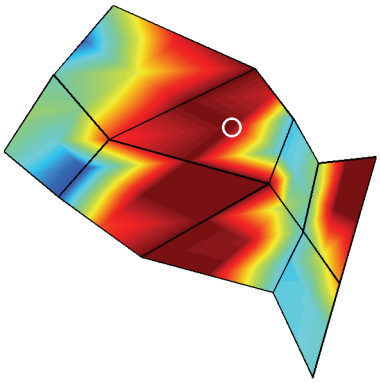

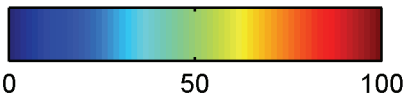

ε_1 (%)

#10

No anomalous fiber realignment detected in this specimen

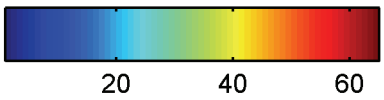

ε_1 (%)

#11

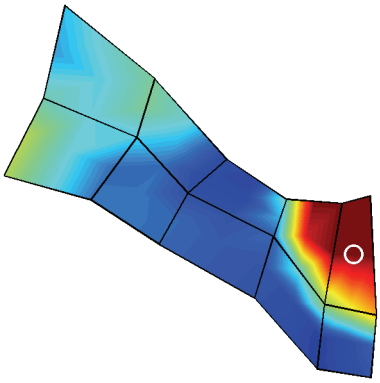

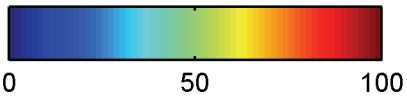

ε_1 (%)

#12

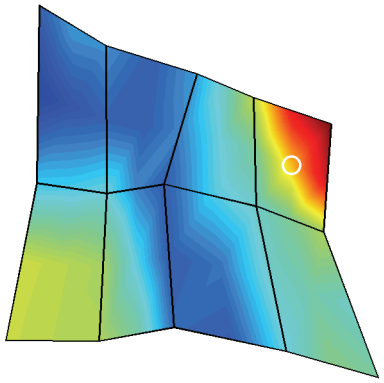

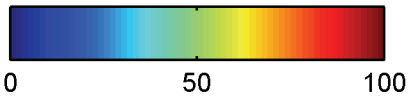

ε_1 (%)

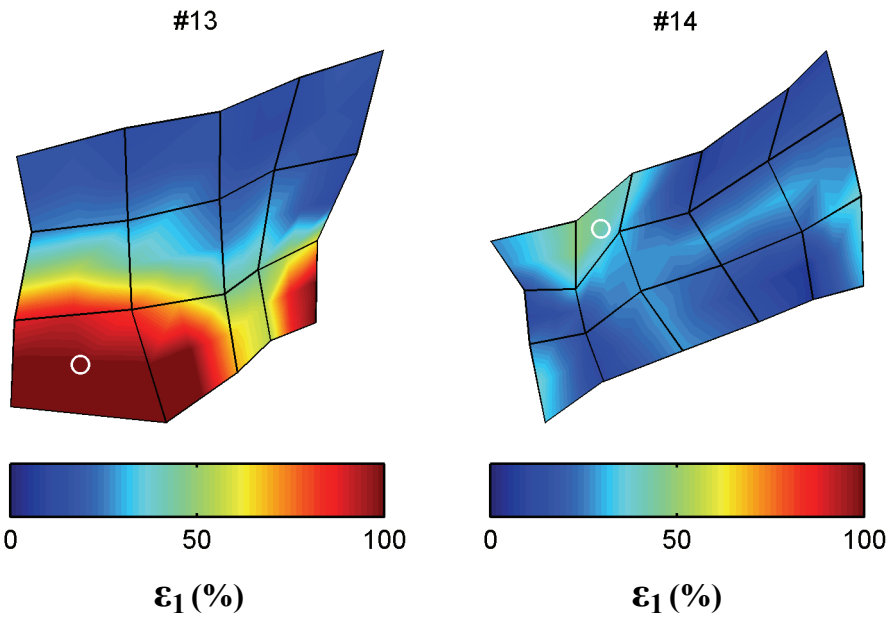
#13
#14
0
50
100
ε_1 (%)
0
50
100
ε_1 (%)

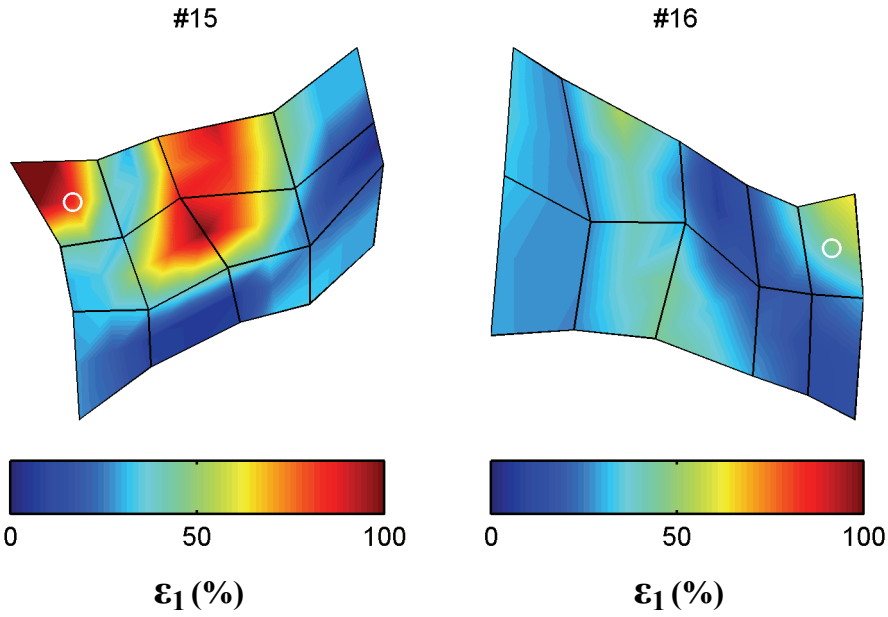
#15
#16
0
50
100
ε_1 (%)
0
50
100
ε_1 (%)

F.2. Full field ε_1 at gross failure

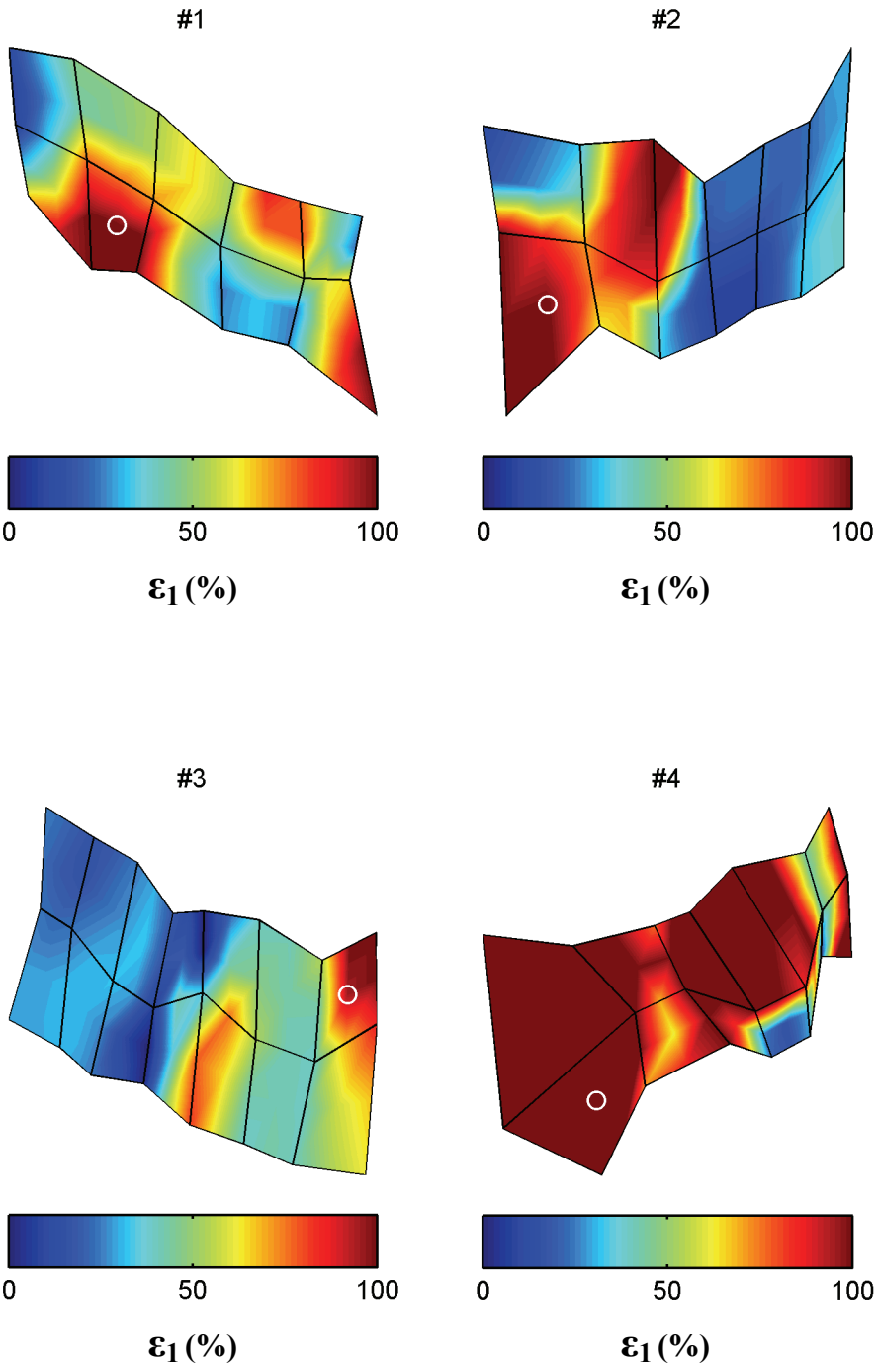

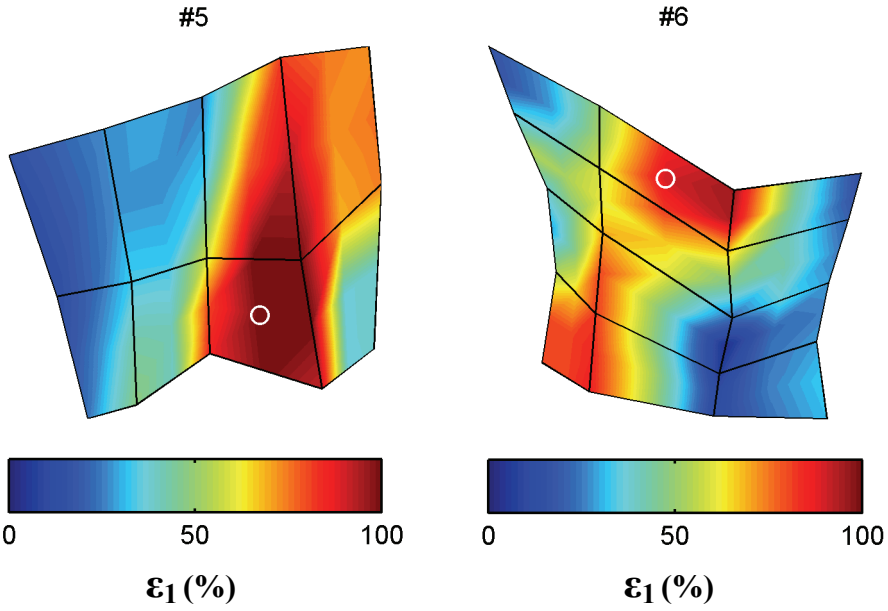
#5
#6
0
50
100
ε_1 (%)
0
50
100
ε_1 (%)

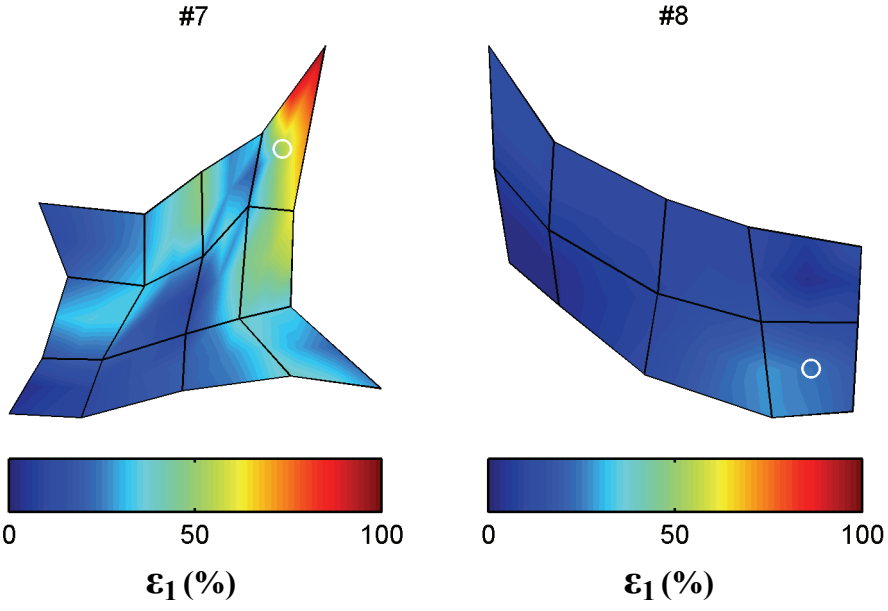
#7
#8
0
50
100
ε_1 (%)
0
50
100
ε_1 (%)

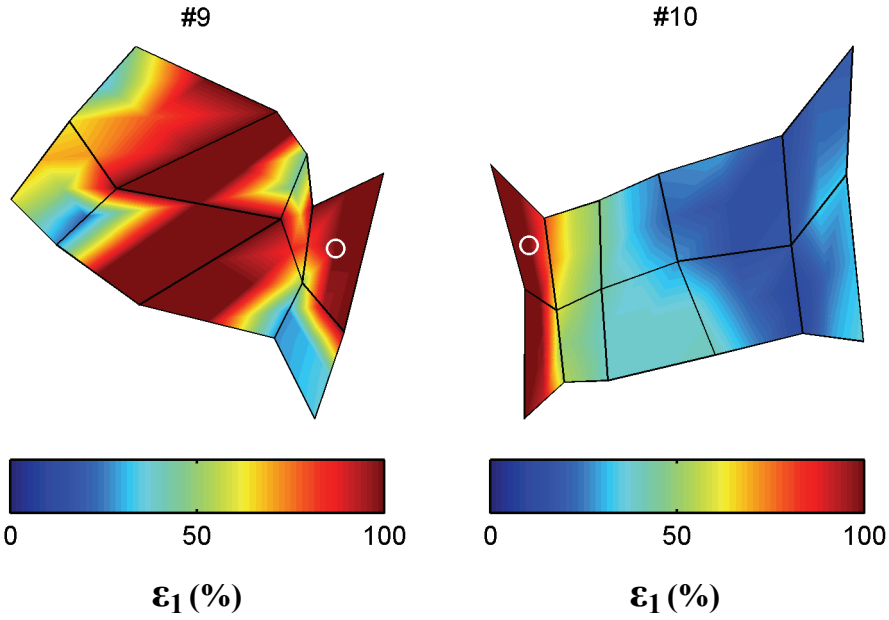
#9
#10
0
50
100
ε_1 (%)
0
50
100
ε_1 (%)

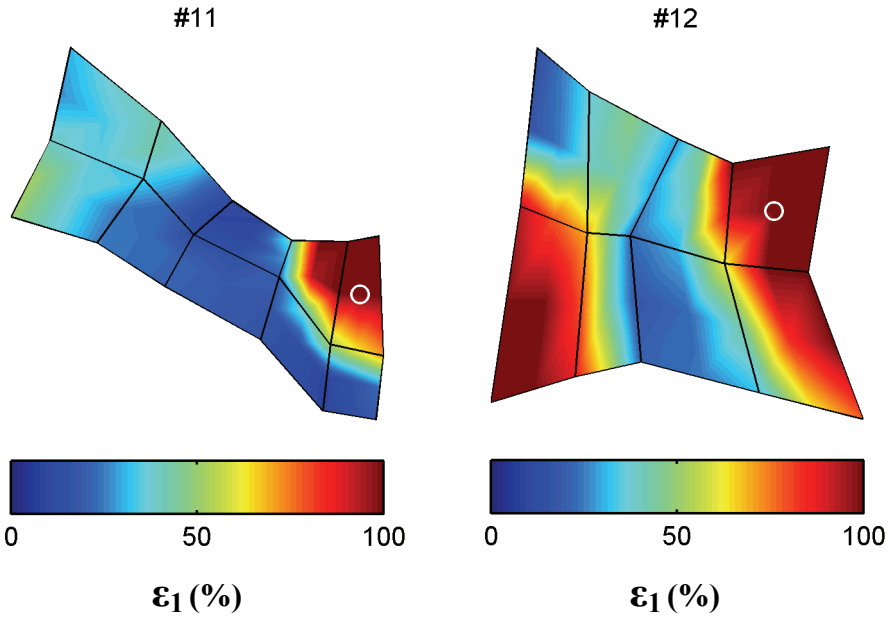
#11
#12
0
50
100
ε_1 (%)
0
50
100
ε_1 (%)

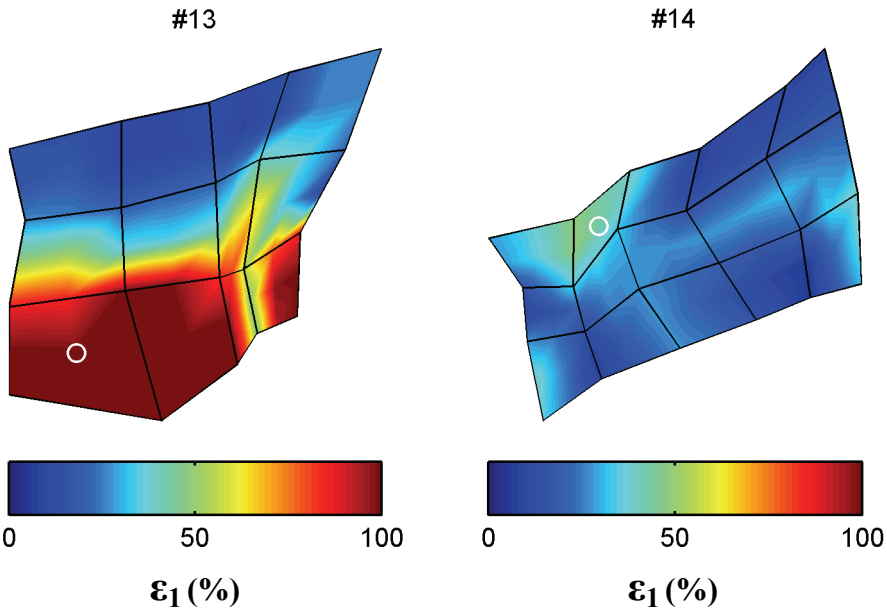
#13
#14
0
50
100
ε_1 (%)
0
50
100
ε_1 (%)

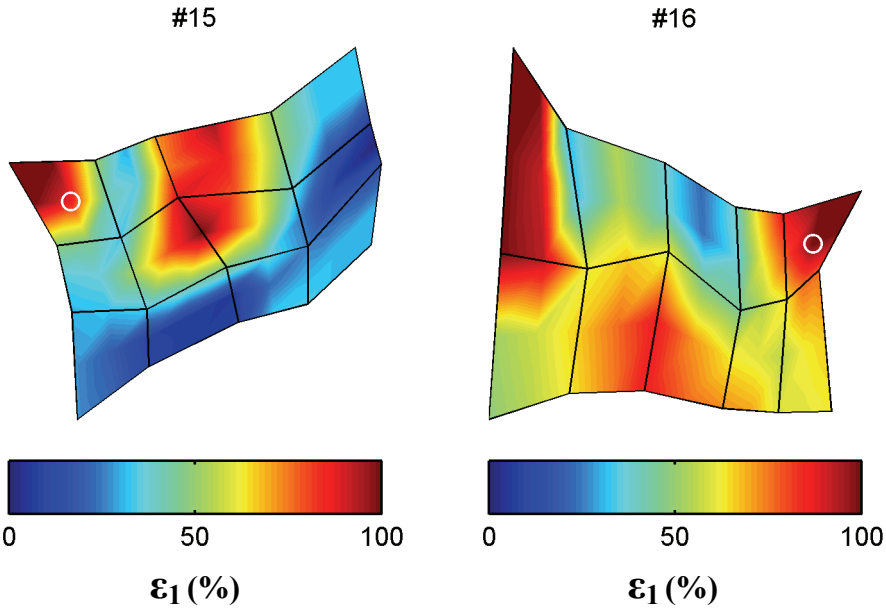
#15
#16
0
50
100
ε_1 (%)
0
50
100
ε_1 (%)

APPENDIX G

Force-displacement responses & vector correlation maps for the rat facet joint

This appendix provides the force-displacement curves of isolated C6/C7 rat facet joints and the spatial map of the change in vector correlation for each specimen at the first detection of anomalous realignment. These data summarize individual specimens for studies described in Chapter 6.

The force-displacement plots for each specimen are detailed in Section G.1. The C6 articular facet was displaced at a rate of 0.08 mm/s to apply tension across the C6/C7 facet capsule as C7 remained fixed. The occurrences of ligament yield or partial failure were evaluated during loading up to gross failure and are indicated in the force-displacement plots (gray circle). Anomalous fiber realignment was also assessed from the collagen fiber alignment maps acquired during loading; each detection of anomalous realignment is labeled in the plots (black circle), with the corresponding force and displacement points specified on each plot.

In Section G.2, the maps of the change in vector correlation corresponding to the first detection of anomalous realignment are summarized. The location where anomalous realignment was detected is indicated by an arrow in each map. Anomalous fiber realignment was identified at any pixel with a signal-to-noise ratio exceeding 2 and a change in vector correlation of less than or equal -0.35. If

regions of 9 or more connected pixels met the signal-to-noise and vector correlation criteria, anomalous realignment was detected.

G.1. Force-displacement responses

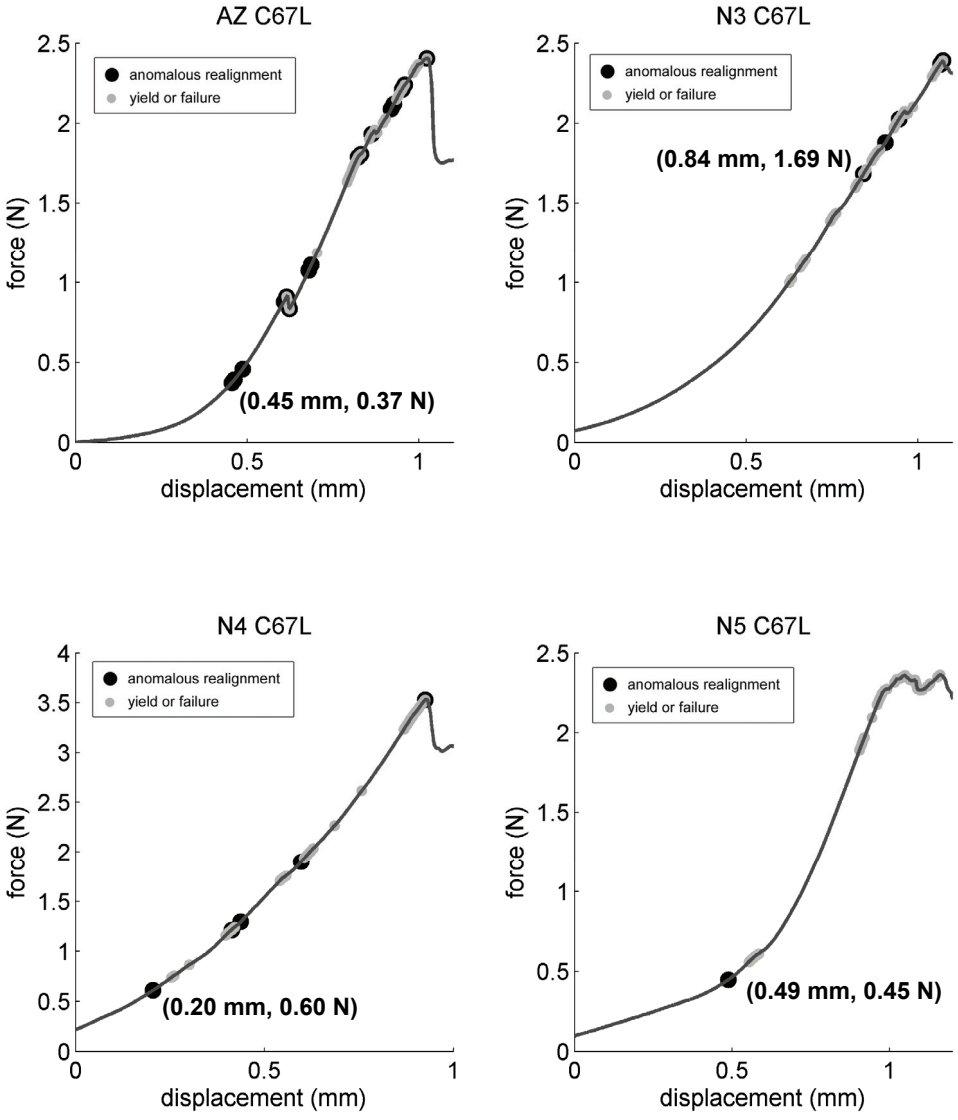

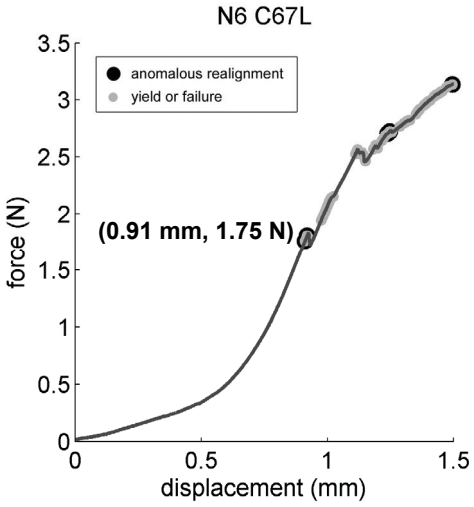
N6 C67L
anomalous realignment
yield or failure
(0.91 mm, 1.75 N)
force (N)
displacement (mm)
0
0.5
1
1.5
2
2.5
3
3.5

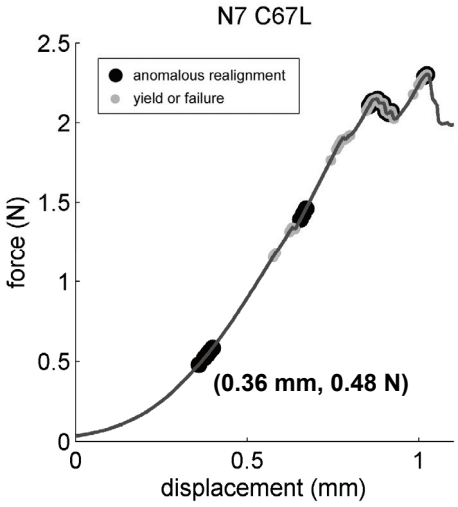
N7 C67L
anomalous realignment
yield or failure
(0.36 mm, 0.48 N)
force (N)
displacement (mm)
0
0.5
1
1.5
2
2.5

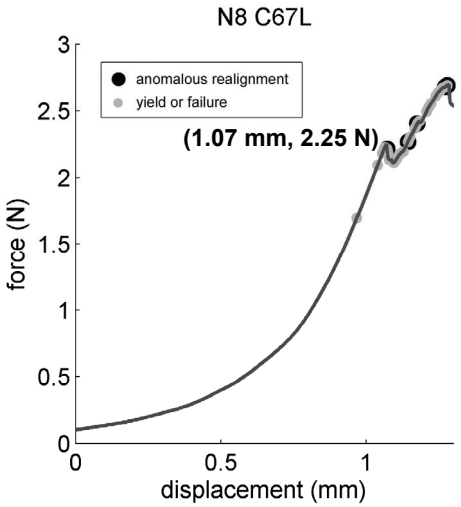
N8 C67L
anomalous realignment
yield or failure
(1.07 mm, 2.25 N)
force (N)
displacement (mm)
0
0.5
1
1.5
2
2.5
3

G.2. Maps of the change in vector correlation

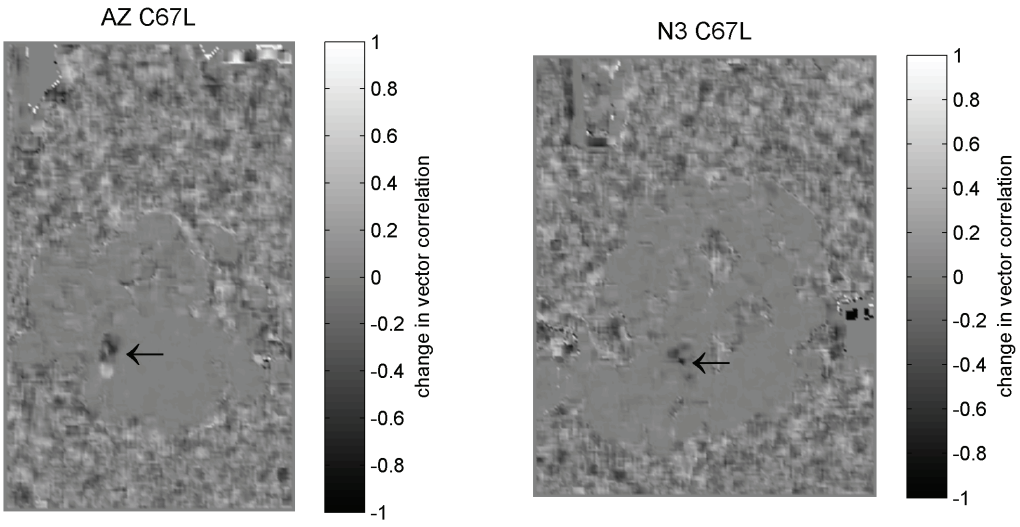

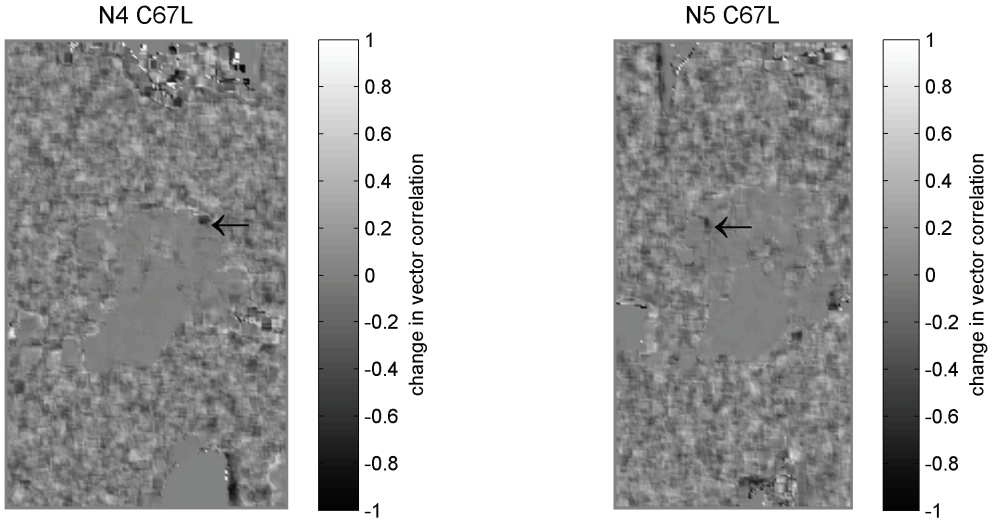

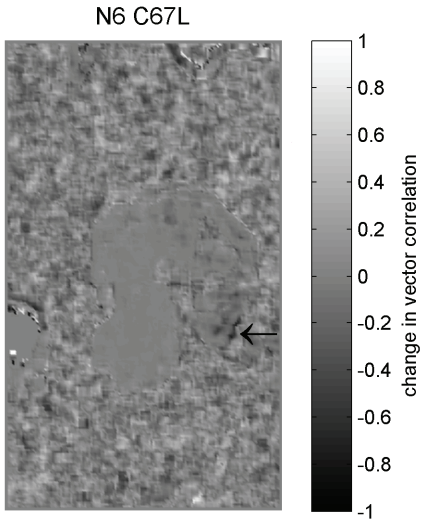
N6 C67L
1
0.8
0.6
0.4
0.2
0
-0.2
-0.4
-0.6
-0.8
-1
change in vector correlation

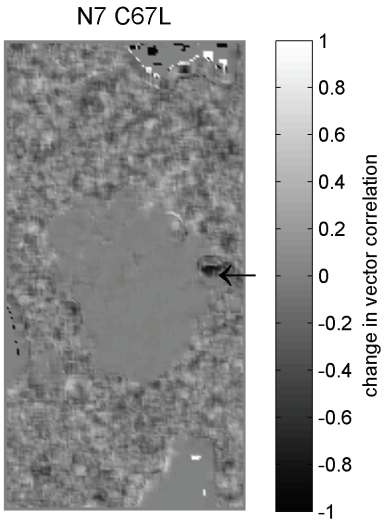
N7 C67L
1
0.8
0.6
0.4
0.2
0
-0.2
-0.4
-0.6
-0.8
-1
change in vector correlation

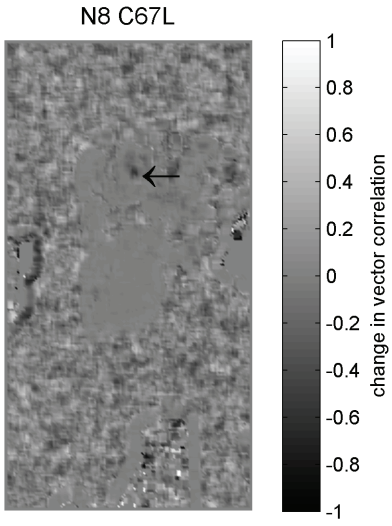
N8 C67L
1
0.8
0.6
0.4
0.2
0
-0.2
-0.4
-0.6
-0.8
-1
change in vector correlation

APPENDIX H

Force-displacement responses of human facet capsular ligaments to retraction & cyclic tensile loading

This appendix details the force-displacement responses of the isolated C6/C7 human facet joints from studies in Chapter 7. Each specimen underwent a 2.5 mm retraction of the C6 vertebra at 0.4 mm/s. These plots are summarized below in Section H.1. In addition, both before and after retraction, specimens also underwent 30 cycles of tensile loading between 0 and 1 mm at 0.4 mm/s. These plots are summarized in Section H.2. For each plot, the tensile cyclic loading response before retraction (black lines) and after retraction (gray lines) are superimposed.

H.1. Force-displacement plots of retraction

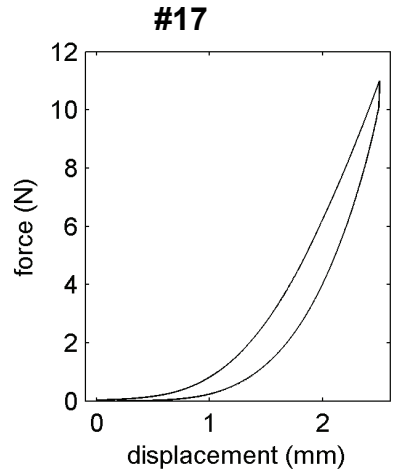

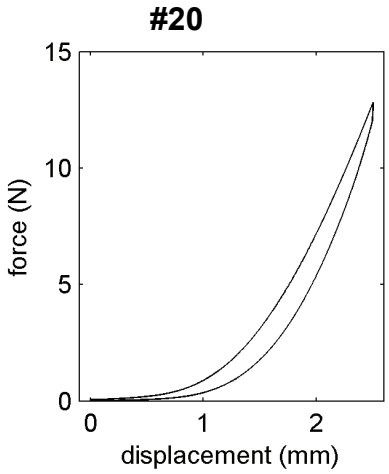

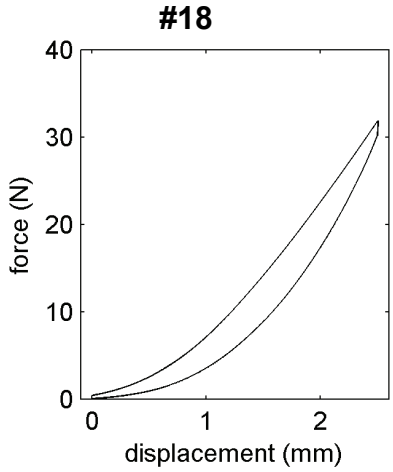

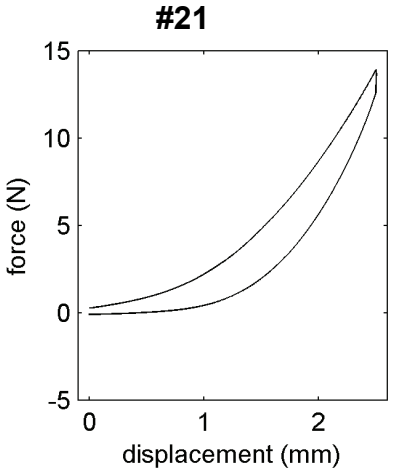

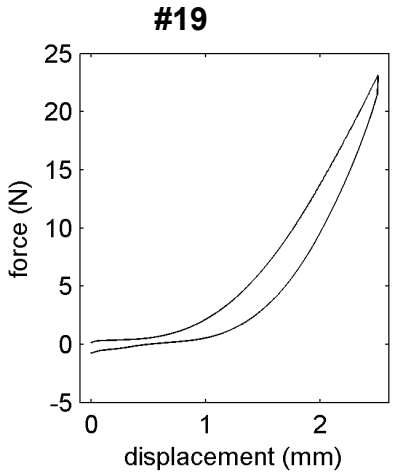

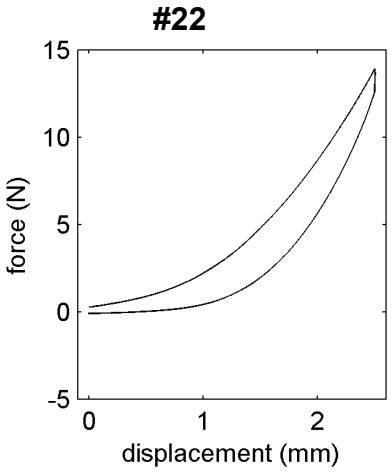

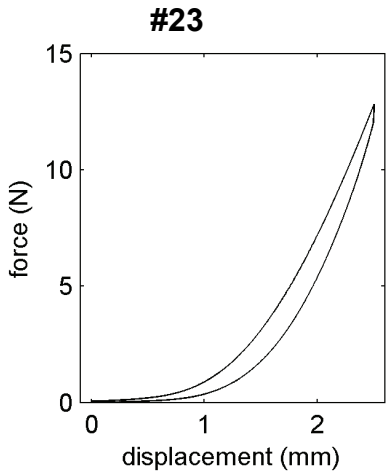

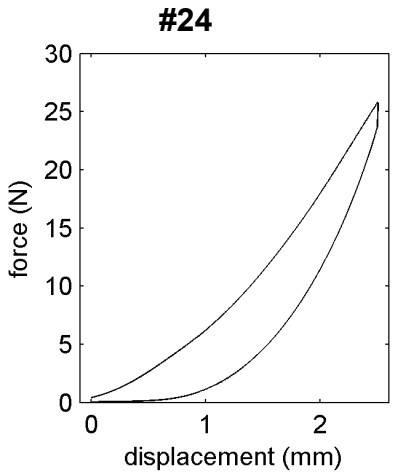

H.2. Force-displacement plots of cyclic tensile loading

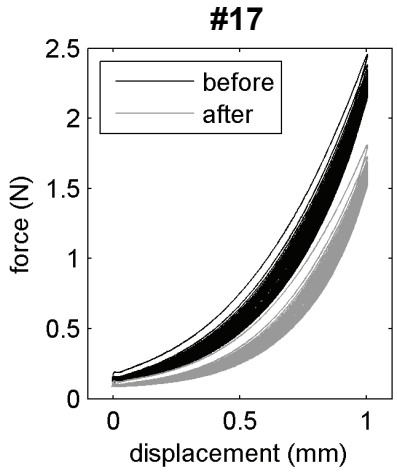

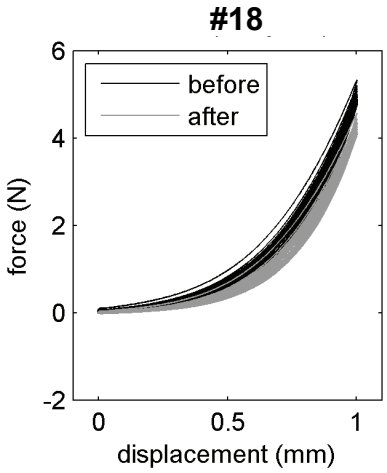

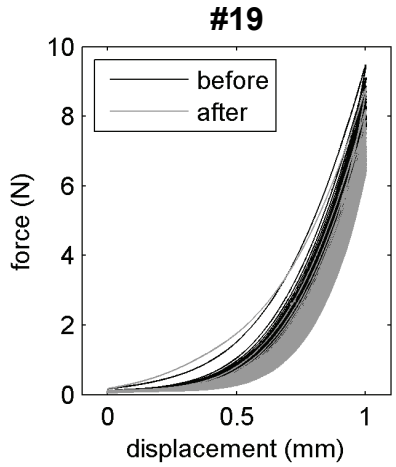
#19
before
after
force (N)
displacement (mm)
0
2
4
6
8
10
0
0.5
1

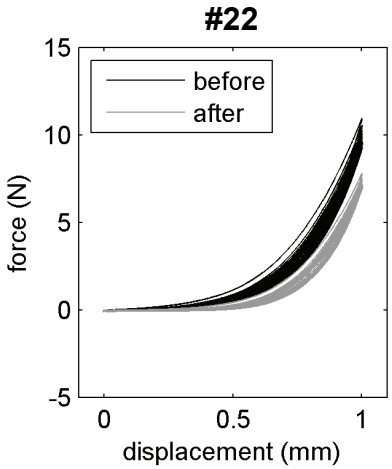
#22
before
after
force (N)
displacement (mm)
-5
0
5
10
15
0
0.5
1

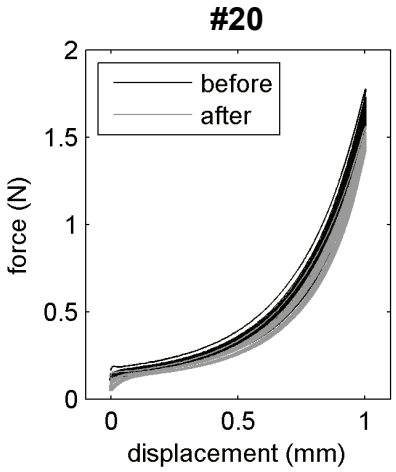
#20
before
after
force (N)
displacement (mm)
0
0.5
1
1.5
2
0
0.5
1

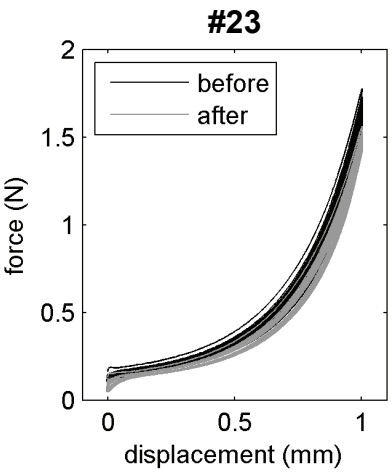
#23
before
after
force (N)
displacement (mm)
0
0.5
1
1.5
2
0
0.5
1

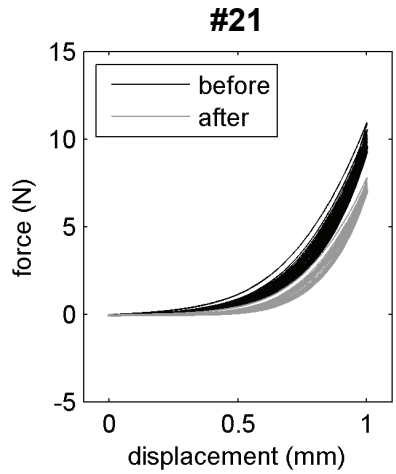
#21
before
after
force (N)
displacement (mm)
-5
0
5
10
15
0
0.5
1

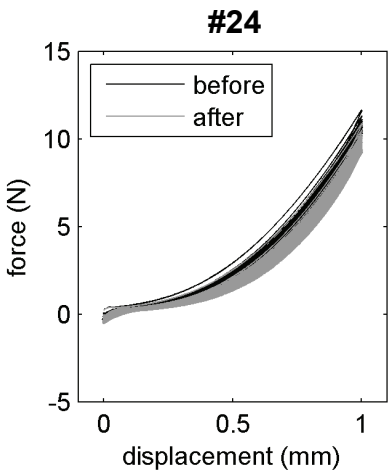
#24
before
after
force (N)
displacement (mm)
-5
0
5
10
15
0
0.5
1

APPENDIX I

Strain fields at peak retraction

This appendix summarizes the strain fields of the isolated C6/C7 human facet joints measured at 2.5 mm of retraction as described in Chapter 7. Strain fields were determined by a vector correlation tracking algorithm described in Section 7.2 using Matlab code (see Appendices P and Q). The maximum and average strain values from each of these fields are listed in Table 7.1. For each specimen, the ε_1 (top image) and γ_{max} (bottom image) fields are shown. For each specimen, the location of the maximum value within the strain field is indicated by a white circle.

#17

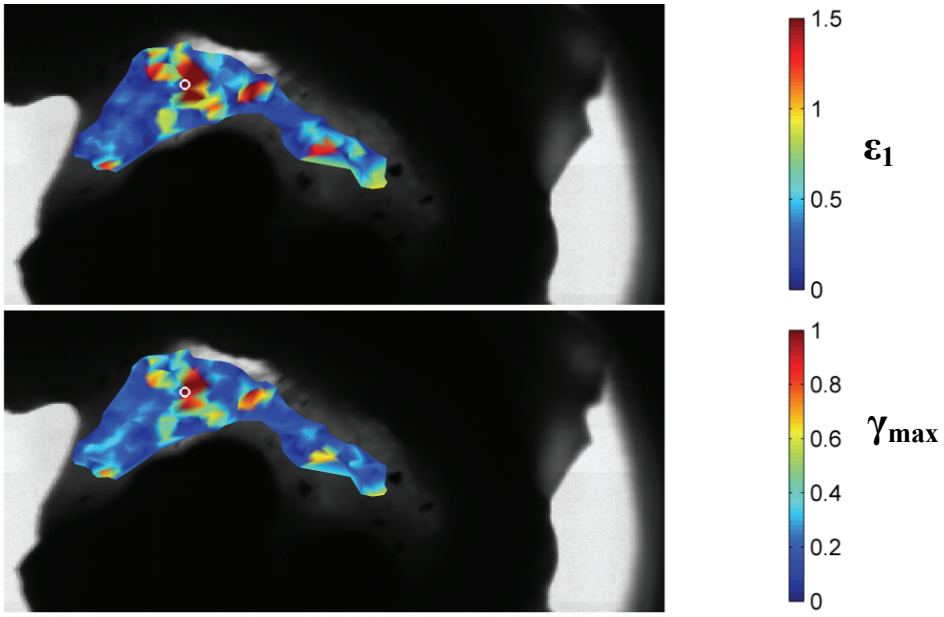
1.5
1
0.5
0
ε_1
1
0.8
0.6
0.4
0.2
0
γ_{max}

#18

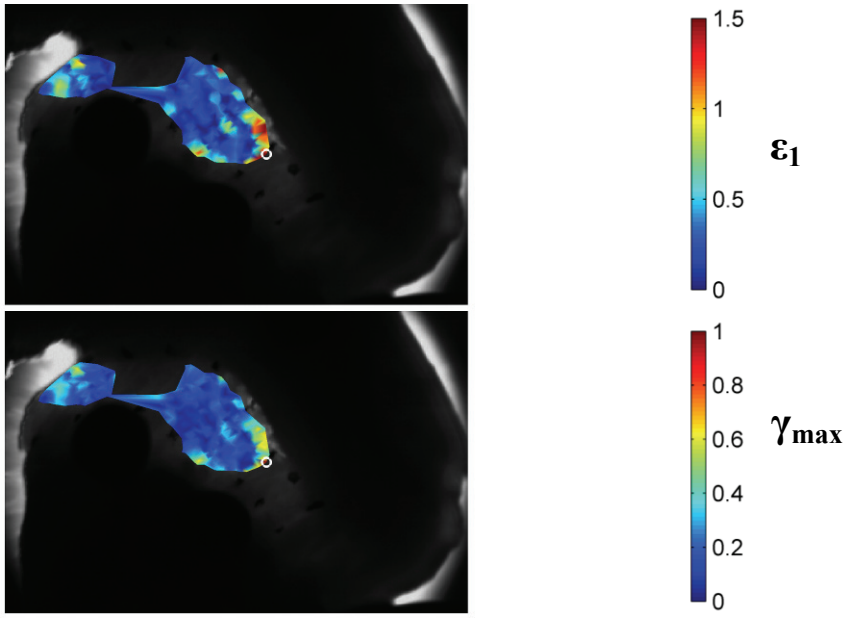
1.5
1
0.5
0
ε_1
1
0.8
0.6
0.4
0.2
0
γ_{max}

#19

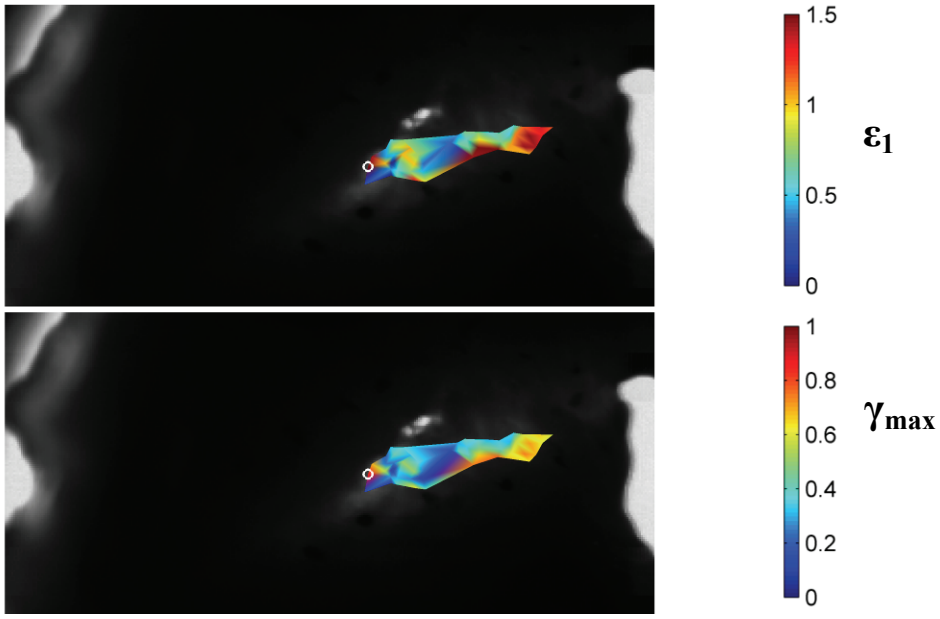
1.5
1
0.5
0
ε_1
1
0.8
0.6
0.4
0.2
0
γ_{max}

#20

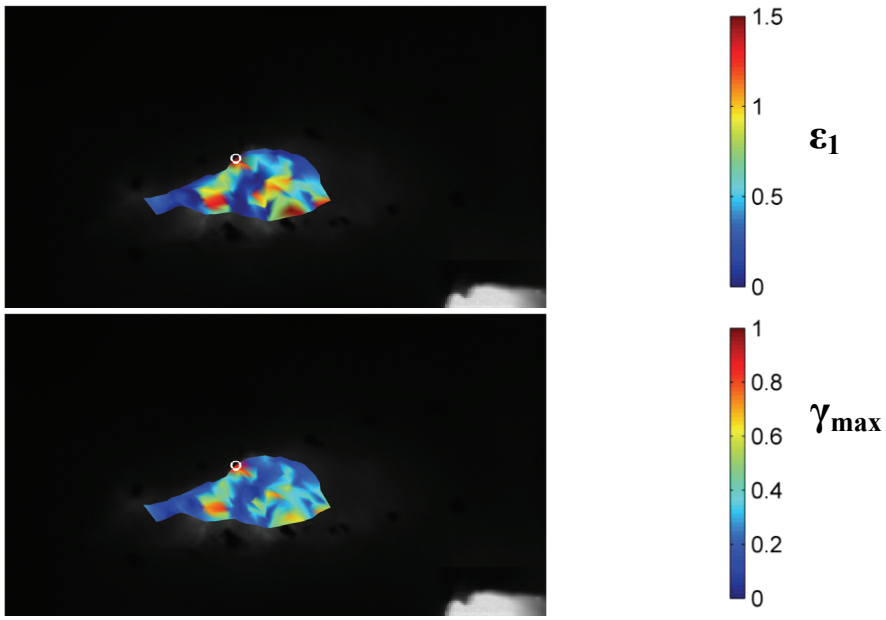
1.5
1
0.5
0
ε_1
1
0.8
0.6
0.4
0.2
0
γ_{max}

#21

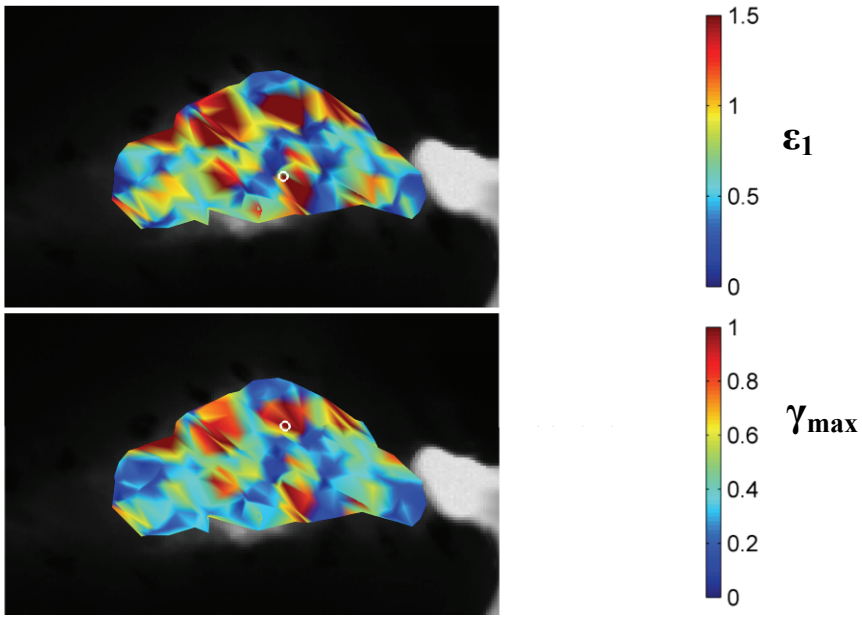
1.5
1
0.5
0
ε_1
1
0.8
0.6
0.4
0.2
0
γ_{max}

#22

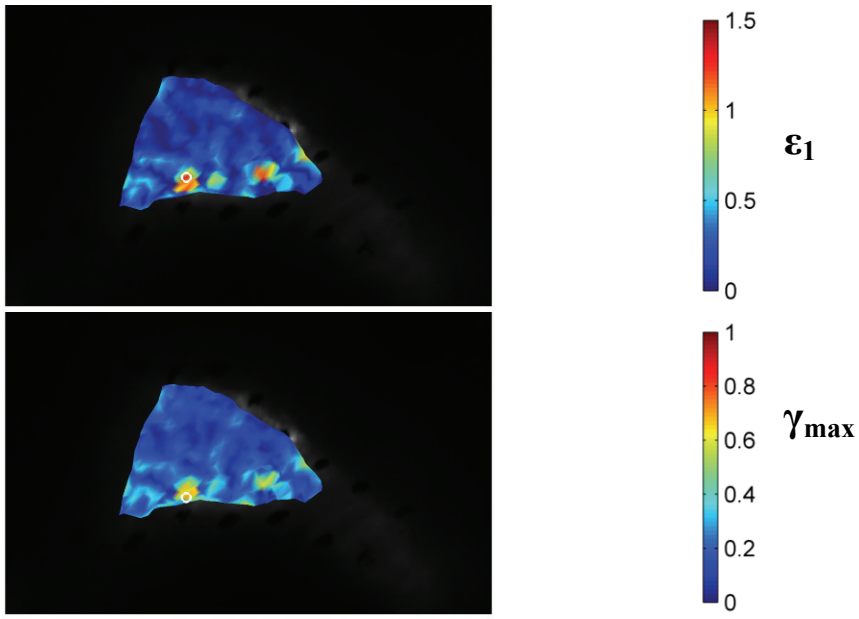
1.5
1
0.5
0
ε_1
1
0.8
0.6
0.4
0.2
0
γ_{max}

#23

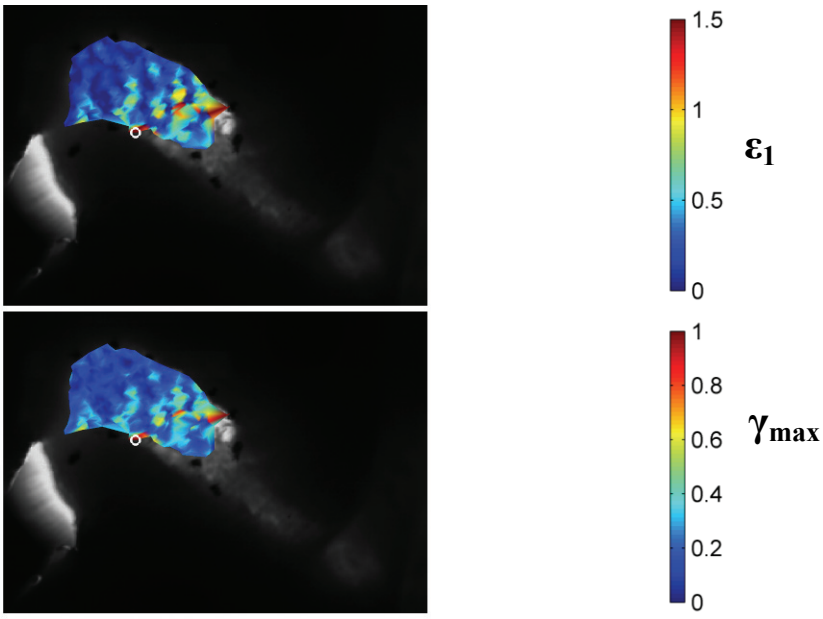
1.5
1
0.5
0
ε_1
1
0.8
0.6
0.4
0.2
0
γ_{max}

#24

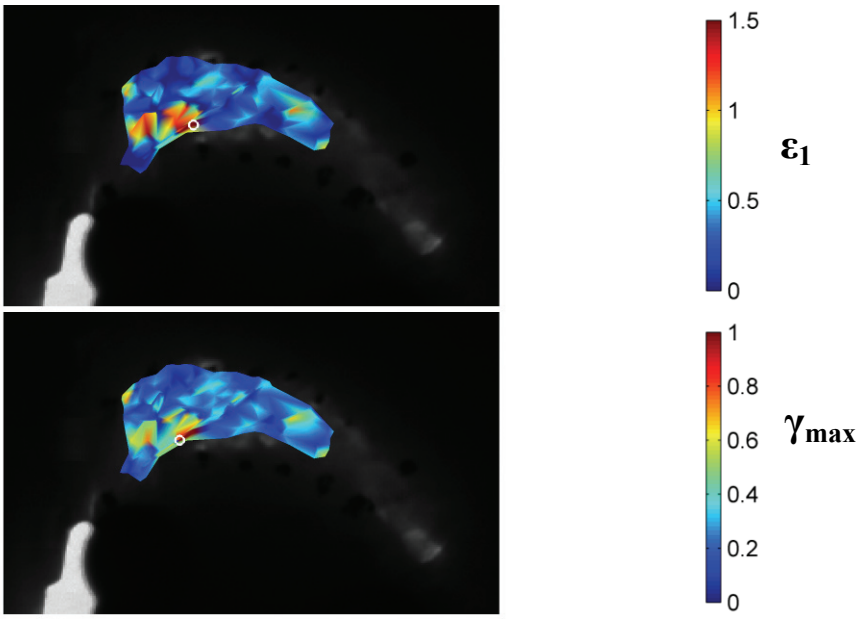
1.5
1
0.5
0
ε_1
1
0.8
0.6
0.4
0.2
0
γ_{max}

APPENDIX J

Maps of unrecovered strain & altered fiber alignment after retraction

This appendix summarizes the individual maps of unrecovered strain and changes in vector correlation detected after retraction of the isolated C6/C7 human facet joints described in Chapter 7. Both ε_1 and γ_{max} fields are provided for each specimen. Unrecovered strain was defined for any node in which the strain exceeded 0.09; altered fiber alignment was defined for any node in which the change in alignment vector correlation was -0.10 or lower. The rationale for those thresholds is provided in Chapter 7. Tissue regions that exceeded these thresholds are also highlighted in maps indicating the co-localization of unrecovered strain and altered fiber alignment for each specimen.

For each individual specimen, the corresponding maps are grouped together. The ε_1 field is plotted above the γ_{max} field for each specimen, and their respective co-localization maps with altered fiber alignment are positioned just to the right. Altered fiber alignment is indicated by red and unrecovered strain is indicated by green in the co-localization maps. Regions with both altered fiber alignment and unrecovered strain are represented by yellow.

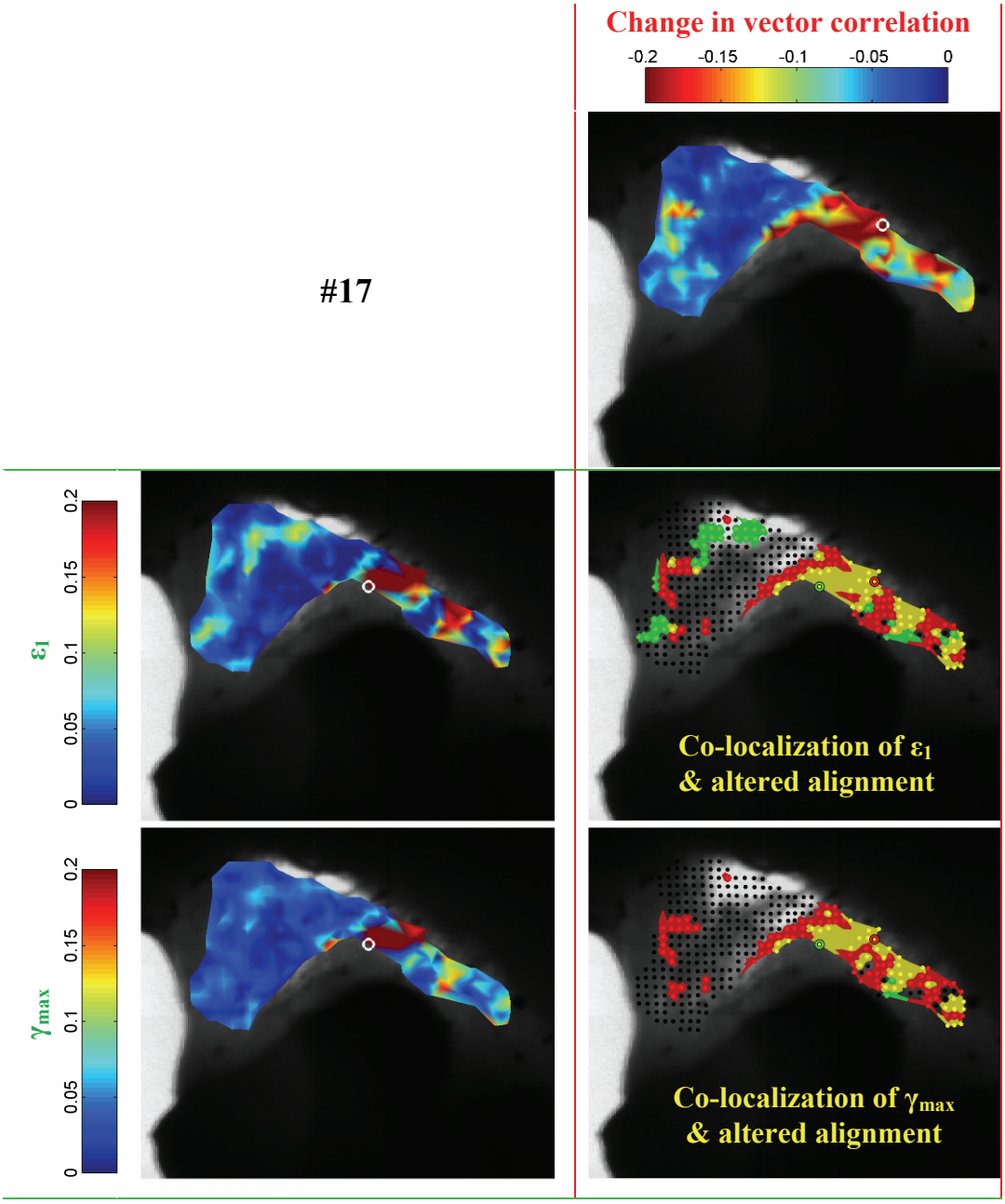
Change in vector correlation
-0.2
-0.15
-0.1
-0.05
0
#17
ε1
0
0.05
0.1
0.15
0.2
γmax
0
0.05
0.1
0.15
0.2
Co-localization of ε1
& altered alignment
Co-localization of γmax
& altered alignment

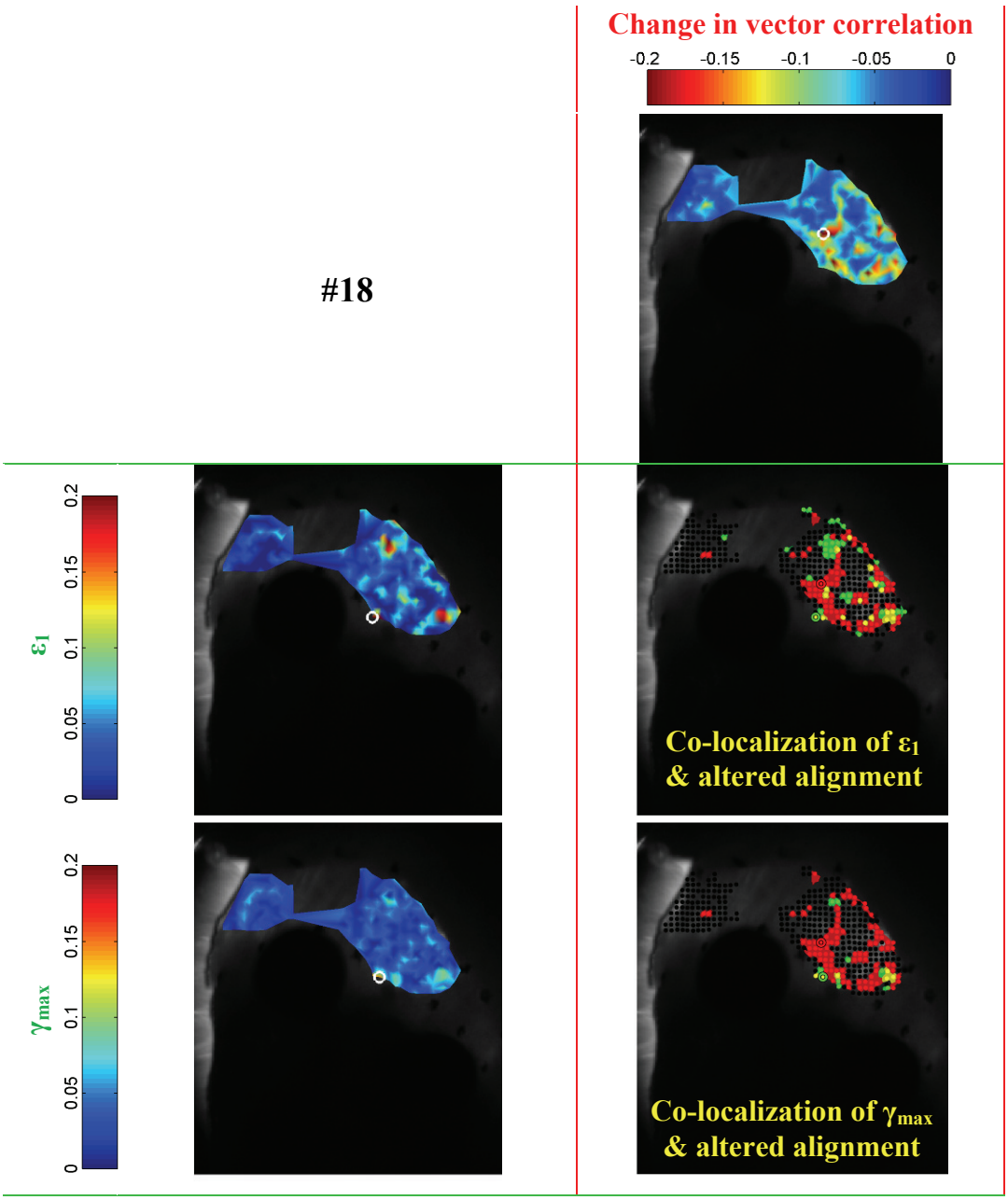
Change in vector correlation
-0.2
-0.15
-0.1
-0.05
0
#18
ε_1
0
0.05
0.1
0.15
0.2
γ_{max}
0
0.05
0.1
0.15
0.2
Co-localization of ε_1 & altered alignment
Co-localization of γ_{max} & altered alignment

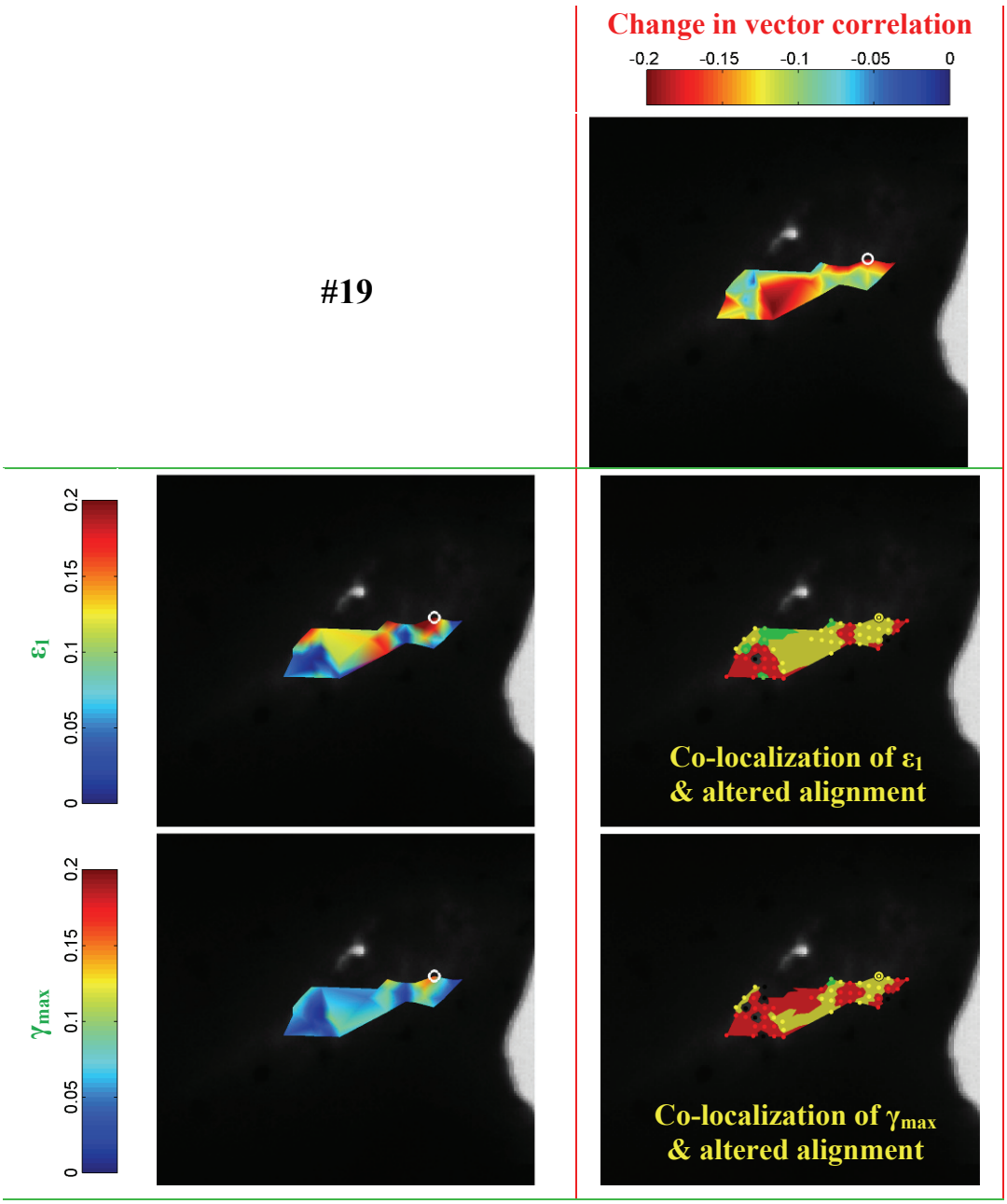
Change in vector correlation
-0.2
-0.15
-0.1
-0.05
0
#19
ε_1
0
0.05
0.1
0.15
0.2
Co-localization of ε_1
& altered alignment
γ_{max}
0
0.05
0.1
0.15
0.2
Co-localization of γ_{max}
& altered alignment

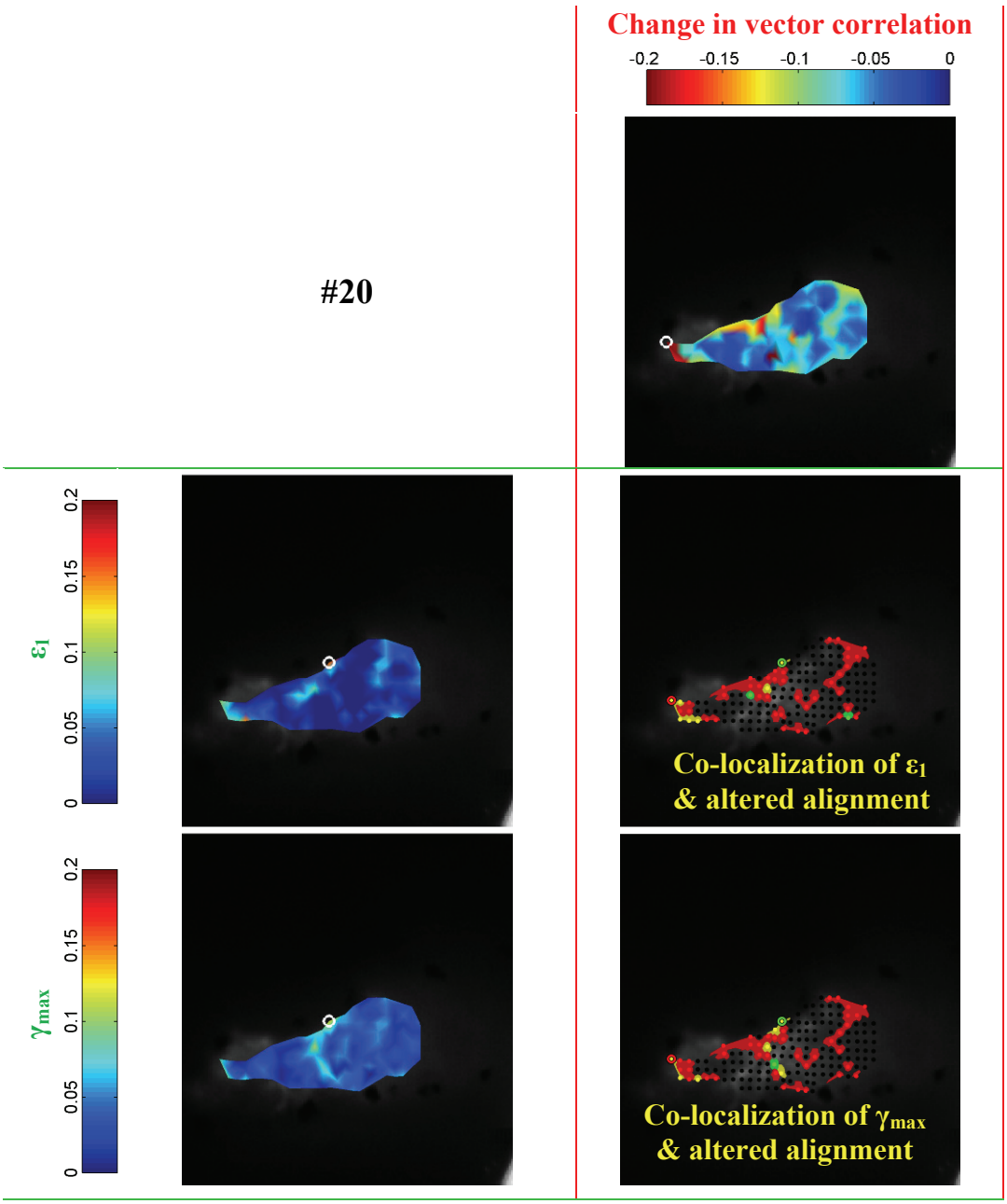
Change in vector correlation
-0.2
-0.15
-0.1
-0.05
0
#20
ε_1
0
0.05
0.1
0.15
0.2
Co-localization of ε_1
& altered alignment
γ_{max}
0
0.05
0.1
0.15
0.2
Co-localization of γ_{max}
& altered alignment

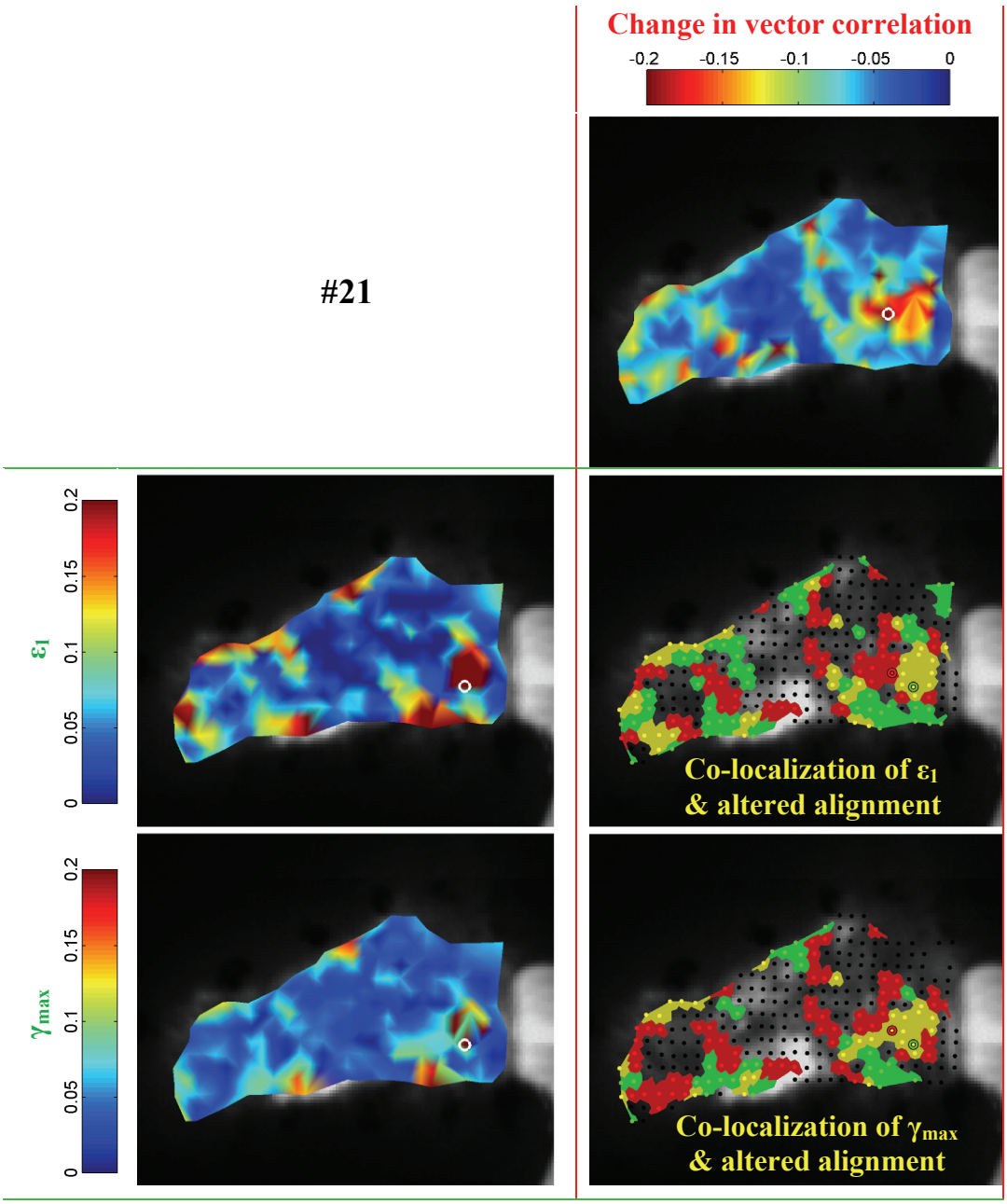
Change in vector correlation
-0.2
-0.15
-0.1
-0.05
0
#21
ε_1
0
0.05
0.1
0.15
0.2
Co-localization of ε_1
& altered alignment
γ_{max}
0
0.05
0.1
0.15
0.2
Co-localization of γ_{max}
& altered alignment

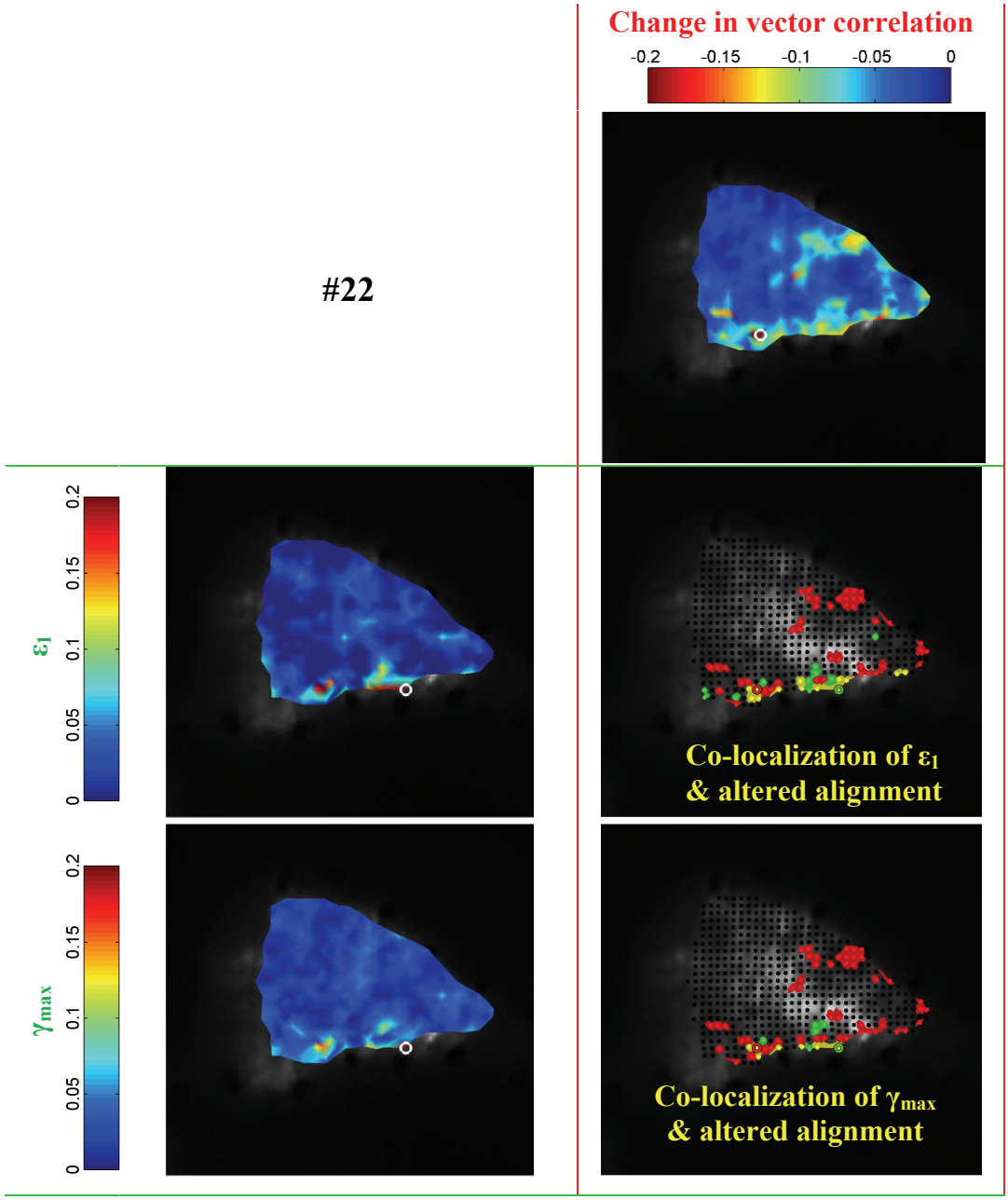
Change in vector correlation
-0.2
-0.15
-0.1
-0.05
0
#22
ε1
0
0.05
0.1
0.15
0.2
γmax
0
0.05
0.1
0.15
0.2
Co-localization of ε1
& altered alignment
Co-localization of γmax
& altered alignment

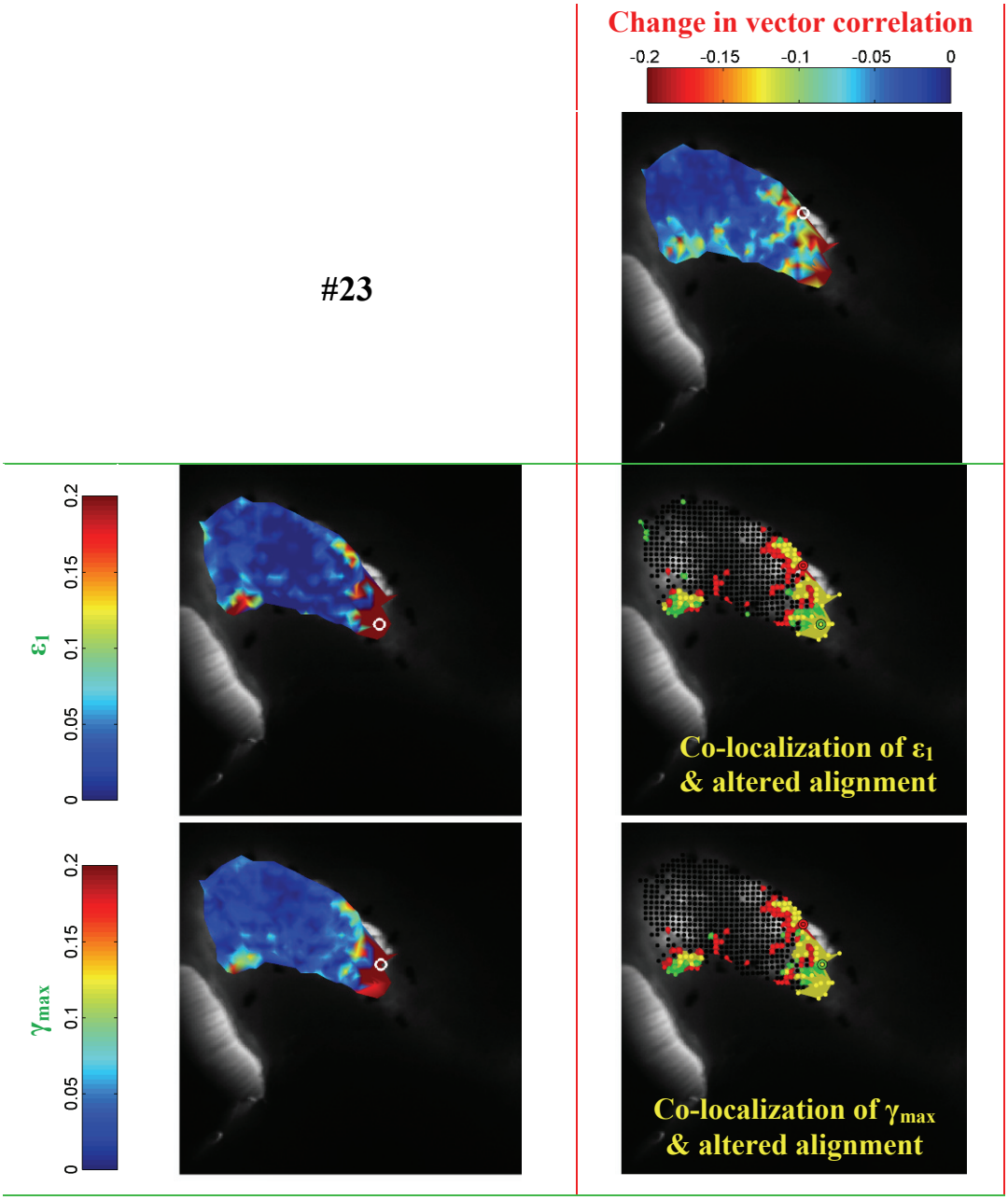
Change in vector correlation
-0.2
-0.15
-0.1
-0.05
0
#23
ε1
0
0.05
0.1
0.15
0.2
γmax
0
0.05
0.1
0.15
0.2
Co-localization of ε1
& altered alignment
Co-localization of γmax
& altered alignment

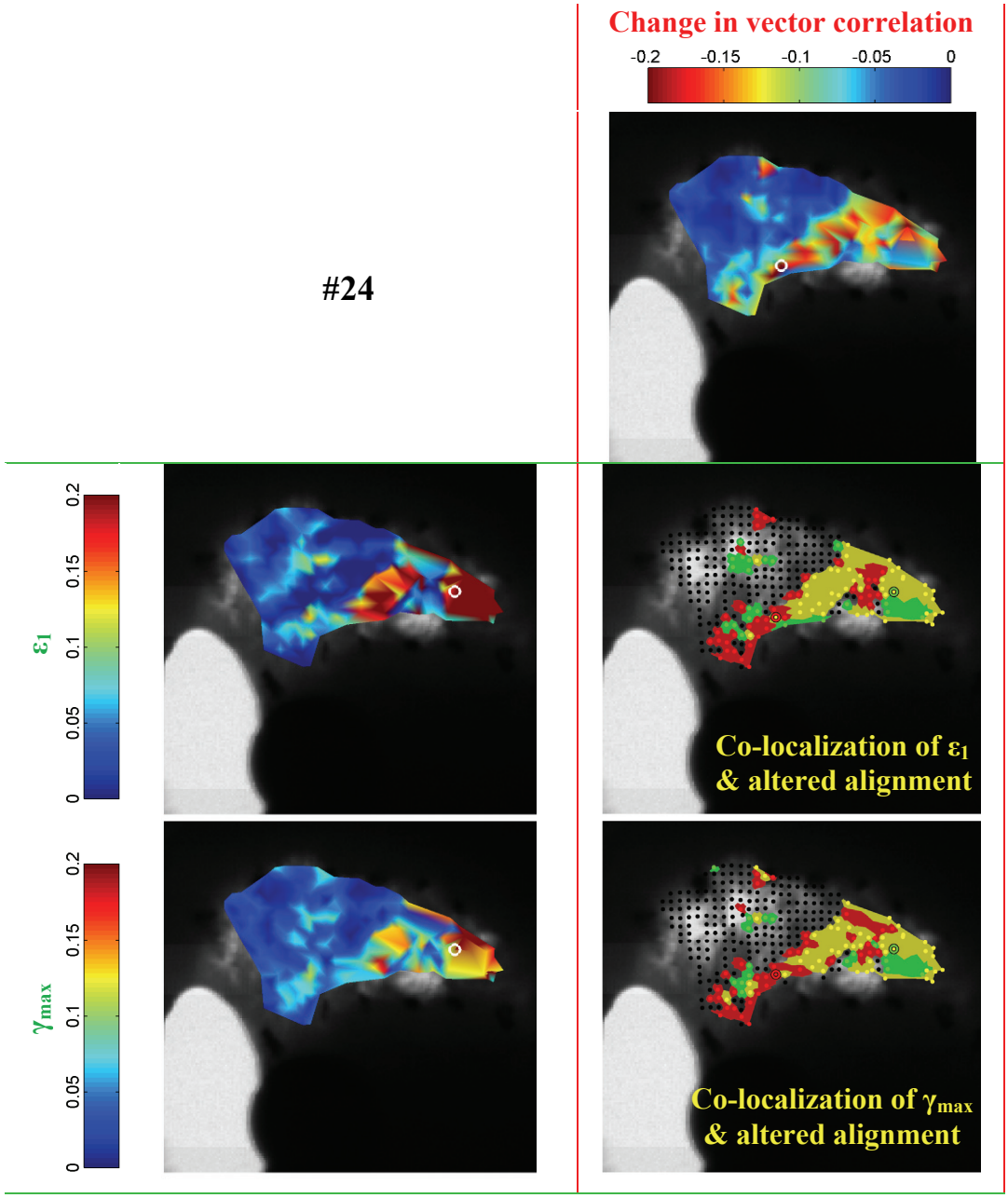
Change in vector correlation
-0.2
-0.15
-0.1
-0.05
0
#24
ε1
0
0.05
0.1
0.15
0.2
γmax
0
0.05
0.1
0.15
0.2
Co-localization of ε1
& altered alignment
Co-localization of γmax
& altered alignment

APPENDIX K

Derivation of QPLI fiber alignment equations using Mueller calculus

This appendix details the derivation of Equation 5.1 which relates light intensity, polarizer angle, collagen fiber alignment and retardation using the quantitative polarized light imaging system described in Chapters 5-7. That equation can be derived by modeling light as a four-element Stokes vector, and manipulating the polarization of light through the use of Mueller calculus (Mueller, 1943). Following the derivation of Equation 5.1 in K.1, potential systematic sources of error are also presented in K.2 based on the assumptions that are made by calculating fiber alignment using these equations.

K.1. Derivation of fiber alignment through Mueller calculus

Incoherent polarized light can be modeled by a Stokes vector (**S**),

$$\mathbf{S} = \begin{bmatrix} S_0 \\ S_1 \\ S_2 \\ S_3 \end{bmatrix}, \tag{K.1}$$

where S_0 represents the total intensity of light, S_1 is the difference in intensities between linear polarized components at 0º and 90º, S_2 is the difference in

intensities between linear polarized components at -45º and 45º, and S_3 is the difference in intensities between right and left circular polarized components. If one describes the electric field vector of the light as two orthogonal, linearly polarized waves, S_3 effectively becomes non-zero as the two linear waves differ in phase.

The Stokes vector can be manipulated by Mueller matrices, which serve as mathematical representations of the optical components used to control the polarization of light. In the QPLI system used in this thesis, the optical components include: two linear polarizers, a linear birefringent sample (capsular ligament tissue in this case), and a wave plate (see Figure 5.2 of Chapter 5). Linear polarizers oriented at 0º are represented in Mueller calculus by:

$$\mathbf{M}_p = \begin{bmatrix} 1 & 1 & 0 & 0 \\ 1 & 1 & 0 & 0 \\ 0 & 0 & 0 & 0 \\ 0 & 0 & 0 & 0 \end{bmatrix}, \tag{K.2}$$

and linear birefringent components (or wave plates) oriented at 0º are represented by:

$$\mathbf{M}_{wp} = \begin{bmatrix} 1 & 0 & 0 & 0 \\ 0 & 1 & 0 & 0 \\ 0 & 0 & \cos\delta & \sin\delta \\ 0 & 0 & -\sin\delta & \cos\delta \end{bmatrix}, \tag{K.3}$$

where δ is the retardation based on the linear birefringence and thickness of the component. The quarter-wave plate used in this QPLI system retards light a quarter turn, so δ= 90º in Equation K.3, which simplifies $\mathbf{M}_{wp}$ to:

$$\mathbf{M}_{wp} = \begin{bmatrix} 1 & 0 & 0 & 0 \\ 0 & 1 & 0 & 0 \\ 0 & 0 & 0 & 1 \\ 0 & 0 & -1 & 0 \end{bmatrix}. \tag{K.4}$$

The orientation of a component can be manipulated with use of the rotation matrix ($\mathbf{R}_M$),

$$\mathbf{R}_M(\theta) = \begin{bmatrix} 1 & 0 & 0 & 0 \\ 0 & \cos(2\theta) & \sin(2\theta) & 0 \\ 0 & -\sin(2\theta) & \cos(2\theta) & 0 \\ 0 & 0 & 0 & 1 \end{bmatrix}, \tag{K.5}$$

so that the Mueller matrix of a linear polarizer, $\mathbf{M}_p$, with orientation θ, can be described as:

$$\mathbf{M}_p(\theta) = \mathbf{R}_M(-\theta)\mathbf{M}_p(0)\mathbf{R}_M(\theta) \tag{K.6}$$

In the QPLI optical train of this system, incoherent white light passes through a linear polarizer with changing orientation (θ), a linear birefringent sample with an unknown orientation (α) and retardation (δ), a quarter-wave plate oriented at -45º, and a fixed linear polarizer at 0º before the total intensity of light is recorded by the sensor of the CCD camera. Accordingly, the optical train can be modeled in Mueller calculus as:

$$\mathbf{S}'(\theta,\alpha,\delta) = \mathbf{M}_p(0)\mathbf{M}_{qw}(-45)\mathbf{M}_{sample}(\alpha,\delta)\mathbf{M}_p(\theta)\mathbf{S} \tag{K.7}$$

Unpolarized white light entering the optical train can be represented by **S**, where S_0 is the only non-zero element. Accordingly, the S_0 element in **S′** that is recorded by the camera sensor will be reduced to:

$$S_0(\theta) = \frac{1}{2} I_o \left(\sin(\delta)\sin(2\theta - 2\alpha) + 1\right), \quad \text{(K.8)}$$

as reported by Glazer et al. (1996), and fit to a simple harmonic equation by Tower et al. (2002). Please see Section 5.3.1 in Chapter 5 and the Matlab code in Appendix L for a description of how collagen fiber alignment was determined based on Equation K.8 using harmonic analysis.

K.2. Potential sources of systematic error in QPLI measurements

The assumptions made during the derivation of Equation K.8 can lead to measurement errors when using a relatively thick biological tissue. Photons can easily be transmitted through thin tissue sections like those used in traditional light microscopy. However, when thicker specimens are used the potential for light scattering increases exponentially (Wang and Wu, 2007). With a sufficient light source and camera exposure time, enough photons can be transmitted through specimens that are as thick as 0.5-1.0 mm. However, photons with a shorter wavelength are more likely to scatter than those with a wavelength closer to the infrared range (Wang and Wu, 2007). The quarter-wave plate used in this thesis was calibrated to retard white light emanating from the fiber optic illuminator by exactly 90º (see Section 5.3.1). However, upon multiple scattering events during the transmission of light through ligament tissue, the average wavelength of light exiting the tissue has the potential to be higher than that measured during the calibration of the wave plate. As a result, it cannot be assumed that the quarter-

wave plate still retards the average photon exactly 90º when a thick specimen is placed in the optical train. If the average wavelength of the light were increased, the quarter-wave plate would retard light at less than 90º. As wave plate retardation is decreased, the harmonic-based QPLI direction measurements can become biased towards 135º, which corresponds to the orientation of the wave plate (Figure K.1a). In addition, the decrease in wave plate retardation causes a decrease in the measured sample retardation near fiber directions of 45º and an increase in measured retardation values for pixels with fiber directions near 135º (Figure K.1b).

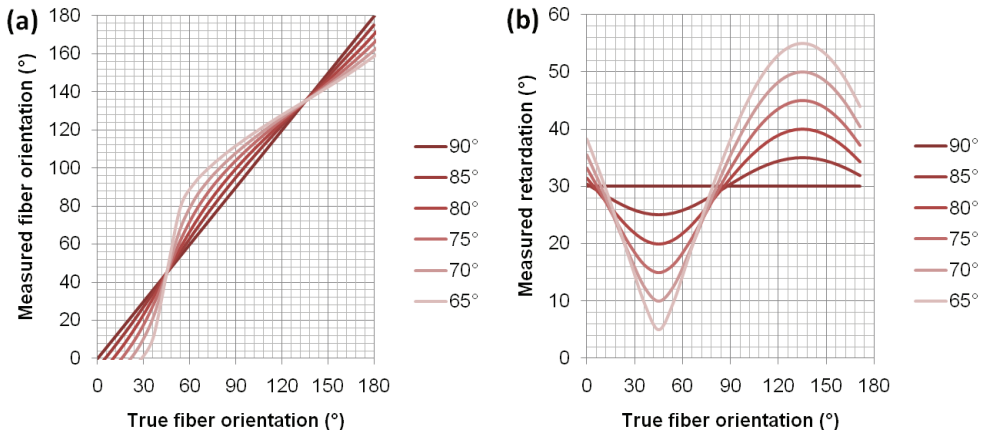

Figure K.1. A theoretical Mueller calculus simulation of QPLI measurements at different fiber orientations. (a) By decreasing the retardation of the quarter-wave plate in the QPLI system from 90º to 65º, fiber direction measurements become biased towards 135º in a sample with 30º of retardation. **(b)** Retardation measurements also increase for orientations between 90-180º and decrease for orientations between 0-90º when the retardation of the quarter-wave plate decreases.

To assess the potential for scattering-based errors from the facet capsular ligament tissue used in the studies in Chapters 5-7, the relationship between

retardation and fiber direction at each pixel was assessed in a subset of the specimens tested in Chapter 5. Specifically, fiber alignment data were taken from the ligament midsubstance of eight unloaded specimens. Because fiber directions from 0-90º produce lower retardation values compared to directions from 90-180º when wavelength-dependent scattering occurs (Figure K.1b), each pixel in the ligament midsubstance was grouped according to whether its fiber direction was less than or greater than 90º. For pixels with fiber directions between 0-90º, the average retardation was 13.58±3.78º in the eight specimens in Chapter 5. This average retardation did not significantly differ (p=0.6844) from the retardation (13.25±2.76º) at pixels between 90-180º (Figure K.2). These data suggest that wavelength-dependent scattering does not significantly affect the QPLI measurements in the facet capsular ligament tissue used in the studies of this thesis.

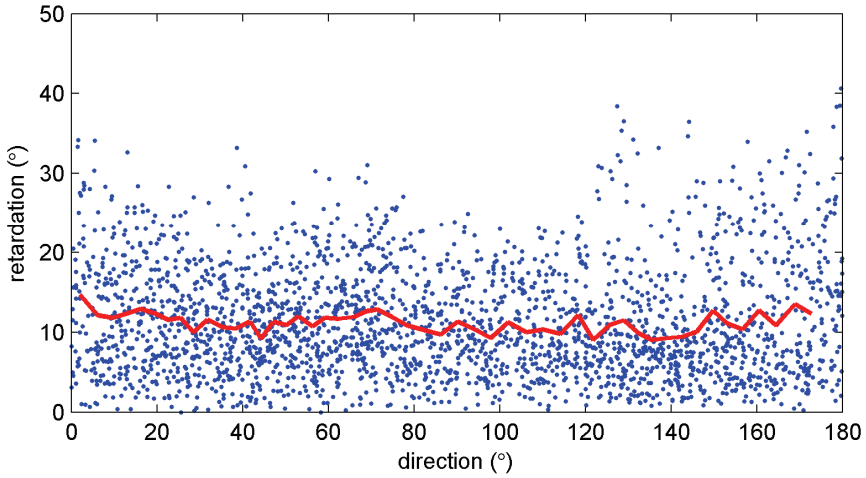

Figure K.2. Retardation values do not depend on the fiber direction, which indicates no significant error in the calibration of the quarter-wave plate in this QPLI system. Each point (blue) represents one pixel, and the line (red) indicates the average retardation value for a given fiber direction.

Error in the fiber direction measurements can also result from the assumption that collagenous tissue can be modeled as a simple linear birefringent material, as described in Equation K.3. Collagen is strongly birefringent; light that is polarized parallel to the fibers will travel at a different speed through the tissue compared to light that is polarized perpendicular to the fibers (Tower et al., 2002; Viidik, 1972). The degree of retardation is a product of the birefringence of the tissue and its thickness. However, collagen can also exhibit weak linear dichroism as well (Laude-Boulesteix et al., 2004). As light travels through a dichroic tissue, diattenuation of the light is produced causing the sample to act as a partial polarizer. Rather than assuming a linear birefringent material, collagenous tissue that exhibits diattenuation should be described by a coaxial linear birefringent, linear dichroic element ($\mathbf{M}_{lb/ld}$):

$$\mathbf{M}_{lb/ld} = e^{-\delta'} \begin{bmatrix} \cosh\delta' & \sinh\delta' & 0 & 0 \\ \sinh\delta' & \cosh\delta' & 0 & 0 \\ 0 & 0 & \cos\delta & \sin\delta \\ 0 & 0 & -\sin\delta & \cos\delta \end{bmatrix}, \tag{K.9}$$

where δ' is degree of diattenuation and δ is the degree of retardation. However, the different contributions of diattenuation and retardation cannot be separated using a QPLI system. Harmonic-based QPLI fiber direction measurements that assume a simple linear birefringent sample in the presence of a linear dichroic contribution will be rotated counterclockwise relative to the true fiber direction (Figure K.3).

This counterclockwise rotation reaches a maximum of 45º when the sample acts as a perfect polarizer rather than a linear birefringent material.

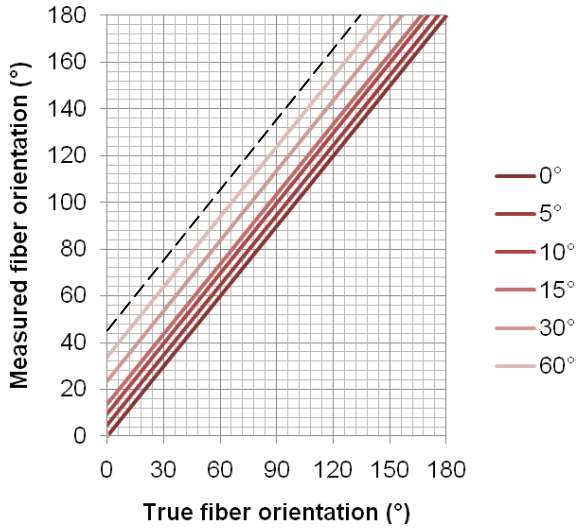

Figure K.3. Increasing degrees of diattenuation in a specimen that exhibits 30º of retardation will cause a counterclockwise rotation of QPLI-based fiber direction measurements. The maximum possible rotation is indicated by the dashed line.

In order to assess the potential for linear dichroism effects in the QPLI measurments of facet capsular ligament tissue, fiber measurements from an alternative optical train were needed for comparison. The standard polarized light microscopy technique to determine collagen fiber orientation is to rotate a pair of crossed polarizers with the sample in between the polarizers (Gimbel et al., 2004; Lake et al., 2009; Viidik, 1972). As with the QPLI system, the light intensity modulated by a crossed polarizer (XP) system can be modeled by Mueller calculus:

$$\boldsymbol{S}'(\alpha,\delta,\theta) = \boldsymbol{M}_p(\theta+90)\boldsymbol{M}_s(\alpha,\delta)\boldsymbol{M}_p(\theta)\boldsymbol{S} \ . \qquad \text{(K.10)}$$

The first Stokes element (S_0') is a function of the polarizer orientation (θ), fiber orientation (α) and sample retardation (δ):

$$S_0'(\alpha,\delta,\theta)=\frac{1}{2}\sin^2(\delta/2)\cdot\sin^2(2\alpha-2\theta)\,, \qquad \text{(K.11)}$$

but the relationship between fiber orientation and light intensity differs from a QPLI system. The light intensity in Equation K.11 reaches a minimum when the polarizer orientation and fiber direction are identical. As a result, a sample exhibiting linear dichroism in addition to linear birefringence will not cause a bias in the measured fiber direction using an XP system.

Although an XP system is not prone to systematic error in its fiber direction measurements as a result of dichroism or scattering, such a system does have some notable limitations relative to a QPLI system. Fiber direction measurements can only span 0º to 90º with an XP system because of the second squared term in Equation K.11. As a result, there is an ambiguity in whether fiber direction measurements correspond to α or $\alpha + 90^o$. Furthermore, the amplitude of the light intensity differs between XP and QPLI systems as the polarizers are rotated in each system. When the CCD camera that measures light intensity is set to accommodate a range of retardation measurements, an XP system produces a much weaker signal than a QPLI system for low retardation values (Figure K.4). Accordingly, XP systems are much more susceptible to random error in fiber direction measurements for regions of a sample that are only moderately birefringent.

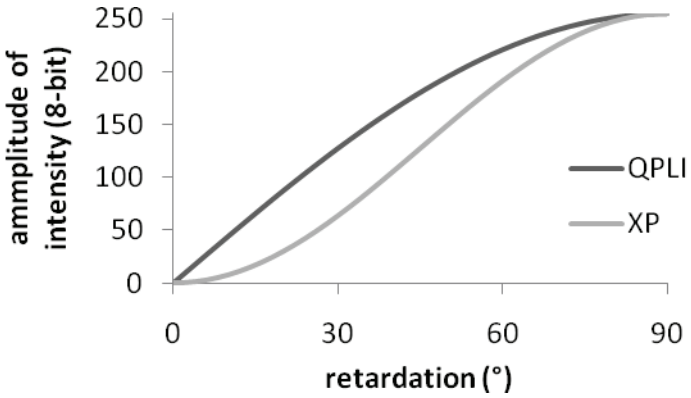

Figure K.4. The light intensity signal measured by an 8-bit camera sensor for retardation values between 0-45° is much stronger when using a QPLI system compared to an XP system.

Despite the potential for increased random error in an XP system, a direct pixel-wise comparison of fiber direction measurements between XP and QPLI systems can demonstrate whether linear dichroism produces an offset in the average fiber direction measurements from a QPLI system. To enable a direct comparison of fiber measurements, QPLI data were first acquired from excised human facet capsular ligament tissue that was fixed to a glass slide. Following QPLI acquisition, a second linear polarizer was placed in between the sample and the circular analyzer (see Figure 5.2 for a schematic of the system). This second linear polarizer was oriented 90° from the other rotating polarizer, and both polarizers were stepped in 9° increments as images were taken. Using equation K.8 for the QPLI images and equation K.11 for the XP images, the fiber directions were calculated at each pixel in the images. The difference in XP and QPLI fiber measurements was then calculated for each pixel and plotted as a function of retardation (Figure K.5). The mean difference in fiber measurements between the

two systems was 0.08°±12.64°. The small mean difference between measurements indicates that linear dichroism does not contribute to systematic error in the QPLI-based measurements. Of note, large differences in the fiber direction measurements existed for pixels with retardation below 15° and contributed to the high standard deviation in the average difference between system measurements (Figure K.5). This random error in fiber direction measurements for pixels with low retardation is likely related to the poor intensity signal produced by the XP system for pixels with low retardation values (Figure K.4).

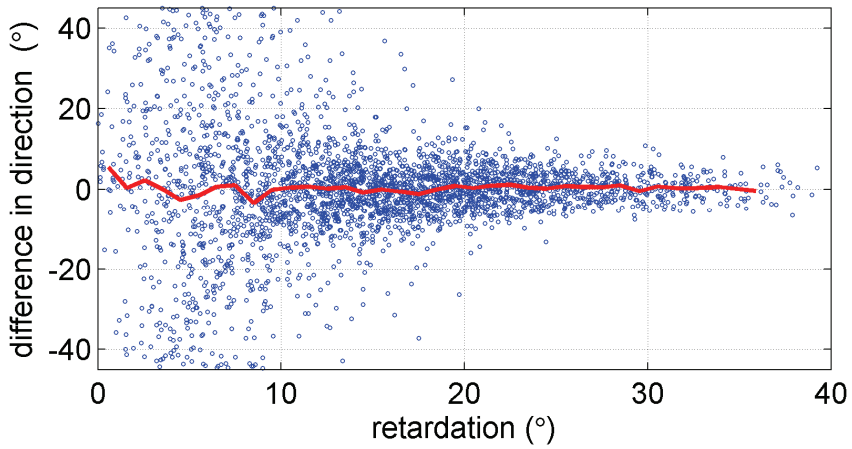

Figure K.5. The difference in fiber direction measurements made using XP and QPLI systems. The blue markers represent pixels in an image of facet capsular ligament. The red line is the mean difference between the measurement techniques.

Collectively, the derivation of light intensity equations and the assessment of systematic error described here highlight a number of important considerations when implementing a QPLI system. Although a QPLI system is capable of defining fiber directions over an entire 180° range, it is prone to systematic

measurement errors produced by linear dichroism and wavelength-dependent scattering. Although the experiments described in this appendix demonstrate that these potential sources of error do not affect fiber direction measurements of facet capsular ligament tissue, caution should be used when applying this system to other thick collagenous tissues.

APPENDIX L

Matlab code to create alignment maps from QPLI data

This appendix includes the Matlab files used to create fiber alignment maps from the images obtained using the QPLI system, as described in Chapter 5. The function **initializeQPLI.m** calls **prepsample3.m**, which prompts the user to examine the multi-page TIFF file created by the camera that monitors the polarizer rotation. The user must identify the first image in which the polarizer is approximately aligned with the horizontal. The file **prepsample3.m** also prompts the user to digitize the exact polarizer orientation within the frame in which the polarizer is somewhat aligned with the horizontal. The file **initializeQPLI.m** then calculates a polarizer orientation for every image collected by each camera. After loading the multi-page TIFF file that corresponds to the light intensity through the sample, **initializeQPLI.m** also calls **analyzesampleIM3.m**, which is used to calculate the fiber direction and retardation for each pixel using the harmonic analysis described in Chapter 5 and Appendix K. Finally, **initializeQPLI.m** creates a fiber alignment map similar to that produced in Figure 5.5.

initializeQPLI.m

```
%PREPARE IMAGE DATA FOR ANALYSIS

clear all

%user must modify these values prior to running the program
specID=[];%text string that is used to identify the proper folder
zer=[]; %force balance in Newtons corresponding to the true zero Newtons
ypix=[]; % y-coordinate in pixels where polarizer in Rotation camera images is at 0 deg


cd(['C:\Documents and Settings\neck\Desktop\QPLI\',specID]);

%loads mechanical data
fail=textread([specID,'_fail.is_tcyclic.raw'],'%f','headerlines', 65, 'delimiter', ',');
fail=reshape(fail,19,length(fail)/19);
fail(5:19,:)=[];

%defines start when camera trigger goes off
for i=1:length(fail)
    if fail(3,i) < -100
        start=i;
        break
    end
end

%cuts pretrigger data, balances load, and sets time =0 when trigger starts
fail(:,1:start-1)=[];
fail(4,:)=fail(4,:)*9.81-zer;
fail(1,:)=fail(1,:)-fail(1,1);

imgstart=1;
imgend=length(imginf)/20-1;


%define polarizer position during acquisition and ROI at initial and
%failure positions

disp('please digitize QPLI polarizer position and ROIs...');
[beg angCOR intpROI dc]=prepsample3([specID,'_fail_img.tif'],[specID,'_fail_rot.tif'],ypix,imgstart,imgend)
%[beg angCOR intpROI dc]=prepsample2('test4_img.tif','test4_rot.tif',243,1.436,1.548)
imginf=imfinfo([specID,'_fail_img.tif']);
clear I
imgend=round(length(imginf)/20)-1;
save PREPDONE
%


%define ROI for QPLI analysis
intpROI=[min(intpROI(:,1)) min(intpROI(:,2)) max(intpROI(:,3)) max(intpROI(:,4))]


%%
%PLOT FIBER ALIGNMENT MAPS

%sets baseline (DC) intensity of pixels by finding median value in the ROI
clear all
load PREPDONE
h=figure;

hsg = waitbar(0,'Please wait...');


%load mechdata2
ii=1;
intpROI=[min(intpROI(:,1)) min(intpROI(:,2)) max(intpROI(:,3)) max(intpROI(:,4))]
dcim=imread([specID,'_dc.bmp']);

dc_crop=dcim(intpROI(2):intpROI(4),intpROI(1):intpROI(3));
dc=double(median(reshape(dc_crop,1,[])));


clear I

SNRs=ones(size(dc_crop,1),size(dc_crop,2),round(1*round(imgend)-1)-1);
inten=zeros(size(dc_crop,1),size(dc_crop,2),round(1*round(imgend)-1)-1);
Rv=ones(size(dc_crop,1),size(dc_crop,2),round(1*round(imgend)-1)-1);
tic
for j=2:round(imgend)-round(imgstart)+1%round(imgend/10-imgstart/10)*10+round(imgstart)
    %switch 2 and 4
    ad=20*j-20;
    clear I
    for i=beg+ad:beg+ad+19
        img=imread([specID,'_fail_img.tif'],i);
        Io(:,:,i-beg-ad+1)=img(intpROI(2):intpROI(4),intpROI(1):intpROI(3));
        imga=imread([specID,'_fail_img.tif'],i+20);
        Ia(:,:,i-beg-ad+1)=imga(intpROI(2):intpROI(4),intpROI(1):intpROI(3));
```

```
        imgb=imread([specID,'_fail_img.tif'],i-20);
        Ib(:,:,i-beg-ad+1)=imgb(intpROI(2):intpROI(4),intpROI(1):intpROI(3));
    end

    I=.25*Ib+.5*Io+.25*Ia;
    %Finds pixel intensities over the course of the polarizer rotation

    jj=j-round(imgstart)+1;
    disp((jj-1)/(round(imgend-imgstart))*100);


    [alphaS deltaS ptp err snr]=analyzesampleIM3(I,0,scale,dc,angCOR);

    image(uint8(round(mean(I,3))),'CDataMapping','scaled')
    colormap(gray);

    hold on;
    snrx=snr.^(1-isinf(snr));

    [X,Y] = meshgrid(2:5:size(alphaS,2)-1,2:4:size(alphaS,1)-1);
    clear u v
    for i=1:size(X,1)
        for j=1:size(Y,2)
            alp=alphaS(Y(i,j),X(i,j));
            del=sin(deltaS(Y(i,j),X(i,j)));
            if snrx(Y(i,j),X(i,j))>2
                u(i,j)=cos(alp)*del;
                v(i,j)=sin(alp)*del;
            else
                u(i,j)=0;
                v(i,j)=0;
            end
        end
    end


    u=reshape(u,1,[]);
    v=reshape(v,1,[]);
    ind=find((u.^2+v.^2)>.00002);
    X=reshape(X,1,[]);
    Y=reshape(Y,1,[]);

    quiver([X(ind) X(ind) 1],[Y(ind) Y(ind) 1],[u(ind) -u(ind) 1],[-v(ind) v(ind) 1],.5,'y-
','ShowArrowHead','off','LineWidth',.5)
    title((jj-1)/5)
    axis image



    drawnow;
    hold off

end
```

prepsample3.m

```
function [beg angCOR intpROI dc]=prepsample2(imgfile,rotfile,zpix,imgstart,imgend)

figure;
disp('getinfo')
A=imfinfo(rotfile);
disp('gotinfo')
for i=1:length(A)
rotat=imread(rotfile,i);
image(rotat,'CDataMapping','scaled');
colormap('gray');
title(num2str(i));
axis image;
hold on;
plot([0 size(rotat,2)],[zpix zpix]);
%set(gcf)
k=waitforbuttonpress;
if k==0
    beg=i
    break
end
drawnow;
end

%%

%determine the offset the beg frame has from true zero deg
rotat=imread(rotfile,beg);
rotat2=imread(rotfile,1);
subplot(1,2,1);
image(rotat,'CDataMapping','scaled');
```

```
colormap('gray');
hold on;
plot([0 size(rotat2,2)],[zpix zpix]);
title('first click on 0 deg mark, then next tick closest to shaft');
axis image;
subplot(1,2,2);
image(rotat2,'CDataMapping','scaled');
colormap('gray');
axis image;
[x,y] = ginput(2);
ninedegdist=abs(y(1)-y(2));
angCOR=(y(1)-zpix)/ninedegdist*pi/20-.08482;%-((rottrig-imgtrig)/1000*4500+4.0275)/180*pi;
%%
%find the appropriate area of interest
iww=1;
clear rotat rotat2
for iw=round(20*imgstart):200:round(20*imgend);
    rotat(:,:,iww)=imread(imgfile,iw);
    iww=iww+1;
end
rotat2=mean(rotat,3);

%rotat=imread(imgfile,round(20*imgstart));
image(rotat2,'CDataMapping','scaled');
colormap('gray');
axis image;


k = waitforbuttonpress;
point1 = get(gca,'CurrentPoint');    % button down detected
finalRect = rbbox;                   % return figure units
point2 = get(gca,'CurrentPoint');    % button up detected
point1 = point1(1,1:2);              % extract x and y
point2 = point2(1,1:2);
point1=round(point1);
point2=round(point2);
p1 = min(point1,point2);             % calculate locations
offset = abs(point1-point2);         % and dimensions
x = [p1(1) p1(1)+offset(1) p1(1)+offset(1) p1(1) p1(1)];
y = [p1(2) p1(2) p1(2)+offset(2) p1(2)+offset(2) p1(2)];
hold on
axis manual
plot(x,y)
%find the appropriate area of interest
intpROI(1,:)=[point1 point2];

%rotat=imread(imgfile,round(20*imgend));
image(rotat2,'CDataMapping','scaled');
colormap('gray');
axis image;
k = waitforbuttonpress;
point1 = get(gca,'CurrentPoint');    % button down detected
finalRect = rbbox;                   % return figure units
point2 = get(gca,'CurrentPoint');    % button up detected
point1 = point1(1,1:2);              % extract x and y
point2 = point2(1,1:2);
point1=round(point1);
point2=round(point2);
p1 = min(point1,point2);             % calculate locations
offset = abs(point1-point2);         % and dimensions
x = [p1(1) p1(1)+offset(1) p1(1)+offset(1) p1(1) p1(1)];
y = [p1(2) p1(2) p1(2)+offset(2) p1(2)+offset(2) p1(2)];
hold on
axis manual
plot(x,y)
intpROI(2,:)=[point1 point2];
%%
%find dc shift

dc=0;
```

analyzesampleIM3.m

```
function [alphaS deltaS ptp err snr]=analyzesampleIM3(I2,angP,scale,dc,angCOR)


ang=0:.05*pi:.95*pi;
ang=ang+angCOR;
sumA=0;
sumB=0;
sumC=0;
N=20;
%image(I(:,:,20))
I2=double(I2);
for i=1:N
    sumA=sumA+I2(:,:,i);
```

```
    sumB=sumB+I2(:,:,i)*cos(2*(ang(i)+angP));
    sumC=sumC+I2(:,:,i)*sin(2*(ang(i)+angP));
end
A=sumA/N;
B=sumB*2/N;
C=sumC*2/N;

for i=1:N
calcSig(:,:,i)=A+B*cos(2*ang(i))+C*sin(2*ang(i));
end
err=I2-calcSig;

dc=double(dc);
scale=double(scale);
scale=scale*(A-dc-.000001);


ptp=sqrt(B.^2+C.^2);
snr=10*(ptp.^2)./sum(err.^2,3);

B=B./scale;
C=C./scale;
alphaS=.5*atan2(-B,C);
deltaS=acos(sqrt(1-B.^2-C.^2));
```

APPENDIX M

Matlab code to detect anomalous fiber realignment based on vector correlation

This appendix provides several Matlab codes that together are used to detect anomalous fiber realignment for the studies described in Chapters 5-7. The file **anomrealign.m** loads data created by the Matlab code in Appendix L, and calls the function **analyzesampleIM3.m** (detailed in Appendix L) in order to create fiber alignment maps from the raw QPLI images. The vector correlation value at each pixel is then calculated by calling the function **corrcoef_vector.m**. Once vector correlation maps are created for every alignment map, **anomrealign.m** determines the regions of the image in which anomalous fiber realignment are detected based on the criteria detailed in Chapters 5-7. When anomalous fiber realignment is detected within one of the four-node elements created in the study described in Chapter 5 (and as detailed in Appendix N), the location of realignment within the element is calculated through inverse isoparametric mapping by calling the function **invisomap.m**. Finally, **anomrealign.m** creates a movie that displays the tissue regions in which anomalous fiber realignment has occurred during loading to gross failure.

anomrealign.m

```
%%

%CALCULATE VECTOR CORRELATION AT EACH PIXEL

%sets baseline (DC) intensity of pixels by finding median value in the ROI
clear all
load PREPDONE
h=figure;

hsg = waitbar(0,'Please wait...');



%load mechdata2
ii=1;
intpROI=[min(intpROI(:,1)) min(intpROI(:,2)) max(intpROI(:,3)) max(intpROI(:,4))]
dcim=imread([specID,'_dc.bmp']);

dc_crop=dcim(intpROI(2):intpROI(4),intpROI(1):intpROI(3));
dc=double(median(reshape(dc_crop,1,[])));

clear I

SNRs=ones(size(dc_crop,1),size(dc_crop,2),round(1*round(imgend)-1)-1);
inten=zeros(size(dc_crop,1),size(dc_crop,2),round(1*round(imgend)-1)-1);
Rv=ones(size(dc_crop,1),size(dc_crop,2),round(1*round(imgend)-1)-1);
tic
for j=2:round(imgend)-round(imgstart)+1%round(imgend/10-imgstart/10)*10+round(imgstart)

    ad=20*j-20;
    clear I
    for i=beg+ad:beg+ad+19
        img=imread([specID,'_fail_img.tif'],i);
        Io(:,:,i-beg-ad+1)=img(intpROI(2):intpROI(4),intpROI(1):intpROI(3));
        imga=imread([specID,'_fail_img.tif'],i+20);
        Ia(:,:,i-beg-ad+1)=imga(intpROI(2):intpROI(4),intpROI(1):intpROI(3));
        imgb=imread([specID,'_fail_img.tif'],i-20);
        Ib(:,:,i-beg-ad+1)=imgb(intpROI(2):intpROI(4),intpROI(1):intpROI(3));
    end

    I=.25*Ib+.5*Io+.25*Ia;
    %Finds pixel intensities over the course of the polarizer rotation

    jj=j-round(imgstart)+1;
    disp((jj-1)/(round(imgend-imgstart))*100);




    [alphaSa deltaSa ptpa erra snra]=analyzesampleIM3(Ia,0,scale,dc,angCOR);
    [alphaSb deltaSb ptpb errb snrb]=analyzesampleIM3(Ib,0,scale,dc,angCOR);

    [x y]=meshgrid(1:size(alphaSa,2),1:size(alphaSa,1));
    asa=reshape(alphaSa,1,[]);
    asb=reshape(alphaSb,1,[]);
    dsb=reshape(deltaSb,1,[]);
    dsa=reshape(deltaSa,1,[]);

    [xpola ypola]= pol2cart(2*asa,1-(cos(dsa)).^.2);
    [xpolb ypolb]= pol2cart(2*asb,1-(cos(dsb)).^.2);
    t2=[(xpolb);(ypolb)]';
    t1=[(xpola);(ypola)]';

    dis=((xpola-xpolb).^2+(ypola-ypolb).^2);
    wi=size(alphaSa,1);
    for i1=3:size(alphaSa,2)-2
        for j1=3:size(alphaSa,1)-2
            [xs ys]=meshgrid(i1-2:i1+2,j1-2:j1+2);
            indx=reshape((xs-1)*wi+ys,1,[]);
            [a b]=max(dis(indx));
            indx(b)=[];
            [rho,r2,err] = corrcoef_vector(t1(indx,:), t2(indx,:));
            Rv(j1,i1,jj)=rho;

        end
    end
    inten(:,:,jj)=mean(I,3);
    SNRs(:,:,jj)=((snra.^(1-isinf(snra)))+(snrb.^(1-isinf(snrb))))/2;
    ttt=toc;
    tlef=(ttt/((jj-1)/(round(imgend-imgstart)))-ttt)/60;
    waitbar((jj-1)/(round(imgend-imgstart)),hsg,[num2str(ttt/60),' min elapsed, ',num2str(tlef),' min left' ])

    % image(Rv(:,:,jj),'CDataMapping','scaled');axis image;colorbar;
    set(0,'CurrentFigure',h);
```

```
    hh=surf(((100*Rv(:,:,jj))),'EdgeColor','none');axis image; axis ij
    caxis([50 100])
    colormap jet
    shading('flat')
    view(0,90)
    set(hh,'FaceLighting','phong','FaceColor','interp',...
        'AmbientStrength',0.5)
    light('Position',[1 1 1],'Style','infinite');
    colorbar



    drawnow;
    hold off

end
% save staticRs Rv SNRs inten
%%
%movie2avi(F,'damage')
%

load mechdata2
load stiff
load fullnode
load strstr
clear inel inel2 pks
load inel
load damivis
load damivis2
%figure('NextPlot','replace');
snrs=snrs.^(1-(SNRs==inf));
inel2=sum(inel,1);
%clear inel
%confid=(snrs>10).*(squeeze(inel2(1,:,:,:)));
%
load liglim
%
xid=[];
etad=[];
elsd=[];
%
for i=121%2:size(snrs,3)-1
    i/size(snrs,3)
    snrsm=.5*snrs(:,:,i)+.25*snrs(:,:,i-1)+.25*snrs(:,:,i+1);
    snrsm=medfilt2(snrsm,[5 5]);

    dintenm=.5*dinten(:,:,i)+.25*dinten(:,:,i-1)+.25*dinten(:,:,i+1);
    confid(:,:,i)=(snrsm>5);
    pixread(i)=length(nonzeros((snrsm>5).*(squeeze(inel2(1,i,:,:)))));
    pixnum(i)=length(nonzeros((squeeze(inel2(1,i,:,:)))));
    %confid(:,:,i)=(snrsm>5).*(dintenm<4).*(squeeze(inel2(1,i,:,:)));

    negg=(confid(:,:,i))==0;
    metr=(((Rv(:,:,i+1)-Rv(:,:,i-1)).*(confid(:,:,i))))+negg-.00000000001;
    %     tstat2=(1-metr)./sqrt((1-(metr).^2)./(24-2));
    %     pv=1-t_alpha22(tstat2);
    %metr(1,1)=-1;
    pv=metr.*(metr<0);

    %      ct(i)=sum(sum(pv<-.2))-1;
    %      ct2(i)=sum(sum(pv<-.4))-1;
    %      ct3(i)=sum(sum((confid(:,:,i)-(pv<-.2))))-1;
    %      ct4(i)=sum(sum(inel2(1,i,:,:)));

    %pv(1,1)=0;
    gre=.5*(confid(:,:,i)-(pv<-.2));
    yel=0;%.5*((pv<-.2)-(pv<-.4));
    redd=.5*(pv<-.2);
    [L,num] = bwlabel(redd,8);
    Lhuge=zeros(size(L,1),size(L,2));
    for jkk=1:num
        [r c]=find(L==jkk);
        lent=length(r);
        if lent < 9
            for jj=1:lent
                L(r(jj),c(jj))=0;
            end
        end
        if lent > 25
            if min(sqrt((fullnode(:,i,1)-mean(c)).^2+(fullnode(:,i,2)-mean(r)).^2))<9;
                for jj=1:lent
                    Lhuge(r(jj),c(jj))=1;
                end
            end
        end
    end

    redd2=(L>0);
```

```
[X Y]=meshgrid(1:size(redd2,2),1:size(redd2,1));
xpot=sort(fullnode(:,i,1));


Xg=X>mean(xpot(1:col));
Xl=X<mean(xpot(end-col+1:end));


ptm=pt-[0 0 0 cvf*(dispT(i)-dispT(2))];
Yl=Y<polyval(pb,X);
Yg=Y>polyval(ptm,X);

limt=((Xg.*Xl.*Yl.*Yg)+squeeze(sum(inel(:,i,:,:),1)))>0;

redd2=redd2.*limt;
redd2=(redd2+Lhuge.*Yl.*Yg)>0;

[L,num] = bwlabel(redd2,8);
for jkk=1:num
    [r c]=find(L==jkk);
    lent=length(r);
    if lent < 9
        for jj=1:lent
            L(r(jj),c(jj))=0;
        end
    end
end
redd2=(L>0);

redd2=redd2*.5;
yel=0;%redd-redd2;
gre=gre+(redd-redd2);
%
%     imgd(:,:,1)=((inten(:,:,i)/255.*(1-redd2)+redd2).*(1-yel)+yel).*(1-gre);
%     imgd(:,:,2)=(inten(:,:,i)/255.*(1-redd2).*(1-yel)+yel).*(1-gre)+gre;
%     imgd(:,:,3)=(inten(:,:,i)/255.*(1-redd2).*(1-yel)).*(1-gre);
%
imgd(:,:,1)=((inten(:,:,i)/200.*(gre).*(1-2*redd2)+2*redd2));


imgd=imgd.*(imgd<=1)+(imgd>1);
imgd=imgd.*(imgd>0);

subplot('Position',[0 0 .5 1]);
%if i<=damivis2
image(imgd,'CDataMapping','scaled');axis image

if i>=gf
    ds=['FAIL disp. = ',num2str(dispT(i+1))];
    text(10,10,ds,'Color',[1 0 0],'FontSize', 11,'FontWeight', 'bold');
elseif length(find(pf==i))>0
    ds=['FAIL disp. = ',num2str(dispT(i+1))];
    text(10,10,ds,'Color',[1 0 0],'FontSize', 11,'FontWeight', 'bold');
elseif length(find(yd==i))>0
    ds=['YIELD disp. = ',num2str(dispT(i+1))];
    text(10,10,ds,'Color',[1 1 0],'FontSize', 11,'FontWeight', 'bold');
else
    ds=['disp. = ',num2str(dispT(i+1))];
    text(10,10,ds,'Color',[1 1 1],'FontSize', 11,'FontWeight', 'bold');
end
hold on
for ff=1:size(elem,1)
    xs=fullnode(elem(ff,:),i,1);
    ys=fullnode(elem(ff,:),i,2);
    plot([xs;xs(1)],[ys;ys(1)],'Color',[.7 .7 .7]);
end
hold off
axis off

subplot('Position',[.5 0 .5 1]);%[left bottom width height]



[yd xd]=find(redd2.*(squeeze(inel2(1,i,:,:))));
eld=[];
xis=[];
etas=[];
xdam=[];
ydam=[];
for iu=1:length(yd)
    eld(iu)=find(inel(:,i,yd(iu),xd(iu)));
    Xc=fullnode(elem(eld(iu),:),i,1);
    Yc=fullnode(elem(eld(iu),:),i,2);
    [xi eta]=invisomap(xd(iu),yd(iu),Xc,Yc);
    xis(iu)=xi;
    etas(iu)=eta;
end
```

```
    xid=[xid xis];
    etad=[etad etas];
    elsd=[elsd eld];
    for iu=1:length(elsd)
        Xc=fullnode(elem(elsd(iu),:),i,1);
        Yc=fullnode(elem(elsd(iu),:),i,2);
        [x y]=isomap2(xid(iu),etad(iu),Xc,Yc);
        xdam(iu)=x;
        ydam(iu)=y;
    end
    numdam(i)=length(elsd);


    image(real(Rv(:,:,i+1)),'CDataMapping','scaled');axis image
    colormap jet
    colorbar

    hold on

    for ff=1:size(elem,1)
        xs=fullnode(elem(ff,:),i,1);
        ys=fullnode(elem(ff,:),i,2);
        plot([xs;xs(1)],[ys;ys(1)],'w');
    end

    hold off
    axis off
    drawnow;
    initdam(i)=length(nonzeros(redd2));

end
```

corrcoef_vector.m

```
function [rho,r2,err] = corrcoef_vector(t1, t2)

z=t1(:,1)+i*t1(:,2);
w=t2(:,1)+i*t2(:,2);
n=length(z);
zm=mean(z);
wm=mean(w);
sz=sum(conj(z-zm).*(z-zm))/n;
sw=sum(conj(w-wm).*(w-wm))/n;
if (sqrt(sz)*sqrt(sw)) ==0
    rho=0;
    r2=0;
    err=zeros(1,n);
else
szw=sum(conj(z-zm).*(w-wm))/n;
rzw=szw/(sqrt(sz)*sqrt(sw));
r2=rzw*conj(rzw);
rho=sqrt(r2);

beta=rzw*sw/sz;
alph=wm-beta*zm;
err=w-beta*z+alph;
end
```

invisomap.m

```
function [xi eta]=invisomap(x,y,X,Y)
%inverse isoparametric mapping
a1=-X(1)+X(2)+X(3)-X(4);
a2=-X(1)-X(2)+X(3)+X(4);
a3=X(1)-X(2)+X(3)-X(4);
a4=X(1)+X(2)+X(3)+X(4)-4*x;
b1=-Y(1)+Y(2)+Y(3)-Y(4);
b2=-Y(1)-Y(2)+Y(3)+Y(4);
b3=Y(1)-Y(2)+Y(3)-Y(4);
b4=Y(1)+Y(2)+Y(3)+Y(4)-4*y;


A=a2*b3-a3*b2;

B=(a2*b1-a1*b2)+(a4*b3-a3*b4);
C=a4*b1-a1*b4;

%Aeta^2+Beta+C=0
if A==0
    eta=-C/B;
else
```

```
    eta=(-B+sqrt(B^2-4*A*C))/(2*A);
    if eta>1
    eta=(-B-sqrt(B^2-4*A*C))/(2*A);
    end
end

if (b1+b3*eta)==0
    xi=-(a4+a2*eta)/(a1+a3*eta);

else
    xi=-(b4+b2*eta)/(b1+b3*eta);

end
```

APPENDIX N

Matlab code to calculate Lagrangian strain

This appendix contains the Matlab codes used to calculate Lagrangian strain fields in Chapters 5 and 7. In Chapter 5, four-node elements are used to calculate principal strain fields based on the displacement of fiduciary markers. The file **four_node_strain.m** creates bright field images from the raw QPLI data by averaging the intensity of every 20 frames. These images are then used to track fiduciary marker displacements using ProAnalyst 3D (Xcitex, Inc.; Cambridge, MA). The marker displacements are then loaded back into Matlab by **four_node_strain.m**, and the function **green2.m** is called to calculate the Lagrangian strain tensor for each element based on plane strain theory (Fung, 1996). Collectively, the functions **infstrain.m** and **inf2green.m** serve the same purpose as **green2.m**, but calculate Lagrangian strain in a two-step process, which allows **four_node_strain.m** to average the nodal values between the two steps. The file **infstrain.m** only calculates the deformation gradient tensor, which **inf2green.m** then uses to calculate the Lagrangian strain tensor. Finally, **four_node_strain.m** plots the ε_1 field for a specified alignment map.

In Chapter 7, vector correlation tracking is implemented as detailed in Section 7.2 and Appendix P. Based on the virtual marker displacements created by

codes in Appendix P, **three_node_strain.m** calculates and displays the ε_1 field by first creating three-node elements from the virtual markers through Delaunay triangulation (Delaunay, 1934). To calculate the Lagrangian strain in each element, **three_node_strain.m** calls **green3.m**, which functions the same as **green2.m**, only it can handle three-node elements rather than four.

four_node_strain.m

```
%
disp('creating brightfield images for fiducial tracking...');
ii=1;
clear strainimg
clear I

%define ROI for QPLI analysis
intpROI=[min(intpROI(:,1)) min(intpROI(:,2)) max(intpROI(:,3)) max(intpROI(:,4))]

%load QPLI images
for j=round(imgstart):round(imgend)%450
    ad=20*j-20;
    for i=beg+ad:beg+ad+19
        img=imread([specID,'_fail_img.tif'],i);

        I(:,:,i-beg-ad+1)=img(intpROI(2):intpROI(4),intpROI(1):intpROI(3));

    end
    %collect the average of every 20 images
    strainimg(:,:,j-round(imgstart)+1)=mean(I,3);
end

timeimg=round(imgstart):round(imgend);
timeimg=timeimg/25;
save strainimg strainimg

load strainimg
strainim=uint8(strainimg);
for i=1:size(strainimg,3)
    imwrite(strainim(:,:,i),['strain',num2str(i),'.tif'],'tif');
end
%%
%%%%%%%%%%%%%%%%
%TRACK MARKERS WITH PROANALYST
%%%%%%%%%%%%%%%%%%

%%
clear all

load mechdata
timeimg=round(imgstart):round(imgend);
timeimg=timeimg/25;
dispT = interp1(fail(1,:),fail(2,:),timeimg);
dispT=dispT-fail(2,offstart);
fail(2,:)=fail(2,:)-fail(2,offstart);
[dd refS]=min(abs(dispT));

%loads proanalyst tracking output: strain.txt
strainraw=textread(['strain.txt'],'%f','headerlines', 11, 'delimiter', ',');
strainraw=reshape(strainraw,numnode*2+2,length(strainraw)/(numnode*2+2));
strainraw(1:2,:)=[];

xnodef=strainraw((1:2:size(strainraw,1)),1:size(strainraw,2));
ynodef=strainraw((2:2:size(strainraw,1)),1:size(strainraw,2));


clear elem
numnode=row*col;
```

```
Nx=row;
for j=1:col-1
    for i=1:row-1
        elem(i+(Nx-1)*(j-1),:)=[i+1+Nx*(j-1) i+Nx*(j-1)  i+Nx*j i+1+Nx*j  ];
    end
end
save mechdata2
plot(xnodef(:,:)',ynodef(:,:)');axis image;axis ij;axis off;

%

%numbers nodes and creates mesh for strain analysis
%left mouse button picks points- start in bottom right and move left
%use right mouse button to select last node and close program
clear nodefull
nodefull(:,:,1)=xnodef;
nodefull(:,:,2)=ynodef;
save straindata nodefull strainimg
fullnode=labelnodes2D(nodefull);
save fullnode fullnode
%plots node order for visual check
scrsz = get(0,'ScreenSize');
figure('Position',[100 50 scrsz(3)-200 scrsz(4)-170])
i=1;
hold off
image(strainimg(:,:,i),'CDataMapping','scaled');
axis image;
axis off
colormap(gray);
hold on;
for f=1:size(fullnode,1)
    text(fullnode(f,i,1),fullnode(f,i,2),num2str(f),'Color','g');
end
for ff=1:size(elem,1)
    xs=fullnode(elem(ff,:),i,1);
    ys=fullnode(elem(ff,:),i,2);
    xs=(xs+mean(xs))/2;
    ys=(ys+mean(ys))/2;
    plot([xs;xs(1)],[ys;ys(1)],li(:,ff));
end
save fullnode
%%
%this module calculates the principal strain field at yield
clear all
load mechdata2
load fullnode
load stiff
for i=1:size(elem,1)
    data(:,:,i)=[fullnode(elem(i,1),:,1)' fullnode(elem(i,1),:,2)' fullnode(elem(i,2),:,1)'
fullnode(elem(i,2),:,2)' fullnode(elem(i,3),:,1)' fullnode(elem(i,3),:,2)' fullnode(elem(i,4),:,1)'
fullnode(elem(i,4),:,2)'];
    %X1 Y1 X2 Y2 X3 Y3 X4 Y4
    [Exx Eyy Exy Ezz E1 E2 dir1 dir2]=green2(data(:,:,i),0,0,refS);
    MPS(i,:)=E1';
    MPD(i,:,:)=dir1';
    [dUdX dVdX dUdY dVdY]=infstrain(data(:,:,i),-1,-1,refS);%1
    strain2(:,:,i,1)=[dUdX dVdX dUdY dVdY];
    [dUdX dVdX dUdY dVdY]=infstrain(data(:,:,i),1,-1,refS);%2
    strain2(:,:,i,2)=[dUdX dVdX dUdY dVdY];
    [dUdX dVdX dUdY dVdY]=infstrain(data(:,:,i),1,1,refS);%3
    strain2(:,:,i,3)=[dUdX dVdX dUdY dVdY];
    [dUdX dVdX dUdY dVdY]=infstrain(data(:,:,i),-1,1,refS);%4
    strain2(:,:,i,4)=[dUdX dVdX dUdY dVdY];
    [dUdX dVdX dUdY dVdY]=infstrain(data(:,:,i),0,-1,refS);%5
    strain2(:,:,i,5)=[dUdX dVdX dUdY dVdY];
    [dUdX dVdX dUdY dVdY]=infstrain(data(:,:,i),1,0,refS);%6
    strain2(:,:,i,6)=[dUdX dVdX dUdY dVdY];
    [dUdX dVdX dUdY dVdY]=infstrain(data(:,:,i),0,1,refS);%7
    strain2(:,:,i,7)=[dUdX dVdX dUdY dVdY];
    [dUdX dVdX dUdY dVdY]=infstrain(data(:,:,i),-1,0,refS);%8
    strain2(:,:,i,8)=[dUdX dVdX dUdY dVdY];
    [dUdX dVdX dUdY dVdY]=infstrain(data(:,:,i),0,0,refS);%9
    strain2(:,:,i,9)=[dUdX dVdX dUdY dVdY];

end
row=col-1;
dum=row;
row=size(elem,1)/row;
col=dum;
%vertical averaging
strain2b=strain2;
for i=1:row
    for j=1:col-1
        clear dum
        dum=.5*(strain2(:,:,i+(j-1)*row,[4 7 3])+strain2(:,:,i+(j)*row,[1 5 2]));
        strain2(:,:,i+(j-1)*row,[4 7 3])=dum;
        strain2(:,:,i+(j)*row,[1 5 2])=dum;
        %disp('avging ',num2str(i+(j-1)), ' and '
    end
```

```
end
%horizontal averaging
for j=1:col
    for i=1:row-1
        clear dum
        dum=.5*(strain2(:,:,i+(j-1)*row,[1 8 4])+strain2(:,:,i+(j-1)*row+1,[2 6 3]));
        strain2(:,:,i+(j-1)*row,[1 8 4])=dum;
        strain2(:,:,i+(j-1)*row+1,[2 6 3])=dum;
    end
end


%[Exx Eyy Exy Ezz E1 E2 dir1 dir2]=green2(data(:,:,i),0,0,ref);
clear X Y
for i = 1:size(elem,1)

    X(:,:,i)=[data(:,1,i) data(:,3,i) data(:,5,i) data(:,7,i) (data(:,1,i)+data(:,3,i))/2
(data(:,3,i)+data(:,5,i))/2 (data(:,5,i)+data(:,7,i))/2 (data(:,1,i)+data(:,7,i))/2
(data(:,1,i)+data(:,3,i)+data(:,5,i)+data(:,7,i))/4];
    Y(:,:,i)=[data(:,2,i) data(:,4,i) data(:,6,i) data(:,8,i) (data(:,2,i)+data(:,4,i))/2
(data(:,4,i)+data(:,6,i))/2 (data(:,6,i)+data(:,8,i))/2 (data(:,2,i)+data(:,8,i))/2
(data(:,2,i)+data(:,4,i)+data(:,6,i)+data(:,8,i))/4];
    for j = 1:9
        [Exx Eyy Exy Ezz E1 E2 dir1
dir2]=inf2green(strain2b(:,1,i,j),strain2b(:,2,i,j),strain2b(:,3,i,j),strain2b(:,4,i,j));
        strain3b(:,:,i,j)=[Exx Eyy Exy Ezz E1 E2];
        [Exx Eyy Exy Ezz E1 E2 dir1
dir2]=inf2green(strain2(:,1,i,j),strain2(:,2,i,j),strain2(:,3,i,j),strain2(:,4,i,j));
        strain3(:,:,i,j)=[Exx Eyy Exy Ezz E1 E2];
        for k=1:length(E1)
            if (j == 2) | (j == 6) | (j == 9) | (j == 5) | (mod(i,row) == 0) | (i > (length(elem)-row))
                if E1(k) > 0
                    upos(k,9*(i-1)+j)=dir1(k,1).*E1(k);
                    vpos(k,9*(i-1)+j)=dir1(k,2).*E1(k);
                    uneg(k,9*(i-1)+j)=0;
                    vneg(k,9*(i-1)+j)=0;
                else
                    upos(k,9*(i-1)+j)=0;
                    vpos(k,9*(i-1)+j)=0;
                    uneg(k,9*(i-1)+j)=dir1(k,1).*E1(k);
                    vneg(k,9*(i-1)+j)=dir1(k,2).*E1(k);
                end
            else
                upos(k,9*(i-1)+j)=0;
                vpos(k,9*(i-1)+j)=0;
                uneg(k,9*(i-1)+j)=0;
                vneg(k,9*(i-1)+j)=0;
            end
        end
    end
end
X=reshape(X,k,9*(i-1)+j);
Y=reshape(Y,k,9*(i-1)+j);
j=0;

ff=figure;

[MMPS ind]=max(MPS);
for j=75

    hold on;
    node=fullnode;

    for i=1:length(elem)

        ch='none';
        Xq=[node(elem(i,1),j,1) node(elem(i,2),j,1) node(elem(i,3),j,1) node(elem(i,4),j,1)
(node(elem(i,1),j,1)+node(elem(i,2),j,1))/2 (node(elem(i,2),j,1)+node(elem(i,3),j,1))/2
(node(elem(i,3),j,1)+node(elem(i,4),j,1))/2 (node(elem(i,1),j,1)+node(elem(i,4),j,1))/2
(node(elem(i,1),j,1)+node(elem(i,2),j,1)+node(elem(i,3),j,1)+node(elem(i,4),j,1))/4];
        g=2;
        Yq=[node(elem(i,1),j,g) node(elem(i,2),j,g) node(elem(i,3),j,g) node(elem(i,4),j,g)
(node(elem(i,1),j,g)+node(elem(i,2),j,g))/2 (node(elem(i,2),j,g)+node(elem(i,3),j,g))/2
(node(elem(i,3),j,g)+node(elem(i,4),j,g))/2 (node(elem(i,1),j,g)+node(elem(i,4),j,g))/2
(node(elem(i,1),j,g)+node(elem(i,2),j,g)+node(elem(i,3),j,g)+node(elem(i,4),j,g))/4];

        uu=5;%1PS
        hh2(i,1)=fill(Xq([1 5 9 8]),Yq([1 5 9 8]),reshape(100*strain3(j,uu,i,[1 5 9 8]),1,4),'LineStyle',ch);
        hh2(i,2)=fill(Xq([5 2 6 9]),Yq([5 2 6 9]),reshape(100*strain3(j,uu,i,[5 2 6 9]),1,4),'LineStyle',ch);
        hh2(i,3)=fill(Xq([8 9 7 4]),Yq([8 9 7 4]),reshape(100*strain3(j,uu,i,[8 9 7 4]),1,4),'LineStyle',ch);
        hh2(i,4)=fill(Xq([9 6 3 7]),Yq([9 6 3 7]),reshape(100*strain3(j,uu,i,[9 6 3 7]),1,4),'LineStyle',ch);

        plot(Xq([1 2 3 4 1]),Yq([1 2 3 4 1]),'k');
        alpha(hh2(i,1),1)
        alpha(hh2(i,2),1)
        alpha(hh2(i,3),1)
        alpha(hh2(i,4),1)
        colormap('jet');
        caxis([0 80]);
```

```
    end
    colormap('gray');
    caxis([0 70])
    %alpha(hh2,.5)

    axis square
    axis tight

end

for i=1:length(elem)
    xx(i)=mean(node(elem(i,:),j,1));
    yy(i)=mean(node(elem(i,:),j,2));

    text(xx(i),yy(i),['El ',num2str(i),':
',num2str(round(100*MPS(i,j))),'%'],'FontWeight','bold','HorizontalAlignment','center');
end

colorbar

axis ij
```

three_node_strain.m

```
load TRACKCOMPLETE

goodi=find((max(ddif(:,2:end),[],2)<2));
xtotf=xtot(goodi,:);
ytotf=ytot(goodi,:);
maxcorf=maxcor(goodi,:);
maxcorfB=maxcorB(goodi,:);
%%

%  xfil=xtot(find(skipk==0),:);
%  yfil=ytot(find(skipk==0),:);
xfil=xtotf;
yfil=ytotf;
mcor=maxcorf;%maxcor(find(skipk==0),:);
mcorB=maxcorfB;
xfils=xfil(:,1:length(tS)-1);
yfils=yfil(:,1:length(tS)-1);
xfils2=xfil(:,2:length(tS));
yfils2=yfil(:,2:length(tS));
dist=((xfils-xfils2).^2+(yfils-yfils2).^2).^.5;
mdist=(max(dist,[],2));


xff1=xfil(find(mdist<500),:);
yff1=yfil(find(mdist<500),:);%used 1.75 before, normally 2.5
mcf1=mcor(find(mdist<500),:);
mcf1B=mcorB(find(mdist<500),:);
avgm=mean(mcf1B,2);
gdpt=ones(size(xff1,1),1);
fr=length(tS)

%distt=((xff1(:,4)-xff1(:,10)).^2+(yff1(:,4)-yff1(:,10)).^2).^.5;
distt=((xff1(:,2)-xff1(:,5)).^2+(yff1(:,2)-yff1(:,5)).^2).^.5;

%%

%figure;
for k=1:200
    %right
    clf reset
    qpt=((avgm<.9).*gdpt);
    qpt2=((distt>.5).*gdpt);
    i=fr;
    image(Im,'CDataMapping','scaled');
    axis image;axis off
    colormap gray
    %hold on;plot(xfil(find(mdist<1.75),1:i)',yfil(find(mdist<1.75),1:i)','w')
    hold on;plot(xff1(find(gdpt),i),yff1(find(gdpt),i),'g.','MarkerSize',6)
    plot(xff1(find(qpt),i),yff1(find(qpt),i),'r.','MarkerSize',6)
    plot(xff1(find(qpt2),i),yff1(find(qpt2),i),'y.','MarkerSize',6)
    %title(dispS(i));
    drawnow;
    [x y but]=ginput(1);
    if but~=1
        break
    end
    mindist=((xff1-x).^2+(yff1-y).^2).^.5;
    [minu mind]=min(mindist(:,fr));
    gdpt(mind)=0;
```

```
end
%
dfrom0=yff1(:,fr).^2+yff1(:,fr).^2;
gdpt(find(dfrom0<5))=0;
%IN = inpolygon(xff1(:,16),yff1(:,16),xr,yr);
%
yff=yff1(find(gdpt),:);
xff=xff1(find(gdpt),:);
mcf=mcf1(find(gdpt),:);
mcfB=mcf1B(find(gdpt),:);

%%
%load trackptsnewed2
mcf4=ones(size(mcfB,1),size(mcfB,2));
mcf4(:,2:length(tS))=mcf(:,2:length(tS))-mcf(:,1:length(tS)-1);
mcf2=(mcf4.*(mcf4<0));
mcf3=(mcf2.*(mcf2>-.2))-.2*(mcf2<=-.2);
mcind=255-round(255*5*(mcf3+.2));
col=jet;
tri = delaunay(xff(:,1),yff(:,1),{'Qt','Qbb','Qc','Qz'});
clear areat perim MPS E1 nodeExx nodeEyy nodeExy Exxs Eyys Exys dir1 dir2 upos vpos Xv Yv
for k=1:size(tri,1)
    areat(k,:)=polyarea(xff(tri(k,:),1),yff(tri(k,:),1));
    perim(k,:)=sum(sqrt((yff(tri(k,[1 2 3]),1)-yff(tri(k,[2 3 1]),1)).^2+(xff(tri(k,[1 2 3]),1)-xff(tri(k,[2 3
1]),1)).^2));
end
%tri(find(perim>(sqrt(2)*median(perim))),:)=[];
tri(find(((perim.^2)>(50*areat))|(perim>(3*median(perim)))),:)=[];

%tri(find(perim>(5*median(perim))),:)=[];

hold off

% image(img)
hold on;
for k=1:size(tri,1)
    fill(xff(tri(k,:),1),yff(tri(k,:),1),1);%,'EdgeColor',[0 0 0]);
end


for k=1:size(tri,1)
    data=[xff(tri(k,1),:)' yff(tri(k,1),:)' xff(tri(k,2),:)' yff(tri(k,2),:)' xff(tri(k,3),:)'
yff(tri(k,3),:)'];
    [Exx Eyy Exy Ezz E1 E2 dir1 dir2]=green3(data,1/3,1/3,1/3,1);
    MPS(k,:)=E1;
    MPShear(k,:)=(E1-E2)/2;
    Exxs(k,:)=Exx;
    Eyys(k,:)=Eyy;
    Exys(k,:)=Exy;
    upos(k,:)=dir1(:,1).*E1;
    vpos(k,:)=dir1(:,2).*E1;
    Xv(k,:)=mean(xff(tri(k,:),:));
    Yv(k,:)=mean(yff(tri(k,:),:));
end

for i=1:size(xff,1)

    nodeExx(i,:)=mean(Exxs([find(tri(:,1)==i);find(tri(:,2)==i);find(tri(:,3)==i)],:),1);
    nodeEyy(i,:)=mean(Eyys([find(tri(:,1)==i);find(tri(:,2)==i);find(tri(:,3)==i)],:),1);
    nodeExy(i,:)=mean(Exys([find(tri(:,1)==i);find(tri(:,2)==i);find(tri(:,3)==i)],:),1);
    for j=1:size(xff,2)
        if isnan(nodeExy(i,j))
            E1(i,j)=0;
        else
            g=[nodeExx(i,j), nodeExy(i,j); nodeExy(i,j), nodeEyy(i,j)];
            [vec princ]=eig(g);
            E1(i,j)=max([princ(1,1) princ(2,2)]);
            E2(i,j)=min([princ(1,1) princ(2,2)]);

        end
        %Exx1=node
    end
end
E12=(E1-E2)/2;


%%
img(:,:,1)=uint8(round(Im));
img(:,:,2)=uint8(round(Im));
img(:,:,3)=uint8(round(Im));
img=uint8(img);

subplot('Position',[sMPS 0 .49 1]); i=42;
image(img,'CDataMapping','scaled');hold on;
for k=1:size(tri,1)
    h=fill(xff(tri(k,:),i),yff(tri(k,:),i),E1(tri(k,:),i),'LineStyle','none');%,'EdgeColor',[0 0 0]);

end
```

```
axis ij
axis image
axis off
set(gcf,'InvertHardCopy', 'off');
set(gca,'CLim',[0 1.2])
colormap((jet))
[ar br]=max(E1(:,i))
hold on;plot(xff(br,i),yff(br,i),'wo','LineWidth',1.5)


E12=(E1-E2)/2;
subplot('Position',[sShear 0 .49 1]);i=42;
image(img,'CDataMapping','scaled');hold on;
for k=1:size(tri,1)
    h=fill(xff(tri(k,:),i),yff(tri(k,:),i),E12(tri(k,:),i),'LineStyle','none');%,'EdgeColor',[0 0 0]);

end
axis ij
axis image
axis off
set(gcf,'InvertHardCopy', 'off');
set(gca,'CLim',[0 .6])
colormap((jet))
[ar br]=max(E12(:,i))
hold on;plot(xff(br,i),yff(br,i),'wo','LineWidth',1.5)
```

green2.m

```
function [Exx Eyy Exy Ezz E1 E2 dir1 dir2]=green2(data,xi,eta,ref)

% Kyle Quinn, 2006
% ******************************************************
% Data should be in the following format                *
% X1 Y1 X2 Y2 X3 Y3 X4 Y4                               *
% ******************************************************

%   Nodes must be labeled like this:
%     3---------4
%    /         /
%   /         /
%  2---------1

% Coordinates
Xone=data(:,1);
Xtwo=data(:,3);
Xthree=data(:,5);
Xfour=data(:,7);
Yone=data(:,2);
Ytwo=data(:,4);
Ythree=data(:,6);
Yfour=data(:,8);

% Initial coordinates of four points
X1=Xone(ref);
Y1=Yone(ref);
X2=Xtwo(ref);
Y2=Ytwo(ref);
X3=Xthree(ref);
Y3=Ythree(ref);
X4=Xfour(ref);
Y4=Yfour(ref);

% % Displacements

  u1=Xone-X1;
  u2=Xtwo-X2;
  u3=Xthree-X3;
  u4=Xfour-X4;
  v1=Yone-Y1;
  v2=Ytwo-Y2;
  v3=Ythree-Y3;
  v4=Yfour-Y4;
% end

% The isoparametric strain-differentials: compute strain at
%   center of element

%fn of eta and time
dUdxi=(-1/4)*(1-eta)*u1+(1/4)*(1-eta)*u2+(1/4)*(1+eta)*u3-(1/4)*(1+eta)*u4;
dYdxi=(-1/4)*(1-eta)*Y1+(1/4)*(1-eta)*Y2+(1/4)*(1+eta)*Y3-(1/4)*(1+eta)*Y4;
%fn of xi and time
dUdeta=(-1/4)*(1-xi)*u1-(1/4)*(1+xi)*u2+(1/4)*(1+xi)*u3+(1/4)*(1-xi)*u4;
```

```
dYdeta=(-1/4)*(1-xi)*Y1-(1/4)*(1+xi)*Y2+(1/4)*(1+xi)*Y3+(1/4)*(1-xi)*Y4;

% Elements of the Jacobian
%fn of eta and time
dXdxi=(-1/4)*(1-eta)*X1+(1/4)*(1-eta)*X2+(1/4)*(1+eta)*X3-(1/4)*(1+eta)*X4;
dVdxi=(-1/4)*(1-eta)*v1+(1/4)*(1-eta)*v2+(1/4)*(1+eta)*v3-(1/4)*(1+eta)*v4;
%fn of xi and time
dXdeta=(-1/4)*(1-xi)*X1-(1/4)*(1+xi)*X2+(1/4)*(1+xi)*X3+(1/4)*(1-xi)*X4;
dVdeta=(-1/4)*(1-xi)*v1-(1/4)*(1+xi)*v2+(1/4)*(1+xi)*v3+(1/4)*(1-xi)*v4;


% Assemble the inverse Jacobian
IJ=inv([dXdxi dYdxi; dXdeta dYdeta]);
A= IJ(1,1);
B=IJ(1,2);
C=IJ(2,1);
D=IJ(2,2);

% Compute elements of the deformation gradiant
dUdX=(A*dUdxi)+(B*dUdeta);
dUdY=(C*dUdxi)+(D*dUdeta);
dVdX=(A*dVdxi)+(B*dVdeta);
dVdY=(C*dVdxi)+(D*dVdeta);

F=[dUdX+1 dUdY; dVdX dVdY+1];
lamZ=1./((dUdX+1).*(dVdY+1)-dUdY.*dVdX);
Ezz=0.5*(lamZ.^2-1);
%  assume incompressibility to estimate Ezz


  Exx=dUdX +(1/2)*(dUdX.^2+dVdX.^2);
  Eyy=dVdY+(1/2)*(dVdY.^2+dUdY.^2);
  Exy=(1/2)*(dUdY+dVdX+(dUdX.*dUdY)+(dVdX.*dVdY));


  %find principle strains
  for i=1:length(Exx)
      g=[Exx(i), Exy(i); Exy(i), Eyy(i)];
      [vec princ]=eig(g);
      E1(i)=princ(1,1);
      E2(i)=princ(2,2);
      dir1(i,:)=vec(:,1);
      dir2(i,:)=vec(:,2);
%        disp(dir1(i,:))
%   disp(eigs(g));
  if (E2(i)) > (E1(i))
          dum=E1(i);
          E1(i)=E2(i);
          E2(i)=dum;
          dum=dir1(i,:);
          dir1(i,:)=dir2(i,:);
          dir2(i,:)=dum;
      end
  end
  E1=E1';
  E2=E2';
```

infstrain.m

```
function [dUdX dVdX dUdY dVdY]=infstrain(data,xi,eta,ref)


% ******************************************************
% Data should be in the following format                 *
% X1 Y1 X2 Y2 X3 Y3 X4 Y4                                *
% ******************************************************

% Coordinates
Xone=data(:,1);
Xtwo=data(:,3);
Xthree=data(:,5);
Xfour=data(:,7);
Yone=data(:,2);
Ytwo=data(:,4);
Ythree=data(:,6);
Yfour=data(:,8);

% Initial coordinates of four points
X1=Xone(ref);
Y1=Yone(ref);
X2=Xtwo(ref);
Y2=Ytwo(ref);
X3=Xthree(ref);
Y3=Ythree(ref);
X4=Xfour(ref);
```

```
Y4=Yfour(ref);


% % Displacements

  u1=Xone-X1;
  u2=Xtwo-X2;
  u3=Xthree-X3;
  u4=Xfour-X4;
  v1=Yone-Y1;
  v2=Ytwo-Y2;
  v3=Ythree-Y3;
  v4=Yfour-Y4;
% end

% The isoparametric strain-differentials: compute strain at
%   center of element

%fn of eta and time
dUdxi=(-1/4)*(1-eta)*u1+(1/4)*(1-eta)*u2+(1/4)*(1+eta)*u3-(1/4)*(1+eta)*u4;
dYdxi=(-1/4)*(1-eta)*Y1+(1/4)*(1-eta)*Y2+(1/4)*(1+eta)*Y3-(1/4)*(1+eta)*Y4;
%fn of xi and time
dUdeta=(-1/4)*(1-xi)*u1-(1/4)*(1+xi)*u2+(1/4)*(1+xi)*u3+(1/4)*(1-xi)*u4;
dYdeta=(-1/4)*(1-xi)*Y1-(1/4)*(1+xi)*Y2+(1/4)*(1+xi)*Y3+(1/4)*(1-xi)*Y4;

% Elements of the Jacobian
%fn of eta and time
dXdxi=(-1/4)*(1-eta)*X1+(1/4)*(1-eta)*X2+(1/4)*(1+eta)*X3-(1/4)*(1+eta)*X4;
dVdxi=(-1/4)*(1-eta)*v1+(1/4)*(1-eta)*v2+(1/4)*(1+eta)*v3-(1/4)*(1+eta)*v4;
%fn of xi and time
dXdeta=(-1/4)*(1-xi)*X1-(1/4)*(1+xi)*X2+(1/4)*(1+xi)*X3+(1/4)*(1-xi)*X4;
dVdeta=(-1/4)*(1-xi)*v1-(1/4)*(1+xi)*v2+(1/4)*(1+xi)*v3+(1/4)*(1-xi)*v4;


% Assemble the inverse Jacobian
IJ=inv([dXdxi dYdxi; dXdeta dYdeta]);
A= IJ(1,1);
B=IJ(1,2);
C=IJ(2,1);
D=IJ(2,2);

% Compute elements of the deformation gradiant
dUdX=(A*dUdxi)+(B*dUdeta);
dUdY=(C*dUdxi)+(D*dUdeta);
dVdX=(A*dVdxi)+(B*dVdeta);
dVdY=(C*dVdxi)+(D*dVdeta);
```

inf2green.m

```
function [Exx Eyy Exy Ezz E1 E2 dir1 dir2]=inf2green(dUdX,dVdX,dUdY,dVdY)

% Compute the Green's strain
%  assume incompressibility to estimate Ezz


  Exx=dUdX +(1/2)*(dUdX.^2+dVdX.^2);
  Eyy=dVdY+(1/2)*(dVdY.^2+dUdY.^2);
  Exy=(1/2)*(dUdY+dVdX+(dUdX.*dUdY)+(dVdX.*dVdY));

  num=(2.*Exy.*Exy-2*Exx.*Eyy-Exx-Eyy);
  den=4.*Exx.*Eyy+2.*Exx+2.*Eyy+1-4.*Exy+.00000001;

  Ezz=num./den;

  %find principle strains
  for i=1:length(Exx)
      g=[Exx(i), Exy(i); Exy(i), Eyy(i)];
      [vec princ]=eig(g);
      E1(i)=princ(1,1);
      E2(i)=princ(2,2);
      dir1(i,:)=vec(1,1:2);
      dir2(i,:)=vec(2,1:2);
      if (E2(i)) > (E1(i))
          dum=E1(i);
          E1(i)=E2(i);
          E2(i)=dum;
          dum=dir1(i,:);
          dir1(i,:)=dir2(i,:);
          dir2(i,:)=dum;
      end
  end
  E1=E1';
  E2=E2';
```

green3.m

```
function [Exx Eyy Exy Ezz E1 E2 dir1 dir2]=green3(data,xi1,xi2,xi3,ref)

% Kyle Quinn, 2009
% ****************************************************
% Data should be in the following format                *
% X1 Y1 X2 Y2 X3 Y3 X4 Y4                               *
% ****************************************************

%   Nodes must be labeled like this:
%     3
%    / \
%   /   \
%  2-----1

% Coordinates
Xone=data(:,1);
Xtwo=data(:,3);
Xthree=data(:,5);

Yone=data(:,2);
Ytwo=data(:,4);
Ythree=data(:,6);


% Initial coordinates of four points
X1=Xone(ref);
Y1=Yone(ref);
X2=Xtwo(ref);
Y2=Ytwo(ref);
X3=Xthree(ref);
Y3=Ythree(ref);


% % Displacements

  u1=Xone-X1;
  u2=Xtwo-X2;
  u3=Xthree-X3;

  v1=Yone-Y1;
  v2=Ytwo-Y2;
  v3=Ythree-Y3;

% end

% The isoparametric strain-differentials: compute strain at
%   center of element

%fn of eta and time

%fn of eta and time
dUdxi2=u2-u1;
dYdxi2=Y2-Y1;
%fn of eta and time
dUdxi3=u3-u1;
dYdxi3=Y3-Y1;

% Elements of the Jacobian
%fn of eta and time

%fn of eta and time
dXdxi2=X2-X1;
dVdxi2=v2-v1;
%fn of eta and time
dXdxi3=X3-X1;
dVdxi3=v3-v1;

% Assemble the inverse Jacobian
IJ=pinv([dXdxi2 dYdxi2; dXdxi3 dYdxi3]);
A= IJ(1,1);
B=IJ(1,2);
C=IJ(2,1);
D=IJ(2,2);


dUdX=(A*dUdxi2)+(B*dUdxi3);
dUdY=(C*dUdxi2)+(D*dUdxi3);
dVdX=(A*dVdxi2)+(B*dVdxi3);
dVdY=(C*dVdxi2)+(D*dVdxi3);


F=[dUdX+1 dUdY; dVdX dVdY+1];
lamZ=1./((dUdX+1).*(dVdY+1)-dUdY.*dVdX);
Ezz=0.5*(lamZ.^2-1);
```

```
% Compute the Green's strain
%  assume incompressibility to estimate Ezz


  Exx=dUdX +(1/2)*(dUdX.^2+dVdX.^2);
  Eyy=dVdY+(1/2)*(dVdY.^2+dUdY.^2);
  Exy=(1/2)*(dUdY+dVdX+(dUdX.*dUdY)+(dVdX.*dVdY));

  %find principle strains
  for i=1:length(Exx)
      g=[Exx(i), Exy(i); Exy(i), Eyy(i)];
      [vec princ]=eig(g);
      E1(i)=princ(1,1);
      E2(i)=princ(2,2);
      dir1(i,:)=vec(:,1);
      dir2(i,:)=vec(:,2);
%        disp(dir1(i,:))
%   disp(eigs(g));
  if (E2(i)) > (E1(i))
          dum=E1(i);
          E1(i)=E2(i);
          E2(i)=dum;
          dum=dir1(i,:);
          dir1(i,:)=dir2(i,:);
          dir2(i,:)=dum;
      end
  end
  E1=E1';
  E2=E2';
```

APPENDIX O

Matlab code to detect yield & failure

This appendix provides the Matlab code used to detect yield and failure from the force-displacement data acquired by the Instron described in the studies in Chapters 5-7. The file **detectyield.m**, loads the force-displacement data and calculates the tangent stiffness throughout loading using a centered finite difference approximation (Quinn and Winkelstein, 2007), as described in Chapter 5. The maximum tangent stiffness during loading is identified, and yield is defined for portions of the curve where the tangent stiffness continuously decreases by 10% of the maximum stiffness or more (Quinn and Winkelstein, 2008). When the tangent stiffness becomes negative (the force decreases), failure is also identified. Failures detected at displacements below the point of maximum force were defined as "partial failures", and failure at the point of maximum force was defined as "gross failure".

detectyield.m

```
yieldthresh=.1;%10% of maximum stiffness decrease
%
%detects yield and failure from mechanical data
%%%%%%%%%%%%%%%%%%%%%%%%%%%%%%%%%%%%%%%%%%%%%%%%%%%%%%%%%%%%%%%%%%%%%%%%%%%%%%%
%clear all
yield=[];

load mechdata2

fail=fail';
fail(:,3)=[];


%%%%%%%%%%%%%%%%%%%%%%%%%%%%%%%%%%%%%%%%%%%%%%%%%%%%%%%%%%%%%%%%%%%%%%%%%%%%%%%
% STEP 1:  Create Stiffness by taking Derivative of Force thru
% centered finite differences
%%%%%%%%%%%%%%%%%%%%%%%%%%%%%%%%%%%%%%%%%%%%%%%%%%%%%%%%%%%%%%%%%%%%%%%%%%%%%%%

s1=fail(:,3);
d1=fail(:,2);
s1(1)=[];
d1(1)=[];
s2=fail(:,3);
d2=fail(:,2);
s2(length(s2))=[];
d2(length(d2))=[];

slope(2:length(s2)+1)=(s1-s2)./(d1-d2);
slope(1)=(fail(2,3)-fail(1,3))/(fail(2,2)-fail(1,2));
len=length(fail);
slope(len)=(fail(len,3)-fail(len-1,3))/(fail(len,2)-fail(len-1,2));
fu=find(isnan(slope));
slope(fu)=slope(fu-1);
[val ind]=max(fail(:,3));
% [val2 ind2]=max(oldforce);

for i=100:ind-1;
    if fail(i,2)> fail(ind,2)*.05
        maxstep=i;
        break
    end
end


slopeX=slope;
%filter slopeX once
a=1;
b = [.1 .1 .1 .1 .1 .1 .1 .1 .1 .1];
slopeX(ind+maxstep:length(slopeX))=[];
slopeX=filtfilt(b,a,slopeX);

m=[];n=1;
j=1;jj=2;
for i=4000:ind-2
    %dropping below 0
    if ((slopeX(i:i+2) < 0) & (slopeX(i-4:i-2) >0))& ( length(m) < length(n))
        m(j)=i;
        j=j+1;
    end
    %rising above 0
    if ((slopeX(i:i+2) > 0) & (slopeX(i-4:i-2) <0)) & ( length(m) == length(n))
        n(jj)=i;
        jj=jj+1;
    end
end
if length(m) ~= length(n)
m(length(m)+1)=ind;
end
parts=[n' m'];
parts2=reshape(parts',1,size(parts,2)*size(parts,1));

slope(ind+maxstep:length(slope))=[];
oldforce=slope;

ii=1;

while (ii < 30)

    for i=1:length(parts2)-1;
        %noise=kylefilt(noise,b);
        slope(parts(i):parts(i+1))=filtfilt(b,a,slope(parts(i):parts(i+1)));
    end
    ii=ii+1;

end
```

```
gg=pwd;


%%%%%%%%%%%%%%%%%%%%%%%%%%%%%%%%%%%%%%%%%%%%%%%%%%%%%%%%%%%%%%%%%%%%%%%%%%%%
%  STEP 2:  Determine Maximum Stiffness
%%%%%%%%%%%%%%%%%%%%%%%%%%%%%%%%%%%%%%%%%%%%%%%%%%%%%%%%%%%%%%%%%%%%%%%%%%%%

[B,IX] = sort(slope(1:ind),'descend'); %sort stiffnesses

for i=1:length(B)%length of slope
    stiff=mean(B(1:i));  %mean stiffness of previous points
    if std(B(1:i))*100 > stiff  %if stdev is 100 times greater than mean of max stiffness, then its no longer a
max stiffness pt
        si=i;
        break
    end
end
IX=sort(IX(1:si));
maxstiff=B(1);


%IX is the index for max stiffness
slope2=slope;

%%%%%%%%%%%%%%%%%%%%%%%%%%%%%%%%%%%%%%%%%%%%%%%%%%%%%%%%%%%%%%%%%%%%%%%%%%%%
%  STEP 3:  Find Decreases in Stiffness and Subcatastrophic Failures
%%%%%%%%%%%%%%%%%%%%%%%%%%%%%%%%%%%%%%%%%%%%%%%%%%%%%%%%%%%%%%%%%%%%%%%%%%%%


%start looking at 10% of the Max Stiffness
for i=100:ind-1;
    if slope(i)> .1*maxstiff
       Begin=i;
       % start looking for negative stiffness once stiffness is at 2 N/mm
       % (prevents false positives due to noise)
       break
    end
end

for i=100:ind-1;
    if fail(i,2)> fail(ind,2)*.05
        if fail(Begin,2) < fail(ind,2)*.05
            Begin=i;
            %replace begin with 5% of disp to failure if 10% stiff is too low
            %ensures the yield search can be done without errors

        end
        maxstep=i;
        break
    end
end

% Subcatastophic Failure due to a negative stiffness
XI=[];
j=1;
for i=Begin:ind-1
    if slopeX(i) < 0;
        % if slope is less than 0 note sub-cat failure
        XI(j)=i;
        j=j+1;
    end
end


%Find Yield

XII=[];
j=1;
for i=Begin:ind%-15
    %i
    below=slope(i-maxstep+1:i-1);
    above=slope(i+1:maxstep+i-1);
    belowrev = fliplr(below);
    diff=above-belowrev;
    checky=(diff < -maxstiff*yieldthresh);


    %for the first element with 0 in checky, check to make sure all
    %diffs(i,:)=checky;
    chek(i)=(length(checky)-length(find(checky)))/length(checky);

    if chek(i) <1
        aa=find(checky);
        ii=aa(1);
        checky2=(diff < 0);
        if checky2(1:ii) == 1
            %     if ((slope(i-:i+10)) < -33)% | (slope2(i) < -300)
            XII(j)=i;
            j=j+1;
```

```
        end
    end
end

integ(1)=0;
oldint=0;
for i=2:length(fail)
    integ(i)=(fail(i,2)-fail(i-1,2))*fail(i,3)+oldint;
    oldint=integ(i);
end
Energy=[integ(XII(1)) integ(ind) integ(length(fail))];
slope2=chek;
pf=round((XI-1)/40)+1;
yd=round((XII-1)/40)+1;
st=round((IX-1)/40)+1;
gf=round((ind)/40)+1;
if length(XI) == 0
    XI=ind;
end



yield=[fail(XII(1),2)];
```

APPENDIX P

Matlab code to track collagenous tissue deformation through vector correlation

The Matlab code in this appendix is used to track tissue deformation through vector correlation, as described in Section 7.2 of Chapter 7 (Quinn and Winkelstein, 2010). The file loads inputs pertaining to the polarizer orientation, field of view, and camera calibrations from variables created by **initializeQPLI.m**, which can be found in Appendix L. The file **VCtracking.m** prompts the user to digitize the region of the tissue where an array of virtual markers is to be placed. That file then creates alignment maps using **analyzesampleIM3.m** (provided in Appendix L), and computes the vector correlation between maps surrounding each virtual marker by calling the function **corrcoef_vector.m** (in Appendix M). **VCtracking.m** then identifies the location of the maximum vector correlation for each virtual marker. As described in Section 7.2, tracking through vector correlation is performed in forward and reverse to enhance the accuracy of the calculated virtual marker locations. The virtual marker displacements determined by **VCtracking.m** are then saved and loaded by the file **three_node_strain.m** to

calculate Lagrangian strain as described in Appendix N in order to plot full field strain maps.

VCtracking.m

```
% TRACKING WITH VECTOR CORR

clear all
load PREPDONE
clear j
h=figure;


imgf=[specID,'_shear_img_']
[a b]=max(fail(4,:));imgend=fail(1,b)*25-1;

%load mechdata2
%sets baseline (DC) intensity of pixels by finding median value in the ROI
ii=1;
intpROI=[min(intpROI(:,1)) min(intpROI(:,2)) max(intpROI(:,3)) max(intpROI(:,4))]
dcim=imread([specID,'_shear_dc.bmp']);
dc_crop=dcim(intpROI(2):intpROI(4),intpROI(1):intpROI(3));
dc=double(median(reshape(dc_crop,1,[])));
clear I
%%%%%%%%%%%%%%%%%%%%%%%%%%%%%%%%%%

%%%%%%%%%%%%%%%%%%%%%%%%%%%%%%%%%%
string1='00000';
%tS=[2:2:660];
tS=[2:1:192]
tsteps=length(tS);
res=4;
rvfres=.05
wisize=4;  %4     %kernel size (number of pix from center) 2=5x5, 3=7x7
searchwi=6;  %3   %search window size (number of pix from center)

hq = waitbar(0,'Please wait...')
tic;
for j=1:tsteps%round(imgend)-round(imgstart)+1%round(imgend/10-imgstart/10)*10+round(imgstart)

    %ad=20*j-20;
    ad=20*tS(j)-20;

    for i=beg+ad:beg+ad+19
        string2o=[string1,num2str(i)];
        string2a=[string1,num2str(i+20)];
        string2b=[string1,num2str(i-20)];
        string3o=string2o(end-4:end);
        string3a=string2a(end-4:end);
        string3b=string2b(end-4:end);

        img=imread([imgf,string3o,'.tif']);
        Io(:,:,i-beg-ad+1)=img(intpROI(2):intpROI(4),intpROI(1):intpROI(3));
        imga=imread([imgf,string3a,'.tif']);
        Ia(:,:,i-beg-ad+1)=imga(intpROI(2):intpROI(4),intpROI(1):intpROI(3));
        imgb=imread([imgf,string3b,'.tif']);
        Ib(:,:,i-beg-ad+1)=imgb(intpROI(2):intpROI(4),intpROI(1):intpROI(3));
    end
    I=.25*Ib+.5*Io+.25*Ia;
    Im=mean(I,3);
    %Finds pixel intensities over the course of the polarizer rotation
    jj=j;


    %clear I
    [alphaSb deltaSb ptpb errb snrb]=analyzesampleIM3(I,0,scale,dc,angCOR);
    clear snrb errb ptpb

    if j==1
       % pick initial pts

                image(Im,'CDataMapping','scaled');
                axis image;axis off
                colormap gray
```

```
            but=1;

            for k=1:400
                %top
                title('top')
                [x y but]=ginput(1);
                if but~=1
                    break
                end
                hold on;
                plot(x,y,'g.');%text(x,y,num2str(k),'Color',[0 1 0])
                xt(k)=x;
                yt(k)=y;
            end
            tris = delaunay(xt,yt,{'Qt','Qbb','Qc','Qz'});
            elon=ones(size(tris,1),1)/10;
            for k=1:size(tris,1)
                hold on;
                h=fill(xt(tris(k,:)),yt(tris(k,:)),'r');
                alpha(h,elon(k));
            end
            for j=1:400
                %top
                title('top')
                [x y but]=ginput(1);
                if but~=1
                    break
                end
                for k=1:size(tris,1)
                    if inpolygon(x,y,xt(tris(k,:)),yt(tris(k,:)));
                        elon(k)=1;
                        h=fill(xt(tris(k,:)),yt(tris(k,:)),'r');
                        alpha(h,elon(k));
                    end
                end

            end

            [X,Y] = meshgrid([1:res:size(Im,2)],[1:res:size(Im,1)])
            xtn=reshape(X,1,[]);
            ytn=reshape(Y,1,[]);
            trikeep=tris(find(elon==1),:);
            clear inroi
            for k=1:size(trikeep,1)
                in=inpolygon(xtn,ytn,xt(trikeep(k,:)),yt(trikeep(k,:)));
                inroi(:,k)=in';
            end
            roi=sum(inroi,2);
            xtnn=xtn(find(roi));
            ytnn=ytn(find(roi));
            hold on;plot(xtnn,ytnn,'b.')

        %load initpts2
        xt=xtnn;
        yt=ytnn;


        xtot=zeros(length(xt),length(tS));
        ytot=zeros(length(xt),length(tS));
        maxcor=ones(length(xt),length(tS));
        ddif=zeros(length(xt),length(tS));
        xtot(:,1)=xt';
        ytot(:,1)=yt';
        skipk=zeros(length(xt),1);
        maxcorB=ones(length(xt),length(tS));
        maxcorF=zeros(length(xt),length(tS));

        %begin tracking

        image(Im,'CDataMapping','scaled');
        axis image;axis off
        colormap gray
        hold on;plot(xtot(:,1),ytot(:,1),'g.')
        drawnow;
        alphaSa=alphaSb;
        deltaSa=deltaSb;

    else
        if j==2
            tic;
        end

        [x y]=meshgrid(1:size(alphaSa,2),1:size(alphaSa,1));
        asa=reshape(alphaSa,1,[]);
        asb=reshape(alphaSb,1,[]);
        dsb=reshape(deltaSb,1,[]);
        dsa=reshape(deltaSa,1,[]);

        [xpola ypola]= pol2cart(2*asa,sin(dsa));
```

```
[xpolb ypolb]= pol2cart(2*asb,sin(dsb));
t2=[(xpolb);(ypolb)]';
t1=[(xpola);(ypola)]';
wi=size(alphaSb,1);  %width of image


for k=1:size(xtot,1)  %each point
    if skipk(k)==0

        %%%%FORWARD%%%%%%
        %get previous point

        xc=xtot(k,j-1);
        yc=ytot(k,j-1);

        clear Rv
        % pick out relevant pixel window from previous frame
        %             ofsI=round(rand*2.5-1.25);
        %             ofsJ=round(rand*2.5-1.25);
        i1=round(xc);%+ofsI;
        j1=round(yc);%+ofsJ;
        yoff=yc-j1;
        xoff=xc-i1;
        [xs ys]=meshgrid(i1-wisize:i1+wisize,j1-wisize:j1+wisize);
        indx=reshape((xs-1)*wi+ys,1,[]);
        if maxcorF(k,j-1)<0.9%j==2
            match(:,:,k)=t1(indx,:);
            yoff(:,:,k)=yc-j1;
            xoff(:,:,k)=xc-i1;
        end



        for i2=i1-searchwi:i1+searchwi;
            for j2=j1-searchwi:j1+searchwi;
                %determine relavent pixels in any given search position

                [xs2 ys2]=meshgrid(i2-wisize:i2+wisize,j2-wisize:j2+wisize);
                indx2=reshape((xs2-1)*wi+ys2,1,[]);

                %calculate vector correlation
                [rho,r2,err] = corrcoef_vector(match(:,:,k), t2(indx2,:));

                Rv(j2-j1+searchwi+1,i2-i1+searchwi+1)=rho;

            end
        end


        %Rvavg(:,:,j,k)=Rv;
        %Rv is the correlation map within the search window with pixel
        %resolution, here we spline fit Rv with 0.01 pixel resolution to
        %find the peak resolution with sub-pixel accuracy
        [X,Y] = meshgrid(1:2*searchwi+1);
        [XI,YI] = meshgrid(1:rvfres:(2*searchwi+1));
        Rvf = interp2(X,Y,Rv,XI,YI,'spine');
        [a b1]=max(Rvf);
        [a2 b2]=max(a);
        xpeak=XI(b1(b2),b2);
        ypeak=YI(b1(b2),b2);

        %define coordinates of peak Rv and add the initial x and y offset
        xpeakm=xpeak-1-searchwi+i1+xoff(:,:,k);%-ofsI;
        ypeakm=ypeak-1-searchwi+j1+yoff(:,:,k);%-ofsJ;
        %text(xpeakm,ypeakm,num2str(i),'Color',[0 1 0])

        %             match=matchnew;
        %              xoff=xoffnew;
        %              yoff=yoffnew;

        %%%%BACKWARD%%%%%
        %get previous point
        xc=xpeakm;
        yc=ypeakm;
        clear Rv
        % pick out relevant pixel window from previous frame
        i1=round(xc);
        xoff=xc-i1;
        j1=round(yc);
        yoff=yc-j1;
        [xs ys]=meshgrid(i1-wisize:i1+wisize,j1-wisize:j1+wisize);
        indx=reshape((xs-1)*wi+ys,1,[]);

        for i2=i1-searchwi:i1+searchwi;
            for j2=j1-searchwi:j1+searchwi;
                %determine relavent pixels in any given search position

                [xs2 ys2]=meshgrid(i2-wisize:i2+wisize,j2-wisize:j2+wisize);
                indx2=reshape((xs2-1)*wi+ys2,1,[]);
```

```
                        %calculate vector correlation
                        [rho,r2,err] = corrcoef_vector(t2(indx,:), t1(indx2,:));
                        %rho2=corrcoef(asa(indx),asb(indx2));rho=rho2(1,2);
                        Rv(j2-j1+searchwi+1,i2-i1+searchwi+1)=rho;

                    end
                end

                %Rv is the correlation map within the search window with pixel
                %resolution, here we spline fit Rv with 0.01 pixel resolution to
                %find the peak resolution with sub-pixel accuracy
                [X,Y] = meshgrid(1:2*searchwi+1);
                [XI,YI] = meshgrid(1:.05:(2*searchwi+1));
                Rvf = interp2(X,Y,Rv,XI,YI,'spine');
                [a b1]=max(Rvf);
                [a3 b2]=max(a);
                xpeak=XI(b1(b2),b2);
                ypeak=YI(b1(b2),b2);

                %define coordinates of peak Rv and add the initial x and y offset
                xpeakm2=xpeak-1-searchwi+i1+xoff;
                ypeakm2=ypeak-1-searchwi+j1+yoff;


                xtot(k,j)=xpeakm-xpeakm2/2+xtot(k,j-1)/2;
                ytot(k,j)=ypeakm-ypeakm2/2+ytot(k,j-1)/2;
                maxcorB(k,j)=a3;
                maxcorF(k,j)=a2;
                maxcor(k,j)=(a2+a3)/2;
                ddif(k,j)=sqrt((xpeakm2-xtot(k,j-1)).^2+(ypeakm2-ytot(k,j-1)).^2);


                if ((xtot(k,j)+wisize+searchwi)<size(Im,2) & (xtot(k,j)-wisize-searchwi)>1 & (ytot(k,j)-wisize-
searchwi)>1 & (ytot(k,j)+wisize+searchwi)<size(Im,1))~=1
                    skipk(k)=1;
                    disp('out of range');
                end

            end

        end
        badpts=find(skipk);



    end
    alphaSa=alphaSb;
    deltaSa=deltaSb;

    telapsed=toc/60;
    tleft=(telapsed/(j-1))*(tsteps-j);
    waitbar(j / tsteps,hq,[num2str(telapsed),' min elapsed, ',num2str(tleft),' min left' ])
end

for i=1:size(xtot,2)
    displ(:,i)=sqrt((xtot(:,i)-xtot(:,1)).^2+(ytot(:,i)-ytot(:,1)).^2);

end

clf reset
image(Im,'CDataMapping','scaled');
axis image;axis off
colormap gray
hold on;plot(xtot(:,1),ytot(:,1),'g.')
plot(xtot(:,j-1),ytot(:,j-1),'r.')
%image(Rv,'CDataMapping','scaled')
drawnow;
title(j)

drawnow;
hold off

load mechdata2
timeimg=round(imgstart):round(194);
timeimg=(timeimg-1)/25;
dispT = interp1(fail(1,:),fail(2,:),timeimg);
save TRACKCOMPLETE
```

REFERENCES

Aniksztejn, L., S. Otani, et al. (1992). "Quisqualate Metabotropic Receptors Modulate NMDA Currents and Facilitate Induction of Long-Term Potentiation Through Protein Kinase C." Eur J Neurosci 4(6): 500-505.

Aprill, C. and N. Bogduk (1992). "The prevalence of cervical zygapophyseal joint pain. A first approximation." Spine 17(7): 744-747.

Bain, A. C. and D. F. Meaney (2000). "Tissue-level thresholds for axonal damage in an experimental model of central nervous system white matter injury." J Biomech Eng 122(6): 615-622.

Banic, B., S. Petersen-Felix, O. K. Andersen, B. P. Radanov, P. M. Villiger, L. Arendt-Nielsen and M. Curatolo (2004). "Evidence for spinal cord hypersensitivity in chronic pain after whiplash injury and in fibromyalgia." Pain 107(1-2): 7-15.

Barnsley, L., S. Lord and N. Bogduk (1993). "Comparative local anaesthetic blocks in the diagnosis of cervical zygapophysial joint pain." Pain 55(1): 99-106.

Barnsley, L., S. Lord and N. Bogduk (1994). "Whiplash injury." Pain 58(3): 283-307.

Barnsley, L., S. M. Lord, B. J. Wallis and N. Bogduk (1995). "The prevalence of chronic cervical zygapophysial joint pain after whiplash." Spine 20(1): 20-25; discussion 26.

Beaman, D. N., G. P. Graziano, R. A. Glover, E. M. Wojtys and V. Chang (1993). "Substance P innervation of lumbar spine facet joints." Spine 18(8): 1044-1049.

Beynnon, B. D., P. M. Vacek, D. Murphy, D. Alosa and D. Paller (2005). "First-time inversion ankle ligament trauma: the effects of sex, level of competition, and sport on the incidence of injury." Am J Sports Med 33(10): 1485-1491.

Billiar, K. L. and M. S. Sacks (1997). "A method to quantify the fiber kinematics of planar tissues under biaxial stretch." J Biomech 30(7): 753-756.

Bogduk, N. and A. Marsland (1988). "The cervical zygapophysial joints as a source of neck pain." Spine 13(6): 610-617.

Bogduk, N. and N. Yoganandan (2001). "Biomechanics of the cervical spine Part 3: minor injuries." Clin Biomech 16(4): 267-275.

Boorman, R. S., T. Norman, F. A. Matsen, 3rd and J. M. Clark (2006). "Using a freeze substitution fixation technique and histological crimp analysis for characterizing regions of strain in ligaments loaded in situ." J Orthop Res 24(4): 793-799.

Braun, B. L. (1999). "Effects of ankle sprain in a general clinic population 6 to 18 months after medical evaluation." Arch Fam Med 8(2): 143-148.

Bruns, J., J. Kampen, J. Kahrs and W. Plitz (2000). "Achilles tendon rupture: experimental results on spontaneous repair in a sheep-model." Knee Surg Sports Traumatol Arthrosc 8(6): 364-369.

Carlton, S. M., J. Du, et al. (2009). "Peripheral and central sensitization in remote spinal cord regions contribute to central neuropathic pain after spinal cord injury." Pain 147(1-3): 265-276.

Cater, H. L., L. E. Sundstrom and B. Morrison (2006). "Temporal development of hippocampal cell death is dependent on tissue strain but not strain rate." J Biomech 39(15): 2810-2818.

Cavanaugh, J. M., A. C. Ozaktay, H. T. Yamashita and A. I. King (1996). "Lumbar facet pain: biomechanics, neuroanatomy and neurophysiology." J Biomech 29(9): 1117-1129.

Chandran, P. L. and V. H. Barocas (2006). "Affine versus non-affine fibril kinematics in collagen networks: theoretical studies of network behavior." J Biomech Eng 128(2): 259-270.

Chang, Y. W., A. Tan, C. Saab and S. Waxman (2010). "Unilateral focal burn injury is followed by long-lasting bilateral allodynia and neuronal hyperexcitability in spinal cord dorsal horn." J Pain 11(2): 119-130.

Chaplan, S. R., F. W. Bach, J. W. Pogrel, J. M. Chung and T. L. Yaksh (1994). "Quantitative assessment of tactile allodynia in the rat paw." J Neurosci Methods 53(1): 55-63.

Chen, C., Y. Lu, J. M. Cavanaugh, S. Kallakuri and A. Patwardhan (2005). "Recording of neural activity from goat cervical facet joint capsule using custom-designed miniature electrodes." Spine 30(12): 1367-1372.

Christensen, M. D. and C. E. Hulsebosch (1997). "Chronic central pain after spinal cord injury." J Neurotrauma 14(8): 517-537.

Coghill, R. C., D. J. Mayer and D. D. Price (1993). "Wide dynamic range but not nociceptive-specific neurons encode multidimensional features of prolonged repetitive heat pain." J Neurophysiol 69(3): 703-716.

Croft, P. R., M. Lewis, A. C. Papageorgiou, E. Thomas, M. I. Jayson, G. J. Macfarlane and A. J. Silman (2001). "Risk factors for neck pain: a longitudinal study in the general population." Pain 93(3): 317-325.

Curatolo, M., S. Petersen-Felix, L. Arendt-Nielsen, C. Giani, A. M. Zbinden and B. P. Radanov (2001). "Central hypersensitivity in chronic pain after whiplash injury." Clin J Pain 17(4): 306-315.

Dado, R. J., J. T. Katter and G. J. Giesler, Jr. (1994). "Spinothalamic and spinohypothalamic tract neurons in the cervical enlargement of rats. II. Responses to innocuous and noxious mechanical and thermal stimuli." J Neurophysiol 71(3): 981-1002.

Defrate, L. E., A. van der Ven, P. J. Boyer, T. J. Gill and G. Li (2006). "The measurement of the variation in the surface strains of Achilles tendon grafts using imaging techniques." J Biomech 39(3): 399-405.

Delaunay, B. (1934). Sur la sphère vide, Izvestia Akademii Nauk SSSR, Otdelenie Matematicheskikh i Estestvennykh Nauk, 7:793-800.

Deng, B., P. C. Begeman, K. H. Yang, S. Tashman and A. I. King (2000). "Kinematics of human cadaver cervical spine during low speed rear-end impacts." Stapp Car Crash J 44: 171-188.

Derwin, K. A., L. J. Soslowsky, W. D. Green and S. H. Elder (1994). "A new optical system for the determination of deformations and strains: calibration characteristics and experimental results." J Biomech 27(10): 1277-1285.

Diamant, J., A. Keller, E. Baer, M. Litt and R. G. Arridge (1972). "Collagen; ultrastructure and its relation to mechanical properties as a function of ageing." Proc R Soc Lond B Biol Sci 180(60): 293-315.

Dickey, J. P., B. R. Hewlett, G. A. Dumas and D. A. Bednar (1998). "Measuring collagen fiber orientation: a two-dimensional quantitative macroscopic technique." J Biomech Eng 120(4): 537-540.

Doehring, T. C., M. Kahelin and I. Vesely (2009). "Direct measurement of nonuniform large deformations in soft tissues during uniaxial extension." J Biomech Eng 131(6): 061001.

Dong, L., A. O. Odeleye, K. L. Jordan-Sciutto and B. A. Winkelstein (2008). "Painful facet joint injury induces neuronal stress activation in the DRG: implications for cellular mechanisms of pain." Neurosci Lett 443(2): 90-94.

Dong, L. and B. A. Winkelstein (2010). "Simulated whiplash modulates expression of the glutamatergic system in the spinal cord suggesting spinal plasticity is associated with painful dynamic cervical facet loading." J Neurotrauma 27(1): 163-174.

Dwyer, A., C. Aprill and N. Bogduk (1990). "Cervical zygapophyseal joint pain patterns. I: A study in normal volunteers." Spine 15(6): 453-457.

Eagar, P., M. L. Hull and S. M. Howell (2001). "A method for quantifying the anterior load-displacement behavior of the human knee in both the low and high stiffness regions." J Biomech 34(12): 1655-1660.

el-Bohy, A., J. M. Cavanaugh, M. L. Getchell, T. Bulas, T. V. Getchell and A. I. King (1988). "Localization of substance P and neurofilament immunoreactive fibers in the lumbar facet joint capsule and supraspinous ligament of the rabbit." Brain Res 460(2): 379-382.

Freeman, M. D., A. C. Croft, A. M. Rossignol, D. S. Weaver and M. Reiser (1999). "A review and methodologic critique of the literature refuting whiplash syndrome." Spine 24(1): 86-96.

Freund, B. J. and M. Schwartz (2002). "Use of botulinum toxin in chronic whiplash-associated disorder." Clin J Pain 18(6 Suppl): S163-168.

Fung, Y.C. (1996). Biomechanics: mechanical properties of living tissues. Second Edition. Springer, New York.

Gargan, M. F. and G. C. Bannister (1994). "The rate of recovery following whiplash injury." Eur Spine J 3(3): 162-164.

Gathercole, L. J. and A. Keller (1991). "Crimp morphology in the fibre-forming collagens." Matrix 11(3): 214-234.

Geday, M. A., W. Kaminsky, J. G. Lewis and A. M. Glazer (2000). "Images of absolute retardance L.Deltan, using the rotating polariser method." J Microsc 198 (Pt 1): 1-9.

Gefen, A., B. van Nierop, D. L. Bader and C. W. Oomens (2008). "Strain-time cell-death threshold for skeletal muscle in a tissue-engineered model system for deep tissue injury." J Biomech 41(9): 2003-2012.

Gilchrist, C. L., S. W. Witvoet-Braam, F. Guilak and L. A. Setton (2007). "Measurement of intracellular strain on deformable substrates with texture correlation." J Biomech 40(4): 786-794.

Gimbel, J. A., J. P. Van Kleunen, S. P. Lake, G. R. Williams and L. J. Soslowsky (2007). "The role of repair tension on tendon to bone healing in an animal model of chronic rotator cuff tears." J Biomech 40(3): 561-568.

Gimbel, J. A., J. P. Van Kleunen, S. Mehta, S. M. Perry, G. R. Williams and L. J. Soslowsky (2004). "Supraspinatus tendon organizational and mechanical properties in a chronic rotator cuff tear animal model." J Biomech 37(5): 739-749.

Grauer, J. N., M. M. Panjabi, J. Cholewicki, K. Nibu and J. Dvorak (1997). "Whiplash produces an S-shaped curvature of the neck with hyperextension at lower levels." Spine 22(21): 2489-2494.

Greening, J., A. Dilley and B. Lynn (2005). "In vivo study of nerve movement and mechanosensitivity of the median nerve in whiplash and non-specific arm pain patients." Pain 115(3): 248-253.

Hains, B. C., K. M. Johnson, M. J. Eaton, W. D. Willis and C. E. Hulsebosch (2003a). "Serotonergic neural precursor cell grafts attenuate bilateral hyperexcitability of dorsal horn neurons after spinal hemisection in rat." Neuroscience 116(4): 1097-1110.

Hains, B. C., W. D. Willis and C. E. Hulsebosch (2002). "Differential electrophysiological effects of brain-derived neurotrophic factor on dorsal horn neurons following chronic spinal cord hemisection injury in the rat." Neurosci Lett 320(3): 125-128.

Hains, B. C., W. D. Willis and C. E. Hulsebosch (2003b). "Temporal plasticity of dorsal horn somatosensory neurons after acute and chronic spinal cord hemisection in rat." Brain Res 970(1-2): 238-241.

Hansen, K. A., J. A. Weiss and J. K. Barton (2002). "Recruitment of tendon crimp with applied tensile strain." J Biomech Eng 124(1): 72-77.

Hanson, B., K. Klink, K. Matsuura, S. M. Robeson and C. J. Willmott (1992). "Vector correlation: review, exposition, and geographic application." Ann Assoc Am Geogr 82(1): 103-116.

Hao, J. X., X. J. Xu, Y. X. Yu, A. Seiger and Z. Wiesenfeld-Hallin (1992). "Transient spinal cord ischemia induces temporary hypersensitivity of dorsal horn wide dynamic range neurons to myelinated, but not unmyelinated, fiber input." J Neurophysiol 68(2): 384-391.

Hakkinen, L., O. Oksala, T. Salo, F. Rahemtulla and H. Larjava (1993). "Immunohistochemical localization of proteoglycans in human periodontium." J Histochem Cytochem 41(11): 1689-1699.

Hildingsson, C. and G. Toolanen (1990). "Outcome after soft-tissue injury of the cervical spine. A prospective study of 93 car-accident victims." Acta Orthop Scand 61(4): 357-359.

Herrero, J. F. and P. M. Headley (1995). "The dominant class of somatosensory neurone recorded in the spinal dorsal horn of awake sheep has wide dynamic range properties." Pain 61(1): 133-138.

Hogg-Johnson, S., G. van der Velde, L. J. Carroll, L. W. Holm, J. D. Cassidy, J. Guzman, P. Cote, S. Haldeman, C. Ammendolia, E. Carragee, E. Hurwitz, M. Nordin and P. Peloso (2008). "The burden and determinants of neck pain in the general population: results of the Bone and Joint Decade 2000-2010 Task Force on Neck Pain and Its Associated Disorders." Spine 33(4 Suppl): S39-51.

Holm, L. W., L. J. Carroll, J. D. Cassidy, S. Hogg-Johnson, P. Cote, J. Guzman, P. Peloso, M. Nordin, E. Hurwitz, G. van der Velde, E. Carragee and S. Haldeman (2008). "The burden and determinants of neck pain in whiplash-associated disorders after traffic collisions: results of the Bone and Joint Decade 2000-2010 Task Force on Neck Pain and Its Associated Disorders." Spine 33(4 Suppl): S52-59.

Hurschler, C., P. P. Provenzano and R. Vanderby (2003). "Scanning electron microscopic characterization of healing and normal rat ligament microstructure under slack and loaded conditions." Connect Tissue Res 44(2): 59-68.

Hylden, J. L., R. L. Nahin, R. J. Traub and R. Dubner (1989). "Expansion of receptive fields of spinal lamina I projection neurons in rats with unilateral adjuvant-induced inflammation: the contribution of dorsal horn mechanisms." Pain 37(2): 229-243.

Iatridis, J. C., J. J. MaClean and D. A. Ryan (2005). "Mechanical damage to the intervertebral disc annulus fibrosus subjected to tensile loading." J Biomech 38(3): 557-565.

Inami, S., T. Shiga, A. Tsujino, T. Yabuki, N. Okado and N. Ochiai (2001). "Immunohistochemical demonstration of nerve fibers in the synovial fold of the human cervical facet joint." J Orthop Res 19(4): 593-596.

Ito S, Ivancic PC, Panjabi MM, Cunningham BW (2004). Soft tissue injury threshold during simulated whiplash: a biomechanical investigation. Spine 29:979-987.

Ivancic, P. C., S. Ito, Y. Tominaga, W. Rubin, M. P. Coe, A. B. Ndu, E. J. Carlson and M. M. Panjabi (2008). "Whiplash causes increased laxity of cervical capsular ligament." Clin Biomech 23(2): 159-165.

Jarvinen, T. A., T. L. Jarvinen, P. Kannus, L. Jozsa and M. Jarvinen (2004). "Collagen fibres of the spontaneously ruptured human tendons display decreased thickness and crimp angle." J Orthop Res 22(6): 1303-1309.

Ji, R. R. and C. J. Woolf (2001). "Neuronal plasticity and signal transduction in nociceptive neurons: implications for the initiation and maintenance of pathological pain." Neurobiol Dis 8(1): 1-10.

Jones, L., Q. Bismil, F. Alyas, D. Connell and J. Bell (2009). "Persistent symptoms following non operative management in low grade MCL injury of the knee - The role of the deep MCL." Knee 16(1): 64-68.

Kallakuri, S., A. Singh, C. Chen and J. M. Cavanaugh (2004). "Demonstration of substance P, calcitonin gene-related peptide, and protein gene product 9.5 containing nerve fibers in human cervical facet joint capsules." Spine 29(11): 1182-1186.

Kallakuri, S., A. Singh, Y. Lu, C. Chen, A. Patwardhan and J. M. Cavanaugh (2008). "Tensile stretching of cervical facet joint capsule and related axonal changes." Eur Spine J 17(4): 556-563.

Kaneoka, K., K. Ono, S. Inami and K. Hayashi (1999). "Motion analysis of cervical vertebrae during whiplash loading." Spine 24(8): 763-769.

Kaufmann, P. and R. O. Weber (1998). Directional correlation coefficient for channeled flow and application to wind data over complex terrain, J Atmos Ocean Technol 15(1): 89-97.

Kerr, B. J., E. J. Bradbury, D. L. Bennett, P. M. Trivedi, P. Dassan, J. French, D. B. Shelton, S. B. McMahon and S. W. Thompson (1999). "Brain-derived neurotrophic factor modulates nociceptive sensory inputs and NMDA-evoked responses in the rat spinal cord." J Neurosci 19(12): 5138-5148.

Khalsa, P. S., A. H. Hoffman and P. Grigg (1996). "Mechanical states encoded by stretch-sensitive neurons in feline joint capsule." J Neurophysiol 76(1): 175-187.

Kitagawa, J., K. Kanda, M. Sugiura, Y. Tsuboi, A. Ogawa, K. Shimizu, N. Koyama, H. Kamo, T. Watanabe, K. Ren and K. Iwata (2005). "Effect of chronic inflammation on dorsal horn nociceptive neurons in aged rats." J Neurophysiol 93(6): 3594-3604.

Kliewer, M. A., L. Gray, J. Paver, W. D. Richardson, J. B. Vogler, J. H. McElhaney and B. S. Myers (1993). "Acute spinal ligament disruption: MR imaging with anatomic correlation." J Magn Reson Imaging 3(6): 855-861.

Koltzenburg, M., L. E. Lundberg and H. E. Torebjork (1992). "Dynamic and static components of mechanical hyperalgesia in human hairy skin." Pain 51(2): 207-219.

Korol, R. M., H. M. Finlay, M. J. Josseau, A. R. Lucas and P. B. Canham (2007). "Fluorescence spectroscopy and birefringence of molecular changes in maturing rat tail tendon." J Biomed Opt 12(2): 024011.

Korstanje, J. W., R. W. Selles, H. J. Stam, S. E. Hovius and J. G. Bosch (2010). "Development and validation of ultrasound speckle tracking to quantify tendon displacement." J Biomech 43(7): 1373-1379.

Lake, S. P., K. S. Miller, D. M. Elliott and L. J. Soslowsky (2009). "Effect of fiber distribution and realignment on the nonlinear and inhomogeneous mechanical properties of human supraspinatus tendon under longitudinal tensile loading." J Orthop Res 27(12): 1596-1602.

Lam, D. K., B. J. Sessle and J. W. Hu (2008). "Surgical incision can alter capsaicin-induced central sensitization in rat brainstem nociceptive neurons." Neuroscience 156(3): 737-747.

Lang, T. C., M. L. Zimny and P. Vijayagopal (1993). "Experimental temporomandibular joint disc perforation in the rabbit: a gross morphologic, biochemical, and ultrastructural analysis." J Oral Maxillofac Surg 51(10): 1115-1128.

LaPlaca, M. C., V. M. Lee and L. E. Thibault (1997). "An in vitro model of traumatic neuronal injury: loading rate-dependent changes in acute cytosolic calcium and lactate dehydrogenase release." J Neurotrauma 14(6): 355-368.

Le Bars, D., M. Gozariu and S. W. Cadden (2001). "Animal models of nociception." Pharmacol Rev 53(4): 597-652.

Lee, K. E., M. B. Davis, R. M. Mejilla and B. A. Winkelstein (2004a). "In vivo cervical facet capsule distraction: mechanical implications for whiplash and neck pain." Stapp Car Crash J 48: 373-395.

Lee, K. E., M. B. Davis and B. A. Winkelstein (2008). "Capsular ligament involvement in the development of mechanical hyperalgesia after facet joint loading: behavioral and inflammatory outcomes in a rodent model of pain." J Neurotrauma 25(11): 1383-1393.

Lee, K. E., J. H. Thinnes, D. S. Gokhin and B. A. Winkelstein (2004b). "A novel rodent neck pain model of facet-mediated behavioral hypersensitivity: implications for persistent pain and whiplash injury." J Neurosci Methods 137(2): 151-159.

Lee, K. E. and B. A. Winkelstein (2009). "Joint distraction magnitude is associated with different behavioral outcomes and substance P levels for cervical facet joint loading in the rat." J Pain 10(4): 436-445.

Lord, S. M., L. Barnsley and N. Bogduk (1995). "Percutaneous radiofrequency neurotomy in the treatment of cervical zygapophysial joint pain: a caution." Neurosurgery 36(4): 732-739.

Lord, S. M., L. Barnsley, B. J. Wallis and N. Bogduk (1996a). "Chronic cervical zygapophysial joint pain after whiplash. A placebo-controlled prevalence study.[see comment]." Spine 21(15): 1737-1744; discussion 1744-1735.

Lord, S. M., L. Barnsley, B. J. Wallis, G. J. McDonald and N. Bogduk (1996b). "Percutaneous radio-frequency neurotomy for chronic cervical zygapophyseal-joint pain." N Engl J Med 335(23): 1721-1726.

Lu, Y., C. Chen, S. Kallakuri, A. Patwardhan and J. M. Cavanaugh (2005a). "Neural response of cervical facet joint capsule to stretch: a study of whiplash pain mechanism." Stapp Car Crash J 49: 49-65.

Lu, Y., C. Chen, S. Kallakuri, A. Patwardhan and J. M. Cavanaugh (2005b). "Neurophysiological and biomechanical characterization of goat cervical facet joint capsules." J Orthop Res 23(4): 779-787.

Luan, F., K. H. Yang, B. Deng, P. C. Begeman, S. Tashman and A. I. King (2000). "Qualitative analysis of neck kinematics during low-speed rear-end impact." Clin Biomech 15(9): 649-657.

Manchikanti, L., V. Singh, J. Rivera and V. Pampati (2002). "Prevalence of cervical facet joint pain in chronic neck pain." Pain Physician 5(3): 243-249.

Matsushita, T., T.B. Sato, K. Hirabayashi, S. Fujimura, T. Asazuma, T. Takatori (1994). “X-Ray study of the neck motion due to head inertia loading.” Stapp Car Crash J 38: 55-64.

McConnell, W.E., R.P. Howard, H.M. Guzman, J.B. Bomar, J.H. Raddin, J.V. Benedict, H.L. Smith, C.P. Hatsell (1993). “Analysis of human test subject kinematic response to low velocity rear end impacts." SAE # 930889.

McConnell, W.E., R.P. Howard, J. Van Poppel, R. Krause, H.M. Guzman, J.B. Bomar, J.H. Raddin, J.V. Benedict, C.P. Hatsell (1995). "Human Head and Neck Kinematics After Low Velocity Rear-End Impacts-Understanding Whiplash" SAE # 952724.

McLain, R. F. (1994). "Mechanoreceptor endings in human cervical facet joints." Spine 19(5): 495-501.

McMahon, P. J., S. Dheer, S. M. Raikin, I. Elias, W. B. Morrison, E. C. Kavanagh and A. Zoga (2009). "MRI of injuries to the first interosseous cuneometatarsal (Lisfranc) ligament." Skeletal Radiol 38(3): 255-260.

McMahon, S. B. and P. D. Wall (1984). "Receptive fields of rat lamina 1 projection cells move to incorporate a nearby region of injury." Pain 19(3): 235-247.

Michalek, A. J., M. R. Buckley, L. J. Bonassar, I. Cohen and J. C. Iatridis (2009). "Measurement of local strains in intervertebral disc anulus fibrosus tissue under dynamic shear: contributions of matrix fiber orientation and elastin content." J Biomech 42(14): 2279-2285.

Mills, C. D., K. M. Johnson and C. E. Hulsebosch (2002). "Group I metabotropic glutamate receptors in spinal cord injury: roles in neuroprotection and the development of chronic central pain." J Neurotrauma 19(1): 23-42.

Moore, K. A., T. Kohno, L. A. Karchewski, J. Scholz, H. Baba and C. J. Woolf (2002). "Partial peripheral nerve injury promotes a selective loss of GABAergic inhibition in the superficial dorsal horn of the spinal cord." J Neurosci 22(15): 6724-6731.

Mueller, H. (1943). “Memorandum on the polarization optics of the photoelastic shutter,” Report No. 2 of the OSRD project OOEMsr-576.

Myklebust, J. B., F. Pintar, N. Yoganandan, J. F. Cusick, D. Maiman, T. J. Myers and A. Sances, Jr. (1988). "Tensile strength of spinal ligaments." Spine 13(5): 526-531.

Norris, S. H. and I. Watt (1983). "The prognosis of neck injuries resulting from rear-end vehicle collisions." J Bone Joint Surg Br 65(5): 608-611.

Noyes, F. R. and E. S. Grood (1976). "The strength of the anterior cruciate ligament in humans and Rhesus monkeys." J Bone Joint Surg Am 58(8): 1074-1082.

O'Donoghue, D. H. (1976). Treatment of Injuries to Athletes. Third Edition. Saunders, Philadelphia.

Offenbaecher, M., B. Bondy, S. de Jonge, K. Glatzeder, M. Kruger, P. Schoeps and M. Ackenheil (1999). "Possible association of fibromyalgia with a polymorphism in the serotonin transporter gene regulatory region." Arthritis Rheum 42(11): 2482-2488.

Ohtori, S., K. Takahashi, T. Chiba, M. Yamagata, H. Sameda and H. Moriya (2001). "Sensory innervation of the cervical facet joints in rats." Spine 26(2): 147-150.

Ono, K., K. Kaneoka, A. Wittek and J. Kajzer (1997). "Cervical injury mechanism based on the analysis of human cervical vertebral motion and head-neck-torso kinematics during low speed rear impacts." Stapp Car Crash J 41: 339-356.

Palecek, J., P. M. Dougherty, S. H. Kim, V. Paleckova, H. Lekan, J. M. Chung, S. M. Carlton and W. D. Willis (1992). "Responses of spinothalamic tract neurons to mechanical and thermal stimuli in an experimental model of peripheral neuropathy in primates." J Neurophysiol 68(6): 1951-1966.

Panjabi, M. M., J. Cholewicki, K. Nibu, J. Grauer and M. Vahldiek (1998). "Capsular ligament stretches during in vitro whiplash simulations." J Spinal Disord 11(3): 227-232.

Panjabi, M. M. and T. W. Courtney (2001). "High-speed subfailure stretch of rabbit anterior cruciate ligament: changes in elastic, failure and viscoelastic characteristics." Clin Biomech 16(4): 334-340.

Panjabi, M. M., P. Moy, T. R. Oxland and J. Cholewicki (1999). "Subfailure injury affects the relaxation behavior of rabbit ACL." Clin Biomech 14(1): 24-31.

Panjabi, M. M., E. Yoldas, T. R. Oxland and J. J. Crisco, 3rd (1996). "Subfailure injury of the rabbit anterior cruciate ligament." J Orthop Res 14(2): 216-222.

Pearson, A. M., P. C. Ivancic, S. Ito and M. M. Panjabi (2004). "Facet joint kinematics and injury mechanisms during simulated whiplash." Spine 29(4): 390-397.

Pettersen, K., C. Hildingsson, G. Toolanen, M. Fagerlund and J. Bjornebrink (1997). "Disc pathology after whiplash injury. A prospective magnetic resonance imaging and clinical investigation." Spine 22(3): 283-287.

Phatak, N. S., Q. Sun, S. E. Kim, D. L. Parker, R. K. Sanders, A. I. Veress, B. J. Ellis and J. A. Weiss (2007). "Noninvasive determination of ligament strain with deformable image registration." Ann Biomed Eng 35(7): 1175-1187.

Pollock, R. G., V. M. Wang, J. S. Bucchieri, N. P. Cohen, C. Y. Huang, R. J. Pawluk, E. L. Flatow, L. U. Bigliani and V. C. Mow (2000). "Effects of repetitive subfailure strains on the mechanical behavior of the inferior glenohumeral ligament." J Shoulder Elbow Surg 9(5): 427-435.

Provenzano, P. P., A. L. Alejandro-Osorio, W. B. Valhmu, K. T. Jensen and R. Vanderby, Jr. (2005). "Intrinsic fibroblast-mediated remodeling of damaged collagenous matrices in vivo." Matrix Biol 23(8): 543-555.

Provenzano, P. P., K. Hayashi, D. N. Kunz, M. D. Markel and R. Vanderby, Jr. (2002). "Healing of subfailure ligament injury: comparison between immature and mature ligaments in a rat model." J Orthop Res 20(5): 975-983.

Provenzano, P. P., D. Heisey, K. Hayashi, R. Lakes and R. Vanderby, Jr. (2002). "Subfailure damage in ligament: a structural and cellular evaluation." J Appl Physiol 92(1): 362-371.

Provenzano, P. P. and R. Vanderby, Jr. (2006). "Collagen fibril morphology and organization: implications for force transmission in ligament and tendon." Matrix Biol 25(2): 71-84.

Psilodimitrakopoulos, S., S. I. Santos, I. Amat-Roldan, A. K. Thayil, D. Artigas and P. Loza-Alvarez (2009). "In vivo, pixel-resolution mapping of thick filaments' orientation in nonfibrilar muscle using polarization-sensitive second harmonic generation microscopy." J Biomed Opt 14(1): 014001.

Quinlan, K. P., J. L. Annest, B. Myers, G. Ryan and H. Hill (2004). "Neck strains and sprains among motor vehicle occupants-United States, 2000." Accid Anal Prev 36(1): 21-27.

Quinn, K. P., J. A. Bauman, N. D. Crosby and B. A. Winkelstein (2010a). "Anomalous fiber realignment during tensile loading of the rat facet capsular ligament identifies mechanically induced damage and physiological dysfunction." J Biomech, 43(10): 1870-1875.

Quinn, K. P., L. Dong, F. J. Golder and B. A. Winkelstein (2010b). "Neuronal hyperexcitability in the dorsal horn after painful facet joint injury." Pain 151(2): 414-21.

Quinn, K. P., K. E. Lee, C. C. Ahaghotu and B. A. Winkelstein (2007). "Structural changes in the cervical facet capsular ligament: potential contributions to pain following subfailure loading." Stapp Car Crash J 51: 169-187.

Quinn, K. P. and B. A. Winkelstein (2005). Defining quasilinear viscoelastic parameters for the rat cervical facet capsule in tension. Biomedical Engineering Society Annual Fall Meeting. Baltimore, MD.

Quinn, K. P. and B. A. Winkelstein (2007). "Cervical facet capsular ligament yield defines the threshold for injury and persistent joint-mediated neck pain." J Biomech 40(10): 2299-2306.

Quinn, K. P. and B. A. Winkelstein (2008). "Altered collagen fiber kinematics define the onset of localized ligament damage during loading." J Appl Physiol 105(6): 1881-1888.

Quinn, K. P. and B. A. Winkelstein (2009). "Vector correlation technique for pixel-wise detection of collagen fiber realignment during injurious tensile loading." J Biomed Opt 14(5): 054010.

Quinn, K. P. and B. A. Winkelstein (2010). "Full field strain measurements of collagenous tissue by tracking fiber alignment through vector correlation." J Biomech 43(13): 2637-40.

Radanov, B. P., M. Sturzenegger and G. Di Stefano (1995). "Long-term outcome after whiplash injury. A 2-year follow-up considering features of injury mechanism and somatic, radiologic, and psychosocial findings." Medicine (Baltimore) 74(5): 281-297.

Ren, K., J. L. Hylden, G. M. Williams, M. A. Ruda and R. Dubner (1992). "The effects of a non-competitive NMDA receptor antagonist, MK-801, on behavioral hyperalgesia and dorsal horn neuronal activity in rats with unilateral inflammation." Pain 50(3): 331-344.

Resnick, D. and G. Niwayama (1981). Diagnosis of bone and joint disorders. Second Edition. Saunders, New York.

Riley, L. H., 3rd, D. Long and L. H. Riley, Jr. (1995). "The science of whiplash." Medicine (Baltimore) 74(5): 298-299.

Robinson, P. S. and R. T. Tranquillo (2009). "Planar Biaxial Behavior of Fibrin-Based Tissue-Engineered Heart Valve Leaflets." Tissue Eng Part A.

Rothman, S. M., R. D. Hubbard, K. E. Lee and B. A. Winkelstein (2008). Detection, transmission, and perception of pain. Interventional spine: an algorithmic approach. C.W. Slipman, F.A. Simeone, R. Derby and T.G. Mayer, Saunders, Philadelphia.

Sander, E. A. and V. H. Barocas (2009). "Comparison of 2D fiber network orientation measurement methods." J Biomed Mater Res A 88(2): 322-331.

Sander, E., T. Stylianopoulos, R.T. Tranquillo and V.H. Barocas (2009). "Image-based biomechanics of collagen-based tissue equivalents." IEEE Eng Med Biol Mag 28(3): 10-18.

Sander, E. A., T. Stylianopoulos, R. T. Tranquillo and V. H. Barocas (2009). "Image-based multiscale modeling predicts tissue-level and network-level fiber reorganization in stretched cell-compacted collagen gels." Proc Natl Acad Sci USA 106(42): 17675-17680.

Sandkuhler, J. (2000). "Learning and memory in pain pathways." Pain 88(2): 113-118.

Scholz, J. and C. J. Woolf (2002). "Can we conquer pain?" Nat Neurosci 5 Suppl: 1062-1067.

Schouenborg, J., H. R. Weng, J. Kalliomaki and H. Holmberg (1995). "A survey of spinal dorsal horn neurones encoding the spatial organization of withdrawal reflexes in the rat." Exp Brain Res 106(1): 19-27.

Screen, H. R., D. A. Lee, D. L. Bader and J. C. Shelton (2004). "An investigation into the effects of the hierarchical structure of tendon fascicles on micromechanical properties." Proc Inst Mech Eng H 218(2): 109-119.

Seal, R. P., X. Wang, Y. Guan, S. N. Raja, C. J. Woodbury, A. I. Basbaum and R. H. Edwards (2009). "Injury-induced mechanical hypersensitivity requires C-low threshold mechanoreceptors." Nature 462(7273): 651-655.

Sheather-Reid, R. B. and M. L. Cohen (1998). "Psychophysical evidence for a neuropathic component of chronic neck pain." Pain 75(2-3): 341-347.

Siegmund, G. P., M. B. Davis, K. P. Quinn, E. Hines, B. S. Myers, S. Ejima, K. Ono, K. Kamiji, T. Yasuki and B. A. Winkelstein (2008). "Head-turned postures increase the risk of cervical facet capsule injury during whiplash." Spine 33(15): 1643-1649.

Siegmund, G. P., B. S. Myers, M. B. Davis, H. F. Bohnet and B. A. Winkelstein (2000). "Human Cervical Motion Segment Flexibility and Facet Capsular Ligament Strain under Combined Posterior Shear, Extension and Axial Compression." Stapp Car Crash J 44: 159-170.

Siegmund, G. P., B. S. Myers, M. B. Davis, H. F. Bohnet and B. A. Winkelstein (2001). "Mechanical evidence of cervical facet capsule injury during whiplash: a cadaveric study using combined shear, compression, and extension loading." Spine 26(19): 2095-2101.

Snedeker, J. G., G. Pelled, Y. Zilberman, A. Ben Arav, E. Huber, R. Muller and D. Gazit (2009). "An analytical model for elucidating tendon tissue structure and biomechanical function from in vivo cellular confocal microscopy images." Cells Tissues Organs 190(2): 111-9.

Snedeker, J. G., G. Pelled, Y. Zilberman, F. Gerhard, R. Muller and D. Gazit (2006). "Endoscopic cellular microscopy for in vivo biomechanical assessment of tendon function." J Biomed Opt 11(6): 064010.

Solomonow, M., B. He Zhou, R. V. Baratta, Y. Lu, M. Zhu and M. Harris (2000). "Biexponential recovery model of lumbar viscoelastic laxity and reflexive muscular activity after prolonged cyclic loading." Clin Biomech (Bristol, Avon) 15(3): 167-75.

Sorkin, L. S., D. G. Ferrington and W. D. Willis, Jr. (1986). "Somatotopic organization and response characteristics of dorsal horn neurons in the cervical spinal cord of the cat." Somatosens Res 3(4): 323-338.

Stemper, B. D., N. Yoganandan and F. A. Pintar (2005). "Effects of abnormal posture on capsular ligament elongations in a computational model subjected to whiplash loading." J Biomech 38(6): 1313-1323.

Sterling, M., G. Jull and J. Kenardy (2006). "Physical and psychological factors maintain long-term predictive capacity post-whiplash injury." Pain 122(1-2): 102-108.

Sterling, M., G. Jull, B. Vicenzino and J. Kenardy (2003). "Sensory hypersensitivity occurs soon after whiplash injury and is associated with poor recovery." Pain 104(3): 509-517.

Sundararajan, S., P. Prasad, C. K. Demetropoulos, S. Tashman, P. C. Begeman, K. H. Yang and A. I. King (2004). "Effect of Head-Neck Position on Cervical Facet Stretch of Post Mortem Human Subjects during Low Speed Rear End Impacts." Stapp Car Crash J 48: 331-372.

Sviridov, A. P., Z. Ulissi, V. Chernomordik, M. Hassan and A. H. Gandjbakhche (2006). "Visualization of biological texture using correlation coefficient images." J Biomed Opt 11(6): 060504.

Taylor, J. R. and L. T. Twomey (1993). "Acute injuries to cervical joints. An autopsy study of neck sprain." Spine 18(9): 1115-1122.

Teo, E. C. and H. W. Ng (2001). "Evaluation of the role of ligaments, facets and disc nucleus in lower cervical spine under compression and sagittal moments using finite element method." Med Eng Phys 23(3): 155-164.

Tower, T. T., M. R. Neidert and R. T. Tranquillo (2002). "Fiber alignment imaging during mechanical testing of soft tissues." Ann Biomed Eng 30(10): 1221-1233.

Tower, T. T. and R. T. Tranquillo (2001). "Alignment maps of tissues: I. Microscopic elliptical polarimetry." Biophys J 81(5): 2954-2963.

Tower, T. T. and R. T. Tranquillo (2001). "Alignment maps of tissues: II. Fast harmonic analysis for imaging." Biophys J 81(5): 2964-2971.

Thomopoulos, S., G. R. Williams, J. A. Gimbel, M. Favata and L. J. Soslowsky (2003). "Variation of biomechanical, structural, and compositional properties along the tendon to bone insertion site." J Orthop Res 21(3): 413-419.

Vernon, H., K. Sun, Y. Zhang, X. M. Yu and B. J. Sessle (2009). "Central sensitization induced in trigeminal and upper cervical dorsal horn neurons by noxious stimulation of deep cervical paraspinal tissues in rats with minimal surgical trauma." J Manipulative Physiol Ther 32(7): 506-514.

Vierck, C. J., Jr. (2006). "Mechanisms underlying development of spatially distributed chronic pain (fibromyalgia)." Pain 124(3): 242-263.

Vidal, B. C., M. L. Mello and E. R. Pimentel (1982). "Polarization microscopy and microspectrophotometry of Sirius Red, Picrosirius and Chlorantine Fast Red aggregates and of their complexes with collagen." Histochem J 14(6): 857-878.

Voyvodic, F., J. Dolinis, V. M. Moore, G. A. Ryan, J. P. Slavotinek, A. M. Whyte, R. D. Hoile and G. W. Taylor (1997). "MRI of car occupants with whiplash injury." Neuroradiology 39(1): 35-40.

Wang, L.V., and H. Wu (2007). Biomedical optics: principles and imaging, Wiley, New York.

Watkins, L. R., E. D. Milligan and S. F. Maier (2001). "Glial activation: a driving force for pathological pain." Trends Neurosci 24(8): 450-455.

Whittaker, P. and P. B. Canham (1991). "Demonstration of quantitative fabric analysis of tendon collagen using two-dimensional polarized light microscopy." Matrix 11(1): 56-62.

Willis, W.D., Jr., , and R.E. Coggeshall (1991). Sensory mechanisms of the spinal cord, Second Edition. Plenum, New York.

Willis, W. D., Jr. (1985). "Pain pathways in the primate." Prog Clin Biol Res 176: 117-133.

Winkelstein, B. A., R. W. Nightingale, W. J. Richardson and B. S. Myers (2000). "The cervical facet capsule and its role in whiplash injury: a biomechanical investigation." Spine 25(10): 1238-1246.

Winkelstein, B. A., R. W. Nightingale, W. J. Richardson and B. S. Myers (1999). "Cervical facet joint mechanics: its application to whiplash injury." Stapp Car Crash J 43: 243-252.

Woo, S. L., S. D. Abramowitch, R. Kilger and R. Liang (2006). "Biomechanics of knee ligaments: injury, healing, and repair." J Biomech 39(1): 1-20.

Woolf, C. J. and M. W. Salter (2000). "Neuronal plasticity: increasing the gain in pain." Science 288(5472): 1765-1769.

Yamashita, T., J. M. Cavanaugh, A. A. el-Bohy, T. V. Getchell and A. I. King (1990). "Mechanosensitive afferent units in the lumbar facet joint." J Bone Joint Surg Am 72(6): 865-870.

Yamashita, T., J. M. Cavanaugh, A. C. Ozaktay, A. I. Avramov, T. V. Getchell and A. I. King (1993). "Effect of substance P on mechanosensitive units of tissues around and in the lumbar facet joint." J Orthop Res 11(2): 205-214.

Yang, K. H. and A. I. King (2003). "Neck kinematics in rear-end impacts." Pain Res Manag 8(2): 79-85.

Yawn, B. P., P. Amadio, W. S. Harmsen, J. Hill, D. Ilstrup and S. Gabriel (2000). "Isolated acute knee injuries in the general population." J Trauma 48(4): 716-723.

Yeh, A. T., B. Choi, J. S. Nelson and B. J. Tromberg (2003). "Reversible dissociation of collagen in tissues." J Invest Dermatol 121(6): 1332-1335.

Yoganandan, N., G. Ray, F. A. Pintar, J. B. Myklebust and A. Sances (1989). "Stiffness and strain energy criteria to evaluate the threshold of injury to an intervertebral joint." J Biomech 22(2): 135-142.

Yoganandan, N., J. F. Cusick, F. A. Pintar and R. D. Rao (2001). "Whiplash injury determination with conventional spine imaging and cryomicrotomy." Spine 26(22): 2443-2448.

Yoganandan, N., S. Kumaresan and F. A. Pintar (2000). "Geometric and mechanical properties of human cervical spine ligaments." J Biomech Eng 122(6): 623-629.

Yoganandan, N. and F. A. Pintar (1997). "Inertial loading of the human cervical spine." J Biomech Eng 119(3): 237-240.

Yoganandan, N., F. A. Pintar and M. Klienberger (1998). "Cervical spine vertebral and facet joint kinematics under whiplash." J Biomech Eng 120(2): 305-307.

Zdeblick, T. A., J. J. Abitbol, D. N. Kunz, R. P. McCabe and S. Garfin (1993). "Cervical stability after sequential capsule resection." Spine 18(14): 2005-2008.

Zhang, D. and D. D. Arola (2004). "Applications of digital image correlation to biological tissues." J Biomed Opt 9(4): 691-699.

Zimmermann, M. (1983). "Ethical guidelines for investigations of experimental pain in conscious animals." Pain 16(2): 109-110.

Zou, X., Q. Lin and W. D. Willis (2000). "Enhanced phosphorylation of NMDA receptor 1 subunits in spinal cord dorsal horn and spinothalamic tract neurons after intradermal injection of capsaicin in rats." J Neurosci 20(18): 6989-6997.